The thesis focuses on the study of two phenomena, both connected to transverse electromagnetic forces, affecting the particles inside an accelerator.

The first study regards the undesired transverse kick given to the particles by the so-called wakefields, electromagnetic fields generated by the interaction of the particles themselves with the surrounding environment (e.g., the vacuum beam pipe of an accelerator, or the inner copper surface of an accelerating structure).
In the thesis, a novel method for assessing the transverse kick induced by wakefields is proposed. This method is used to study the wakefields excited by the beam in the latest prototype of the high gradient accelerating structure developed for future compact accelerators, in the framework of the CLIC study at CERN.
The experimental results have been compared with simulations, and the comparison shows a good agreement.
The results clearly indicate that the dominant effect in this case is given by the short-range part of the wakefield. The investigation explored also the often neglected dependence of the wakefield kick on the length of the particle bunch.

The second study also regards the interaction of a particle bunch with a transverse electromagnetic field, but in this case the field is intentionally applied in order to perform a measurement of the bunch length.
Firstly, an overview of the standard measurement technique is presented.
In this layout two novel measurement methods that allows to obtain additional information on the bunch properties are presented.
Such extension allows in particular to estimate the energy chirp and energy spread and to obtain information about the correlations between particle position, angular divergences, and energy.
Later, an improved layout for performing the measurement is presented. Such layout does not alter the conventional measurement properties and, at the same time, gives the flexibility to directly measure the correlations between particle position, divergences, and energy.
Besides, using the improved layout it is possible to enhance the method's metrological performance improving the resolution and the uncertainty.
A detailed study of these two topics is presented, comparing the result obtained with the two layouts.
All derived theoretical models were benchmarked with simulation and experimental measures performed on the CLEAR linear electron accelerator at CERN. A satisfying agreement was found in all cases.

Antonio Gilardi

Università degli Studi di Napoli Federico II

Ph.D itee Information Technology Electrical Engineering

Measurements of wakefields and bunch length with beam in linear electron accelerators: a case study at the CLEAR facility

2020 - XXXIII

Measurements of wakefields and bunch length with beam in linear electron accelerators: a case study at the CLEAR facility

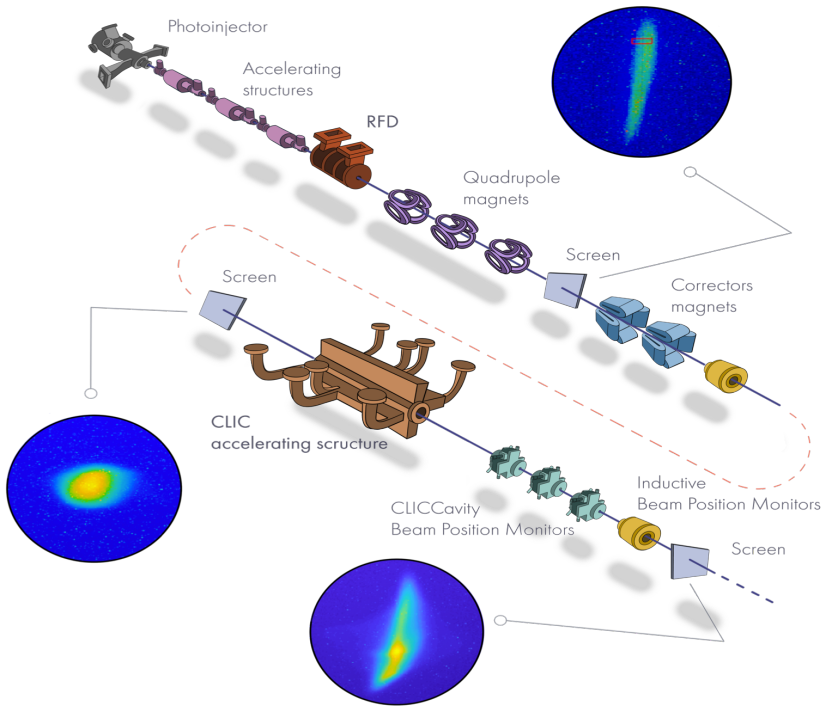

Antonio Gilardi

Ph.D. in Information Technology and Electrical Engineering

UNIVERSITÀ DEGLI STUDI DI NAPOLI
FEDERICO II

UNIVERSITÀ DEGLI STUDI DI NAPOLI FEDERICO II

PH.D. THESIS

IN

INFORMATION TECHNOLOGY AND ELECTRICAL ENGINEERING

MEASUREMENTS OF WAKEFIELDS AND BUNCH LENGTH WITH BEAM IN LINEAR ELECTRON ACCELERATORS: A CASE STUDY AT THE CLEAR FACILITY

ANTONIO GILARDI

TUTOR: PROF. PASQUALE ARPAIA

COORDINATOR: PROF. DANIELE RICCIO

XXXIII CICLO

SCUOLA POLITECNICA E DELLE SCIENZE DI BASE
DIPARTIMENTO DI INGEGNERIA ELETTRICA E TECNOLOGIE DELL'INFORMAZIONE

UNIVERSITY OF NAPLES FEDERICO II

PH.D. THESIS
IN
INFORMATION TECHNOLOGY AND ELECTRICAL ENGINEERING

Measurements of wakefields and bunch length with beam in linear electron accelerators: a case study at the CLEAR facility

Supervisors:
Prof. Pasquale Arpaia
Dr. Roberto Corsini

Candidate:
Antonio Gilardi

2020 - 2021

"The more I work, the more luck I seem to have"
cit. Thomas Jefferson

To my incredible family,
to Federica,
to my true friends,
and to my fervent teachers.
You are the motivation behind all the endeavours.

Preface

WRITTEN BY *Wilfrid Farabolini*

There have been many sources of satisfaction for me over the last few years working at CERN and indubitably, my daily relations with Antonio are a significant one. He joined the CLEAR team with great enthusiasm that has never diminished. His creativity, originality, analytical skills, practical knowledge, and go-forward spirit have been a key factor in the success of many experiments.

As with many PhD students, Antonio has provided essential support in accelerator operations, but in his case, this contribution was literally a devotion. He has continuously been available to help the facility users to think, develop, and install their experiments. Finding solutions to last minute problems that otherwise would have prevented the success, preparing beams with the desired characteristics, never accepting a substandard beam and often working long shifts during the night.

Nevertheless, his dedication to CLEAR never made him forget the subject of his thesis, which is so important for the future of LINACs.He made accurate measurements of the kick experienced by the beam when passing off axis in the structure and compared them to models. The initial observed discrepancy led to the discovery of an error in the calibration of the beam charge monitor and thus prevented significant problems for the facility. The high accuracy requested for these measures made it necessary to improve many diagnostics and to master the beam setup. I can say that Antonio has become an expert in beam preparation and diagnostics conception.

Among these beam diagnostics, Antonio has greatly improved the measurement of bunch length using a deflecting cavity. Firstly, developing two measurement models for investigating additional bunch parameters; later, he rigorously demonstrated the measurement method's validity in association with a quadrupole. His extensive computations provide guidance to set the parameters of the magnets and diagnostics in order to obtain the best possible resolution and uncertainty.

Despite the time and energy requested to achieve his PhD studies, Antonio always found time to propose machine developments and to participate to their deployment, even in their hardware construction.
In addition to a solid knowledge of accelerator physics, his competencies and passion for new technologies opened new exciting fields to us. Antonio also took an essential part in promoting the science of accelerators towards young students, giving many talks in high-prestige institutions and contributing to the Joint Universities Accelerator School (JUAS) accelerator school, a school he had himself attended.

It is also worth mentioning the important grant he won from the Gruppo Di Misure Elettriche Ed Elettroniche (GMEE) for developing a robotic device to manipulate samples in the beam for medical research. This research topic is nowadays under intense development and, thanks to his effort, many satisfactory milestones have already been achieved. I really enjoy the time spent together and hope that Antonio will continue his activities in the CLEAR facility. I look forward to continue to work with him.

Abstract

The thesis focuses on the study of two phenomena, both connected to transverse electromagnetic forces, affecting the particles inside an accelerator.

The first study regards the undesired transverse kick given to the particles by the so-called wakefields, electromagnetic fields generated by the interaction of the particles themselves with the surrounding environment (e.g., the vacuum beam pipe of an accelerator, or the inner copper surface of an accelerating structure). In the thesis, a novel method for assessing the transverse kick induced by wakefields is proposed. This method is used to study the wakefields excited by the beam in the latest prototype of the high gradient accelerating structure developed for future compact accelerators, in the framework of the CLIC study at CERN. The experimental results are compared with simulations, and the comparison shows a good agreement. The results clearly indicate that the dominant effect in this case is given by the short-range part of the wakefield. The investigation explored also the often neglected dependence of the wakefield kick on the length of the particle bunch.

The second study also regards the interaction of a particle bunch with a transverse electromagnetic field, but in this case the field is intentionally applied in order to perform a measurement of the bunch length. Firstly, an overview of the standard measurement technique is presented. In this layout two novel measurement methods that allows to obtain additional information on the bunch properties are presented. Such extension allows in particular to estimate the energy chirp and energy spread and to obtain information about the correlations between particle position, angular divergences, and energy. Later, an improved layout for performing the measurement is presented. Such layout does not alter the conventional measurement properties and, at the same time, gives the flexibility to directly measure the correlations between particle position, divergences, and energy. Besides, using the improved layout it is possible to enhance the method's metrological performance improving the resolution and the uncertainty. A detailed study of these two topics is presented, by comparing the result obtained with the two layouts. All derived theoretical models were benchmarked with simulation and experimental measures performed on the CLEAR linear electron accelerator at CERN. A satisfying agreement was found in all cases.

Keywords: Particle accelerators, wakefield measurements, accelerating structures, bunch length measurements, Radio Frequency Deflector.

Cover Image: An artistic view of the two main experimental areas described in the dissertation, the deflecting cavity and the accelerating structure, including some of the instrumentation and beam devices around them.

Sommario

La tesi si focalizza sullo studio di due fenomeni, entrambi connessi alle forze elettromagnetiche che influenzano le particelle all'interno di un acceleratore.

Il primo studio riguarda i kick trasversi indesiderati dati alle particelle dai cosiddetti wakefields, campi elettromagnetici generati dall'interazione delle particelle con l'ambiente circostante (ad esempio, la camera a vuoto dell'acceleratore, o la superficie interna in rame di una struttura accelerante). Nella tesi, viene proposto un nuovo metodo per valutare il calcio trasversale indotto dai wakefields. Questo metodo viene utilizzato per studiare i wakefields eccitati dal fascio nell'ultimo prototipo di struttura accelerante ad alto gradiente sviluppata per futuri acceleratori compatti, nell'ambito dello studio CLIC al CERN. I risultati sperimentali sono stati confrontati con le simulazioni, e il confronto mostra un buon accordo. I risultati indicano chiaramente che l'effetto dominante in questo caso è dato dalla parte a corto raggio del wakefield. L'indagine ha esplorato anche la dipendenza spesso trascurata del wakefield kick dalla lunghezza del pacchetto di particelle.

Il secondo studio riguarda l'interazione di un fascio di particelle con un campo elettromagnetico trasversale, ma in questo caso il campo è intenzionalmente applicato per effettuare una misura della lunghezza del pacchetto di particelle. In primo luogo viene presentata una panoramica della tecnica di misurazione standard, ma estendendo i metodi di misurazione al fine di ottenere ulteriori informazioni sulle proprietà del pacchetto di particelle. Tale estensione consente, in particolare, di stimare il chirp e lo spread energetico e di ottenere informazioni sulle correlazioni tra posizione delle particelle, divergenze angolari ed energia. Successivamente, viene presentato un layout migliorato per eseguire la misurazione. Tale layout non altera le proprietà di misurazione convenzionali e allo stesso tempo, offre la flessibilità per misurare direttamente le correlazioni tra posizione delle particelle, divergenze ed energia. Inoltre, utilizzando il layout migliorato è possibile migliorare le prestazioni metrologiche del metodo migliorando la risoluzione e l'incertezza. Viene presentato uno studio dettagliato di questi due argomenti, confrontando il risultato ottenuto con i due layout. Tutti i modelli teorici derivati sono stati confrontati con simulazioni e misure sperimentali eseguite sull'acceleratore di elettroni lineare CLEAR al CERN. In tutti i casi è stato trovato un accordo soddisfacente.

Keywords: Accelleratori di particelle , misure di wakefield, strutture accelleranti, misure di lunghezza di bunch , Deflettore a Radio Frequenza.

Cover Image: Una visione artistica delle due principali aree sperimentali descritte nella dissertazione, la cavità deflettrice e la struttura accelerante, comprese alcune delle strumentazioni e dispositivi attorno ad esse.

List of publications

Journal publications:

(i) D. Söderström, L.M. Luza, H. Kettunen, A. Javanainen, W. Farabolini, A. Gilardi, A. Coronetti, C. Poivey and L. Dilillo; *"Electron-Induced Upsets and Stuck Bits in SDRAMs in the Jovian Environment."* **IEEE Transactions on Nuclear Science** (March, 2021).
doi:10.1109/TNS.2021.3068186

(ii) K. Kokurewicz, E. Brunetti, A. Curcio, D. Gamba, L. Garolfi, A. Gilardi, E. Senes, K.N. Sjobak, W. Farabolini, R. Corsini, and D. Jaroszynski; *"An experimental study of the dose distribution of focused very high energy electron (VHEE) beams for radiotherapy". Accepted at Nature Communications Physics."* **Nature Communication Physics** 4, no. 33 (February, 2021).
doi:10.1038/s42005-021-00536-0

(iii) K.L. Small, N.T. Henthorn, D. Angal-Kalinin, A.L. Chadwick, R.C. Morris, E. Santina, A. Aitkenhead, K.J. Kirkby, R.J. Smith, M. Surman, J. Jones, W. Farabolini, R. Corsini, D. Gamba, A. Gilardi, M.J. Merchant, and R.M. Jones. *"Evaluating Very High Energy Electron RBE from nanodosimetric pBR322 plasmid DNA damage"*. **Scientific Reports** 11, no. 3341 (February, 2021).
doi:10.1038/s41598-021-82772-6

(iv) D. Poppinga, R. Kranzer, W. Farabolini, A. Gilardi, R. Corsini, V. Wyrwoll, H.K. Looe, B. Delfs, L. Gabrisch and B. Poppe; *"VHEE Beam Dosimetry at CERN Linear Electron Accelerator for Research Under Ultra-High Dose Rate Conditions."* **Biomedical Physics & Engineering Express** 7, no. 1 (December, 2020).
doi:10.1088/2057-1976/abcae5.

(v) F. Romano, A. Subiel, A. McManus, N.D. Lee, H. Palmans, R. Thomas, S. McCallum, G. Milluzzo, M. Borghesi, A. McIlvenny, H. Ahmed, W. Farabolini, A. Gilardi, and A. Schüller; *"Challenges in Dosimetry of Particle Beams with Ultra-High Pulse Dose Rates."* **Journal of Physics: Conference Series** 1662 (October, 2020).
doi:10.1088/1742-6596/1662/1/012028.

(vi) L. Sabato, P. Arpaia, A. Gilardi, A. Mostacci, L. Palumbo, and A. Variola; *"A Measurement Method Based on RF Deflector for Particle Bunch Longitudinal Parameters in Linear Accelerators."* **IEEE Transactions on Instrumentation and Measurement** 70 (July, 2021).
doi:10.1109/tim.2020.3009342.

(vii) P. Arpaia, R. Corsini, A. Gilardi, A. Mostacci, L. Sabato, and K.N. Sjobak; *"Enhancing Particle Bunch-Length Measurements Based on Radio Frequency Deflector by the Use of Focusing Elements."* **Scientific Reports** 10, no. 1 (July, 2020).
doi:10.1038/s41598-020-67997-1.

(viii) M. McManus, F. Romano, N.D. Lee, W. Farabolini, A. Gilardi, G. Royle, H. Palmans, and A. Subiel; *"The Challenge of Ionisation Chamber Dosimetry in Ultra-Short Pulsed High Dose-Rate Very High Energy Electron Beams."* **Scientific Reports** 10, no. 1 (June, 2020).
doi:10.1038/s41598-020-65819-y.

(ix) A. Curcio, M. Bergamaschi, R. Corsini, W. Farabolini, D. Gamba, L. Garolfi, R. Kieffer, T. Lefevre, S. Mazzoni, K. Fedorov, J. Gardelle, A. Gilardi, P. Karataev, K. Lekomtsev, T. Pacey, Y. Saveliev, A. Potylitsyn, and E. Senes; *"Noninvasive bunch length measurements exploiting Cherenkov diffraction radiation."* **Physical Review Accelerators and Beams**, vol. 23, no. 2 (February, 2020).
doi:10.1103/physrevaccelbeams.23.022802.

(x) P. Arpaia, O.E. Berrig, L. De Vito, and A. Gilardi; *"Reducing Parasitic Resonances in Particle Accelerators Components by Broadband Higher–Order–Mode Couplers."* **Measurement** 146: 938–947 (November, 2019).
doi:10.1016/j.measurement.2019.07.034.

Conference proceedings:

(i) D. Soderstrom, L.M. Luza, H. Kettunen, A. Javanainen, W. Farabolini, A. Gilardi, A. Coronetti, C. Poivey, and L. Dilillo; *"Electron-Induced Upsets and Stuck Bits in SDRAMs in the Jovian Environment."* **IEEE Nuclear and Space Radiation Effects Conference (NSREC)** (November, 2020).
Available at: https://hal-lirmm.ccsd.cnrs.fr/lirmm-03028881.

(ii) F. Wilfrid, A. Gilardi, B. Gkotse, A. Mapelli, I. Mateu, V. Meskova, G. Pezzullo, F. Ravotti, and O. Sidiropoulou; *"A beam profile monitor for high energy proton beams using microfabrication techniques."* **9th International Beam Instrumentation Conference (IBIC)** (September, 2020).
doi:10.18429/JACoW-IBIC2020-TUPP37

(iii) V. Meskova, D. Bouvet, W. Farabolini, A. Gilardi, B. Gkotse, I. Mateu, G. Pezzullo, F. Ravotti, M. Ritala; J.M. Sallese, and O. Sidiropoulou; *"Ultra high-level Radiation Monitoring with Thin Metal Nano-Layers (NanoRadMet)."* **ATTRACT Final Conference** (September, 2020).
Available at:
https://attract-eu.com/wp-content/uploads/2019/05/NanoRadMet.pdf.

(iv) P. Arpaia, R. Corsini, A. Gilardi, and K.N. Sjobak; *"Beam–based Alignment of the CLIC High-Gradient X-Band Accelerating Structure Using Beam-Screen"*; **IEEE International Instrumentation and Measurement Technology Conference (I2MTC)** (May, 2019).
doi:10.1109/i2mtc.2019.8827121.

(v) K. Sjobak, E. Adli, M. Bergamaschi, S. Burger, R. Corsini, A. Curcio, S. Curt, S. Döbert, W. Farabolini, D. Gamba, L. Garolfi, A. Gilardi, I. Gorgisyan, E. Granados, H. Guerin, R. Kieffer, M. Krupa, T. Lefevre, C.Lindstrøm, A. Lyapin, S. Mazzoni, G. McMonagle, J. Nadenau, H. Panuganti, S. Pitman, V. Rude, A. Schlogelhofer, P. Skowroński, M. Wendt, and A. Zemanek; *"Status of the CLEAR electron beam user facility at CERN."* **10th Int. Particle Accelerator Conference (IPAC'19)**, Melbourne, Australia (May, 2019).
doi: 10.18429/JACoW-IPAC2019-MOPTS054.

(vi) P. Arpaia, O.B. Berrig, L. De Vito, and A. Gilardi; *"Experimental Analysis for the Optimal Choice of High-Order Modes Couplers Design Parameters for Resonance Damping."* **IEEE International Instrumentation and Measurement Technology Conference (I2MTC)** (May, 2018).
doi:10.1109/i2mtc.2018.8409858.

Books:

(i) CLIC collaborations. *"The Compact Linear e^+–e^- Collider (CLIC): Physics Potential."* **CERN Yellow Reports: Monographs** (December, 2018) - CLICdp-Note-2018-010.
Available at: https://cds.cern.ch/record/2652257.

(ii) CLIC collaborations. *The Compact Linear e^+–e^- Collider (CLIC): Accelerator and Detector.* **CERN Yellow Reports: Monographs** (December, 2018) - arXiv:1812.07987.
Available at: https://cds.cern.ch/record/2652846.

(iii) CLIC collaborations. *"The Compact Linear e^+–e^- Collider (CLIC) - 2018 Summary Report."* **CERN Yellow Reports: Monographs** (December, 2018) - arXiv: 1812.06018.
doi: 10.23731/CYRM-2018-002.

Acknowledgements

Once more, unexpectedly, here we are. It is time to sit down and look back on the days spent during this journey. I have thought about this moment a lot over the last few months, and I would like to say many things. But in the end, I'm not sure that I'm going to be able to express in words the huge feelings I have. But, I am sure you will understand. Many people indeed deserve to be mentioned here, so it will take a bit. To make it easy, I will mostly write in English, but I will switch to French and Italian for those with a strict preference.

All the research presented in this dissertation was carried out at CERN laboratories, particularly at the CLEAR facility. One can imagine this accelerator as a lighthouse that pushes the light of knowledge further each day. Over the last few years, it has been the only accelerator in operation in a place where accelerators are a must. Furthermore, the people contributing to its operation day after day endure many difficulties, only for the love of research: I had the luck of calling these people friends and colleagues. Each one taught me so much from a personal and scientific point of view.

Firstly, I feel deeply grateful to Roberto Corsini, my CERN supervisor and our facility coordinator, for always believing in me. Thank you for the constant guidance, excellent advice, confidence, and opportunities for professional growth you have given me. Wilfrid Farabolini, and Kyrre Sjobaek, you have been two guiding lights that have lit my way, showing me how a mature researcher of a very high profile must behave. You are so different, but at the same time so close. For me, you represent the ideal of a genuine researcher. You taught me so much; I can barely remember how I was before meeting you. I will always carry a piece of you with me, thanks a lot.

A huge thanks to Davide Gamba, Andrea Latina, Luca Garolfi, and Luke Dyks, for the time spent together and for the helpful and fruitful discussions. You have been an essential piece of my journey, always there to support my ideas.

I would like to take the time to thank all the collaborators/friends that have always been forthcoming with their knowledge. In particular, I feel proud to mention Thibaut Lefevre, Stefano Mazzoni, Eugenio Senes, Michele Bergamschi, Gerrard Mcmonagle, Steffen Doebert,and Edu Granados. Thank you for your friendly and kind attitude, I learned a lot.

What's more, two important people have greatly contributed to my professional and personal growth: Luca Sabato and Andrea Mostacci. Luca Sabato, who not only is an impressive football player but is also an important friend with huge knowledge. And Andrea Mostacci, indeed an incredible example to be inspired by, a special person. Without a doubt, I can state that I found in him one of the most enthusiastic researchers I have ever met. I hope to keep collaborating with you from the bottom of my heart and maintaining the wonderful relationship we

have built. Thank you so much.

I am profoundly pleased to thank my mentor, Prof. Pasquale Arpaia, for the invaluable academic supervision, for presenting the opportunity to start my CERN career, and teaching me to embrace new challenges without fear.

On a personal note, many actors have played a key role in my daily life. I think it is mandatory to start with Federica. She has been through the difficult times, through the long working hours, through it all and always there supporting me. For this, I thank you from the bottom of my heart.

I would like to thank the whole team of Dynamo Weasels. It has been an honor playing with you all and especially as your captain; you have been an important part of these years. I wish you, past and present players, all the best. I sincerely hope to play and win with you again.

How can I forget "Rue des Cheminets", the place where I found the love of my life and some of the best friends ever? Simone and Manuel, you have been two precious friends and accomplices. The first time we met, I felt something really cool was happening, and indeed it was. Thanks for your friendship. Then there are Mattia, Lorenzo, Eleonora, Shukri, Francesco, Stefano, Caterina, and little Samuele, you have been wonderful. I will remember forever the amazing time spent together.

I would also like to mention the people without whom it would not have been possible to go through this journey far from home. Particularly, Andrea, Mariano, Barbara, Carmine, Agostino, and Alessandro. You have all been an important part of my life here; thank you all. Since I cited it, I would also like to spend a few words about home, my city Naples. Despite the thousand reasons that have pushed me to go abroad, I still hope to come back one day and give back something to this wonderful place that has made me the man I am today.

Je suis honoré d'avoir travaillé avec des techniciens d'aussi haut niveau que Stéphane, Alan, Thomas, Renaud, Arthur et Serge. Vous m'avez toujours fasciné, m'apprenant beaucoup grâce à vos connaissances impressionnantes et votre attitude amicale. Votre professionnalisme et votre précision resteront toujours une grande source d'inspiration. Merci à vous tous.
La mia più profonda gratitudine va alla mia famiglia. Siete un fulcro importante della mia vita, avete sempre dimostrato di supportare le mie scelte, anche se so che spesso non le condividete. Ringrazio dal profondo del mio cuore mia madre e mio padre, Rita e Vincenzo, siete due genitori magnifici. Mi avete insegnato a non arrendermi mai e a prendere le cose con leggerezza, grazie infinitamente. Mamma io penso di sapere cosa provi ogni volta che vado via, ma sappi che io vi porto con me ogni volta che vado, ovunque io vado. Papa, so che tra di noi uno sguardo, una risata vale più di mille parole. So quanto sei orgoglioso di me e questo mi da la forza di continuare a cercare di migliorare. Un enorme grazie

a mia sorella Monica, per la sua disponibilità e la tua gentilezza, ovunque io mi trovi, sono sicuro di poter contare su di te. Ad Alessandro, un cognato ed un prezioso amico sempre disponibile, ed alla sua magnifica famiglia, grazie a voi la nostra piccola famiglia si sta estendendo e sta diventando qualcosa di ancora più bello.
Grazie a zia Anna, zia Rita e zio Peppe so di poter contare sempre su di voi. Spero di rendervi orgogliosi almeno la meta di quanto io lo sono di voi. Siete una parte importante che custodisco con gelosia. A mio cugino Andrea, spero con tutto me stesso tu possa trovare in me un aiuto ogni volta che ne avrai bisogno. Saro sempre pronto a supportarti.
Grazie nonna, per la tua infinita gentilezza, per i tuoi sorrisi e per quell'attitudine che ti ha portata negli anni ad essere cosi forte. È uno dei momenti più rassicuranti quando ti chiedo come va e tu mi rispondi sempre "eh diciamo bene".
Grazie al nonno, anche se la tua mancanza si fa sentire quotidianamente da ormai quasi sette anni i nostri ricordi sono nitidi dentro di me come fosse ieri che mi guardavi e dicevi che non capivo niente. Più passa il tempo e più capisco quanto tu avessi (ed hai) ragione.
Grazie alla meravigliosa famiglia Murgia, mi hanno sempre fatto sentire a casa con la loro gentilezza ed allegria.
Grazie gli amici di sempre, che oggi sono sparsi un po' in giro nel mondo, persone speciali con capacita e determinazione fuori dal normale. Grazie a Armando, Luca, Marco, Andrea, Tommaso, Enrico, Ernesto, Giacomo, Antonio, Roberto, Manuela e Fabiana. Grazie per la vostra amicizia, ogni volta che ci vediamo sento sempre come se fosse passato solo un giorno dall'ultima volta. Nel mio percorso mi portato per sempre con me quella fame e voglia di riscatto che ho sempre sentito chiaramente in tutti voi.
Vorrei anche ringraziare i miei professori, persone uniche con una devozione infinita per il loro lavoro. Siete una contante fonte di inspirazione.

After writing so much, I just realized that I will probably never be able to express how lucky I was meeting all of you and how much all of you all have contributed to my journey.
THANK YOU.

CERN - Geneva, Switzerland
Antonio Gilardi

Contents

List of Abbreviations

ACE3P	**A**dvanced **C**omputational, **E**lectromagnetics **3**D **P**arallel
ADC	**A**nalog to **D**igital **C**onverter
AOI	**A**rea **O**f **I**nterest
ASTRA	**A** **S**pace **C**harge **T**racking **A**lgorithm
ATF	**A**ccelerator **T**est **F**acility
ATF2	**A**ccelerator **T**est **F**acility **2**
AWAKE	**A**dvanced proton driven plasma **WAK**field **E**xperiment
BBU	**B**eam **B**reak**U**p
BNL	**B**rookhaven **N**ational **L**ab
BPM	**B**eam **P**osition **M**onitors
CALIFES	**C**oncept d'**A**ccélérateur **L**inéaire pour **F**aisceau d'**E**lectron **S**onde
CCD	**C**harge **C**oupled **D**evice
CCR	**C**oherent **C**herenkov **R**adiation
CDF	**C**umulative **D**istribution **F**unction
CDR	**C**onceptual **D**esign **R**eport
CERN	**C**onseil **E**uropéen pour la **R**echerche **N**ucléaire
CLEAR	**C**ERN **L**inear **E**lectron **A**ccelerator for **R**esearch
CLIC	**C**ompact **LI**near **C**ollider
CSPR	**C**oherent **S**mith-**P**urcell **R**adiation
CST	**C**omputer **S**imulation **T**echnology
CTF3	**C**LIC **T**est **F**acility **3**
CTR	**C**oherent **T**ransition **R**adiation
DESY	**D**eutsches **E**lektronen **SY**nchrotron
EBT3	**E**lectron **B**eam **T**herapy-**3**
ELI-NP	**E**xtreme **L**ight **I**nfrastructure-**N**uclear **P**hysics
ELEGANT	**ELE**ctron **G**eneration **AN**d **T**racking
EM	**E**lectro **M**agnetic
EOS	**E**lectro-**O**ptical **S**ampling
ESA	**E**uropean **S**pace **A**gency
ESPP	**E**uropean **S**trategy for **P**article **P**hysics
FCC	**F**uture **C**ircular **C**ollider
FEL	**F**ree **E**lectron **L**aser
FLASH	**F**ree electron **LAS**er in **H**amburg
FODO	**FO**cusing **D**ef**O**cusing
FOV	**F**ield **O**f **V**iew
GBS	**G**amma **B**eam **S**ource
GdfidL	**G**itter **d**rüber, **f**ertig **i**st **d**ie **L**aube
GUM	**G**uide **U**ncertainty **M**easurement
HOM	**H**igher **O**rder **M**ode

ILC	**I**nternational **L**inear **C**ollider
IP	**I**nteraction **P**oint
JUAS	**J**oint **U**niversities **A**ccelerator **S**chool
JUICE	**JU**piter **I**cy **M**oon **E**xplorer mission
LAL	**L**aboratoire de l'**A**ccélérateur **L**inéaire
LHC	**L**arge **H**adron **C**ollider
LIL	**L**epton **I**njector **L**INAC
LINAC	**LIN**ear **AC**celerators
MAD-X	**M**ethodical **A**ccelerator **D**esign-**X**
MIT	**M**assachusetts **I**nstitute of **T**echnology
OTR	**O**ptical **T**ransition **R**adiation
PDF	**P**robability **D**ensity **F**unction
PETS	**P**ower **E**xtraction and **T**ransfer **S**tructures
PSFC	**P**lasma **S**cience and **F**usion **C**enter
R&D	**R**esearch **&** **D**evelopment
RF	**R**adio **F**requency
RFD	**R**adio **F**requency **D**eflector
RMS	**R**oot **M**ean **S**quare
RW	**R**esistive **W**all
SCRF	**S**uper**C**onducting **RF**
SEU	**S**ingle **E**vent **U**psets
SLAC	**S**tanford **L**inear **A**ccelerator **C**enter
SLC	**S**tanford **L**inear **C**ollider
SM	**S**tandard **M**odel
SPARC LAB	**S**ources for **P**lasma **A**ccelerators and **R**adiation **C**ompton with **L**asers **A**nd **B**eams
SUSY	**SU**per**SY**mmetric
SW	**S**tanding **W**ave
TDCC26	**T**apered **D**amped **C**oupling **C**ells **26**
TDS	**T**ransverse **D**eflecting **S**tructures
TE	**T**ransverse **E**lectric
TM	**T**ransverse **M**agnetic
TW	**T**ravelling **W**ave
WFM	**W**ake**F**ield **M**onitor
VESPER	**V**ery energetic **E**lectron facility for **S**pace **P**lanetary **E**xploration missions in harsh **R**adiative environments
VHEE	**V**ery-**H**igh **E**nergy **E**lectrons
WFS	**W**akefield-**F**ree **S**teering
YAG	**Y**ttrium **A**luminum **G**arnet

Introduction

In the field of particle accelerators, and in particular for high-brightness electron LINear ACcelerators (LINACs), two topics appear nowadays as fundamental and are thoroughly investigated. The first is naturally how the particles can be accelerated efficiently and rapidly, and the second one is the advanced beam diagnostics required to assess the beam characteristics and control the beam itself during acceleration.

During the years, many research activities have been carried out to compare, study, and develop advanced technologies to accelerate particles [1]. Examples of such an effort are: the fascinating idea of using a plasma-based method to realize compact accelerators [2], the use of superconducting accelerating cavities [3], and the high-gradient and high-frequency normal conducting structures prototyped and tested in the framework of future compact accelerators [4]. Unfortunately, to reach high accelerating gradients, in the order of $100\,\mathrm{MV/m}$, (i.e., several times larger than the ones used nowadays to accelerate particles, e.g., in standard electron LINACs [5]), the use of narrow apertures in the accelerating structures is required [6]. Such a requirement is driving a non-negligible drawback, the unwanted effects of wakefields [7]. The strong Electro-Magnetic (EM) field produced by high-energy charged particles can remain trapped inside the beam pipe and affect the subsequent particles passing through it. A beam that experiences an external force by such EM fields is going to be perturbed from its reference motion. Both the transverse and longitudinal motion, with respect to the direction of acceleration, of the particles are affected. This (especially in the transverse plane) can be one of the main limitations for reaching the targeted beam/accelerator characteristics. With some approximation, the transverse effect is linear with the beam transverse offset while passing through the accelerating cells.

Such an effect was already well known at the design stage of the accelerating structure [8]. For this reason, different strategies were foreseen to study and mitigate the wakefield impact on the beam in the modern accelerating structures.

One of the main ingredient in such strategies is active re-alignment of the accelerating structures, obtained using pickup antennas and movers. In detail, the accelerating structures are manufactured with ad-hoc antennas, named Wake-Field Monitors (WFMs), installed at the Higher **O**rder Mode (HOM) coupler waveguides of an accelerating cell to directly detect the wakefield [9] excited by the beam passage. Based on the signal read from the WFM, the whole accelerating structure's position can be modified (in both horizontal and vertical plane), to recenter the accelerating structure's iris position with respect to the beam (i.e., minimizing the WFM signals).

The structure position can be changed actively thanks to a complex and accurate system of movers installed between the structure and the supporting pillars [10, 11]. At the first order, such an alignment process is equivalent if performed moving the accelerating structure or the beam (with horizontal and vertical corrector magnets), but moving the beam can be rather tricky if the beam has to pass through many accelerating structures. Such strategies have two main drawbacks: (i) the WFMs may give rather local information, i.e. only relative to the reference cell were they are installed, and (ii) the noise coming from the beam at higher frequency. In this thesis a beam-based measurement strategy to investigate the wakefields and their impact on the beam is proposed, in order to quantify better the effect of wakefields and to assess the above mentioned limitations of WFMs.

The second topic, advanced beam diagnostics, embraces several studies that are strongly growing since the measurement and the control of the beam characteristics are becoming drastically important in modern accelerators, as the required performances increase. In the thesis, novel studies on the measure of the bunch length, one of the beam's main characteristics, are reported. There are different possible ways to assess the bunch length. In the thesis, the methodology that uses the Radio Frequency Deflector (RFD) is pursued [12]. The RFD provides a transverse kick to the incoming electron bunch, introducing a relationship between its longitudinal dime**n**sion (i.e., its length) and its vertical dimension (i.e., spot size), which can be measured at a screen placed after the RFD [13, 14]. After a proper calibration (performed varying the RFD phase and measuring the bunch centroid variation), the bunch length can be assessed through the vertical spot size measurements at the screen. This type of measurement is destructive since the beam must be intercepted by a device to perform the measurement. After the calibration, which requires multiple acquisitions, the measurement can be performed as a single-shot acquisition. In the thesis, both an improvement of the standard measurement method and an improvement of the standard layout for performing the measurement are presented [15]. The improved layout uses quadrupole focusing magnets that are often already installed but usually not powered during the measurement [16]. Thus, no beamline modifications are in general required.

The transverse kicks induced by the RFD are conceptually similar to what is caused by the transverse wakefield. The main difference is that in the case of the RFD, the transverse kick is desired and can be controlled. Naturally, when the measurement is not being performed, the RFD can be switched off and the kick can be removed. Different case studies are presented to validate the proposed measurement methods. The derived theory is validated against simulations and measurement.

An interesting experimental case study for both research activities is the CERN (Conseil Européen pour la Recherche Nucléaire) Linear Electron Accelerator for Research (CLEAR) facility [17].

The proposed method for wakefield investigation is tested on the latest prototype of the Compact LInear Collider (CLIC) accelerating structure is installed in the CLEAR beamline [18]. Simultaneously, for bunch length studies, several

different methods are used at CLEAR, including an RFD. Moreover, thanks to the hardware installed in the CLEAR beamline, the proposed improved layout could be easily tested [19].

This thesis is divided into two parts: part I, Background, and part II, Proposal. In part I the context and the basic knowledge on particle accelerators needed to fully understand both studies is presented, together with their state of the art. In part II, the proposed methodology, the simulation, and the experimental results are reported separately for the two studies.

The structure of the Chapters is as follows:

- **Chapter 1: Linear particle accelerators**. An overview of the particle accelerators concept and history is presented, then one of the most advanced and ready proposal as a future accelerator, CLIC, and its last Test Facility (CTF3) are described. Finally, the CLEAR accelerator is presented, describing its characteristics, its experimental program and the main activities performed there.

- **Chapter 2: State of the Art**. First, a basic introduction to the most used mathematical treatment in beam dynamics is presented. After that, the central concept for the two studies is separately reported. Finally, an overview of the state of the art of the two central studies discussed is presented.

- **Chapter 3: Wakefield and Kick**. The methodology used to measure the wakefield and its effects is presented. Then, the equipment and the devices used are presented. Finally, the simulations and the experiments, with the relative results, are reported.

- **Chapter 4: Bunch length measurements**. The two layouts, standard and improved, are studied in detail. The mathematical derivation of the measurement method is derived and presented for both layouts. Following the case, studies are presented. Finally, the derived theories are carefully validated using simulations and measurement.

Part I

Background

Chapter 1

Linear particle accelerators

In this chapter, an overview of the reasons to accelerate particles is presented. Later, one of the most mature and ready future accelerators is presented, highlighting its latest test facility. Finally, the accelerator on which all the experimental stu**d**ies are performed during the thesis is introduced, detailing the main research areas.

1.1 Overview of the Standard Model

The use of particles to study the structure of matter started at the beginning of the 20^{th} century with the experiments of J.J.Thomson [20] and E. Rutherford [21] where the atomic structures were for the first time under investigation. The experiments were performed using the precursors of the contemporary accelerators (cathode ray tubes and alpha/beta particle sources), and the results revealed that atoms are composed of smaller particles. From that time onwards, the scientific community started to see particle physics and accelerator technology as a fundamental tool for future studies.

In the following centuries, a zoo made of many different elementary and composite particles were discovered. Throughout this period, several theories were proposed and nowadays are collectively known as the Standard Model (SM) [22].

This global theory is perhaps the most abstract description of the universe and indisputably represents one of the greatest achievements of 20^{th} century. The SM attempts to describe all subatomic particles and their interactions through a few fundamental particles in a simple way (using a loose definition of the word "simple"). In detail, the SM describes three of the four fundamental forces: electromagnetism, the weak interaction, and the strong interaction. The fourth force, unfortunately not described, is gravity. The SM theorized 17 different elementary particles (Fig. 1.1), organized into matter (fermions) and force carriers (bosons). After the discovery of the Higgs Boson [24], the existence of all fundamental particles predicted by the SM of particle physics was confirmed.

Unfortunately, there are still multiple physical phenomena that cannot be explained or described within the framework of the SM, such as gravity, dark matter, dark energy, neutrino masses, and matter-antimatter symmetry. One candidate theory, or more properly a family of multiple theories, that may solve these problems are the SUperSYmmetric theories (SUSY) [25].

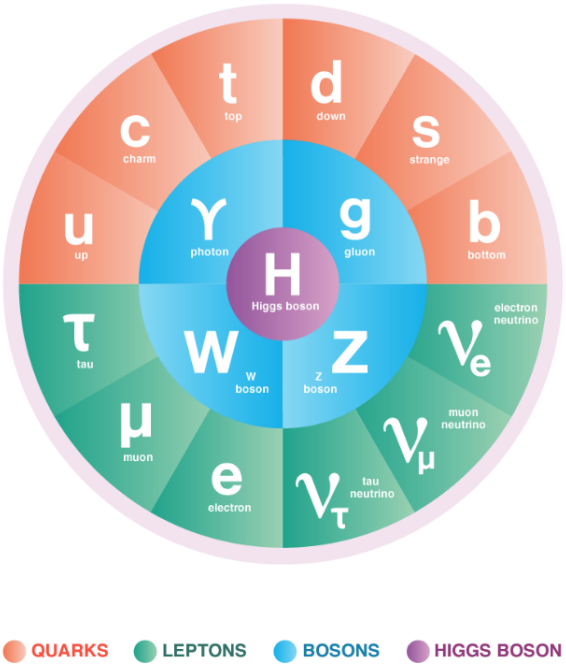

FIGURE 1.1: The 17 particles of the Standard Model, all experimentally verified. Two types of matter particles (fermions): quarks and leptons. Force carriers (bosons), mediating electromagnetism (photon), the weak interaction (W and Z), and the strong interaction (gluon). Lastly, the Higgs boson is responsible for giving particles mass [23].

1.2 Accelerated particles

The reason why accelerated particles are used to probe matter and to prove/disprove theories about ultimate constituents of the universe and their interactions can be explained using a simple parallel. The visible light is characterized by a wavelength (λ) approximately of $10\,\mu\mathrm{m}$, and this determines its spatial resolution limit. On the other hand, the Bohr radius [26], the approximate distance between the proton and the electron in a hydrogen atom, is much smaller (in the order of $10\,\mathrm{pm}$), and for this reason the atomic structure cannot be studied with visible light. However to a particle with a certain momentum p can be associate an equivalent "de Broglie wavelength" [27], $\lambda_{eq} = h/p$, where h is the Planck constant [28]. As a consequence, increasing the momentum p by means of acceleration, the equivalent wavelength λ_{eq} can be decreased. This results in an enhancement in its spatial resolution limit.

From a particle physics point of view, when two accelerated particles collide, their combined energy is then converted randomly into any and all available particles, as long as it conserves energy-momentum and various quantum numbers. Repeating these collisions between particles with higher and higher momentum a large number of times, increasingly rare processes and particles can thus be studied. Unfortunately, the higher the energy scale the bigger and/or more complex particle accelerators become.

In the years, as they were developed more and more in order to improve performances, particle accelerator technologies have found a variety of uses, from consumer products (e.g., microwave ovens) [29, 30] and industrial applications (e.g., semiconductor implantation) [31], to medical applications (e.g., cancer treatment) [32], and maybe in future for power production (e.g., accelerator-driven nuclear reactors) [33]. However, these are mostly spin-offs of machines that were initially made for fundamental physics research [34]. The largest and most powerful existing accelerator to date is the Large Hadron Collider (LHC) [35] at CERN, which is a $27\,\mathrm{km}$ long storage ring, where protons and heavy ions are stored and accelerated up to $7\,\mathrm{TeV}$. The LHC will continue to run until at least 2035. After it, many different projects are on the table, such as the Future Circular Collider (FCC) [36], the Compact Linear Collider (CLIC) [37], and the International Linear Collider (ILC) [38]. While considering plans for future machines and which kind of particles should be accelerated by them, one needs to take into account the fact that protons are composite particles. This means that the collisions take place between their constituent (quarks and gluons), but there is no a-priori knowledge of which particles collide and at which energy, which adds complexity to the detector design and data reconstruction and enhance the so-called background signal (i.e., uninteresting events). In this sense, building a lepton collider (using electrons and positrons, which are elementary particles) gives much more control of the interaction because the energy of the collision is very well defined and can be controlled and varied at convenience. According to the European Strategy for Particle Physics (ESPP), one of the main priorities is to undertake design studies for the post-LHC era, a strong interest in electron-positron collider designs is expressed [39]. Furthermore, at high-energy LINear ACceleratos (LINACs) are the only viable solution for electron-positron collides, due to the energy loss from synchrotron radiation [40]. During the past years, many different studies (simulations and experimental) were performed on the CLIC scheme, which is indeed one of the most mature projects [37].

1.3 The Compact Linear Collider (CLIC)

CLIC is a multi-TeV high-luminosity linear e^+ e^- collider under studyt [37, 41, 42]. CLIC uses a novel two-beam acceleration technique [43], and to reach high beam energy while keeping the length of the accelerator "compact", normal conducting accelerating structures with an accelerating gradient in the range of $100\,\mathrm{MV/m}$ were chosen,since superconducting cavities are not able to support such high gradients. The optimization of cost and power consumption, taking also into account the limitations due to geometric tolerances and Radio Frequency (RF) breakdown phenomena, resulted in the choice of $12\,\mathrm{GHz}$ RF (X-Band) and a beam pulse length of $240\,\mathrm{ns}$ [44]. Using such a high gradient accelerating structures makes it possible to reach very high energies with a reasonable machine length. The accelerator length scales from 11.4 to $50.1\,\mathrm{km}$, depending on the collision energy, and it's meant to be built in three stages, extending its center of mass collision energy from $380\,\mathrm{GeV}$ to $3\,\mathrm{TeV}$ [37]. An overview of the CLIC installation project and the three relative stages is illustrated in Fig. 1.2. The two-beam

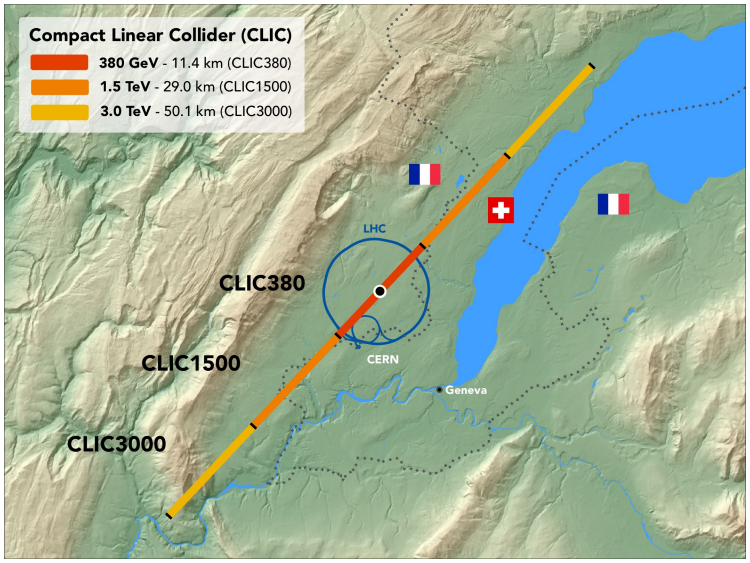

FIGURE 1.2: The CLIC main LINAC footprint near CERN, showing the three implementation stages [37].

acceleration scheme has been chosen since using the conventional RF powering scheme for each accelerating structure (i.e., using high-performance klystrons and other related RF components) would be very challenging. The two main reasons: (i) the number of needed active components is extremely high, taking into account the final stage of CLIC it would require about $30\,\mathrm{km}$ of RF components (i.e., 587 klystrons), and (ii) high-performance klystrons have a non-negligible failure rate. These drawbacks make the klystron-based full-energy CLIC very hard to run reliably. A cost analysis has also shown a slightly lower cost for the Two-Beam solution already at $380\,\mathrm{GeV}$ c.m. energy and a clearly unfavorable cost scaling of the conventional RF powering scheme with energy. The two-beam acceleration scheme is illustrated in Figs 1.3. The idea is based on a second beamline that runs in the same tunnel of the main beam accelerator and parallel to it, carrying a second electron beam. Such beam, characterized by high intensity (approximately $100\,\mathrm{A}$) and lower energy (approximately $2.4\,\mathrm{GeV}$), is named "drive beam" and is decelerated using Power Extraction and Transfer Structures (PETS) [45], generating the RF pulse needed to power the accelerating structures of the main beam. Thanks to this system, up to 90% of the energy of the drive beam is extracted in the decelerator and efficiently transferred to the main beam [46]. This scheme reduces the amount and complexity of the equipment which needs to be located in the underground tunnel and is much easier to scale to higher collision energies than a Klystron-based accelerator (such as the ILC [38]). However, an alternative CLIC scenario for the first energy stage, where the accelerating structures are powered by X-band klystrons, is also under study [48, 49]. The drive beam requires a large number of beam manipulation before being usable. The temporal structure of the beam needs to be tuned such to match the accelerating requirement of the probe beam.

A schematic layout of the final stage of CLIC is reported in Fig. 1.4. The CLIC Conceptual Design Report (CDR) was published in the past years [44] with the

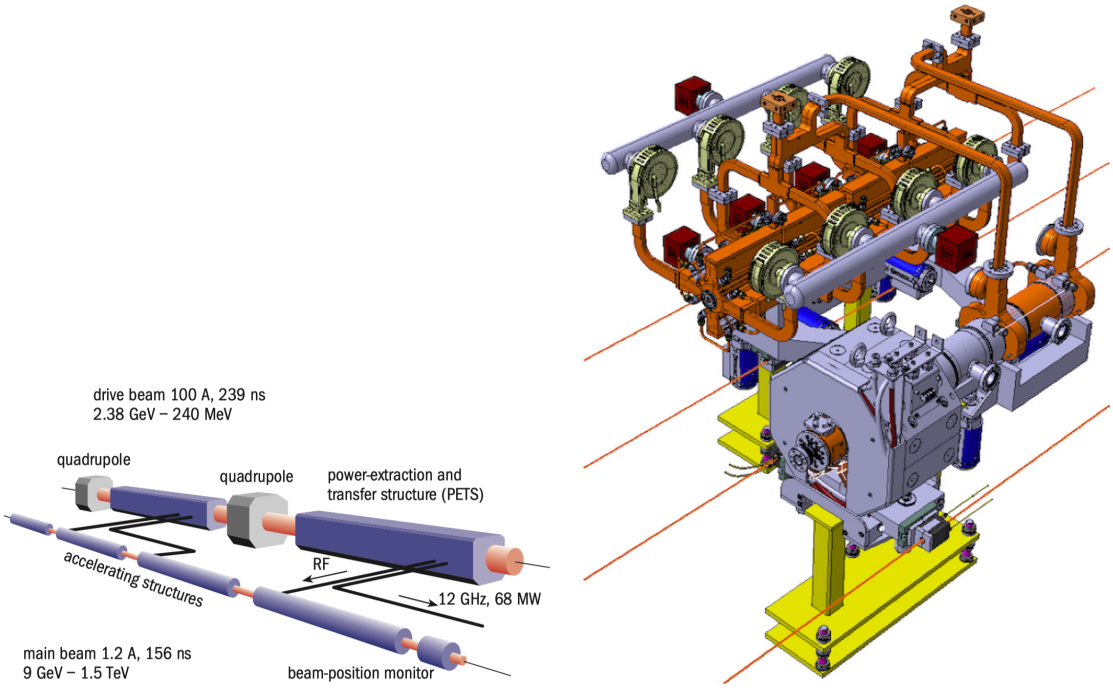

(A) (B)

FIGURE 1.3: The principle of the two-beam scheme. The beam power in the Drive Beam is converted to RF power in PETS. The conceptual schematic and a 3D rendering in (A) and (B), respectively [44, 47].

scope of demonstrating the feasibility of the CLIC accelerator at high energy and to confirm that high-precision physics measurements can be performed. CLIC indeed will push forward the threshold of physic knowledge, as summarized in [50]. An overview of the main observable process predicted by the SM observable in the CLIC machine is reported in Fig. 1.5. Figure 1.5 shows the cross-section (i.e., the probability that two particles will collide and react in a certain way [51]) as a function of the center of mass energy up to $3\,\mathrm{TeV}$. The construction of the first CLIC energy stage could start by 2026 (the estimated cost is at the level of 6 billion CHF/5.5 billion €/6.5 billion $) and the first beams would be available by 2035, marking the beginning of a broad CLIC physics program spanning 25–30 years.

1.4 CLIC Test Facility 3 (CTF3)

Many aspects of the CLIC project are very challenging, and several issues were addressed experimentally in different test accelerators built for this purpose in the recent past. The CLIC Test Facilities 1,2, and 3 [52] and the X-box facility [53], based at CERN, were built and operated to develop, test, and validate the needed technologies [54]. In particular, the latest accelerator test facility, CTF3, provided a full demonstration of the feasibility of the generation, control and use of a high-charge drive beam for high gradient X-band acceleration in a

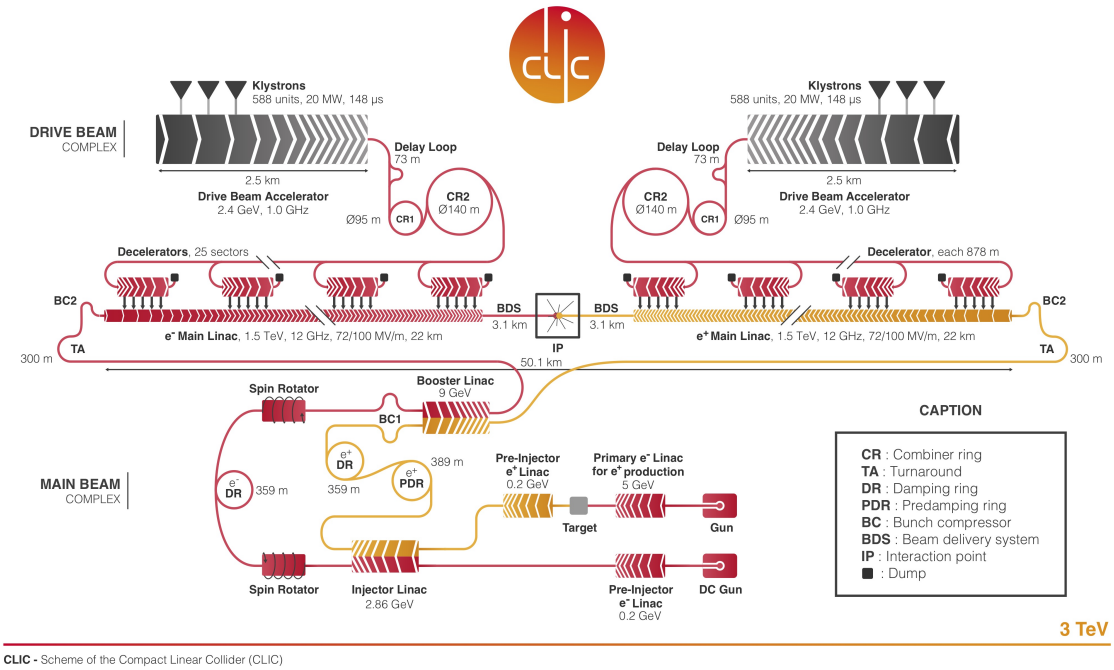

FIGURE 1.4: The latest schematic layout of the CLIC complex at 3 TeV [37].

Two-Beam scheme [55, 56, 57, 58]. At the end of 2016, having fulfilled its experimental program, CTF3 was stopped and decommissioned. However a part of the accelerating complex, shown in Fig. 1.6, the CALIFES beamline, was reborn as the CERN Linear Electron Accelerator for Research (CLEAR) facility. Nowadays, the CLEAR represents certainly a vanguard to the Research & Development (R&D) efforts committed to improving/upgrading components and increase knowledge in the accelerator field. Research and development related to the CLIC technology is still a relevant part of the scientific program of CLEAR.

1.5 CERN Linear Electron Accelerator for Research (CLEAR)

The CLEAR facility at CERN started its operation in fall 2017 [19].After about three years of operation, CLEAR has demonstrated to be a competitive R&D facility to explore novel accelerator concepts, and it has shown its flexibility and reliability. CLEAR results from the conversion of the so-called probe beamline of the former CLIC Test Facility, CTF3 into a new test-bed for general accelerator R&D and component studies for existing and possible future accelerator applications. As the acronyms describes, it is a linear accelerator, accelerating electrons (generated by photoemission from a cathode), that operates independently from CERN's main accelerator complex allowing significant flexibility in terms of operation.

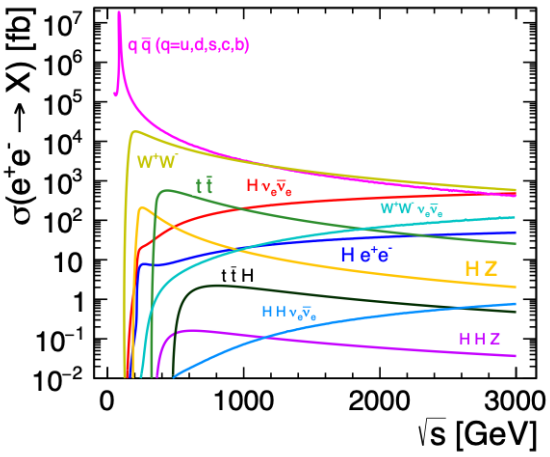

FIGURE 1.5: The cross-section versus the center of mass energy for the main SM processes at a high-energy for a e^+e^- collider [37].

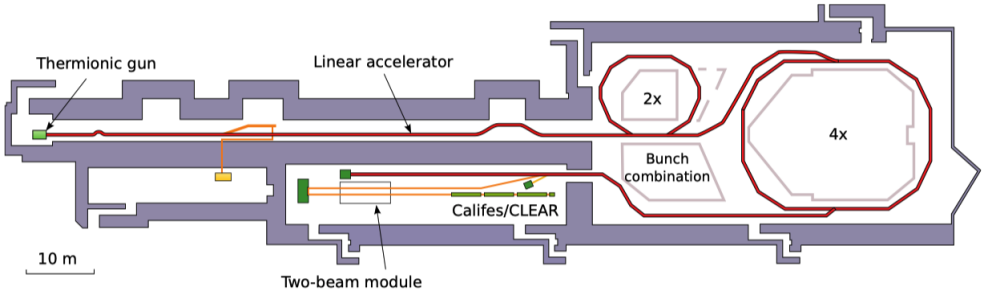

FIGURE 1.6: The sketch of the CLIC Test Facility 3 (CTF3) layout. The CALIFES line (at the bottom) was later reborn into the CLEAR facility.

The main field covered are: the test of high-gradient X-band structures, plasma focusing technology, THz emission studies, novel beam instrumentation R&D, and so on. Another important research field consists of investigating the possible use of electron beams for medical purposes and radiation hardness irradiation tests for electronic components. Thanks to the continuous technology development compact linear high energy electron accelerators are becoming more and more attractive for many different fields.

The CLEAR facility consists of a 20-meter-long accelerator (with 3 accelerating structures) followed by a 21-meter-long experimental beamline which can host several experiments. A photo of the experimental line is shown in Fig. 1.7. The facility is conveniently located in a shielded building on the surface of the CERN site. The easy access to the accelerator hall and the possibility to quickly adapt the experimental beamline to the user's needs make CLEAR a unique facility for fast and efficient beam-based research.

CLEAR is well equipped with diagnostics for measuring and optimizing the beam parameters such as bunch/train charge, bunch/train length, energy, energy-spread, and Twiss parameters [59], as well as combinations thereof. The layout of the machine is shown in Fig. 1.8.

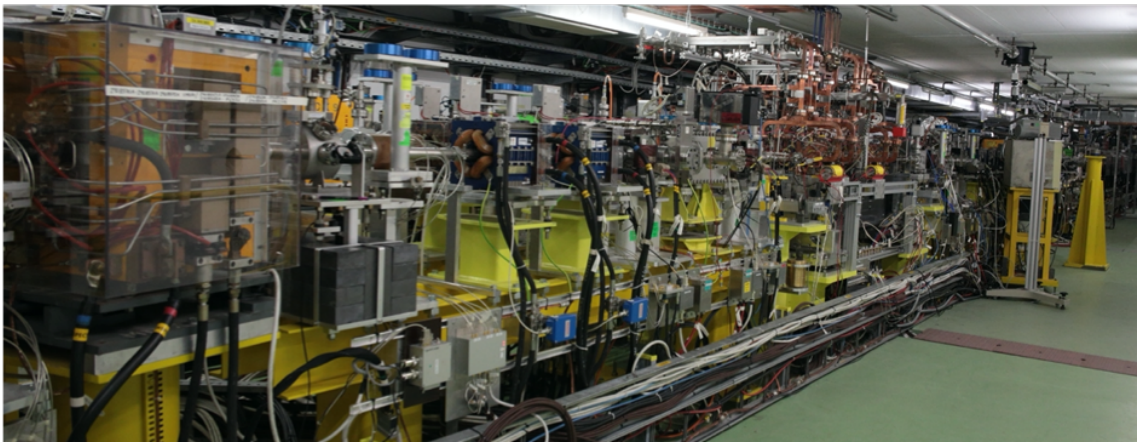

FIGURE 1.7: A photo of the experimental beamline of the CLEAR test facility.

TABLE 1.1: Range of beam main beam parameters in CLEAR.

Parameter	Range
Beam energy	60 – 220 MeV
Bunch charge	0.01 – 2.0 nC
Bunch length	0.2 – 4 ps
Bunch frequency	1.5 GHz
RF frequency	3.0 GHz
Number of bunches	1 – 200
Beam repetition rate	0.83 – 10 Hz
RMS energy spread	< 0.2 %
RMS ϵ_N	1 – 20 μm
β	1 – 40 m
α	-10 – 10

CLEAR inherited not only part of the equipment but also the operational experience acquired in the previous CTF3 facility: the first beam was set up in August and after only a few weeks-long commissioning the first users could take the beam to perform ex**p**eriments, during September 2017 [60]. Supported by a broad community of internal and external users and experts, the CLEAR group is inquiring issues on the leading edge of research in several fields. A group photo of most of the main actors in the CLEAR team is shown in Fig. 1.9.

In CLEAR it possible to quickly set up a wide variety of beams with widely different range of beams parameters; the operational ranges of the main parameters are listed in Table 1.1.

Moreover, CLEAR plays a strategic role in maintaining at CERN direct and practical expertise in generating, accelerating, and manipulating electron beams, a crucial subject given the priority allocated by the last European Strategy Update [61] to a future e+/e- collider project, be it linear or circular. For all these reasons, the CLEAR facility was set up at CERN to expand the local testing capabilities of new ideas and technologies and to provide possibilities to perform direct

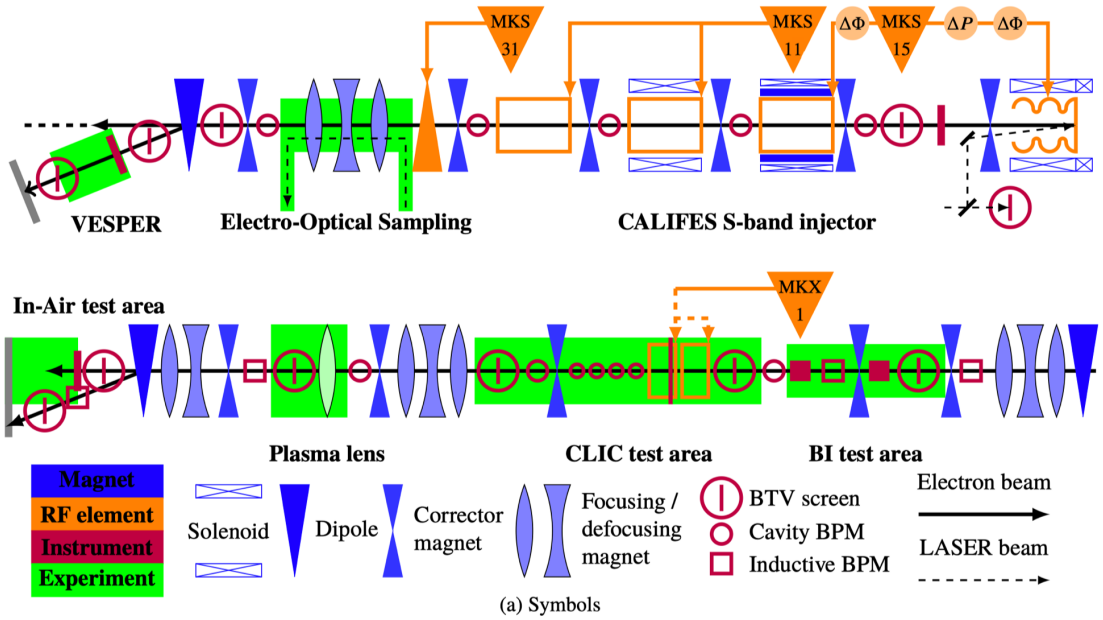

FIGURE 1.8: The CLEAR layout and the location of the main experimental stations [17].

beam-based measurements of future accelerator components. Finally, CLEAR offers also a unique learning opportunity for young accelerator physics. Several PhD thesis so far were centred on experimental work done in CLEAR, by students both based at CERN or visiting from collaboration institutes. Moreover, during March in the past years the students from the Joint Universities Accelerator School (JUAS) [62] had the opportunity of spending one day at the facility performing hands-on experiments. More information on the CLEAR activities and plans are available on the official CLEAR web page [63].

Three macro-categories of experiments performed in CLEAR can be identified: (i) CLIC-related experiments, (ii) irradiation experiments, and (iii) innovative beam technology.

1.5.1 CLIC-related tests

CLEAR is continuing the R&D effort devoted to the CLIC technology, which was at the center of the experimental program of the previous facility, CTF3. Presently the CLEAR beamline hosts a prototype of the latest versions of the CLIC accelerating structure and three prototypes of CLIC cavity Beam Position Monitors (BPMs). The CLIC BPMs are monitoring devices which measure the beam charge and position while it passes into the accelerator pipe. Similar devices are needed and used in all accelerators but in CLIC, due to the high resolution required, the design of such a device represents a very ambitious challenge. The tests on the CLIC accelerating structure represent a key topic for the whole accelerator community, since if on one side it is a fundamental component of the CLIC project, on the other it is a keystone for extending the energy reach of small accelerators, with many potential applications [53, 64]. In the CLIC project, it is required to

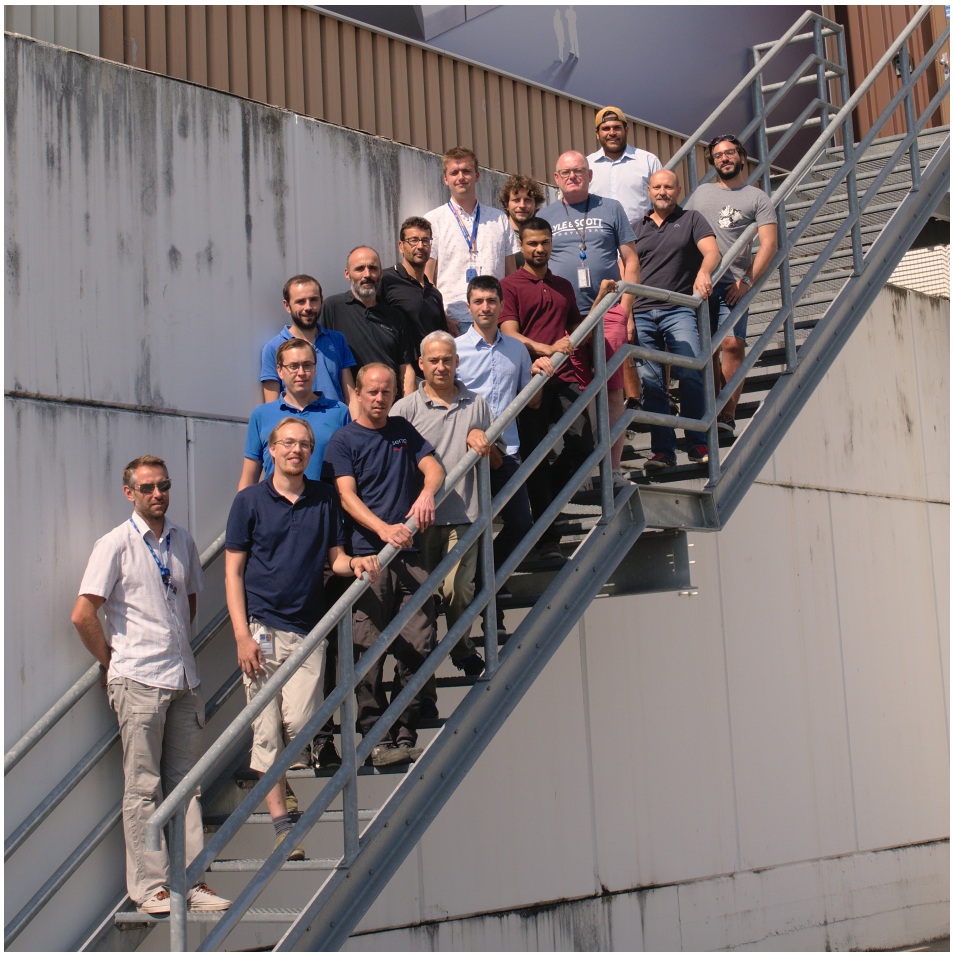

FIGURE 1.9: The CLEAR group photo (Wilfrid Farabolini is a big piece missing).

actively align such structure to the beam trajectory, with an accuracy of $3.5\,\mathrm{um}$, a key point in order to achieve the nominal performances of the accelerator.

The reason behind this requirement are wakefields, whose effect on the extremely small CLIC beams is dramatic, and to which a deeper discussion will be dedicated in Ch. 3. In order to determine the relative position of the beam and the structures, the installation of WakeField Monitors (WFMs) in the structures was foreseen already in the design phase. Such devices are still under development, and for this reason it is of strong interest to compare their results with independent measurements. Of particular interest is to measure the transverse kicks received by the beam from the dipole modes in the CLIC structure, which should also allow to precisely locate the electrical center of the accelerating structure and compare it to the one ideentified by using the WFMs [18]. A final stage of the test foresees to connect the CLIC structure to a $12\,\mathrm{GHz}$ klystron, extending previous tests done in CTF3 using a two-beam scheme. This studies will represent a further big step forward in the field of high-gradient accelerator research.

1.5.2 Irradiation Experiments

Once speaking of irradiation experiments, two main branches can be distinguished: tests of electronic components (i.e., radiation hardness test) and medical-related irradiation. The scope of both tests is to investigate the effects of radiation delivered from direct/indirect exposure to the CLEAR electron beam.

Electronic irradiation

The very first use of the CLEAR beam in 2017 was the continuation of the irradiation tests performed in the VESPER (Very energetic Electron facility for Space Planetary Exploration missions in harsh Radiative environments) test station, located in the CLEAR experimental beam line, which was set-up and qualified already during the CTF3 era. VESPER was initially set up to characterize electronic components meant for on-board operation for a space mission in a Jovian environment, as foreseen in the JUpiter Icy M**o**on Explorer mission (JUICE) [65] of the European Space Agency (ESA). In fact, in the vicinity of Jupiter it is expected that trapped electrons with energies of up to several hundred MeV, in the range that can be covered by the CLEAR accelerator, are present with very large fluxes. The CLEAR energy flexibility is therefore a key feature to continue the study [66]. Initial measurements indeed showed the first experimental evidence of electron-induced Single Event Upsets (SEU) on electronic components, pointing to the necessity of extending such an investigation to different electron energies [67, 68].

Many different devices realized with different technologies have been tested in CLEAR since then, and many experiments with several different aims are presently ongoing.

Medical irradiation

A few months after the commissioning, the scope of the VESPER area was extended to dosimetry for medical applications [69]. The advances in compact high-gradient accelerator technology, largely prompted by the CLIC study, renewed the interest in using Very-High Energy Electrons (VHEE) in the 50-$250\,\mathrm{MeV}$ energy range for radiotherapy of deep-seated tumors [70]. Understanding the dosimetry of such beams is essential to assess their viability for treatment, and several studies have been carried out on energy deposition using a set of Electron Beam Therapy 3 (EBT3) Gafchromic [71] films submerged in water to emulate the condition of the human body. The dose deposition profile was evaluated by Monte Carlo tracking simulations and compared with the measured one. Differences between measured and simulated dose profiles and beam spread curves were less than 5% [72, 73]. The obtained results indicated that VHEE has the potential to be a reliable mode of radiotherapy for treating tumors also in highly inhomogeneous and mobile regions such as the lung [74]. Further studies on the dose distribution of a converging beam as opposed to a parallel wide beam, have also been performed showing really promising results [75]. Several experimental campaigns are nowadays ongoing supported by many different institutes also investigating the so-called FLASH effects [76]. This innovative irradiation

method has the potentiality of delivering the same amount of required dose in a much shorter time. Moreover, thanks to the short exposure time this seems deeply promising because looks to don't damage the close by cells.

1.5.3 Innovative beam technology

CLEAR opens up the possibility of exploring several new innovative beam technologies. An example of this is the active plasma lens, which is a promising technology to strongly focus particle beams [77, 78]. The compact size and the extreme focusing gradient is a key feature for novel accelerators. The correspondent experimental set-up was installed in the CLEAR beamline in September 2017 and after a short commissioning it was possible to show that this type of device can be operated without the previously observed nonlinearities in the magnetic focusing field, and therefore preserve the beam emittance [79]. Further measurements are planned to validate and extend the studies done so far. Another technology being explored at CLEAR is the possibility of producing terahertz radiation [80]. This technology has a strong impact in many areas of research, spanning from quantum control of materials, plasmonics, and tunable optical devices based on Dirac-electron systems to technological applications such as medical imaging and security. The aim at CLEAR is to characterize a LINAC-based THz source, exploiting relativistic electron bunches that emit coherent radiation in the THz domain [81]. For such a source sub-picosecond electron bunches are needed. This triggered a study and optimization of the CLEAR injector in collaboration with the Laboratoire de l'Accélérateur Linéaire (LAL), thanks to which, bunches with Gaussian longitudinal distribution from sub-ps bunches down to $200\,\mathrm{fs}$ Root Mean Square (RMS) were demonstrated in the machine, paving the way to the THz radiation generation [82]. Note that, in particle accelerator physics, it is common to describe quantities like bunch size or length as the square root of the variance of the distribution.

The current studies at CLEAR are focused on the production of (sub-)THz radiation by Coherent Transition Radiation (CTR) [83], Coherent Smith-Purcell Radiation (CSPR) [84], and Coherent Cherenkov Radiation (CCR) [85] mechanism. CLEAR serves also as an available testbed for new beam instrumentation to be used in other machines. For example, at CLEAR it was possible to perform a first calibration of the scintillator screen used in the electron spectrometer of the Advanced proton driven plasma WAKefield Experiment acceleration (AWAKE) experiment [86]. In a similar form, collaboration with the beam impedance team at CERN was set up to measure impedance and beam-induced heating of equipment before being installed in other CERN machine.

Chapter 2

State of the Art

In this chapter, a recall of the formalism used in beam dynamics is presented first, which will be largely used in the thesis. Later the topic the wakefield and the bunch length measurement are presented. In the thesis, a particular focus is devoted to the transverse wakefield and on the bunch length measurement method performed using the Radio Frequency Deflector (RFD). These two topics are strongly related, as both are linked with an external field that is perturbing the nominal particle trajectory. The differences are that in the case of the bunch length studies the perturbation source is external driven (i.e., a klystron) and is a wanted effect, while in the case of transverse wakefield the source is internal (i.e., the beam itself) and it an unwanted effect.

2.1 Introduction to the Matrix Formalism in Linear Beam Dynamics

In this section, a brief introduction to the matrix formalism in linear beam dynamics is treated, which is necessary for the understanding of the next sections.

2.1.1 Single Particle Dynamics

A particle in an accelerator can be characterized from a vector of six quantities [59]:

$$\mathbf{u}^T = \begin{bmatrix} x & x' & y & y' & t & \delta \end{bmatrix}, \tag{2.1}$$

where x and x' are the position and divergence in the horizontal plane, respectively, y and y' are the position and divergence in the vertical plane, respectively, t is the longitudinal position in seconds of the reference particle in the laboratory frame, $\delta = (E - \langle E \rangle)/\langle E \rangle$, E is the beam energy, and $\langle E \rangle$ is the average of the particle energy of the bunch. The transverse (vertical and horizontal) divergences describe how the particle transverse position change while the particle moves along the longitudinal accelerator axis.

An element of the particle accelerator lattice is characterized from a matrix $\mathbf{R}$ according to its working principle. An incoming particle with parameters $\mathbf{u}_0$ will have the parameters $\mathbf{u}_1$ at the exit of the lattice element [59]:

$$\mathbf{u}_1 = \mathbf{R}\mathbf{u}_0, \tag{2.2}$$

where **R** is the transfer matrix of the lattice element.

2.1.2 Lattice Elements

Many different elements can be designed to act, in a controlled and well-known manner, on one or more specific quantities reported in Eq. 2.2. For example, a particle that passes through a drift space will see altered transverse and l**o**ngitudinal positions but not the transverse divergence or the energy. For these reasons, an L–long drift space is characterized with the transfer matrix [59, 87]

$$\mathbf{R}_{drift} = \begin{bmatrix} 1 & L & 0 & 0 & 0 & 0 \\ 0 & 1 & 0 & 0 & 0 & 0 \\ 0 & 0 & 1 & L & 0 & 0 \\ 0 & 0 & 0 & 1 & 0 & 0 \\ 0 & 0 & 0 & 0 & 1 & 0 \\ 0 & 0 & 0 & 0 & 0 & 1 \end{bmatrix}. \tag{2.3}$$

This formalism works for all the linear elements (i.e., not for sextupole, octupole, and so on). The terms off from the diagonal are the correlations between the plane. Each plane can be analyzed separately, neglecting the effects of the elements on the correlation terms, thanks to a 2×2 matrix. The 6×6 matrix can be decomposed by three 2×2 matrix, one for each plane: horizontal, vertical, and longitudinal in red, blue, and green respectively in Eq. 2.3.

A collection of N particles they compose a bunch. Each particle of the bunch is characterized with $\mathbf{u}_i$, and, therefore, the bunch can be described using the bunch matrix [59, 88]

$$\mathbf{\Sigma} = \left\langle (\mathbf{u} - \langle \mathbf{u} \rangle) (\mathbf{u} - \langle \mathbf{u} \rangle)^T \right\rangle = \begin{bmatrix} \sigma_x^2 & \sigma_{xx'} & \sigma_{xy} & \sigma_{xy'} & \sigma_{xt} & \sigma_{x\delta} \\ \sigma_{xx'} & \sigma_{x'}^2 & \sigma_{x'y} & \sigma_{x'y'} & \sigma_{x't} & \sigma_{x'\delta} \\ \sigma_{xy} & \sigma_{x'y} & \sigma_y^2 & \sigma_{yy'} & \sigma_{yt} & \sigma_{y\delta} \\ \sigma_{xy'} & \sigma_{x'y'} & \sigma_{yy'} & \sigma_{y'}^2 & \sigma_{y't} & \sigma_{y'\delta} \\ \sigma_{xt} & \sigma_{x't} & \sigma_{yt} & \sigma_{y't} & \sigma_t^2 & \sigma_{t\delta} \\ \sigma_{x\delta} & \sigma_{x'\delta} & \sigma_{y\delta} & \sigma_{y'\delta} & \sigma_{t\delta} & \sigma_\delta^2 \end{bmatrix}, \tag{2.4}$$

where

$$\begin{aligned} \sigma_i^2 &= \langle (i - \langle i \rangle)^2 \rangle, && \text{with } i = x, x', y, y', t, \delta, \\ \sigma_{ij} &= \langle (i - \langle i \rangle)(j - \langle j \rangle) \rangle, && \text{with } i \neq j = x, x', y, y', t, \delta, \end{aligned} \tag{2.5}$$

where σ_i^2 is the variance of bunch parameter i and σ_{ij} is the covariance between the bunch parameters i and j. The physical meanings of the main matrix elements are: σ_x and σ_y are the RMS horizontal and vertical bunch dimension, respectively; σ_t is the longitudinal bunch dimension (also called bunch length); σ_δ is the RMS of energy the distribution (also called energy spread); $\sigma_{xx'}$ and $\sigma_{yy'}$ express how much the bunch is focused or defocused in the horizontal and vertical plane,

respectively; $\sigma_{t\delta}$ is the energy chirp, which expresses the correlation in the longitudinal plane. The correlation coefficients can be defined as

$$r_{ij} = \frac{\sigma_{ij}}{\sigma_i \sigma_k}, \qquad \text{with } i \neq j = x, x', y, y', t, \delta. \tag{2.6}$$

The correlation coefficient is an useful index to understand how much two bunch parameters are correlated. If $r_{ij} = 0$ the bunch parameters i and j are not correlated at all, while $r_{ij} = |1|$ they are perfectly correlated [89] and knowing one parameters allows to identify the other.

The Eq. 2.4, is not the only way to represent the bunch, other useful representations can be introduced. The most common, is the one that uses the Twiss parameters [59]

$$\mathbf{\Sigma}_i = \epsilon_i \begin{bmatrix} \beta_i & -\alpha_i \\ -\alpha_i & \gamma_i \end{bmatrix}, \qquad \text{with } i = x, y, \tag{2.7}$$

where ϵ_i is the transverse emittance (a measure to quantify the average spread of particle coordinates in position and momentum), α_i, β_i, and γ_i are the transverse Twiss parameters. They are linked as follows

$$\begin{aligned} \alpha(S) &= -\frac{1}{2}\beta'(S), \\ \gamma(S) &= \frac{1 + \alpha^2(S)}{\beta(S)}. \end{aligned} \tag{2.8}$$

The $\beta(S)$, also named betatron function, represents the envelope of all particle trajectories at a given position S, $\alpha(S)$ represent the beam tilt at a given position S, and the $\gamma(S)$ depends from the two above parameters. Thanks to the Twiss parameters the phase space of the system can be written as

$$\gamma(S)x^2(S) + 2\alpha(S)x(S)x'(S) + \beta(S) = \epsilon. \tag{2.9}$$

In Eq. 2.9, ϵ (the beam emittance) is the area of the ellipse. It is a motion constant, does not depends on the longitudinal position S. A graphical representation is reported in Fig. 2.1. In this formalism a bunch, with an associated matrix $\mathbf{\Sigma_0}$, passing through an element characterized with a transfer matrix $\mathbf{R}$ gets modified. The bunch matrix becomes $\mathbf{\Sigma_1}$, in accordance with the relation [59]

$$\mathbf{\Sigma_1} = \mathbf{u}_1 \mathbf{u}_1^T = \mathbf{R}\mathbf{u_0} \left(\mathbf{R}\mathbf{u_0}\right)^T = \mathbf{R}\mathbf{\Sigma_0}\mathbf{R}^T. \tag{2.10}$$

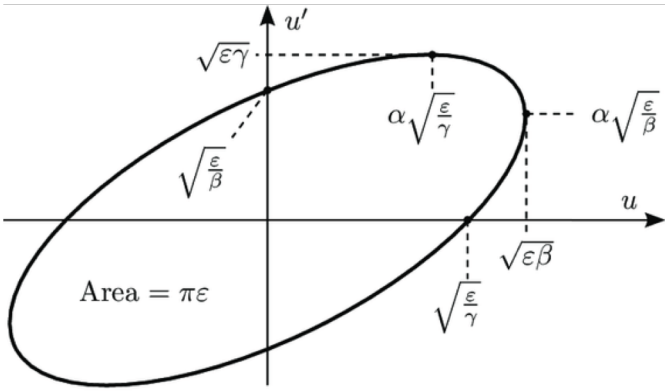

FIGURE 2.1: The phase space representation. The position on the horizontal axis and momentum on the vertical axis.

Two different presented representation of the bunch (Eqs. 2.4 and 2.7) can be linked using the formulas

$$\epsilon_i = \sqrt{\sigma_i^2\sigma_{i'}^2 - \sigma_{ii'}^2} = \sigma_i\sigma_{i'}\sqrt{1 - r_{ii'}^2}, \tag{2.11}$$

$$\beta_i = \frac{\sigma_i^2}{\epsilon_i} = \frac{\sigma_i^2}{\sqrt{\sigma_i^2\sigma_{i'}^2 - \sigma_{ii'}^2}} = \frac{\sigma_i}{\sigma_{i'}\sqrt{1 - r_{ii'}^2}}, \tag{2.12}$$

$$\alpha_i = \frac{\sigma_{ii'}}{\epsilon_i} = \frac{\sigma_{ii'}}{\sqrt{\sigma_i^2\sigma_{i'}^2 - \sigma_{ii'}^2}} = \frac{\sigma_{ii'}}{\sigma_i\sigma_{i'}\sqrt{1 - r_{ii'}^2}}, \tag{2.13}$$

$$\gamma_i = \frac{\sigma_{i'}^2}{\epsilon_i} = \frac{\sigma_{i'}^2}{\sqrt{\sigma_i^2\sigma_{i'}^2 - \sigma_{ii'}^2}} = \frac{\sigma_{i'}}{\sigma_i\sqrt{1 - r_{ii'}^2}}. \tag{2.14}$$

2.2 Wakefield

In this section, the wakefield phenomenon is introduced. Moreover, two very useful concepts: wake functions and wake potentials are presented. Later, the concept of dipole kick is introduced and an overview of the state of the art is presented.

2.2.1 Wake potentials

It is useful, in order to understand the wakefields, to consider two point-like charges one after the other that are on the same or on a parallel path moving in free space at a velocity close to the velocity of light. In such a scenario, the electric and magnetic fields of such relativistic particles are perpendicular to the particle path (if observed from an outside frame). In reality, the fields are perpendicular **b**ut emitted in a region defined by the speed of the particle, expressed by the inverse of the Lorenz factor

$$\gamma = \frac{1}{\sqrt{1 - (\frac{v}{c})^2}} = \frac{1}{\sqrt{1 - \beta^2}}. \tag{2.15}$$

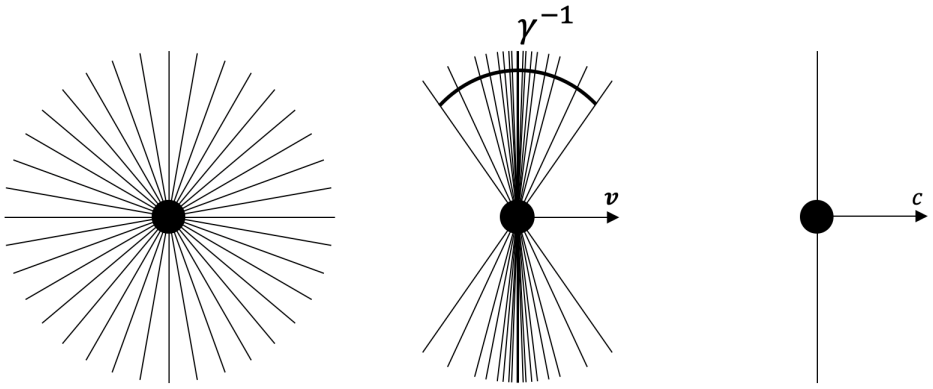

FIGURE 2.2: The three different field distributions of a charged particle: not in movement (left), at certain speed v (center), and at the speed of light (right).

A schematic example of three different field distribution of a charged particle are reported in Fig. 2.2. As a consequence, if the particle is moving at the speed of light, the second charge moving behind the first charge, will not be subjected to any forces from the fields produced by the leading charge at a distance $s = ct - z$.The situation already changes if the two point-like charges move in the proximity of a boundary. In this scenario, the trailing witness charge still will not experience the direct fields from the lead charge can scatter from the boundary, and this scattered radiation can reach the trailing charge and exert forces on it, perturbing its motion. These scattered waves are termed wakefields, and the integrated effects of these wakefields over a given path length of the trailing charge q, give rise to longitudinal and transverse wake potentials that can be defined as

$$\begin{aligned} W_z(\vec{r},\vec{r}\,',s) &= -\frac{1}{q}\int_{z_1}^{z_2} E_z(\vec{r},z,t_{test})dz, \\ W_\perp(\vec{r},\vec{r}\,',s) &= \frac{1}{q}\int_{z_1}^{z_2}\left[\vec{E_\perp}(\vec{r},z,t_{test}) + c(\hat{z}\times\vec{B}(\vec{r},z,t_{test}))\right]dz. \end{aligned} \tag{2.16}$$

Here, $t_{test} = \frac{z+s}{c}$ is the temporal position of the test charge where both the charges are assumed to travel at the speed of light and z is the position of the driving charges. In general, the wake potentials are functions of both $\vec{r}$ and $\vec{r}\,'$ that are the transverse offsets of the driving and test charges from the z-axis, respectively. Moreover, $\hat{z}$ is a unit vector in the direction of motion of both the driving and test charges, which are taken to be parallel to the z-axis [90]. The dimensions of the wake functions are voltage per witness charge. These functions are strictly related to the characteristic properties of the geometric perturbation and they can be seen as a Greens functions of the system. A representation of the wakefield effects between two particles is reported in Fig. 2.3. In Eq. 2.16, the driving charge is

assumed to enter the cavity structure at $z = z_1$ and $t = 0$ and to exit at $z = L = z_2$. Such expression is valid only for a point-like charge. Following the concept will be extended for a charge distribution. The wake functions can be normalized to the charge Q of the driving bunch, and sometimes (as in the case for a periodic structure) it is convenient to also normalize them to the period L. The wake potentials, Eqs. 2.16, correctly represent the integrated force on the charges in the assumption that the witness charge travels in a straight path (i.e., that its trajectory is not affected by this force). The advantage of using the wake potential instead of directly using the fields, is that it represents the cumulative effect on the witness particle, only depending on the relative position of the source and witness particles, which are assumed to travel along parallel trajectories [91].

If the point-like charges move on the axis of a perfectly conducting round pipe, the fields in the pipe are identical to the free space fields and hence there are no wakefields. Already in the scenario that the point charges move in the same perfectly conducting round pipe but following a trajectory which is parallel to the axis but offset from it, the fields in the interior of the pipe are perturbed from their free space values. However, no wakefields are left behind the moving charge thanks to the ideal boundary conditions (the charge induced on the surface can follow perfectly the real charge). Unfortunately, the situation drastically changes if the pipe is not perfectly conducting. In such a scenario, a small orbit variation or a small boundary discontinuity generates a perturbation on the following charge due to the radiation left beyond the lead charge, from causality the field of the lead particle can interact with the trailing and not vice versa. An overview of the phenomena is reported in Fig. 2.4, where the wakefields generated by a Gaussian bunch traversing a cavity are shown.

2.2.2 Bunch potentials

The wake potentials, derived in Eqs. 2.16 can be used as Green's functions to compute the potentials in and behind an arbitrary charge distribution [93]. Normally, except in some simplified cases, the wake potentials (i.e., $W_\perp$ and W_z in Eq. 2.16) are obtained using 3D electromagnetic solvers (e.g., Gitter drüber, fertig ist die Laube (GdfidL) [94] Computer Simulation Technology (CST) [95], or Advanced

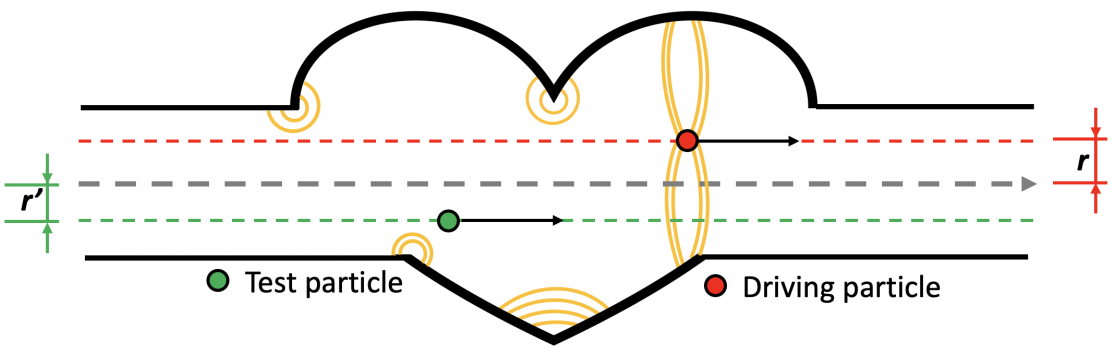

FIGURE 2.3: The wakefield scheme for the two-particles model into a cavity.

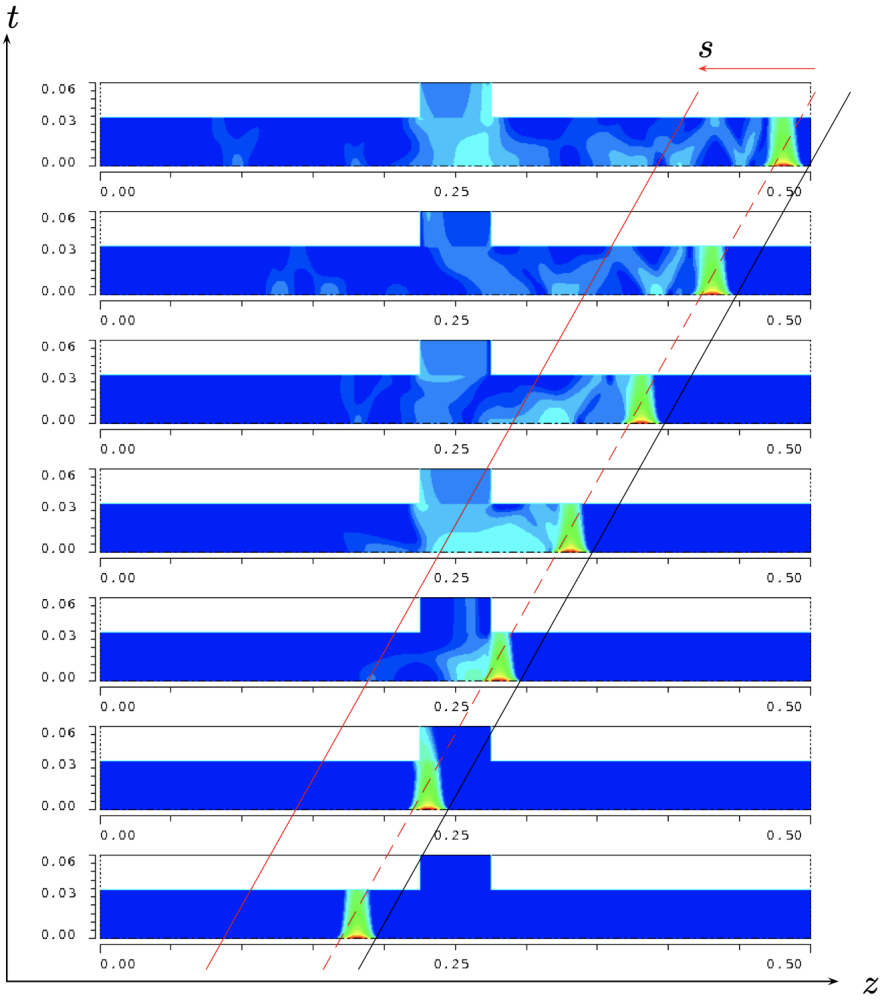

FIGURE 2.4: The wakefields generated by a Gaussian bunch travelling through a cavity [92].

Computational Electromagnetics 3D Parallel (ACE3P) [96]). If the line density of the charge distribution is $\lambda(s)$ per unit length, the longitudinal and transverse potentials are

$$\begin{aligned} V_z(s) &= \int_0^\infty \lambda(s-s')W_z(s')ds', \\ \vec{V_\perp}(s) &= \int_0^\infty \lambda(s-s')\vec{W_\perp}(s')ds'. \end{aligned} \tag{2.17}$$

The potentials in Eqs. 2.17 are called bunch potentials.

A bunch passing thought the accelerator experience both longitudinal and transverse fields. The longitudinal wakefield changes the energy of the charges. On the other hand, the transverse wakefield tends to deform the shape of the bunch. An example of a longitudinal wake-potential for different Gaussian beam

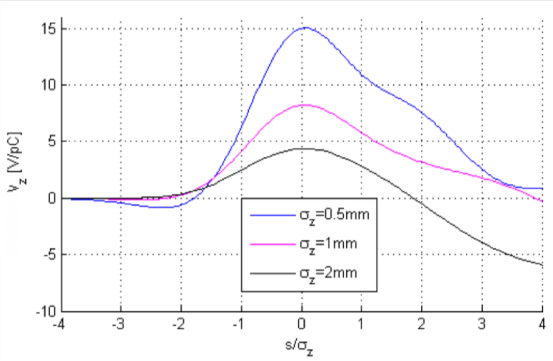

FIGURE 2.5: The first part of the longitudinal bunch-potential generated by three different Gaussian beams with different bunch lengths in a pillbox cavity [97].

with bunch lengths for a pillbox cavity is shown in Fig. 2.5. For the case of a short bunch, the wake potential is positive over the bunch length (i.e., the particles lose energy). For the longest bunch, the wake potential changes sign (i.e., the particles in the bunch tail gain energy).

2.2.3 Beam impedance

The Fourier transform of the wake potential is called the impedance or coupling-impedance, naming i as the imaginary unit, can be written as

$$\begin{aligned} Z_z[r, r', \omega] &= \frac{1}{c} \int_{-\infty}^{\infty} W_z(r, r', s) e^{-\frac{j\omega s}{v}} ds \\ Z_\perp[r, r', \omega] &= \frac{-i}{c} \int_{-\infty}^{\infty} W_\perp(r, r', s) e^{-\frac{j\omega s}{v}} ds. \end{aligned} \tag{2.18}$$

The wake potential and impedance are two descriptions of the same thing, the coupling between the beam and its environment. The wake potential is the time domain description while the impedance is in the frequency domain description. From Eq. 2.18, the dimensions of the impedance is Ω. The reason for the usefulness of the impedance is that it often contains a number of sharply defined frequencies corresponding to the modes of the cavity or the long-range part of the wake potential. In Fig. 2.6 shows the real part of a typical impedance for a cavity. Below the cut-off frequency of the beam pipe there is a sharp peak for each cavity mode. Above the cut-off frequency a continuous spectrum of beam pipe modes contribute to the impedance. These are important for the short-range wake-field effects over the bunch, especially for very short bunches.

Observing Eq. 2.17, the bunch potential is obtained convolving the wake function with the bunch charge distribution. Using the convolution theorem in the

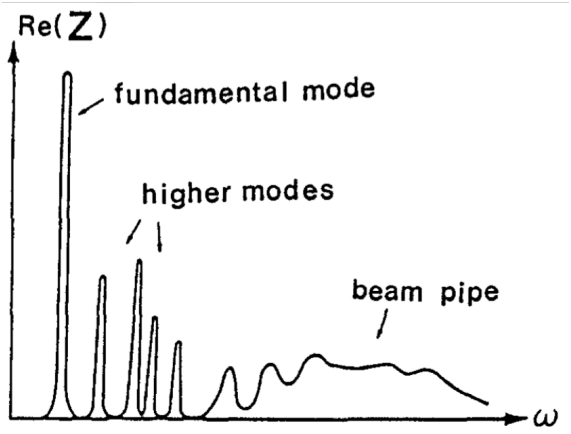

FIGURE 2.6: The real part of the impedance for a cavity with side pipes. The sharp peaks correspond to cavity modes, while above the cut-off frequency, the continuous spectrum of beam pipe modes contributes to the impedance [7].

frequency domain, the complex bunch potential in frequency domain can be assessed

$$\begin{aligned} V_z(\omega) &= Z_z(\omega)I(\omega), \\ V_\perp(\omega) &= -Z_\perp(\omega)I(\omega) \end{aligned} \tag{2.19}$$

where $I(\omega)$ is the Fourier transformation of the bunch charge distribution.

2.2.4 Multipoles

In geometries with cylindrical symmetry (most of the accelerating structures and many accelerator compo**n**ents), the wake potential can be written as a multipole expansion [98, 99, 100]. As a consequence, it can be written as

$$W_y + iW_x = \sum_{n=0}^{\infty} C_n(x+iy)^n. \tag{2.20}$$

The coefficients C_n characterize the strength and the orientation of each multipole component. Explicitly writing the first multipoles we have

$$\begin{aligned} W_y + iW_x = \underbrace{C_0}_{\text{Monopolar}} + \overbrace{C_1(x+iy)}^{\text{Dipole}} + \underbrace{C_2(x^2-y^2+2ixy)}_{\text{Quadrupole}} + \\ + \overbrace{C_3(x^3-3xy^2+i(3x^2y-y^3))}^{\text{Sextupole}} + \underbrace{C_4(x^4-6x^2y^2+y^4+i4(x^3y-xy^3))}_{\text{Octupole}} + ... \end{aligned} \tag{2.21}$$

These are the most common types of component in a particle accelerator. It is sometimes more convenient to express the field using polar coordinates instead

of the Cartesian one. Writing $x = r\cos(\theta)$ and $y = r\sin(\theta)$, the Eq. 2.20 becomes

$$W_y + iW_x = \sum_{n=0}^{\infty} C_n r^n e^{in\theta}. \tag{2.22}$$

By convention multipoles with $\Im(C_n) = 0$ are called normal and multipoles with $\Re(C_n) = 0$ are called skew. From Eq. 2.21 it can be seen that monopolar components have no dependence on the transverse position, while the dipole component has a linear dependence. Then there are all the other field components such as sextupoles and octupoles where the strength depends nonlinearly on the transverse position. Not all of the components are always present, for example for the longitudinal wake potential the first component is monopolar while for the transverse wake potential the first component the dipole component [99]. Moreover, the geometry of the structure can also be a discriminant for the components of the field.

If the beam radial displacement is small compared to the aperture radius of the beam pipe, then the **d**ecomposition can be stopped at the first term. As a consequence, the transverse dipole wake potential is often the most interesting part of the transverse wake to study [87]. At the first order, the amplitude of the dipole wake induced by a particle traveling at an offset Δ_x (or Δ_y) is proportional to the offset Δ_x (or Δ_y), respectively.

2.2.5 Trajectory perturbation

Because of the wakefields, the test particle receives a longitudinal force that changes its energy and a transverse force which deflects its trajectory. A particle with charge q and velocity v in the presence of electric and magnetic fields (i.e., $\vec{E}$ and $\vec{B}$) is subjected to the Lorentz force

$$\vec{F} = q(\vec{E} + \vec{v} \times \vec{B}). \tag{2.23}$$

The longitudinal electric field component of the RF fields accelerates and the transverse components of the magnetic field steer and focus the beam.

As a consequence, to observe a change of trajectory of the beam, it is needed that a transverse component of the Lorentz force is affecting the beam while is passing. The so-called transverse voltage, that has the dimension of voltage, can be defined as

$$\vec{V}_{\perp}' = \int_0^L \frac{\vec{F}_{\perp}}{q} dz \int_0^L \vec{E} + c\hat{z} \times \vec{B} dz. \tag{2.24}$$

In Eq. 2.24, the particle is assumed to travel at the speed of light in the direction of the z-axis (i.e., $\vec{v} = c\hat{z}$). From Eq. 2.24 changing the coordinates from length to

time, using the relationship $z = ct$ (assuming $s = 0$), it can be written that

$$q\vec{V}_{\perp}^{\prime} = \int_0^L \vec{F}_{\perp} dz = c \int_0^{L/c} \vec{F}_{\perp} dt = c \int_0^{L/c} \frac{d\vec{p}_{\perp}}{dt} dt = c\Delta\vec{p}_{\perp}. \tag{2.25}$$

Therefore, the change in angle can be written as

$$\vec{\Delta_{\perp}^{\prime}} = \frac{\Delta\vec{p}_{\perp}}{p_s} = \frac{q\vec{V}_{\perp}^{\prime}}{cp_s}, \tag{2.26}$$

where p_s is the particle momenta along the beam axis (e.g., the beam reference momentum), and the $\vec{\Delta_{\perp}^{\prime}}$ can be decomposed in the two planes ($\Delta_x^{\prime}$ and $\Delta_y^{\prime}$) [101].

2.2.6 Long and short range wakefields

Conventionally it useful to distinguish between two types of wakefield effects, this phenomena effects can occur: (i) between two different charged distribution (i.e., between two bunches) and it is named bunch-by-bunch interaction, or (ii) inside the charged distribution (i.e, inside the bunch) where the head of the distribution may excite electromagnetic fields that interact the tail of the distribution, and it is named intra-bunch. This kind of classification can be referenced in the type of wakefield that is generated. In the first case, they are called long-range-wake, while in the second case they are called short-range-wake. The two main beam configuration that can drive wakefield issues in an accelerator: (i) the beam travels with an offset or with an angle relatively with the accelerator axis, or (ii) offsets of elements in the beamline. Both effects can yield a limit for the acceptable strength of the wakefields [102]. In a ring the perturbed bunches come back to the same locations, for this reason, long-range wakefields are fundamental to be damped before the beam comes back in the same position. On the other hand, for the LINAC machine, where a high gradient (often obtained with narrow aperture) and high beam quality are required, both effects need to be considered. Even if the same bunch does not travel more than once inside a device, the long term wakefield can perturb the following one. In CLIC, the long-range wakefield contributions were studied and strongly damped thanks to installing dumping material inside the structure. On the other hand, it is not easy to deal with the short-range one, for which the main solution found was to mitigate their effects.

The long-range wakefields are dominated by high Q-factor, while the short-range-wakefields are dominated by the immediate response of the field following the driver. Both these effects in the transverse plane, that can be seen as a transverse deflection, can cause Beam BreakUp (BBU) instabilities and lead to emittance growth or, in the worse case, beam losses on the walls. Many machines can be identified as a wakefield dominated accelerator [47, 103, 104, 105], thus several studies have been devoted to investigating such effects. Often simulation tools

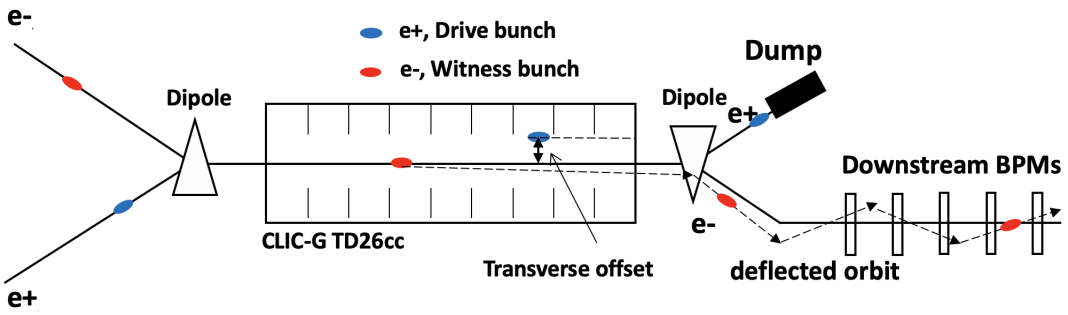

FIGURE 2.7: The experimental layout for the long-range wakefield measurements [110].

are essential to study such effects [106, 107], both based on a semi-analytical approach or purely based on electromagnetic simulations. Following, an overview of the previous measurements performed on both short and long-range wake.

Long-range wake measurements

One of the first time this effect was observed was at the ISR [108] and at the Stanford Linear Accelerator Center (SLAC) LINAC [109]. One of the most recent and accurate measurements performed was on X-band normal conducting accelerating structures with an operating frequency of 12 GHz [47]. A schematic of the measurement scheme is shown in Fig. 2.7 In the performed experiment, the positron beam (driver bunch) passes through the structure under test with a tunable transverse offset, thus generating a transverse wakefield. The following electron bunch (witness bunch) is then deflected by this wakefield. Downstream of the structure, a dipole magnet splits the trajectories of the driver and witness bunches. The positron bunch is damped, and the deflection of the electron orbit is measured by the BPMs [111]. The wakefield is then deduced from the perturbation of the electron orbit. This study was performed to assess the possibility of maintaining the targeted beam stability in multi-bunch operation and the results demonstrated that the beam dynamics specifications could be met.

A similar experiment was performed before at Stanford Linear Collider (SLC), where a train consisting of one positron bunch followed by two electron bunches were used [112]. Long-range transverse wakefields from the leading bunch were found to cause up to a factor three increase in beam jitter for the trailing bunches.

Another example where the study of the long-range wakefields is critical is in SuperConducting RF (SCRF) cavities for Free Electron Laser (FEL) beamlines. Even if couplers with loads are installed to damp the Higher Order Mode (HOM), they can persist for long periods in superconducting structures, which leads to long-range wakefields. Several numerical tools for simulating long-range wakefields are being developed, in order to solve such issues [113].

Short-range wake measurements

Intra-bunch effects are of particular concern where the catch-up distance is small, such as in collimators, or apertures with particularly small iris. Here the bunch

passes extremely close to the surface and the frequency domain, modal summation approach is not appropriate. A big effort has been devoted to finding numerical approaches for studying such effects [114]. At the same time, practical solutions for achieving the best possible performance are investigating. An example of this effort is the so-called Wakefield-Free Steering (WFS) applied in many different facilities [115, 116, 117]. Tests of WFS are already performed at the Accelerator Test Facility 2 (ATF2) [118] during the past years [115]. Moreover, on the same accelerators, different studies were carried out for evaluating the effects of short-range wakefield on the beam size on the Interaction Point (IP) [119, 120, 121].

Another family of components for which several studies were carried out in the field of short-range wakefield are the collimators. Due to the type of materials they are made and the proximity with the beam path a strong impact in terms of wakefields is expected. In this particular case, the transverse short-range wakefields that arise due to a change in dimensions of the vacuum chamber at the collimator are collectively referred to as the geometric wakefields [122]. And the component of the wakefield, due to the resistance of the beam pipe walls used in such structures, is called the Resistive Wall (RW) wakefield. The measurements setup is based on the test of different structures for collimating the beam and using a BPMs series to establish the angular deflection of the beam [123, 124, 125, 126, 127].

Other more exotic experiments carried out with the short-range wakefields are the so-called passive dechirper. In these applications, the wakefields are generated in a controlled way using a geometrical discontinuity to mitigate the beam longitudinal distortion, which is often created by the acceleration process. [128, 129, 130, 131].

2.3 Bunch length

In this section, firstly, a recall of the beam structure is presented, highlighting why most accelerators deal with a bunched beam. Later, an overview of the bunch length measurement methods is presented, focusing on the Radio Frequency Deflector (RFD) method.

2.3.1 Bunched beam

The fundamental reason why most of the accelerators work with a bunched beam is driven from the RF field used to accelerate them. As a consequence, the bunch spacing and the maximum bunch length is a direct consequence of the frequency of the RF accelerating field (e.g., an accelerating structure working at $1.5\,\mathrm{GHz}$ impose a bunch spacing and a maximum bunch length of $666\,\mathrm{ps}$).

To enhance the luminosity in a collider [132] or the brightness in a radiation source [133]; different schemes are designed to work at high operational frequency [134].

Often proton machines use RF accelerating structures at lower accelerating gradients thanks to the possibility of multiple passages through the cavity. This

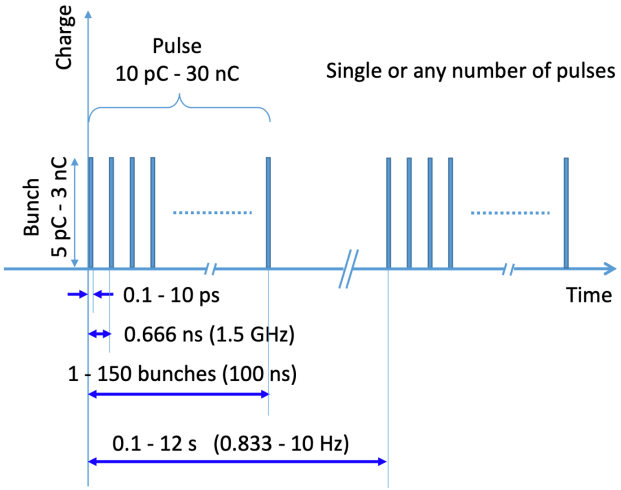

FIGURE 2.8: An overview of the CLEAR bunch spacing.

consideration is completely different in LINACs, where it is needed to maximize the energy gain due to the single passages in the accelerating structure. Often the frequency of an accelerating structure is strictly related to the accelerating gradients. Accelerating structures operating at the frequency results in having higher accelerating gradients [135]. For this reason, the LINACs are usually characterized by shorter bunches compared to a circular machine. Moreover, modern accelerators are finding increasing interest in the investigation of ultra-short bunches.

It is important to mention that even if the RF imposes a maximum threshold on the bunch length, the actual quantity that characterizes an accelerator is strictly correlated with the way of generating it and with the type of particle. For example, in a CLEAR-like configuration, the electrons are generated from photo emissions by a pulsed laser. In this case, the bunch result much shorter than the maximum length imposed from the RF used to accelerate them. In Fig. 2.8, an overview of the CLEAR bunch spacing is shown.

Due to the growing interest in past years, many studies have been devoted to shortening the bunch length. For example, in accelerators where the charge density is a crucial feature (i.e., plasma-based accelerators), the bunch length needs to be kept as small as possible [86, 136]. Another driving reason is the hope of using the accelerators as a reliable source of high frequencies electromagnetic fields. The shorter the bunch, the more the emitted field has a high frequency [82].

Two of the main ways of shortening a bunch, both based on the chirp in the bunch (obtainable sitting on the rising or falling edge of the accelerating wave), are the velocity bunching and the magnetic chicane. In the velocity bunching, the accelerating field is not used on crest but on the zero-crossing; such to accelerate less the head and more the tail, resulting in an overall shortening of the bunch [137]. Such a method is more effective for non-ultrarelativistic particles. For this reason, the accelerating structure for performing this task, commonly named buncher, is often installed as an early stage in the accelerators. In the magnetic chicane, the beam passes through a magnetic path meant to induce a

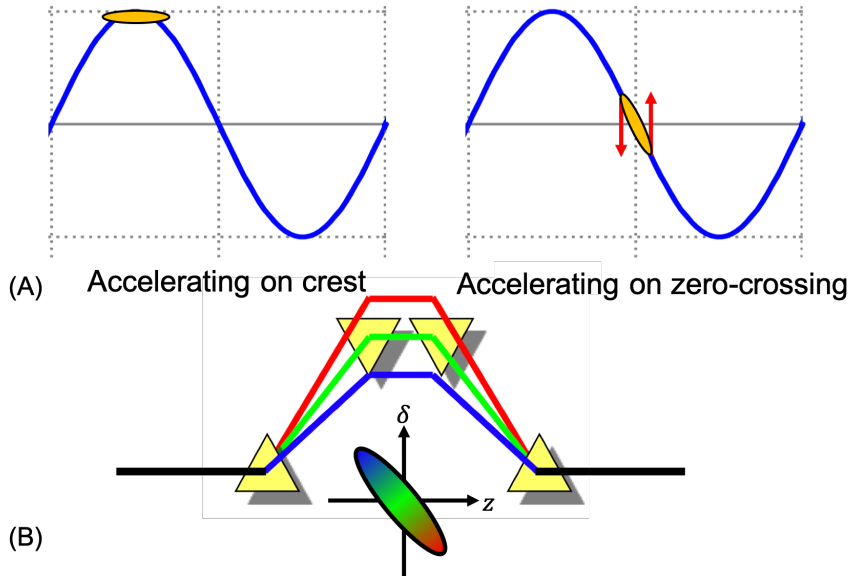

FIGURE 2.9: The two operating principles for shortening a bunch. In (A), using the velocity bunching and in (B), using the magnetic chicane.

different path length for the different energy that compose the beam. This method has the advantage of being effective also for ultra-relativistic beams. A schematic overview of the two presented methods is reported in Fig 2.9 (A) and (B), respectively.

2.3.2 Bunch length measurement methods

As introduced in Sec. 2.3.1, one of the main beam parameters to be precisely measured in all the accelerators is the bunch length. Given the strong interest in knowing such quantities, many different methods have been developed for measuring it [138]. At the first order, to distinguish between two different macro-categories of diagnostics can be identified. One gives information on the whole longitudinal profile, while the other one can estimate the bunch length. Another difference to be stressed is related to the number of acquisition to perform the measurement (single-shot acquisition or multiple acquisitions) Moreover, it is important to distinguish between diagnostics that intercept or not the beam (i.e., if the beam is intercepted, it is destroyed to perform the measurements). The most used and well-known techniques to perform bunch length measurements are all used in CLEAR. Following, they will be explained and described.

Streak camera

The streak camera is a high-speed detector that in a single frame captures the time evolution of light emission phenomena by effectively sweeping the light across the frame. One examples is the light produced from a specific screen (e.g., an Optical Transition Radiation (OTR)) once the bunch hits such screen [139]). The light

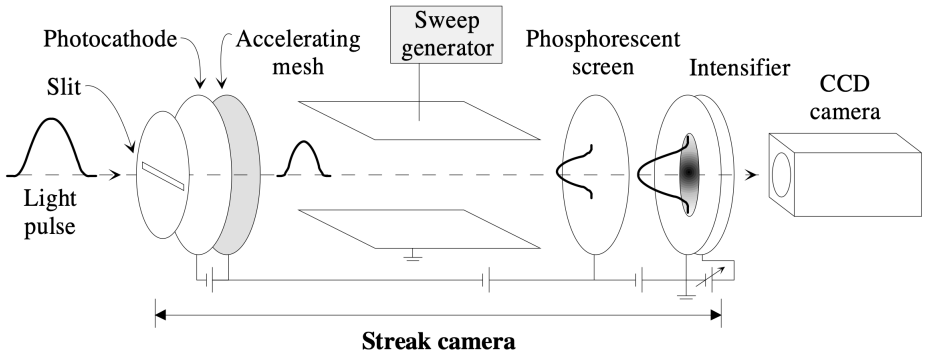

FIGURE 2.10: The schematic layout for assessing the bunch length using a streak camera [140].

pulse generated is characterized by the same length as the electron bunch. Therefore, by measuring the length and structure of the light pulse, the particle bunch length and structure can be obtained. The schematic layout of the measurement is reported in Fig. 2.10. Usually, only a fraction of the light emitted by the screen impinged by the beam is investigated. A slit is placed at the input of the system, in order to reduce the light impacting the photocathode. The photons that pass the slit will hit a photocathode producing an electron beam with a temporal structure proportional to the light pulse. After an accelerating mash, these electrons are swept by a deflecting electric field generated by a fast ramped voltage applied to two metallic plates. In this **w**ay, the temporal variation of intensity is transformed into spatial information when hitting a phosphorescent screen. The phosphor screen's light intensity is usually recorded by a Charge Coupled Device (CCD) camera [141].

This measurement method gives information on the whole longitudinal profile potentially in a single shot but has the drawback of being a destructive method. The resolution of the streak camera depends on several factors, mainly: (i) the electron energy spread generated from the photocathode (this will also depend on the chromaticity of the light pulse), (ii) the size of the slit, and (iii) the deflection ramp speed. Time resolutions of a few hundred femtoseconds can be achieved by measuring monochromatic laser pulses [142].

Electro-Optical Sampling (EOS)

When a relativistic bunch passes close to an electro-optic crystal, its transient electric field is equivalent to a half-cycle RF pulse impacting on the crystal (the frequency depends on the bunch-length). The temporal profile of the RF pulse provides a faithful image of the longitudinal charge distribution inside the bunch if the particles are highly relativistic. The transient electric field induces birefringence in the electro-optic crystal, and as the electric field propagates through the crystal, the birefringent properties of the crystal also propagate. This birefringence can be probed by a copropagating optical laser pulse and later, analyzing the polarization modulation on the laser pulse the information on the bunch can be retrieved [143, 144, 145]; This measurement method gives information on

the whole longitudinal profile potentially in a single shot and is not a destructive method. The drawback of this method is hidden in the complexity of the setup. In this study, a time resolution of a few hundred femtoseconds can be achieved [146].

Analysis of the bunch frequency content

Generally speaking, once a beam passes through the accelerators, many different types of electromagnetic interaction mig**h**t occur, and as a consequence, they generate many different types of electromagnetic radiation. The main are: (i) the Bremsstrahlung radiation [147] emitted when the beam interacts with the atomic nuclei of a target element, an important subclass of this interaction is the transition radiation[148] (i.e., the beam passes between two media with different refraction index) or even the diffraction radiation [149] (i.e., the beam passes close to a boundary and the induced charge produce the radiation), (ii) the synchrotron radiation [150] emitted when the beam under the effects of an external electromagnetic field change its trajectory, and (iii) Cerenkov radiation [151] emitted when the speed of a particle traveling in a medium is larger than the speed of light in the medium (i.e., the phase velocity). A subclass of this emission is the so-called Cerenkov-like radiation [152] that, equivalently to the diffraction radiation (i.e., the field of the beam travels in a medium with a velocity larger than the phase velocity in the medium; meanwhile, the beam particles are out of it).

The temporal distribution of the radiation is directly related to the beam of charged particles that emitted it. Moreover, the bunches' electromagnetic radiation is coherently enhanced at wavelengths of the order or longer of the bunch length. Thus, the frequency spectrum of the coherent radiation carries information of the bunch distribution. Such information can be used to assess the bunch length thanks to autocorrelation technique or spectral analysis techniques [153]. The main limitation is that the signal is usually measured at a few fixed frequencies, so only a few frequency spectrum points can be obtained. Thus for the reconstruction of the spectrum, only a few points are usually available.

The main advantages are that these techniques are a very fast way of monitoring the bunch length. Any change in the bunch length can be immediately detected, and often, it results in not a destructive technique[82, 154, 155]. On the other hand, the big drawback is that the measurements can require measuring relatively high-frequency (in the THz range), and thus the measurement becomes complicated. Moreover, the calibration is difficult and usually requires alternative cross-checking methods.

Energy spread

This technique is based on the relationship between the energy spread and the phase of the accelerating RF. [156]. The relative phase between two consecutive accelerating structures is varied, while the energy spectra are monitored downstream in a spectrometer [157]. The properties of the longitudinal distribution are then extracted from the energy spectra [158]. The main contribution to the energy

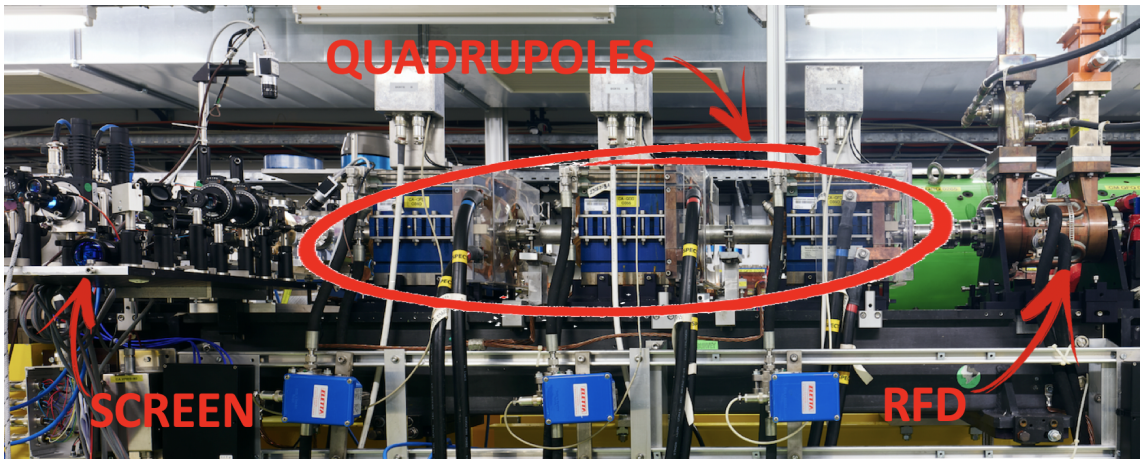

FIGURE 2.11: An overview of the CLEAR test facility layout currently installed.

spread for a given bunch length should depend on the relative position between the bunch and the RF.

The advantage of such a technique is that it is a direct method for observing the whole longitudinal distribution. However, its result is a qualitative evaluation due to the strong dependence on the RF stability. Moreover, the beam-loading contributions need to negligible (i.e., the measurement is more reliable with low charge).

2.3.3 RFD method

The most common and exploits methods to measure the bunch length, uses a transverse deflecting structure [13, 159], namely RFD [160, 161, 162].

The combination of an RFD and a dispersive element (i.e., a dipole) can be exploited to measure the longitudinal phase space distribution of the beam [163, 164]. An overview of the layout currently installed in the CLEAR test facility is shown in Fig. 2.11. The RFDs are widely used in LINACs around the world, owing to their very high resolutions. For example, RFDs are used at SLAC [12, 165], Deutsches Elektronen SYnchrotron (DESY) [166], Massachusetts Institute of Technology (MIT) Plasma Science and Fusion Center (PSFC) [167], Sources for Plasma Accelerators and Radiation Compton with Lasers And Beams (SPARC LAB) [168, 169], the ultraviolet and soft x-ray FEL facility Free-electron LASer in Hamburg (FLASH) [170], the Accelerator Test Facility (ATF) in Brookhaven National Lab (BNL) [171], and so on.

The method allows to measure ultra-short electron beam bunches down to few fs [13, 160, 172, 173] and can be performed as a single-shot measurement, after a proper calibration. The only drawback of the measurement methods is that the measurement is a destructive process.

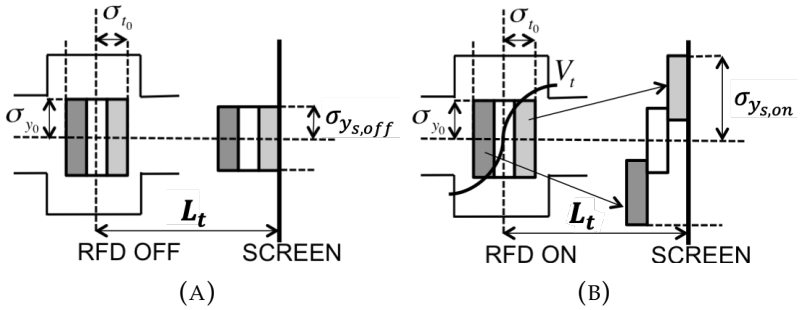

FIGURE 2.12: The longitudinal behavior of a bunch traveling from left to the right with the RFD off and on in (A) and (B), respectively. Where σ_{y_0} is the bunch vertical dimension at RFD center, L_t is the distance between RFD centre and screen, V_t is the deflecting voltage amplitude, σ_{t_0} is the bunch length, $\sigma_{y_s,off}$ and $\sigma_{y_s,on}$ are the vertical spot sizes at the screen once the RFD is off and on, respectively [174].

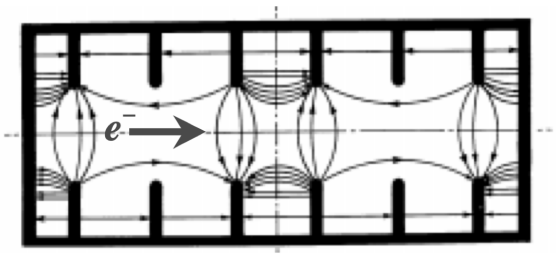

FIGURE 2.13: A time snap-shot of the field distribution of the TM_{11} mode with a $2\pi/3$ cell length [176].

Measurement concept

The basic concept beyond the bunch length measurement by means of the RFD, sometimes called Transverse Deflecting Structures (TDS) [13], involves the deflecting structure and a screen. The bunch parameters at the RFD entrance are indicated with the subscript e, at the RFD center are indicated with the subscript 0, and at the screen location with the subscript s. Initially, the RFD is switched off (Fig. 2.12, (A)), and the spot size is measured on the screen. For the measurement, the RFD is switched on (Fig. 2.12, (B)) and, as a consequence, a Transverse Magnetic (TM)-like deflecting modes (shown in Fig. 2.13) propagates in the cavity giving a time-dependent transverse kick to the electron bunch passing through the RFD [175]. The vertical kick produces a sudden change of the vertical particle divergence $\Delta y_0'$.

The change of the vertical divergence depends on the deflecting voltage that can be written as

$$V(z_0) = V_t \sin(kz_0 + \varphi) = V_t \left[\sin(kz_0)\cos(\varphi) + \cos(kz_0)\sin(\varphi)\right], \tag{2.27}$$

where z_0 is the position of the particles along the beam axis with the origin in the RFD center, $k = 2\pi f_{RF}/c$ is the wavenumber, f_{RF}, V_t, and φ are the deflecting voltage frequency, amplitude, and phase, respectively. A summary of the quantities,

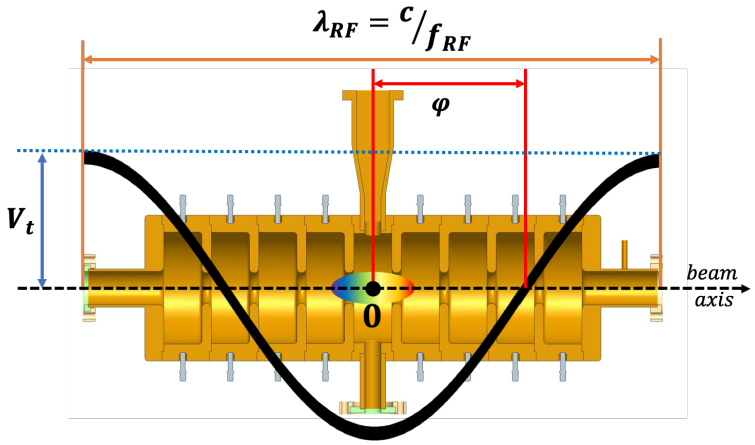

FIGURE 2.14: An overview of the RFD main parameters, λ_{RF}, V_t, and φ are the deflecting voltage wavelength, amplitude, and phase, respectively.

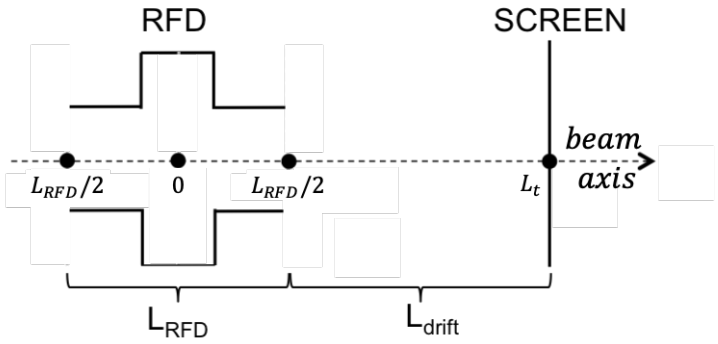

FIGURE 2.15: The measurement layout of bunch length using the RFD; where L_{RFD} is the RFD length, L_{drift} is the distance between the RFD exit and the screen, and L_t is the longitudinal position of the screen with the origin in the RFD center.

highlighting their physical meaning, is reported in Fig. 2.14. Thanks to the usual dimension of the bunch length (i.e., few of µm) and the characteristic wavelength of the deflector (i.e., larger than tens of mm), using the linear approximation of the sine and cosine, Eq. 2.27 can be rewritten as

$$V(z_0) \approx V_t \left[kz_0 \cos(\varphi) + \sin(\varphi)\right]. \tag{2.28}$$

Therefore, the vertical kick gives the vertical divergence change to the *i*-th particle

$$\Delta y'_{0_i}(z_{0_i}) = \frac{q}{p_{0_i} c} V(z_{0_i}) = C_{RFD0_i} \left[kz_{0_i} \cos(\varphi) + \sin(\varphi)\right], \tag{2.29}$$

where $C_{RFD0_i} = qV_t/(p_{0_i}c)$ is the RFD coefficient, q is the electron charge, and p_{0_i} is the particle momentum at RFD centre [176, 177]. In the ultra–relativistic

regime, the RFD coefficient is

$$C_{RFD0_i} \approx V_t/E_{0_i}, \tag{2.30}$$

where E_{0_i} is the particle energy at RFD center expressed in eV.

In the measurement method, the longitudinal and transverse bunch dimensions of the beam on the screen are correlated. Thanks to this, the bunch length can be assessed from the measurement of the spot size, in the direction of the deflection, after a calibration of the beam position displacement driven from the deflecting voltage RF phase [163].

The conventional model of the RFD and the screen is shown in Fig. 2.15. Where L_{RFD} is the RFD length, L_{drift} is the distance between the RFD exit and the screen, and L_t is the longitudinal position of the screen with the origin of the beam axis in the RFD center (i.e., $L_t = {}^{L_{RFD}}/_2 + L_{drift}$). The RFD can be treated as a $L_{RFD}/2$ long drift space, a vertical kicker, and another $L_{RFD}/2$ long drift space [13, 178]. The kick is applied at the center of the RFD instead of considering it as a distributed effect inside the whole deflector length. However, this model neglects the possibility of inducing energy chirp and energy spread on the bunch. The deflecting voltage is directly related to the longitudinal electric field gradient, through the Panofsky-Wenzel theorem [99], which can induce such effects to the bunch [163].

Part II

Proposal

Chapter 3

Wakefield and Kick

The interest in a more compact and efficient solution to accelerate particles is growing. The new technology, developed within the CLIC accelerator framework, represents a promising solution for new compact accelerators. However, due to their geometry and the high-gradients, such structures are strongly suffering from the wakefield.

In this chapter, the wakefield studies and the measurement results obtained are presented. In particular, two different met**h**odologies of measuring the wakefield are presented. The first one relies on the measurement of the effect that the wakefield has on the beam. Thus the measurement of a transverse kick of the beam thanks to a beam screen is performed. The second one uses the Wake Field Monitors (WFMs) to detect the accelerating structure's electromagnetic field.

The whole study is carried out using the CLIC baseline accelerating structure. In CLEAR it is installed as a superstructure composed of two accelerating structures, which is currently not connected to any power source. Firstly the proposed simulation and measurement methodology are presented. Following the accelerating structure and the devices used in the measurement are shown. Later, the simulation and the experiments are reported, followed by their results.

3.1 Methods

In this sections, the simulation and the experimental campaign's methods are presented, respectively.

3.1.1 Simulation method

The simulations are performed with the assumption of being dominated by the short-range wakefield, particularly by its dipolar component. The long-range wakefield is assumed to be damped by the HOM installed in the structure. The basis of the simulations are the Karl-Bane model for short range wake [179], in which the wake potential per unit structure length, beam offset, and bunch charge is given as

$$W_T = \frac{4Z_0 c s_0}{\pi a^4}\phi(s)\left(1-\left(1+\sqrt{\frac{s}{s_0}}\right)e^{-\sqrt{\frac{s}{s_0}}}\right), \tag{3.1}$$

where Z_0 is the characteristic impedance (in case of vacuum $Z_0 = c\mu_0$, where μ_0 is the magnetic permeability of the vacuum), $\phi(s)$ is a step function ($\phi(s) = 1$ for

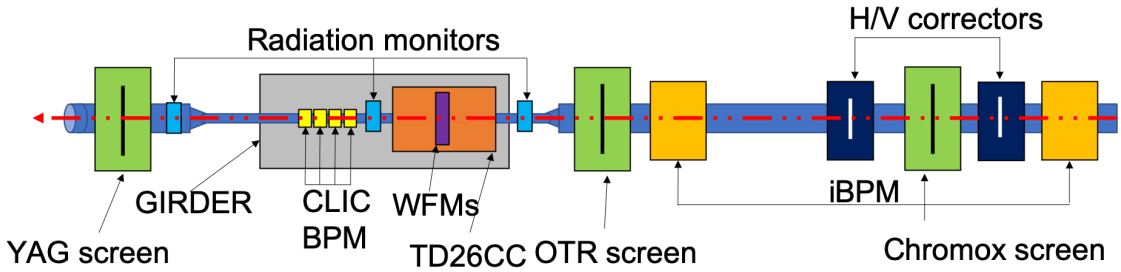

FIGURE 3.1: The schematic layout of the experimental area, the red arrow points the beam path and direction.

$s > 0$ and $\phi(s) = 0$ for $s \leq 0$), s is position on the accelerator axis, and s_0 is defined as:

$$s_0 = 0.169 \frac{a^{1.79} g^{0.38}}{l'^{1.17}}. \tag{3.2}$$

In Eqs. 3.1 and 3.2 the quantities a, g, and l' are the geometrical characteristics of the cell, which is described in Sec. 3.2.1.

Two main quantities that can be derived from the simulations are: (i) the wake potential, and (ii) the beam distribution on a later screen.

3.1.2 Experimental method

The measurement methods foresee different displacements between the structure and the beam. The displacement will lead to an increase of the wakefield that, as discussed in Sec. 2.2.4 and 2.2.5, will induce growth in the wakefield. In the approximation of being dominated by the dipole mode, the wakefield is linearly dependent on the distance between the beam and the structure center. This effect can be measured by directly sensing the field thanks to the pickup antennas integrated into the structure or the effect that the transverse field has on the beam position (i.e., a transverse kick), that can be monitored in the downstream beamline.

Several beam instrumentation devices were used, in order to perform the measurements. A schematic layout of the experimental area is reported in Fig. 3.1. In particular, the layout is composed of: two horizontal/vertical correctors (in dark blue in Fig. 3.1), two inductive BPMs (in dark yellow in Fig. 3.1), three CLIC cavity BPMs (in light yellow in Fig. 3.1), three beam screens (in green in Fig. 3.1), three radiation monitors (in light blue in Fig. 3.1), the girder for supporting the accelerating structure (in grey in Fig. 3.1), the CLIC accelerating structure (in orange in Fig. 3.1), and the WFMs installed in the middle of the accelerating superstructure i.e., two accelerating structure brased together (in purple in Fig. 3.1).

Each device installed on the beamline performs a specific task in order to carry out the wakefield and kick measurements. The inductive BPMs, the CLIC BPMs, and the screens were installed to monitor the beam position and trajectory. BPMs

using two different technologies were installed because the incredibly challenging CLIC parameters range and the required resolution [180] require the development of specialized devices. Unfortunately, both of these devices are not designed for a single bunch/short train operation, commonly used in CLEAR. The inductive BPMs are in the process of becoming operational, and are soon expected to support the measurements. The CLIC BPMs are currently only operated as a separate experiment in order to develop suitable electronics and characterize their performance. The measurement methods propose to monitor the position and the trajectory use the beam screens, particularly the one located after the CLIC structure, made of Yttrium Aluminum Garnet (YAG) [181].

The correctors and the girder, which is installed on movers, were installed to change the relative displacement between the accelerating structure and the beam. Such degrees of freedom was needed to study the effect of different displacement on the wakefield. The radiation monitors were installed to monitor the beam losses along the beam line. Such monitors are intentionally installed in proximity of the accelerating structure because it represent a bottleneck for the beam passage. An additional one is installed later in the beam line to monitor losses in the CLIC BPMs, typically driven by large angle. The first method for measuring wakefield relies on the use of WFMs. This device is composed of eight pickup antennas for sensing the filed in the accelerating structure at two different beam harmonic frequencies, the first at $18\,\mathrm{GHz}$, and the second at $24\,\mathrm{GHz}$. The WFMs are installed in the first regular cell of the second accelerating structure in the superstructure, which is close to the middle of it. The signal obtained is mainly dependent on the beam characteristics (i.e., charge, and bunch length) and on the relative displacement between the structure and the beam. During an experiment, the beam characteristics can be realistically assumed almost constant. Thus the signal obtained from the WFMs will depend only on the relative displacement. However, since the WFMs are designed to work with the CLIC beam (larger charge and longer trains), they cannot provide the specified accuracy of $3.5\,\mu\mathrm{m}$ in a single bunch or short train operating mode, widely used in CLEAR. More information on this device are reported in Sec. 3.2.2

The second method assesses the wakefield from the transverse kick, using the beam screen after the structure was used. In particular, to assess the strength of the transverse wakefield, the change of the beam position on the screen was monitored while inducing a different displacement between the structure and the beam. The operating principle is reported in Fig. 3.2. Taking into account the small-angle approximation, the change of angle Δ'_x can be written as

$$\Delta'_x = \frac{\Delta_x}{l}, \tag{3.3}$$

where Δ_x is the displacement on the screen, and l is the distance between the screen and the middle of the accelerating structure. Combining Eq. 2.26 with Eq. 3.3 and isolating the transverse bunch voltage

$$V'_x = \frac{\Delta_x}{l}\frac{cp_s}{e^-}, \tag{3.4}$$

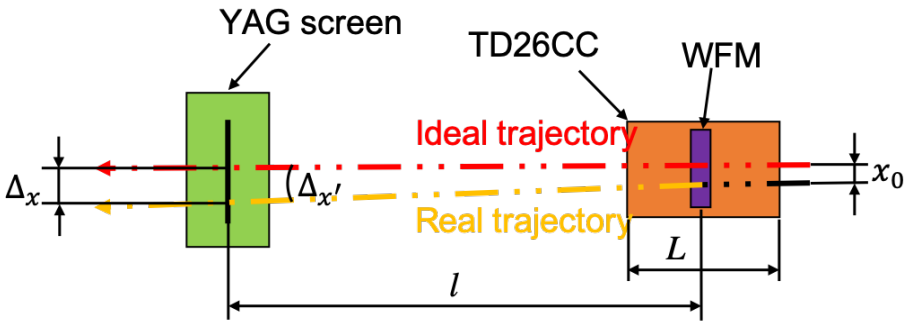

FIGURE 3.2: The operating principle to investigate the strength of the transverse wakefield.

where q is the witness charge typically equal to the negatice electron charge (i.e., $-1e$). Under the assumptions that: the dipolar wakefield component dominates the kick, short excitation, linear dependence with the length of the accelerating structure, and linear dependence of the charge the quantity V_x' can be rewritten as

$$V_x = \frac{V_x'}{Lx_0q}, \tag{3.5}$$

where V_x is the transverse bunch potential, L is the length of the accelerator structure, x_0 is the displacement between the electrical center of the structure and the beam trajectory, and q is the charge of the bunch. Combining Eq. 3.4 and 3.5 yields

$$V_x = \frac{\Delta_x}{x_0}\frac{p_sc}{lLqe^-}. \tag{3.6}$$

The units of the transverse bunch voltage are $\frac{\mathrm{V}}{\mathrm{m\,mm\,pC}}$. While varying the displacement between the beam and the accelerating structure, and monitoring the variation of the beam centroid on the screen, the ratio $\frac{\Delta_x}{x_0}$ is equal to the derivative of the variation of the centroid position of the beam while performing the scan. From Eq. 3.6, taking the bunch length into account (i.e., removing the assumption of short excitation) can be written as

$$V_\perp = \frac{\Delta_x}{x_0}\frac{p_sc}{lLqe^-}F(\sigma_{t_0}), \tag{3.7}$$

here $F(\sigma_{t_0})$ is the form factor, which is the ratio of the average voltage seen by a bunch with the given bunch length and a bunch with a reference bunch length. For the case of the short range wake, the voltage seen by a zero-length bunch is zero, so the typical bunch length $\sigma_{t_0} = 4\,\mathrm{ps}$ is chosen as the reference. Note that if the beam is moved relative to the structure, as will be discussed in Sec. 3.4.2, Eqs. 3.6 and 3.7 are modified by replacing $\Delta_x \to \Delta_x - x_0$. On the other hand, if the structure is moved, as discussed in Sec. 3.4.1, Eqs. 3.6 and 3.7 are not modified.

As for the methods that use the WFMs, each experiment in the kick study is characterized by a specific beam condition (in terms of energy, charge, and bunch length) that can be reasonably assumed to be constant over the whole experiment.

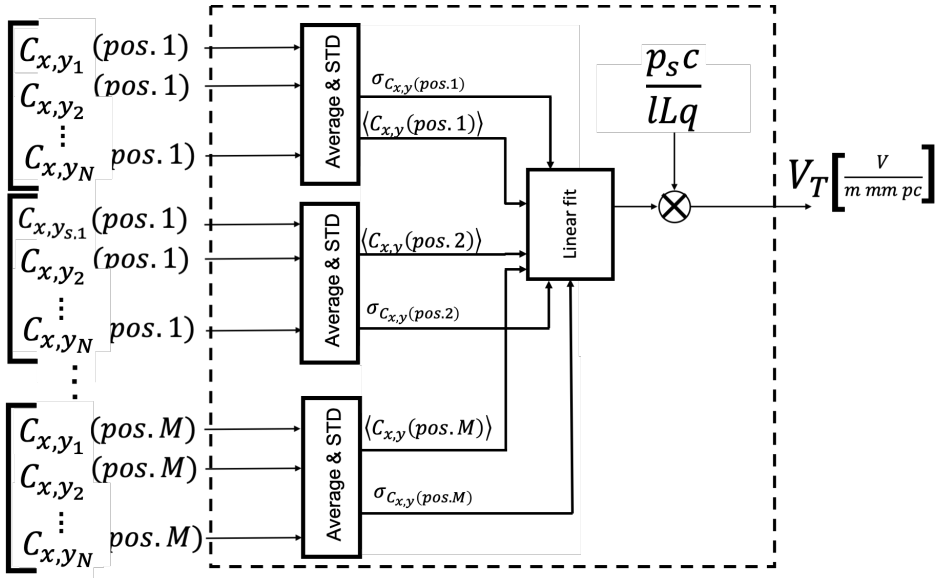

FIGURE 3.3: The model of the measurement production to assesses the transverse kick.

A schematic representation of the measurement method is reported in Fig. 3.3. Each experiment, also referred as scan, is composed of M-points (one for each relative displacement), and the acquisition of the signals is repeated N-times.

Before analysis, all the acquired beam images are background subtracted, first using a reference image of the screen without beam in order to reduce inhomogeneity. A second uniform background subtract is then performed, in order to remove possible illumination discrepancies; this uses an area of the screen without beam as the reference. Moreover, for practical reason, the Area Of Interest (AOI) is manually selected in order to avoid including screen artifacts (e.g., screen border and screen imperfections) which were disturbing the attempted automatic selection of the AOI. Such a procedure has the aim of making the post-processing more robust. It is needed for each acquisition to assess the beam's centroid $C_{x,y}$. Such quantity can be defined in two different ways. The first way assesses $C_{x,y}$ directly by the weighted average on the beam distribution projection on the vertical and horizontal axes. The second way is based on a Gaussian function to fit the beam distribution on the vertical and horizontal axes. The first processing was used to handle also non-Gaussian beam distribution impacting the screen.

Besides, for each method, the $C_{x,y}$ assessment is performed in two ways. For the first one, perform the assessment directly on the beam profile average. In contrast, the second one performs the assessment individually for each beam profile, and then the results are averaged. The results are usually very close (i.e., discrepancy less than 2%); however, atypical beam profiles can be individually identified thanks to this technique In case the results are close, the one assessing $C_{x,y}$ individually for each image is taken into account. As described presenting Fig. 3.3, each point that compose the scan represent on offset between the beam a the structure. For each point, N-acquisitions are repeated to identify the beam

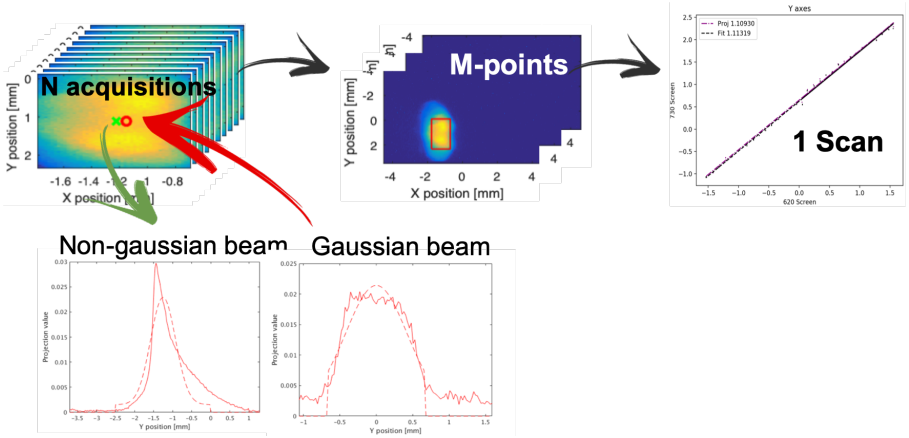

FIGURE 3.4: The acquisition procedure from right to left; the two methodology to assessment of the beam centroids from N-acquisitions repeated for each of the M-points that compose the scan.

centroid using two different procedure beam in order to take into account Gaussian beam and non-Gaussian beam. An overview of the acquisition procedure is reported in Fig. 3.4. A sketch of the result post-processing script is reported in Figs. 3.5

The scan can be performed in the two planes (horizontal and vertical), moving the CLIC accelerating structure and keeping the beam position constant or the other way around. Depending on the beam distribution, the most suitable processing is used; moreover, all for comparison convenience, all the results refer to vertical scans.

3.2 Equipment and devices

In this section, the accelerating structure principle adopted in CLIC is presented, investigating the characteristic of the accelerating structure and the parameters of the CLIC geometry. Later the WFMs operating principle and their acquisition system are presented.

3.2.1 CLIC accelerating structure

The force used for accelerating electrically charged particles is the electric field. The electric field is varying with time and is synchronized to the particle motion, using the principle of resonance or RF acceleration [182, 183].

A significant effort in studying new accelerating structures has been performed for the CLIC accelerator, where many different structures, even exploiting different technology, have been developed and tested [1]. One of the main critical phenomena that must be avoided to reach high gradients reliably is the vacuum arcs. It was proven that the targeted average accelerating gradient of $100\,\mathrm{MeV/m}$ can

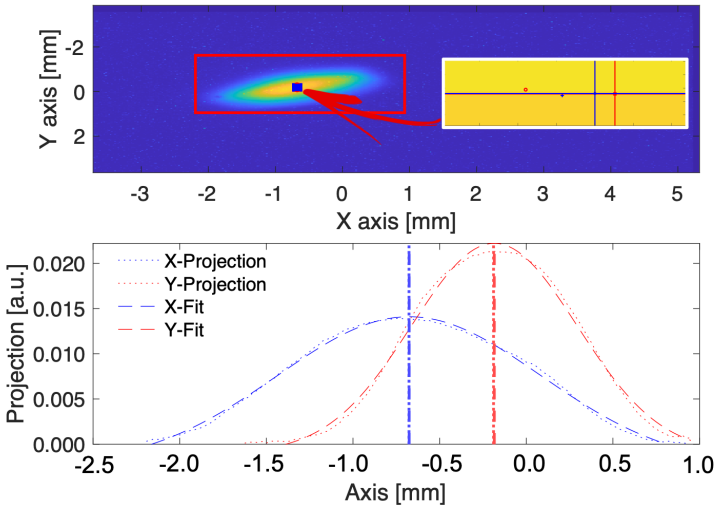

FIGURE 3.5: On the top, the beam image with a zoom on the identified centroids on both planes with both methods. On the bottom, the projections and the fits used to estimate the centroid positions are highlighted using vertical lines.

be reached by carefully designing the structure geometry such that high surface fields and large local power flows are avoided [101, 184].

The baseline reference structure for CLIC study is represented by the so-called TD26CC [4], the latest prototype of the CLIC accelerating structure developed. Such structure is Travelling Wave (TW) one. It is made of several accelerating cells, which are coupled such that an oscillating field in one cell will drive an oscillation in the next cell and so on. This effect generates an accelerating field which has the peak position is moving with a phase velocity, v_p , synchronous to the particle velocity. The phase advance between two cells spaced by a distance l' needs to be

$$\Delta\phi = \frac{l'}{\lambda} 2\pi, \tag{3.8}$$

where λ is the wavelength.

This structure operates in the X-band regime, with the acceleration mode at $12\,\mathrm{GHz}$; thus, it is powered from an X-band source. Such source, as foreseen in the CLIC project [47]) can be or a drive beam or an X-band klystron (as described in Sec. 1.3).

In addition to the accelerating mode, there will be numerous HOMs present in the accelerating structures, which can either be excited by the beam or possibly transferred from the drive beam. These modes, which often degrade the beam quality, can be monopole, dipole, quadrupole modes, and so on. The structure is Tapered and Damped Coupling Cells, composed of 26 cells (i.e., TDCC26), and two of these structures are usually brazed together into a so-called superstructure. The adjective tapered means that the iris radius decrease along with the accelerating structure and, damped means that to minimize the impact of the HOM, the accelerating cells are equipped with damping wave**g**uides designed to

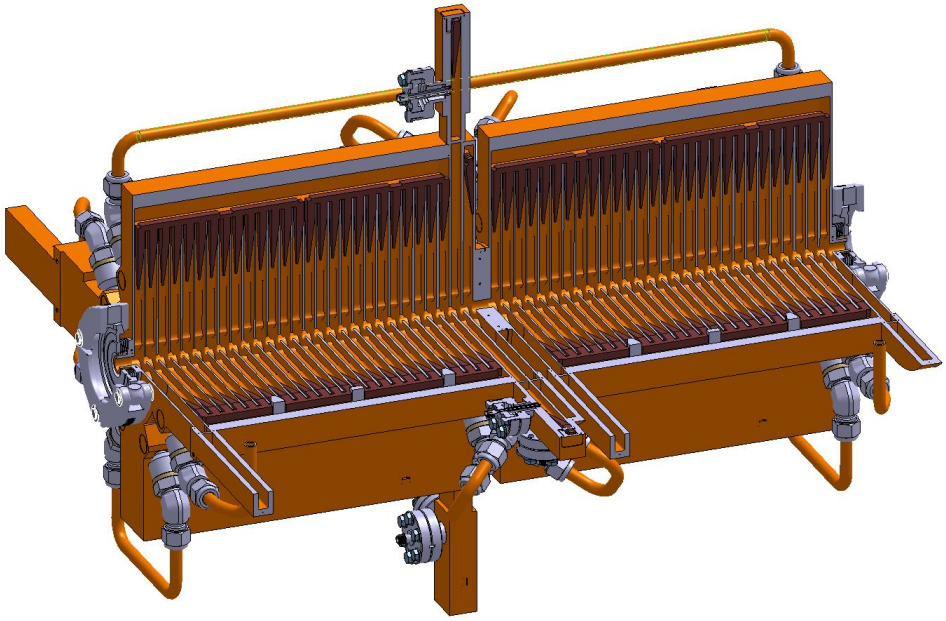

FIGURE 3.6: The 3D-cad drawing of a superstructure composed of two TD26CC accelerating structures, where longitudinal and transverse cuts highlight the tapering and the damping of the structure [37].

couple with the HOMs and damp them [185]. A 3D-cad drawing with one quarter removed is reported in Fig. 3.6. With a maximum iris radius of about $4\,\mathrm{mm}$ in CLIC X-band accelerating structures, allows to reach a high gradient up to a $100\,\frac{\mathrm{MV}}{\mathrm{m}}$. As comparison, the Lepton Injector LINAC (LIL) cavities with an aperture of $25\,\mathrm{mm}$, working at $2.9985\,\mathrm{GHz}$ currently used in CLEAR can only reach a gradient up to a $20\,\frac{\mathrm{MV}}{\mathrm{m}}$ [186]. Unfortunately, due to the narrow apertures, the wakefields are much more intense in CLIC structures. Such a wakefield problem was known during the design phase of the structure. For this reason, the WFMs, a method for assessing the wakefield strength, were designed [187].

In the second structure of the superstructure, the damping waveguides of the first cell are extended with the WFMs [188, 189] A photo of the TD26CC CLIC accelerating superstructure is shown in Fig. 3.7.

This type of accelerating structures has the advantage of short fill time, allowing to tolerate extensive beam loading and allow more extended structures and shorter filling times compared to the other possible type, the Standing Wave (SW) structures [101]. The SW structures can be considered the superposition of two TW to obtain a wave that oscillates in time but whose peaks does not move in space. The peak amplitude of the wave oscillations at any point in space simultaneously and the oscillations at different points throughout the wave are in phase [190].

It is quite comfortable in a cavity to describe the field patterns as eigenmodes, which are solutions to Maxwell's equations obtained by factorizing out the time

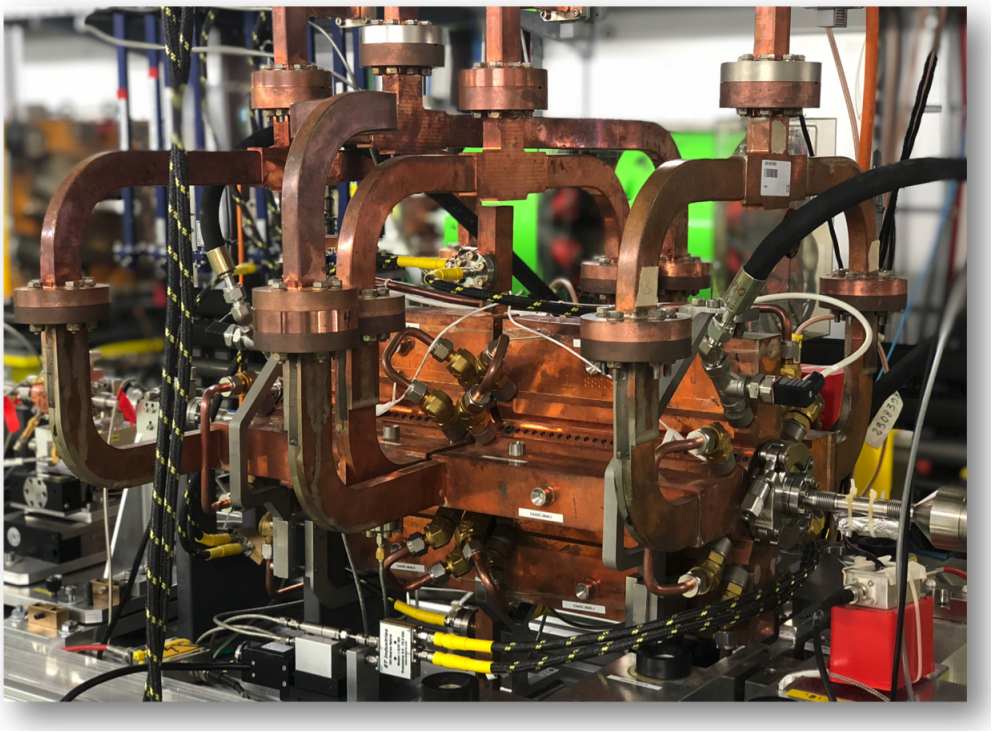

FIGURE 3.7: The prototype of the CLIC accelerating superstructure; currently installed in CLEAR.

dependency. Different parameters are particularly useful for describing a particular structure. One of the most famous is the so-called Q-factor

$$Q = \frac{\omega U}{P}. \tag{3.9}$$

The ratio of the stored energy U to the power lost P in one RF cycle. It represents how fast the amplitude and stored energy of the mode oscillating at is damped. Another significant quantity is the effective shunt impedance

$$R = \frac{V^2}{P}, \tag{3.10}$$

which relates the accelerating voltage V to the power loss. Such quantities can be normalized with the length of the structure $R' = {}^{R}/_{L}$. Sometimes it is useful to write the ratio between Eq. 3.9 and 3.10

$$\frac{R}{Q} = \frac{V^2}{\omega U}. \tag{3.11}$$

This quantity is describing how quickly the voltage rises with stored energy, it is independent of the power loss and thus independent of the cavity's material, determined only by the field pattern determined by the geometry. Another useful

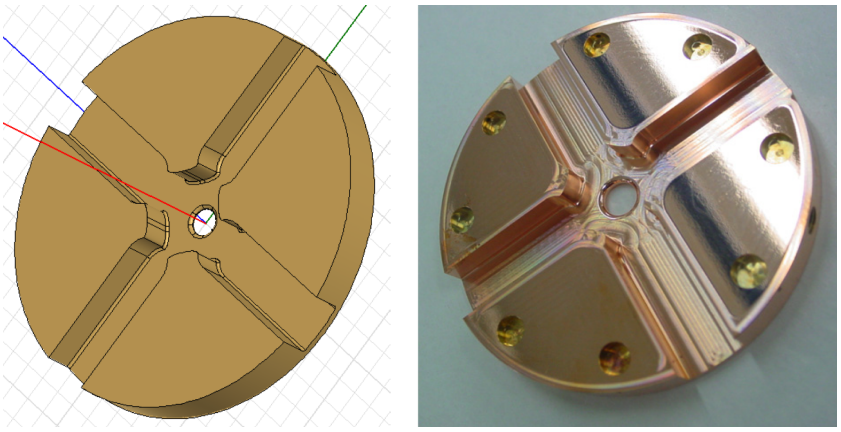

FIGURE 3.8: The cell geometry of the accelerating structure with strong waveguide HOM damping, a 3D model (left) and a copper piece (right) [6].

quantity is the filling time that in the TW is defined as

$$t_f = \int_0^L \frac{1}{v_g} dz, \tag{3.12}$$

where v_g is the group velocity. It represents the time needed for the electromagnetic energy to fill the cavity of length L.

Cell geometry

The geometry of the accelerating cells for these TW structures were carefully optimized, in order to maximize the gradient capability of the accelerating structure designs for CLIC, .

An example of the cell geometry is shown in Figs. 3.8. It consists of a central volume that traps the accelerating mode, and four narrow waveguides allow higher frequency modes excited by the beam to radiate out of the central volume. The design avoids radiation of the fundamental mode, as its frequency is below the cutoff frequency of the four damping waveguides. The structure was tuned such that the phase velocity of the principle wave is synchronized with the electrons, which should be accelerated. Such tuning is obtained by changing the iris apertures a, cell thicknesses d, cell radius b, and cell length l' over the length of the structure [6]. A graphical representation of the geometry cell's main parameters is shown in Fig. 3.9. In Tab. 3.1 the main parameters, and the relative ranges are reported.

The TD26CC is a tapered disc-loaded waveguide structure; each cell is equipped with four damping waveguides (terminated with a silicon carbide load), designed to strongly suppress the long-range wakefield [6].

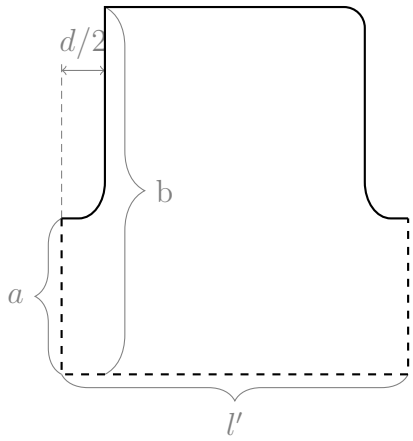

FIGURE 3.9: A quarter of a single accelerating cell geometry [101].

TABLE 3.1: The CLIC TD26CC main parameters.

Parameter	Range
Accelerating gradient	$100\,\mathrm{MV/m}$
Frequency (f)	$11.9942\,\mathrm{GHz}$
RF phase advance per cell ($\Delta\phi$)	$2\pi/3\,\mathrm{rad}$
Cell length (l')	$8.3333\,\mathrm{mm}$
Structure length (L)	$230\,\mathrm{mm}$
Number of cells	26
Iris radii (a)	$3.15 - 2.35\,\mathrm{mm}$
Iris thickness (d)	$1.67 - 1.00\,\mathrm{mm}$
Q-factor (Q)	$5536 - 5738$
Shunt impedance ($\frac{R}{Q}$)	$81 - 103\,\mathrm{M\Omega/m}$
Filling time (t_f)	$67\,\mathrm{ns}$

3.2.2 Wake Field Monitors (WFMs)

As explained in Sec. 2.2, it is essential to avoid as much as possible the misalignment between the beam and the accelerating structure to minimize the wakes. The wakes themselves are measured by the WFMs. Such a device can measure the dipole modes, and from them, the beam position in the structure can be estimated, which is used as input information for the alignment strategy.

In CLIC, the accelerating structures are placed on girders that can be moved using high precision movers. The wakes from individual structures cannot be canceled, but the strategy is to align the girder such that the net wake effect is close to zero over the whole girder. The WFMs are pickup antennas used for measuring the beam position. Each waveguide is equipped wit**h** two antennas for measuring two different dipole modes. The TM-like mode is around $16.9\,\mathrm{GHz}$, while the Transverse Electric (TE)-like (transverse electric) mode is around $27.3\,\mathrm{GHz}$. The real part of the transverse impedance of the TD26 structure at three different cells (the first, the middle, and the last) is shown in Fig. 3.10. The blue line represents the cell where the WFMs are installed. This result was obtained with the

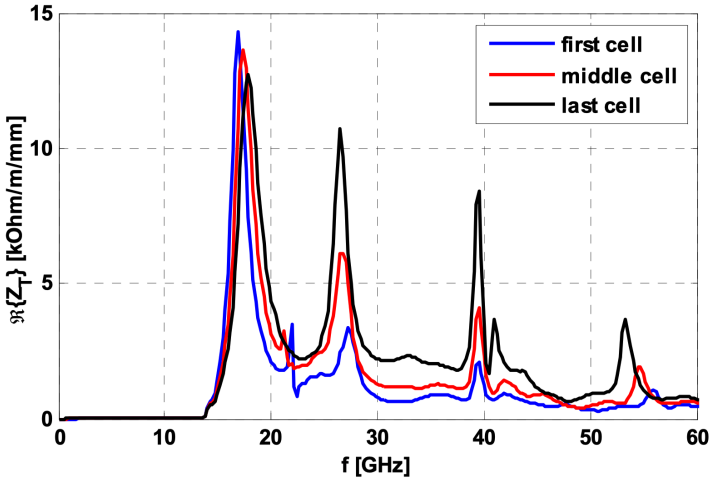

FIGURE 3.10: The real part of the transverse impedance simulated in GdfidL for different cell types [6].

simulation tool GdfidL [94]. The peaks at $16.9\,\mathrm{GHz}$ and $27.3\,\mathrm{GHz}$ represent the TM-like and TE-like modes, respectively [191].

A simplified drawing of the field patterns of the electric fields inside the CLIC accelerating structure equipped with WFM is shown in Fig. 3.11. A vertical offset is present between the beam and the cell, and such offset induces the two dipole modes. The TE-like field lines are shown in blue in Fig. 3.11, and they are stronger in the horizontal plane outside the center. The magnitude of this field is linearly dependent on the vertical beam offset. An important feature of the TE-like mode is that it is symmetric in the horizontal plane with respect to the cell axis. Therefore, the modes couples to both the horizontal waveguides with symmetric fields without coupling with the vertical waveguides. In this configuration (beam offset only in vertical), the pickup antennas on the horizontal waveguides will give the same signal on both sides.

The TM-like mode lines are shown in orange in Fig. 3.11. This electric field has two nodes in the vertical plane inside the cell, where it enters the plane on one side and comes out of the plane on the other side. The TM-like field is therefore asymmetric and couples with opposite polarities to the two vertical waveguides. Consequently, the pickup antennas placed at a similar distance on the vertical waveguides will therefore give similar signals with a $180\,\mathrm{deg}$ phase difference. Note that Fig. 3.11 shows a simplified example where the fields are given only from the vertically displaced bunch.

In case of a horizontal beam displacement, the field patterns will be rotated by $90\,\mathrm{deg}$. Therefore, there are also TE antennae on the vertical waveguides and TM antennae on the horizontal waveguides. Moreover, such antennas were installed in different positions on the same waveguide due to the TE-like and TM-like modes' directions.

The pickups are then connected to $180\,\mathrm{deg}$ hybrids with suitable coaxial cables (with K-type connectors) to remove possible monopole mode. Pairs of phase shifters are installed between between the antennas and the input of the hybrid to correct possible cable length mismatch. In particular, on the TM horizontal

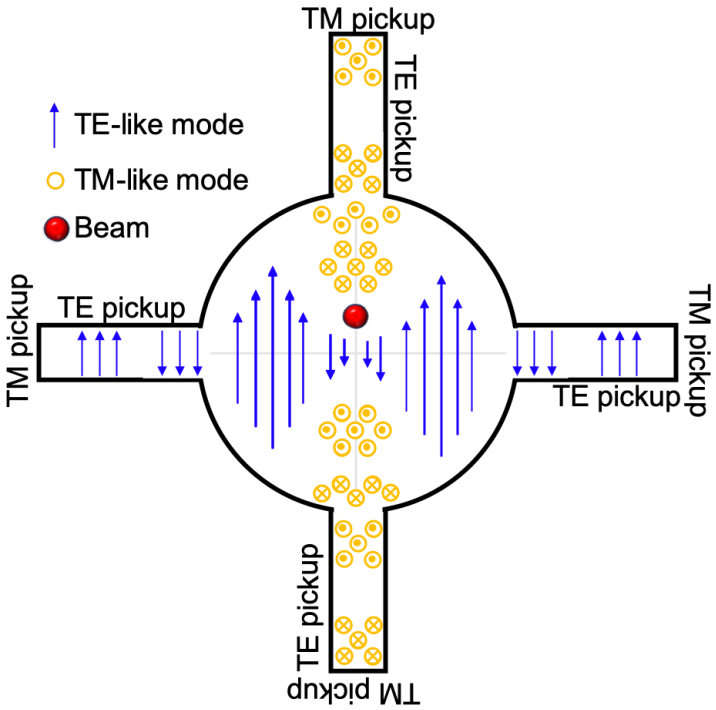

FIGURE 3.11: The field map of TE and TM like mode in the CLIC accelerating structure.

channel, a remotely controllable movable phase shift was added to check while the beam passed through a possible difference in the center identification.

The desired information is in the sum or in the delta signals depending on the offset and mode. In particular, in the case of vertical or horizontal offset, the displacement information is in the vertical or horizontal delta signals of the TM-like mode, or horizontal or vertical sum signals of the TE-like mode. Later, the hybrid outputs are transported to the readout area (above the experimental hall) in waveguides to minimize losses.

The signals pass through a band-pass filter (waveguide filters) to remove frequencies different from the desired mode at the waveguides' exit. Downstream, the signals are limited using limiters before entering they enter into the logarithmic detectors, which were chosen due to the extended dynamic range (around $30\,\mathrm{dB}$). It was chosen to investigate both small signals (obtained when the beam passes close to the structure center) and large signals (obtained when the beam passes close to the pipe's edge). Finally, the signals are digitized using Analog to Digital Converters (ADCs) with a sampling rate of $1\,\mathrm{GS/s}$.

A schematic of the whole WFM acquisition system from the accelerating structure cell to the sampler is shown in Fig. 3.12.

Ideally, the two modes should show the same linear dependence on the beam position, which provides redundancy. For reducing the number of needed readout devices, one of the two dipole modes should be elected as the one used to determine the beam position. One of the current WFM study goals is to decide on which mode needs to be selected as the one to be used.

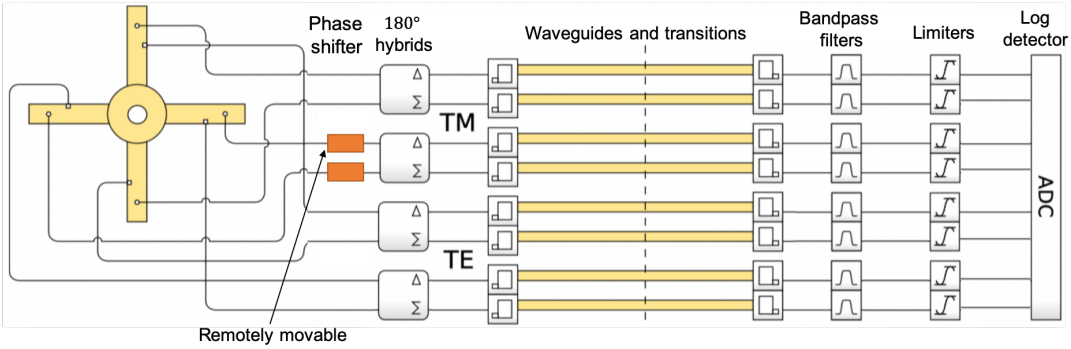

FIGURE 3.12: The WFM acquisition system.

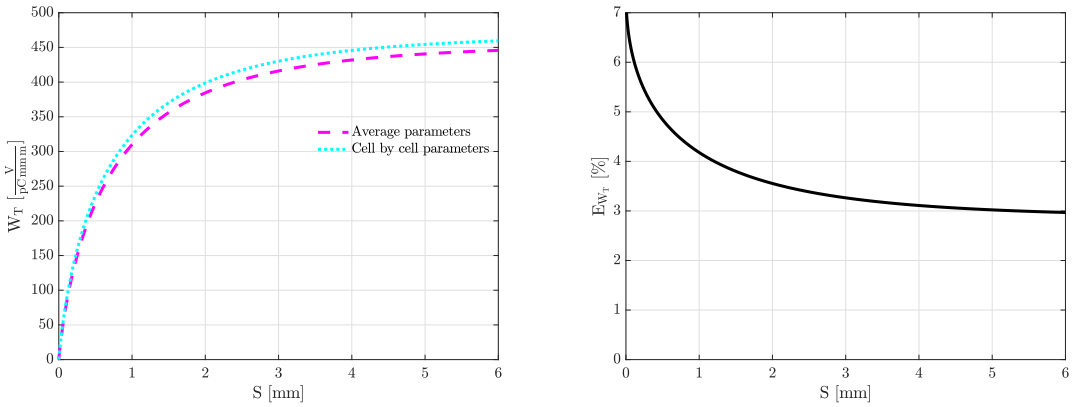

(A) (B)

FIGURE 3.13: In (A) the wake potential for the two different evaluation methods. In (B) the percentage relative error between the two wake potential.

3.3 Simulation

In this section, an overview of the simulations performed is presented. Firstly, the simulations of the wake potential are performed using two different simulation methods. Later, thanks to the simulations, another interesting quantity (the beam distribution) that can be **m**onitored while studying the wakefield effects is investigated. Also in this study, two different procedures are tested.

3.3.1 Wake potential simulation

From Eqs. 3.1 and 3.2, to simulate the wake potential it is evident the critical role that the geometry parameters are playing. For understanding the impact of these parameters, two different types of simulations were performed. The first one uses an average value for the cell parameters, while the second one uses cell by cell defined parameters equal to the technical specifications reported in Tab. 3.1. In Fig. 3.13 (A), the result of the two different simulation methods for estimating the

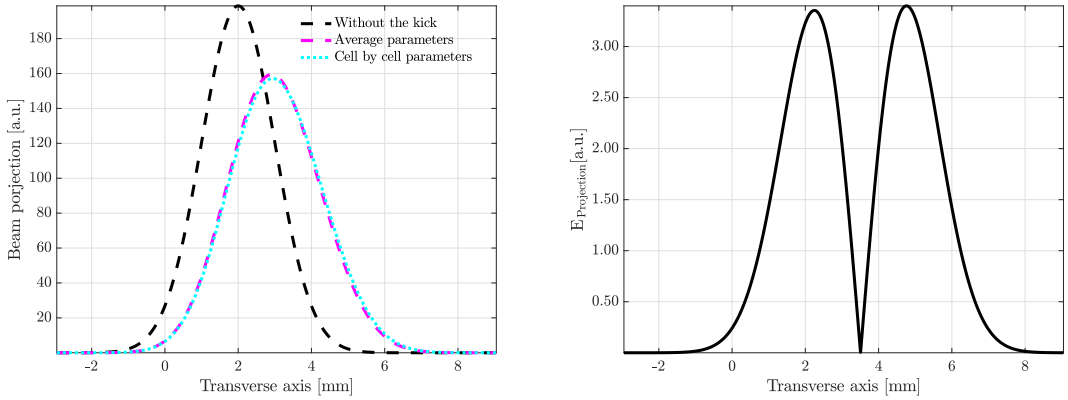

(A) (B)

FIGURE 3.14: In (A), the beam distribution without (dashed black) and with (dashed magenta and cyan) the kicks, for the two different cell parameters distribution. In (B), the absolute error between the beam kicked distributions obtained with the two cell parameters.

wake potential are shown; while in (B), the percentage relative error,

$$E_{W_T} = 100 \frac{|W_{T_{Average}} - W_{T_{CellByCell}}|}{W_{T_{CellByCell}}}, \tag{3.13}$$

between them is reported. Figure 3.13 (B) shows that the percentage relative error is below 7% and that as S increases, it tends to 3%.

The result obtained using the cell by cell parameters are a more reliable representation of the structure's real geometry; thus, its results can be expected to be more reliable. Moreover, as will be shown in the next Sec. 3.3.2, the discrepancy in the calculation of the wake potential can drive a wrong assessment in the beam distribution.

3.3.2 Beam distribution simulation

Computing the transverse voltage, given the wake potential and the longitudinal profile of the bunch, the expected transverse beam distribution on the measurement screen can be reconstructed. As a consequence, for the beam distribution simulations on the screen, it is needed to distinguish between two different simulation procedures. The expected beam distribution **o**btained on the screen after the accelerating structure can be simulated using either the average parameters or the cell by cell parameters. In the simulations, a bunch with a Gaussian charge distribution in all three planes with a total charge of $500\,\mathrm{pC}$, a RMS bunch length of $4\,\mathrm{ps}$, and a transverse sigma of $1\,\mathrm{mm}$. A initial transverse beam displacement of $2\,\mathrm{mm}$, and the energy of $200\,\mathrm{MeV}$ was used.

In Fig. 3.14 (A), the beam distribution obtained without (dashed black) and with (dashed magenta and cyan) the kicks using the two different approaches for

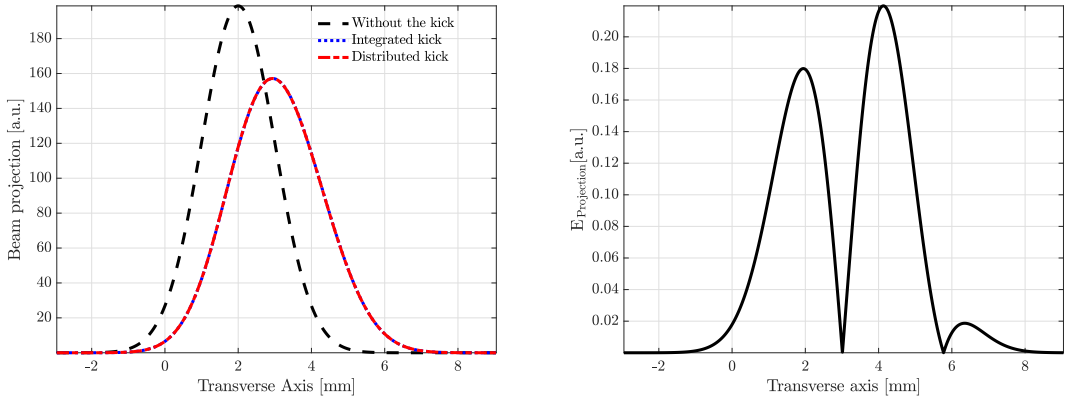

(A) (B)

FIGURE 3.15: In (A), the beam distribution without (dashed black) and with (dashed red and blue) the kicks, for the two different simulation procedures. In (B), the absolute error between the kicked beam distributions obtained with the two simulation procedures.

describing the cell parameters are shown. In Fig. 3.14 (B), the absolute error,

$$E_{Projection} = |Proj_{CellByCell} - Proj_{Average}|, \tag{3.14}$$

between them is reported. The methods that use the integrated value for the cell parameter are not in agreement with the one that specifies each cell's parameters. As anticipated in Sec. 3.3.1, the discrepancy of the wake potential drives a discrepancy in the beam distribution assessment as highlighted from the absolute error in Fig. 3.14 (B). This discrepancy drives an error in the identification of the beam centroid larger than 3%.

While analyzing the wakefield effect on the bunch (i.e., the transverse kick), it is interesting to distinguish between two other possible simulation approaches. The transverse kick can be applied as an integrated quantity to the bunch at one point in the structure, or it can be applied for each cell. In the first simulation procedure, the beam displace**m**ent induced from the structure while traveling is neglected. In contrast, in the second case, the offset variation induced from the wakefield is taken into account for each cell, and it influences the wakefield generated from the following one. For the first simulation procedure, the integrated kick is applied in the longitudinal center of the accelerating structure. After, the bunch is assumed to propagate in a drift space. In Fig. 3.15 (A), the beam distribution obtained without (dashed black) and with (dashed red and blue) the kicks for the two different approaches integrated and distributed are shown. In Fig. 3.15 (B), the absolute relative error,

$$E_{Projection} = |Proj_{Distributed} - Proj_{Integrated}|, \tag{3.15}$$

between them is reported. From the simulation results in Fig. 3.15 (A), the approximation of applying an integrated kick in the middle of the structure is in good agreement with the result obtained using distributed kicks. The absolute

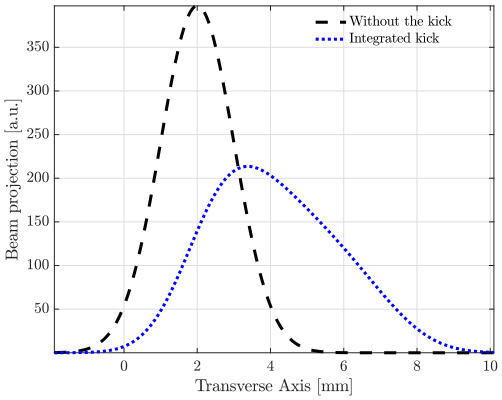

FIGURE 3.16: The simulation results of the beam distributions without (dashed black) and with (dashed blue) the kicks, for a bunch with the double of the charge compared to the once previously used.

errors between the beam distribution, in Fig. 3.15 (B), is well below the one obtained by comparing the different type of cell parameters, in Fig. 3.14 (B). This error drives an error in the assessment of the beam centroid that is less than 1%. For this reason, both methods can be used to determine the beam distribution. From the results obtained in Figs. 3.13, 3.14, and 3.15; the method that uses the integrated kick and describing each cell using the design parameters is used for all the future simulations.

Repeating the simulations with the same parameters but increasing the bunch charge to $1\,\mathrm{nC}$; the transverse kick grow with the charge and how the tail of the bunch suffer from this effect. In Fig. 3.16 the transverse beam distribution is reported without (dashed black) and with (dashed blue) the kick, showing that the transverse beam profile on the screen has no longer a Gaussian shape.

It is interesting to simulate the effects of kick for bunches with non-Gaussian longitudinal distribution since Gaussian bunches are an approximation of the real longitudinal distribution of the bunch. In particular, bunches with skew-Gaussian distribution where simulated. The skew-Gaussian charge density distribution is

$$\xi(x) = q\,\frac{2}{\sigma_{t^*}}\phi\left(\frac{x-\mu}{\sigma_{t^*}}\right)\Phi\left(\Gamma\cdot\frac{x-\mu}{\sigma_{t^*}}\right), \tag{3.16}$$

where $\phi(x)$ if the Probability Density Function (PDF) of a standard Gaussian distribution, $\Phi(x)$ is the Cumulative Distribution Function (CDF) of a standard Gaussian distribution, and Γ is the so-called skew parameter. The distribution is front-heavy skew-Gaussian if $\Gamma > 0$ and is tail-heavy skew-Gaussian if $\Gamma < 0$. If $\Gamma = 0$, the distribution becomes a normal Gaussian. While modifying the longitudinal distribution, it is needed to take into account the variation of bunch length as

$$\sigma_{t^*} = \frac{\sigma_{t_0}}{\sqrt{1-\frac{2\Gamma^2}{\pi(1+\Gamma^2)}}} \tag{3.17}$$

where, σ_{t_0} is the RMS bunch length, and σ_{t^*} is the bunch length parameter for the skew-Gaussian distribution. In Figs. 3.17, the simulations performed hold-

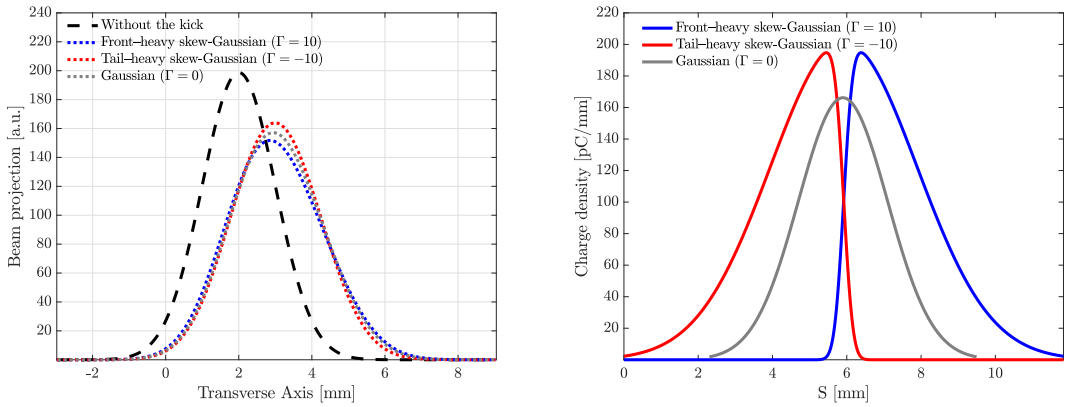

(A) (B)

FIGURE 3.17: In (A), the transverse beam distributions on the screen without (black dashed) and with (dashed blue, red, and grey) the kicks, for the front-heavy skew-Gaussian ($\Gamma = 10$), tail-heavy skew-Gaussian ($\Gamma = -10$), and Gaussian ($\Gamma = 0$) longitudinal distribution. In (B), the three respective charge density distributions.

ing the initial bunch parameters (i.e., charge of $500\,\mathrm{pC}$) but using three different type of longitudinal distribution (i.e., front-heavy skew-Gaussian ($\Gamma = 10$), tail-heavy skew-Gaussian ($\Gamma = -10$), and Gaussian ($\Gamma = 0$)) are shown. The skew parameters adopted were chosen to mimic the profile observed in the accelerator while performing measurements on the longitudinal plane. In Fig. 3.17 (A) the beam distribution without (black dashed) and with (dashed blue, red, and grey) the kick for the three above listed distributions are shown. In Fig. 3.17 (B), the respective longitudinal distributions are reported. The results show that the longitudinal distribution impacts the centroid's evaluation, about 1% in the considered case. However, its effect is strongly related to the wakefield impact on the bunch (e.g., for five times the charge, the centroid discrepancy achieve around 6%). A larger kick is experienced from the tail-heavy skew-Gaussian distribution because, in Fig. 3.13 (A), the wakefield is excited from the head and, once it has reached a larger value strongly impacts the high-charged tail. Thus, it needs to be taken into account once comparing the measurements and the simulations.

3.4 Experiments

In this section, the experiments are presented. Firstly, the ways to scan the relative displacement between the accelerating structure and the beam are presented. Two possible methodologies were tested, the first one is CLIC-like and does not require any adjustment on the beam, while the second one requires to modify directly on the beam trajectory. Later the experimental calibration of the WFMs is presented.

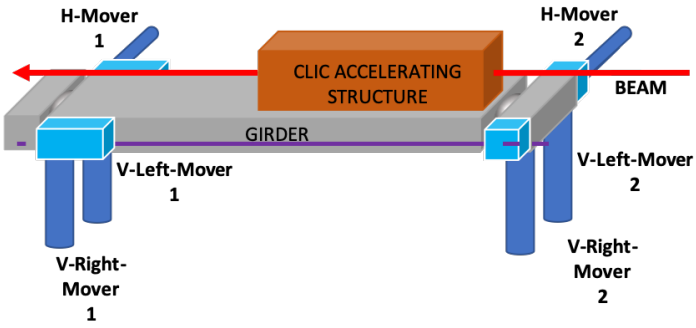

FIGURE 3.18: The schematic overview of the system designed to move the accelerating structure.

3.4.1 Structure movers

In the case the beam is kept constant, the transverse kick is given directly from the structure position. All the perturbations observed on the beam screen are given by the transverse wakefield inside the CLIC accelerating structure. For this reason, movers are installed on the girder supporting the CLIC accelerating structure to allows all the freedom for moving the structure. Two capacitive sensors with a metallic stretched wire inserted in the middle are attached on each side of the girder for relative position measurements. In addition, absolute position measurements are possible thanks to a static reference sensor. A schematic overview of the system is reported in Fig. 3.18. The beam path and direction are represented by a red arrow, the accelerating structure in orange, the girder in gray, the movers in blue, the magnetic sensor in light blue, and the starched wire in purple.

From Fig. 3.18, it can be noted the presence of articulation points, and the motors are installed before such articulation. This configuration was designed to be suitable for the CLIC requirements. For this reason, to minimize the number of movers needed for aligning the different structures, a snake-like system was chosen. It is crucial once dealing with many kilometers of beamline to reduce the number of devices that can induce features and increase the cost.

A measurement campaign was carried out on both axes (vertical and horizontal), in order to calibrate and better understand the movement system. While performing the calibration campaign for the horizontal plane, as expected, imposing a specific horizontal movement correspond to the expected relative movement in the horizontal plane without affecting the vertical one. On the other hand, while performing the calibration campaign for the vertical plane, a coupling between the planes was observed.

The scan was performed between $\pm 1\,\mathrm{mm}$ with steps of $200\,\mu\mathrm{m}$. From Figs. 3.19 the measured displacement of the structure, on both front and back sensors, versus the imposed displacement is shown. In From Fig. 3.19 (B), as expected, a linear trend is obtained (i.e., while moving the system in vertical, a vertical correspondent shift was detected). While in Fig. 3.19 (A) a clear coupling effect is observed. From $-1\,\mathrm{mm}$ to $0\,\mathrm{mm}$ an acceptable behaviour is presented while moving from $0\,\mathrm{mm}$ to $1\,\mathrm{mm}$ a large correlation is observed.

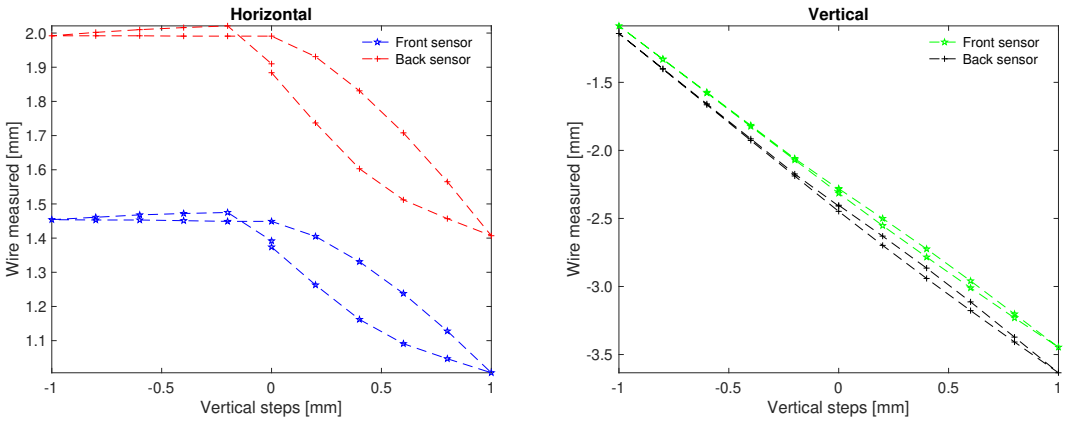

(A) (B)

FIGURE 3.19: The measurement results for an imposed vertical movement. In (A), the sensor's measurement results on the horizontal plane. In (B), the sensor's measurement results on the vertical plane.

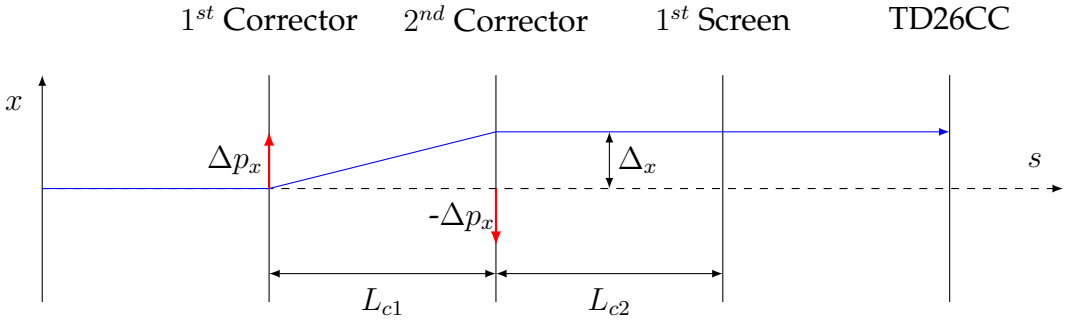

FIGURE 3.20: The layout of the beamline in front of the CLIC structure, using a thin elements representation for the elements.

Due to this issue and by the cumbersome controller setup, another system for scanning the relative displacement between the structure and the beam was developed; it is described in the following section.

3.4.2 Orbit bumps

In order to avoid the issues relented to physically move the structure (as discussed in Sec. 3.4.1), a method to shift the beam trajectory transversely using twp corrector magnets was developed. The physical targeted result is indicated in Fig. 3.20. Assuming that the two magnets are identical, such an effects is obtained imposing the same magnitude but opposite in sign magnetic field in both magnets.

Thanks to magnets installed in CLEAR, which are DJ-type correctors [192], a trajectory change in both planes can be imposed. Following the formalism proposed in Eq. 2.26, the change of angle, for example in the horizontal axis, can be

written as

$$\Delta_{x'} = \frac{\Delta p_x}{p_s} = \frac{-B_y\, L_{\text{kick}}\, \kappa}{p_s}, \tag{3.18}$$

where $L_{kick} = 248\,\text{mm}$ is the magnetic length of the corrector, and B_y is the magnetic field produced from the magnet in the vertical plane. Substituting in Eq. 3.18 $B_y = -I\kappa$ where I is the current powering the magnet, and κ is the calibration factor of the magnet, the change of angle can be written as

$$\Delta_{x'} = \frac{L_{kick}\kappa I c}{p_s}. \tag{3.19}$$

Assuming that the incoming beam is parallel to the accelerator axis ($x'_0 = 0$), the shift is simply given as

$$\Delta_x = L_{c1}\Delta_{x'}. \tag{3.20}$$

The derived formula assumes that the CLIC accelerating superstructure is perfectly aligned to the reference accelerator axis (defined by the quadrupoles position in the beamline). If a position offset x_{offset} is present, the only effect is that the current needed to pass through on the reference axis (i.e., in the center of the structure) would be non-zero. As a consequence, it will drive an offset in the current applied for scanning the relative displacement between the structure and the beam.

Such a procedure allows scanning the aperture in a much more convenient way than the one that implies moving the structure itself. **T**he movement of the structure can thus be used as a cross-check only, as well as for aligning if its position is found to be far off. A suitable procedure for performing the displacement scan is to first align the beam on the center of the upstream quadrupole triplet to avoid unwanted feed-down effects [193] (using the screen before the accelerating structure) and then use correctors to pass through the structure without losses. Only after, use the bump to scan the relative displacement between the CLIC structure and the beam by changing the magnet currents as described above.

It is important to underline that, to correctly use the presented method, a good characterization of the beam energy (as underlined in Eq. 3.19) is needed. In CLEAR, such information results from multiple measurements performed in the spectrometer line before the experiment, and it is checked before and after each experiment.

The value κ was computed thanks to a calibration of the magnet performed scanning over the whole range of available powering current (i.e., scanning over the magnetic field), $\pm 10\,\text{A}$, and observing on the screen before the structure the displacement of the beam. Each scan was executed by following the same powering cycle to avoid possible mismatch driven from a residual magnetic field.

In Figs. 3.21 the position of centroids versus the imposed displacement after the calibration of the corrector is reported. In Figs. 3.21 (A) and (B) the results obtained on the screen upstream the CLIC accelerating structure, while in Figs. 3.21 (C) and (D) the results obtained on the screen downstream the CLIC accelerating structure.

The scans were performed with a probe-like beam to excite as little wakefield

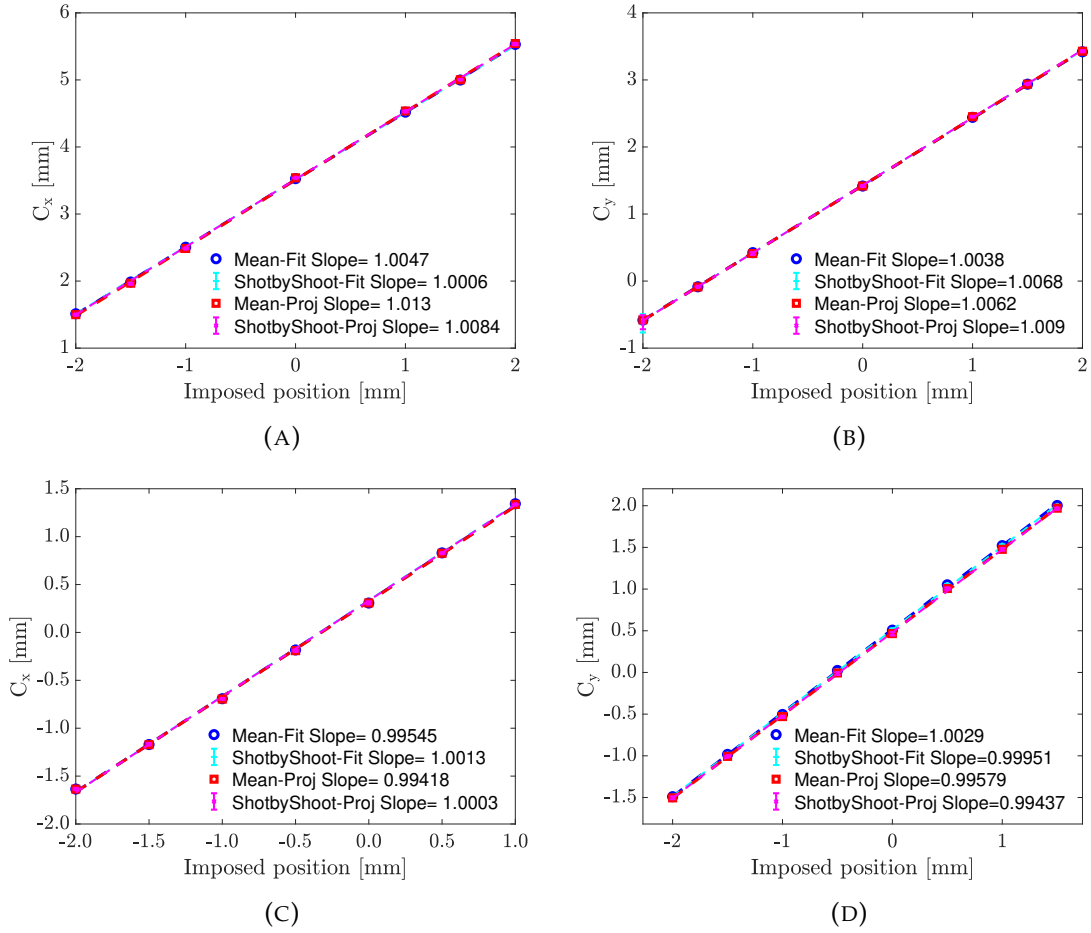

FIGURE 3.21: The scans of the centroid position versus the imposed displacement, after calibrating the correctors. In (A) and (B), the scans were performed on the screen installed upstream the accelerating structure for the horizontal and vertical planes, respectively. In (C) and (D), the scans were performed on the screen installed downstream the accelerating structure for the horizontal and vertical planes, respectively.

as possible while traveling through the structure. In particular, the beam energy was $200\,\mathrm{MeV}$, the bunch length was $2.71\,\mathrm{ps}$, the charge per bunch was around $10\,\mathrm{pC}$, and the number of bunches was twenty. The four ways for identifying the beam centroid position (i.e., $C_{x,y}$) in all the cases are in agreement with a discrepancy less than 2%. Such discrepancy can be an issue while operating with extremely low charge. However, in the range of charge of our interest, it results in a negligible impact, especially considering the dominant source of errors driven by beam and charge jitter.

These results are obtained repeatedly over time (different years) and different beam conditions (a different charge, a different charge upstream trajectories, a different bunch length, and so on). The results in Figs. 3.21 shows a good agreement between all the screens in all the planes, indicating that the beam is shifted parallel to the original beam axis without imposing an additional angle.

TABLE 3.2: Measured calibration factors for both correctors in both planes.

Calibration factors	Value $\left[\frac{\mathrm{mT}}{\mathrm{A}}\right]$
κ_{1st_H}	1.74
κ_{1st_V}	1.68
κ_{2nd_H}	1.74
κ_{2nd_V}	1.65

The values of the calibration factors used (one for each plane) of both the correctors are reported in Tab. 3.2. As expected, the correctors have similar behavior and act similarly in both planes. However, thanks to the characterization, a small discrepancy between the two in the vertical plane was found as well as a discr**e**pancy between the horizontal and vertical plane. Moreover, the obtained results in terms of calibration factors are in reasonable agreement with the reference value for this magnet (i.e., $1.8\,\mathrm{mT/A}$ [192]). This agreement gives confidence in how the scan is performed and how the beam energy is measured. In the CLEAR layout, the distance are $L_{c1} = 737\,\mathrm{mm}$ and $L_{c2} = 123\,\mathrm{mm}$.

An uncertainty of L_{c1} and/or L_{c2} will generate a parallelism error in the trajectory that will affect the calibration. Therefore, the discrepancy obtained in the centroid position (the quantity of interest) reported in Fig. 3.21 includes any measurement error in the length.

3.4.3 Calibration of WFMs

As reported in 3.2.2, the signals detected from the pickup antennas before arrive at the log detector are passing through band-pass filters and, to be sure that the signals are not distorted and/or accidentally attenuate it is needed to verify the S_{12} response of such devices. In Figs. 3.22, the measurement of the $|S_{12}|$ parameters of four (out of eight) filters, obtained using the frequency generator HP 83640A [194] and the power meter Keysight E4413A [195], controlled by HP E4418B [196] through a GPIB driver, scanning around the interested frequency, is reported. For the TM-like mode (centered at $16.9\,\mathrm{GHz}$), the flat top region goes approximately, from $17.8\,\mathrm{GHz}$ to $18.3\,\mathrm{GHz}$. Instead, for the TE-like mode (centered at $27.3\,\mathrm{GHz}$), the flat top region goes approximately, from $23.7\,\mathrm{GHz}$ to $24.3\,\mathrm{GHz}$. In the flat top region, the two filters' response is pretty similar, with a discrepancy less than 1%. The similarity of the measurements indicated that in the region of interest, the filters can be assumed identical; since 1% variation will imply a negligible difference in the power response measured compared with beam and charge jitter (approximately 10%). After checking the first four filter, it was decided, in order to avoid fully dismantling all the fragile experimental setups, that it was reasonable to assume that the other filters have the same frequency response, and all are suitable for the filtering of the WFMs signals.

The frequency of the filters must be centered on beam harmonic (i.e., in CLEAR multiple of $1.5\,\mathrm{GHz}$), and should also be in a frequency region where the signal

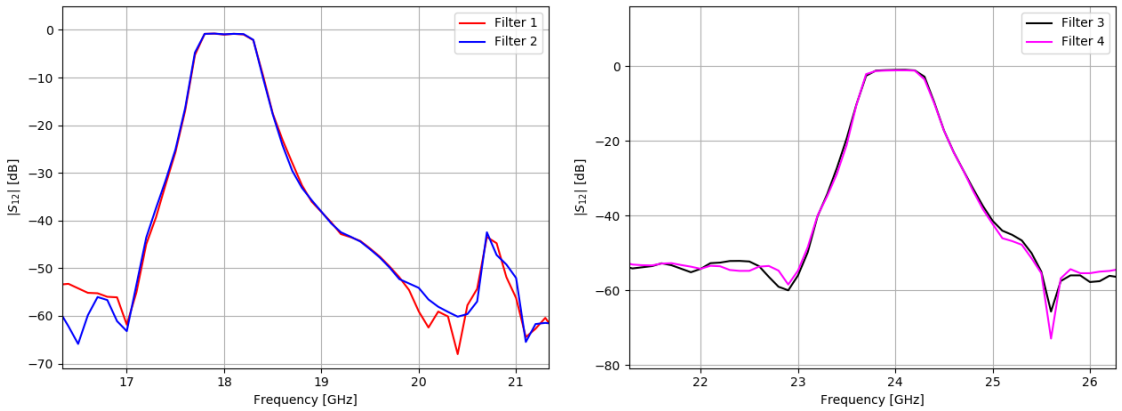

(A) (B)

FIGURE 3.22: The $|S_{12}|$ parameters of four different filters, two around $18\,\mathrm{GHz}$ and two around $24\,\mathrm{GHz}$ in (A) and (B), respectively.

from dipole wakefield is expected. Unfortunately, the filters are offset from resonance frequency of the two modes. However, as can be seen from Fig. 3.10, the frequency spectrum is quite broad. Thus, even if some reduction of the signals are foreseen, such filters can still be used to detect the two modes. Later, the two modes are referred as located in the central frequency of the two filters (i.e., $18\,\mathrm{GHz}$ and $24\,\mathrm{GHz}$).

It is needed to calibrate the response of the log detector in order to perform the measurement correctly, . The same frequency generator (i.e., HP 83640A [194]) and power-meter (i.e., Keysight E4413A [195]) presented in Sec. 3.4.3 were used. Firstly, each channel at both frequencies was tested to very the possible cross-talk inside the devices. In Figs. 3.23, the output voltage versus the input power is reported for each signal. The output from each channel is obtained by sweeping the input power at $18\,\mathrm{GHz}$ and $24\,\mathrm{GHz}$, the results are shown in Figs. 3.23 in the first and second row, respectively. A comparative visualization of the channels where the power is injected is reported in Fig. 3.24, at $18\,\mathrm{GHz}$ and $24\,\mathrm{GHz}$ in (A) and (B), respectively. From Figs. 3.24, it is evident that for each channel, between $-40\,\mathrm{dBm}$ and $-10\,\mathrm{dBm}$ a linear response is obtained. Consequently, the calibration is performed fitting the response in such region for a known input. In Tab. 3.3, the fitted parameters, slope and intercept (p and q, respectively), for each channels at both frequency are reported. The cross-talk between the channels was assessed, powering one channel at the time with an input power of $0\,\mathrm{dBm}$, and measuring the output voltage from all the channels. The results are resumed in Fig. 3.25, where it can be seen that all the terms not on the diagonal (i.e., the one representing the cross-talk) show a very low power ratio in the order of $-30\,\mathrm{dB}$ or lower, which is around the noise level, therefore negligible.

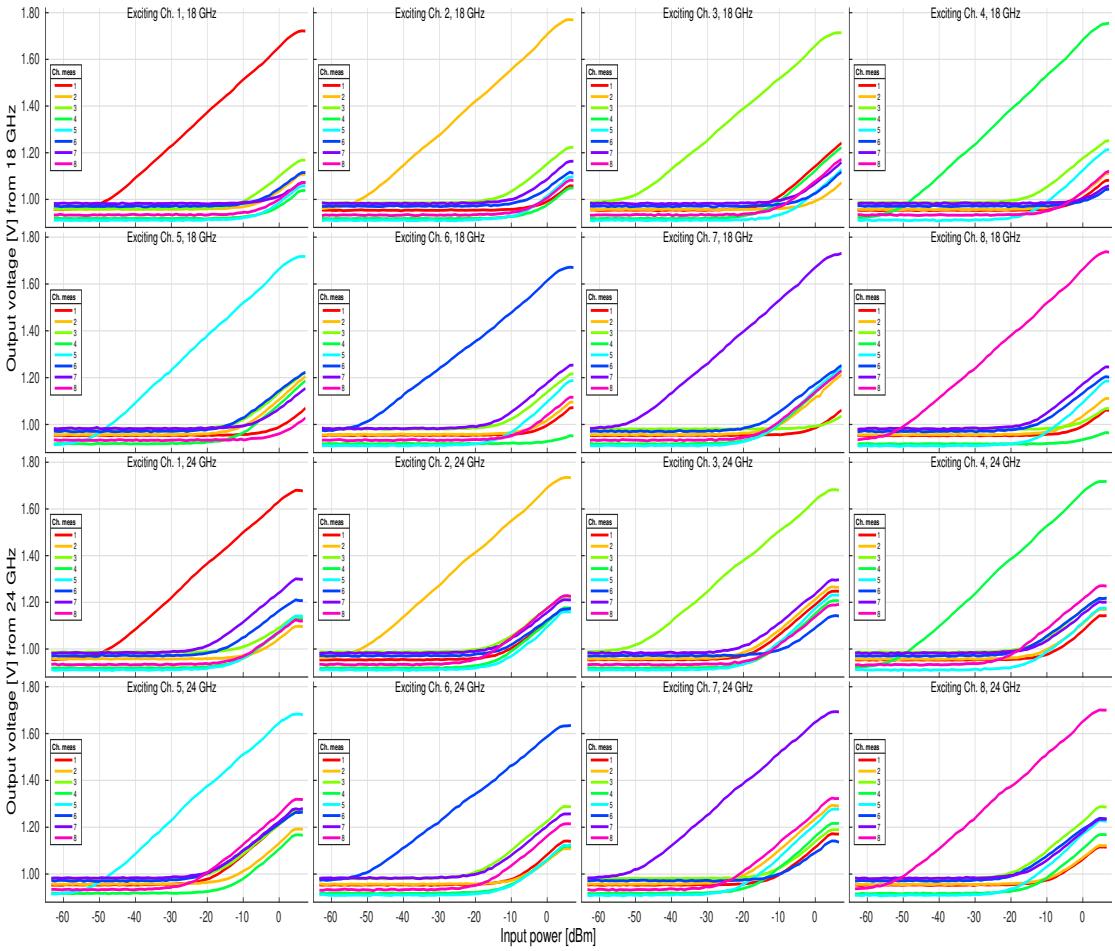

FIGURE 3.23: The output power from the eight channels of the log detector, versus the input power. Each channel is tested individually at 18 GHz and 24 GHz first and second row, respectively.

3.5 Results

In this section, the results obtained from the kick and the WFM studies are presented. For the kick studies, a comparison between the simulations and the measurements data is performed, also analyzing the often neglected dependence of the wakefield kick on the particle bunch's length. While from the WFM studies, the experimental data are analyzed, and the main limitations are presented.

3.5.1 Kick results

The results obtained with the kick studies are divided into three sub-cases, from the one with more constrain to the one more general. In particular, as described in Sec. 3.4, each displacement scan is performed using the bump scan methods and considering the projected image of the beam to assess the centroid position. Furthermore, each scan is characterized by $N = 10$ measurements performed at

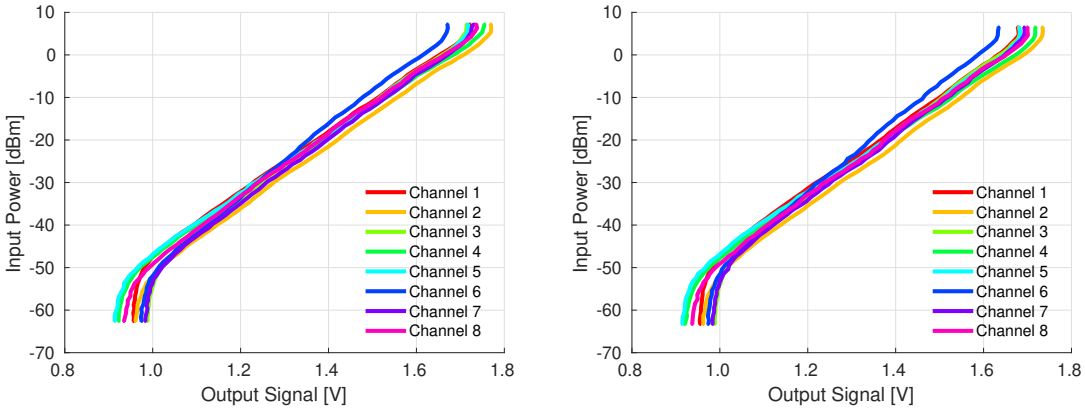

(A) (B)

FIGURE 3.24: The output power from the log detector, versus input power for each channel at 18 GHz and 24 GHz in (A) and (B), respectively.

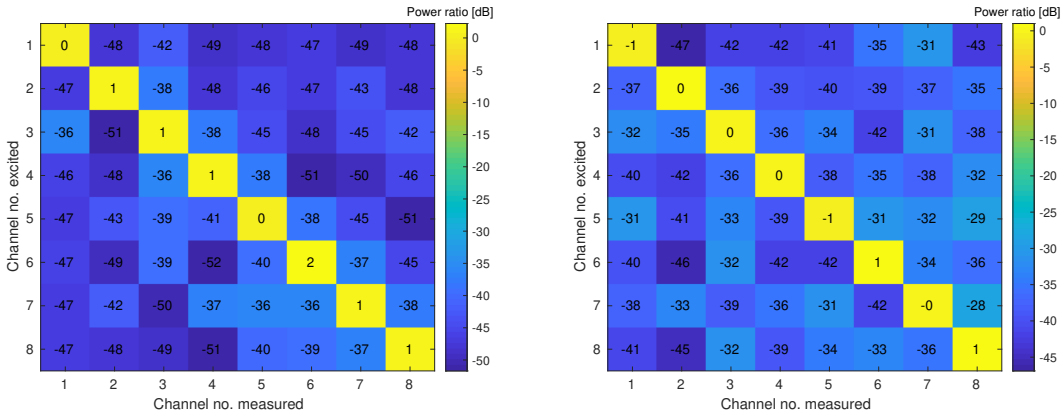

(A) (B)

FIGURE 3.25: The power ratio matrix for each channel combination. All the combination are tested individually at 18 GHz and 24 GHz in (A) and (B), respectively.

the same displacement, and $M = 16$ different displacements. For each beam configuration, a full displacement scan was performed, and the relative derivative of the centroid variation was assessed by means of a linear fit that takes into account the different uncertainties for each displacement, in order to measure the $\mathrm{Kick} = V_{\perp} q$, where $V_{\perp}$ is defined in Eq. 3.7. The uncertainty of the measurement is obtained thanks to the propagation of uncertainty from the slope, energy, and beam displacement from the orbit bump. The uncertainties distances were not considered, as their small value (below 1%) made their impact negligible compared to the other uncertainty sources.

In a conserv**a**tive estimation, the energy's uncertainty was assumed $2.5\,\mathrm{MeV}$ and the uncertainty on the calibration factor of the bump was assumed 1%. The energy uncertainty is expected to grow with train charge because the energy

TABLE 3.3: Fitted parameters from the linear fit needed for calibrate the log detector for each channel at both frequency.

Frequency	Channel	Slope [$\frac{\mathrm{V}}{\mathrm{dBm}}$] ($p$)	Intercept [V] (q)
18 GHz	1	71.09	−117.47
18 GHz	2	73.08	−123.61
18 GHz	3	76.82	−126.60
18 GHz	4	69.36	−116.04
18 GHz	5	70.36	−116.94
18 GHz	6	86.10	−136.79
18 GHz	7	75.65	−125.61
18 GHz	8	74.36	−122.54
24 GHz	1	71.64	−117.58
24 GHz	2	73.00	−123.12
24 GHz	3	77.41	−126.65
24 GHz	4	69.48	−116.26
24 GHz	5	70.69	−117.02
24 GHz	6	86.08	−136.59
24 GHz	7	75.93	−125.18
24 GHz	8	74.77	−122.89

spread increases due to beam loading effects, and the camera for the beam screen in the spectrometer line is saturated. Moreover, the assumed uncertainty of the calibration factor includes the uncertainty of the energy. The charge stability was also evaluated, taking into account both the jitter (i.e., shot by shot fluctuation) and the drift (i.e., the long term variation). The standard deviation of the charge measured N times at each displacement at the beginning of the accelerator line is reported in the experimental results.

The charge error in 3.25 is the std of the charge measurement over the scans for the used shots, the jitter was discussed on the charge section.

The first experiment was in a single bunch configuration for excluding possible long-range effects. Moreover, the bunch length was kept constant between the different displacement scans performed. Thus only the charge was varying. The second experiment was performed in a multi bunch regime to analyze the influence of the long-range wakefield. In this case, the bunch length was not constant, however the range of range of variation was limited by the deterioration of the beam quality. In the last experiment, all the possible variables (i.e., charge, number of bunches, and bunch length) were varying between the scans. In each experiment, the linear fit performed is imposing the condition that at $0\,\mathrm{pC}$, the obtained kick is equal to $0\,\frac{\mathrm{V}}{\mathrm{mmm}}$. This condition is justified since a particle with an ideally zero charge does not rise any wakefield. Also, it was verified that, no appreciable offset is present in the charge monitoring system at CLEAR. Each fit was performed using a weighted least square method, taking into account the uncertainty of the Kick described above, and the reported uncertainty corresponds to a 1-sigma interval. It is also important to mention that the results are affected by considerable uncertainty, driven by the complexity of the measurements. In this

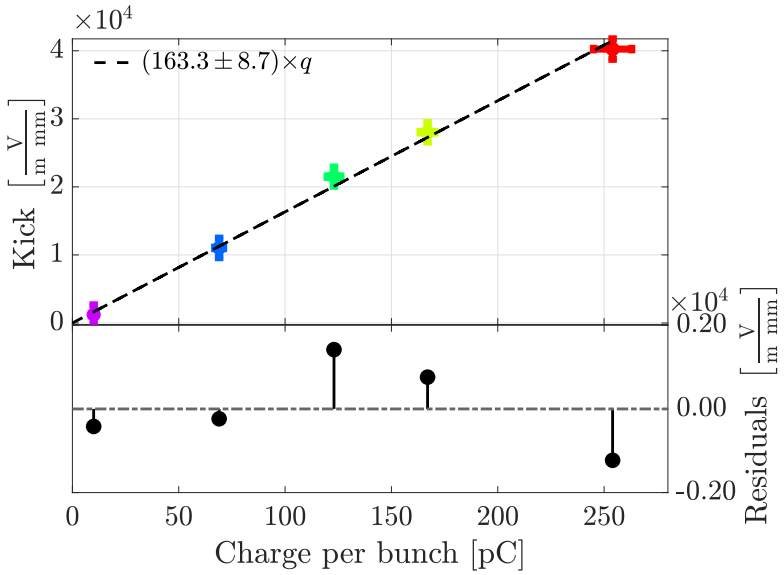

FIGURE 3.26: The kick measurement results for a single bunch setup versus the charge per bunch.

indirect measurement, many key parameters (e.g., charge, beam profile, energy) are difficult to stabilize and assess, especially at high beam charge.

Single bunch

In the first experiment, with the aim of excluding the possible contribution from long-range wakefield, a single bunch configuration was used.

In particular, five different charges were investigated ($10\,\mathrm{pC}$, $69\,\mathrm{pC}$, $123\,\mathrm{pC}$, $167\,\mathrm{pC}$, $254\,\mathrm{pC}$) holding the bunch length constant around $4\,\mathrm{ps}$ with a maximum variation of 2.5%. Later, using Eq. 3.6, the transverse kick in terms of $\frac{\mathrm{V}}{\mathrm{mm\ m}}$ (i.e., without normalizing on the charge) was calculated. The result is shown in Fig. 3.26, where a linear trend, as expected, is found. This result is pointing out that method used shows consistent result in the single bunch configuration. Fitting the results, a slope of $163.3 \pm 8.7\,\mathrm{V/(mm\,m\,pC)}$ is obtained. Moreover, in Fig. 3.27, the centroid assessment in the single bunch configuration for the case of highest charge (i.e., $256\,\mathrm{pC}$) is shown. In the regime of single bunch, the assumption of being dominate from dipole mode wakefield is solid. In case such assumption was not correct, the linearity with the displacement should not be so clear.

Multi bunch

Similar to the study with the single bunch configuration, a multi bunch study was performed. This study has four different aims: (i) validate the consistency of the study for the multi bunch configuration, (ii) investigate the validity of the assumption of being dominated by dipole mode wakefield is reasonable also bunch operating in a multi bunch scenario, (iii) use the simulation to correct the possible

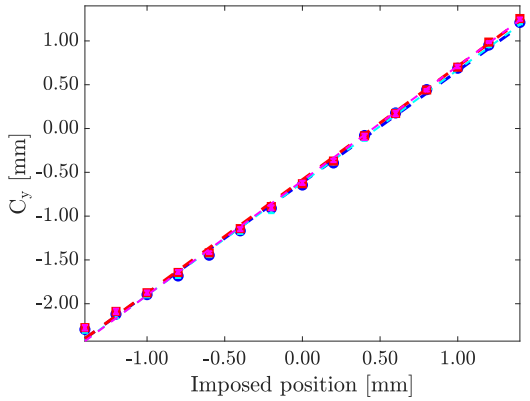

FIGURE 3.27: The centroid assessment between $\pm 1.5\,\mathrm{mm}$, with steps of $0.2\,\mathrm{mm}$ for the highest charge (i.e., $256\,\mathrm{pC}$) in the single bunch configuration.

difference of bunch length between the experiment, and (iv) check the repeatability of the measurement.

For this reasons, in this study, the number of bunches was kept constant (i.e., twenty bunches), the bunch length varying between each scan (i.e., $2.91\,\mathrm{ps}$, $3.01\,\mathrm{ps}$, $3.33\,\mathrm{ps}$, $3.03\,\mathrm{ps}$, $3.28\,\mathrm{ps}$, and $3.90\,\mathrm{ps}$), and each scan was repeated three times.

In Fig. 3.28, the kick in units of $\frac{\mathrm{V}}{\mathrm{m\ mm}}$ (i.e., without normalizing on the charge) versus the charge per pulse is shown. From Fig. 3.28, many different interesting results to address the different aims of the experiment can be deduced. Firstly, the results show that the methods produce consistent results also for trains. Furthermore, the estimated errors increase at a high charge. Such an effect is typical for particle accelerators, as increasing the charge drives an increase of charge jitter, beam instabilities, and emittance growth. In the CLEAR accelerator, these effects make, as a consequence, more difficult to achieved and maintain a wanted set of beam parameters over a long time. Besides, at high charge, a large spread in the charge measurements (both in relative and absolute) is present. This effect was always appreciated beyond these measures.

Fitting the results, normalizing the charge over the number of bunches, a slope of $163.7 \pm 2.9\,\mathrm{V/(mm\,m\,pC)}$ is obtained.

However, there are points (e.g., the one at $3.33\,\mathrm{ps}$ and the one at $3.28\,\mathrm{ps}$) that are not fully in agreement with the overall trend. Several simulations at several different bunch lengths are performed, in order to understand if this disagreement is driven by the bunch length. Fitting the result, a model for correcting the difference in bunch length is derived.

The fitting model, Eq. 3.21, is inspired by Eq. 3.1 where s_0 and the scaling factor are made as free parameters, K_1 and K_2, respectively.

$$f_{fit}(x) = K_2 \left(1 - \left(\sqrt{\frac{\sigma_t}{K_1}}\right) + 1\right) e^{\frac{\sigma_t}{K_1}}, \tag{3.21}$$

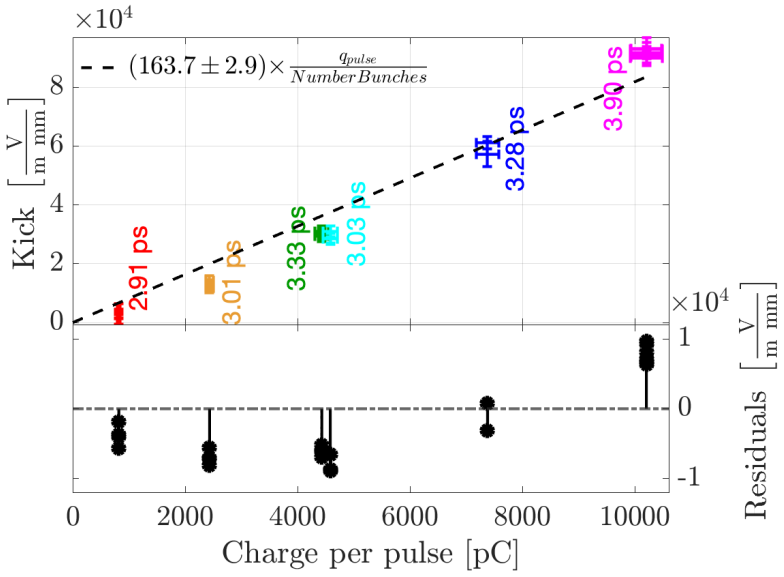

FIGURE 3.28: The kick measurement results for multiple bunches setup versus the charge per pulse.

where $K_1 = 0.5134\,\mathrm{ps}$ and $K_2 = 179.3769\,\mathrm{V/(mm\,m\,pC)}$ are obtained by equal-weighted least-squares fitting to the analytical model, which was evaluated at every bunch length between $1\,\mathrm{ps}$ and $5\,\mathrm{ps}$.

The results of the simulations (i.e., the expected kick normalized with the pulse charge versus as a function of the bunch length) as well as the fitted model are reported in Fig 3.29, where the dots highlight the simulation performed with the same bunch length of the experimental data. Moreover, in Fig 3.29 on the right vertical axis the form factor scale at $4\,\mathrm{ps}$ is reported. Thanks to these results, dividing the experimental result obtained in Fig. 3.28 with $F(\sigma_{t_0}) = f(\sigma_{t_0})/f(4\,\mathrm{ps})$ in Fig 3.29, the data scaled as they where produced from bunch having the same bunch length (chosen equal to $4\,\mathrm{ps}$, in order to have results compatible with the previous study). In Fig. 3.30, the kick versus the charge is reported, once correcting for the different bunch length.

From Fig. 3.29, the difference of the correction by including the form factor, is smaller than the residual seen in Fig. 3.28, due to the small range of bunch lengths. Including these corrections, dose not reduce the residuals significantly in Fig. 3.30. In order to appreciate such effect, an experimental campaign using a broader range of bunch length is needed.

As before, normalizing the charge over the number of bunches, a slope of $168.4 \pm 2.9\,\mathrm{V/(mm\,m\,pC)}$ is obtained, which is comparable to the number found for the single bunch. It is a first indication that the short-range wakefields are dominating the long-range ones. Moreover, in Fig. 3.31, the centroid assessment for the multiple bunches setup for the highest charge (i.e., $10\,\mathrm{nC}$) is shown. From this result, a quite linear trend is argued and this support the assumption of being dominate from dipole mode wakefield.

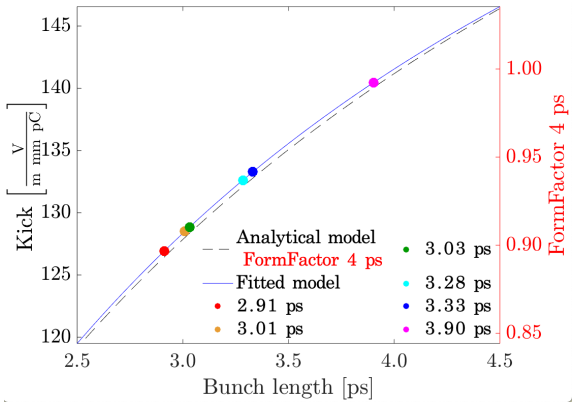

FIGURE 3.29: On the left axis, the simulated kicks, normalized with charge, for the analytical (dotted line) and fitted (solid line) models versus the bunch length. On the right axis, the scale for the form factor, derived from the fitted model, to normalize the bunch length at 4 ps.

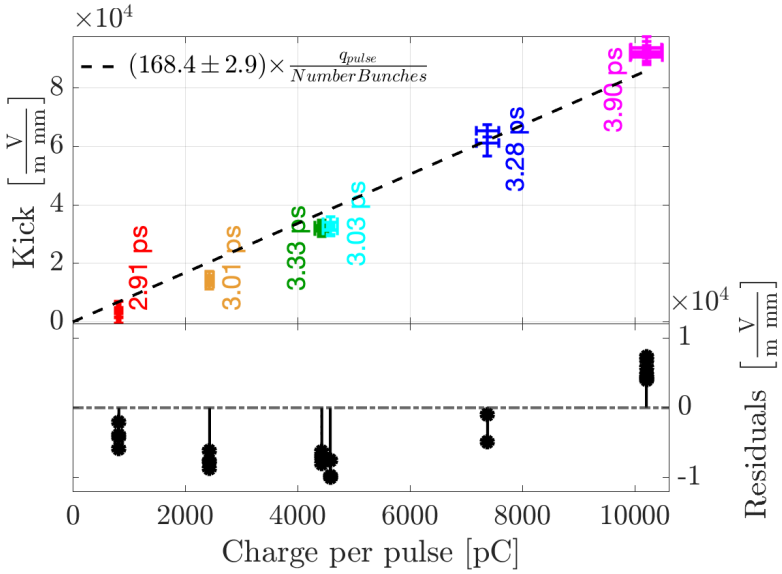

FIGURE 3.30: The kick measurement results, corrected with the form factor for multiple bunches setup versus the charge per pulse.

General study

Once assessed the consistency of the methods and the validity of the assumption of being dominated from the dipole mode wakefield in a single multi bunch regime and correcting for different bunch length, the effects of long-range wakefield can be investigated. For this purpose, experiments with a different number of bunches were performed.

In Figs. 3.32, the kick calculated from each scan not normalized on the charge is reported versus the charge per pulse and versus the charge per bunch in (A) and (B), respectively. Comparing Fig. 3.32 (A) and (B), the evidence of linearity in one of the two plots can be found. Plotting the data as a function of the charge

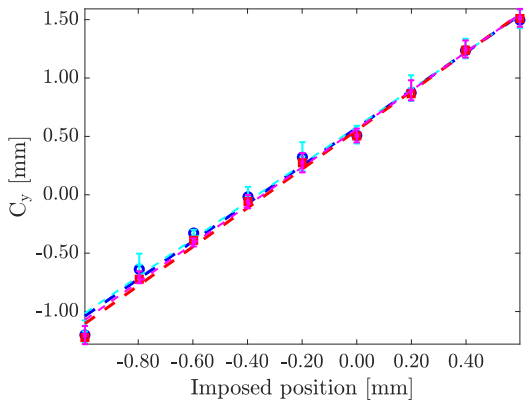

FIGURE 3.31: The centroid assessment between $\pm 1\,\mathrm{mm}$, with steps of $0.2\,\mathrm{mm}$ for the highest charge (i.e., $10\,\mathrm{nC}$) in the multiple bunches setup.

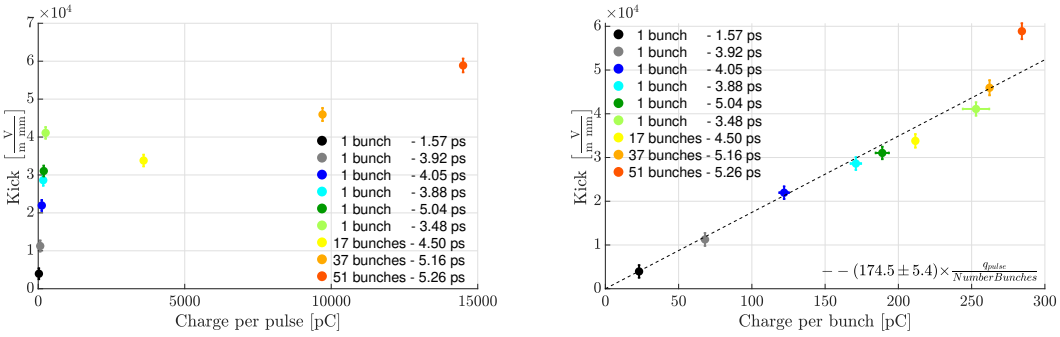

(A) (B)

FIGURE 3.32: The kick measurements versus the charge per pulse and versus the charge per bunch in (A) and (B), respectively.

per bunch (i.e., Fig. 3.32 (B)), a linear trend is obtained while reporting the data as a function of the charge per pulse, it is impossible to identify a linear trend. By applying a linear fit to the data of Fig. 3.32 (B) a slope of $174.5 \pm 5.4\,\mathrm{V/(mm\,m\,pC)}$ is obtained. This is in agreement with the case multi bunch presented before. This result shows that the short-range wakefields are the dominant source in the structure.

So far, a Gaussian longitudinal distribution was assumed. However, this information is not easy to assess. For this reason, two longitudinal bunch distributions are tested to understand if this can be the source of the errors. The tested distributions are the same used in Sec. 3.3.2, with the same charge and σ_{t_0} as for the Gaussian bunch, and $\Gamma = -10$. The case of tail-heavy Gaussian was chosen as a limit case, since it is the one that during the simulations reported in Fig. 3.17 was more impacted by the wakefield. A direct comparison between the experimental results (dots), the simulation results using Gaussian distribution (crosses), and the simulation results using tail-heavy skew-Gaussian distribution (plus signs) versus the bunch per charge is reported in Fig. 3.33. Comparing the results of in Fig. 3.33, the experiments and the simulations are showing the same behavior

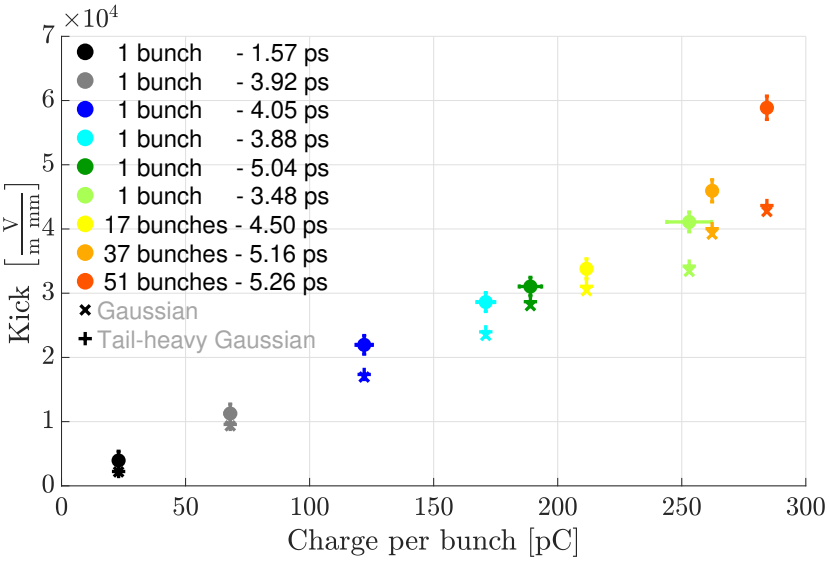

FIGURE 3.33: The kick measurement results (dots), the simulation results using bunch with Gaussian distribution (crosses), and the simulation results using bunch with tail-heavy skew-Gaussian distribution (plus) versus the charge per bunch.

and the same scaling. However, the simulations are predicting a kick consistently smaller.

Unfortunately, the different simulations are not approaching closer to the experimental results. However, by comparing the two simulations, a change in the simulated kick is obtained, changing the longitudinal distribution of the bunch (on average, a discrepancy about 3% is found). This result, as already mentioned in Sec. 3.3.2, highlights a hitherto neglected so far aspect. For this reason, a more detailed study is warranted, which would require an investigation on the longitudinal profile, vary systematically the number of bunches, and measure over a broader bunch length range.

3.5.2 WFM results

While scanning the relative displacement between the beam and the structure, using either the structure movers or the orbit bump, the log-detector receives signals coming from the WFM depending on the relative displacement between the structure and the beam. An example of these signals, particularly the TE-like sum and the TM-like delta signal (i.e., the one used to identify the structure center) while performing a vertical scan, is reported in Figs. 3.34. From such signals, the information on the position can be retrieved. Firstly to the response shown in Figs. 3.34 it needed to apply for each channel, depending on the relative operating frequency, the inverse calibration factor (Tab. 3.3) assessed for establish the input power of the log detector . Later, to convert the power into RMS voltage the following equation was used

$$V_{rms} = \sqrt{P \cdot Z}, \tag{3.22}$$

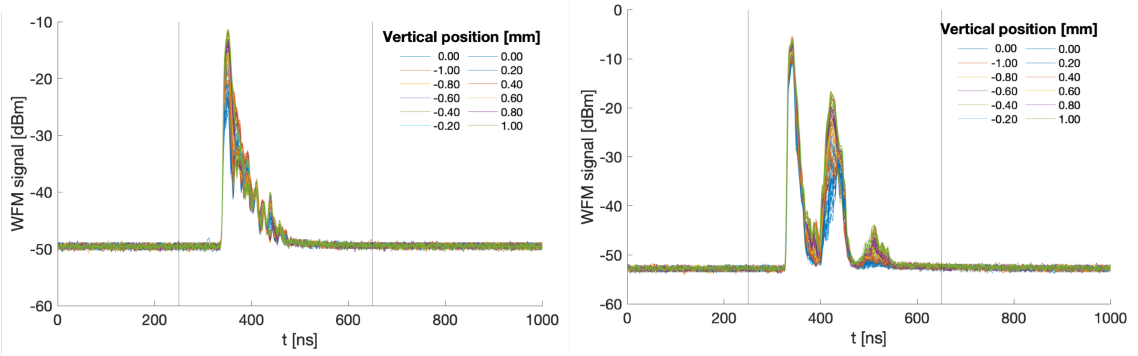

(A) (B)

FIGURE 3.34: The power measured at the output of the log detectors versus time, while performing a vertical scan between $\pm 1\,\mathrm{mm}$ with steps of $0.2\,\mathrm{mm}$. The TE-like (at $24\,\mathrm{GHz}$) sum and the TM-like (at $18\,\mathrm{GHz}$) delta in (A) and (B), respectively.

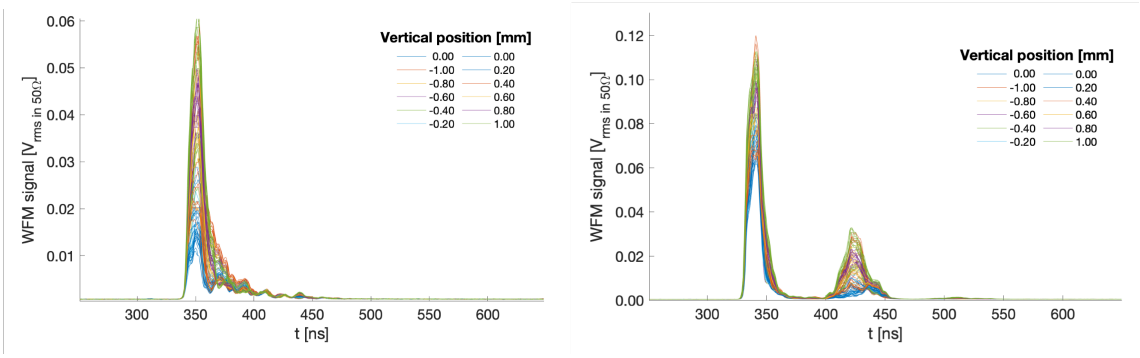

(A) (B)

FIGURE 3.35: The voltage measured at the output of the log detectors versus time, while performing a vertical scan between $\pm 1\,\mathrm{mm}$ with steps of $0.2\,\mathrm{mm}$. The TE-like (at $24\,\mathrm{GHz}$) sum and the TM-like (at $18\,\mathrm{GHz}$) delta in (A) and (B), respectively.

where the impedance Z is equal to $50\,\Omega$, the characteristic impedance of the coaxial cable used. This is done to obtain a signal that is proportional to the field strength excited by the beam. The WFMs signals in units of volts is reported in Figs. 3.35.

Finally, the information on the position is assessed by averaging the signal into the windows reported in Figs. 3.35. By repeating the acquisition procedure for each displacement, by averaging the results obtained at the same displacement, the displacement that induces the smallest signals is assessed. Under the assumption of a dominating dipole mode, the displacement that induces the smallest signals allows the beam to pass at the center of the cell where the WFMs are installed.

By applying the above described treatment a result like the one in Figs. 3.36 can be obtained. The linear fit applied to the results reported in Figs. 3.36 helps

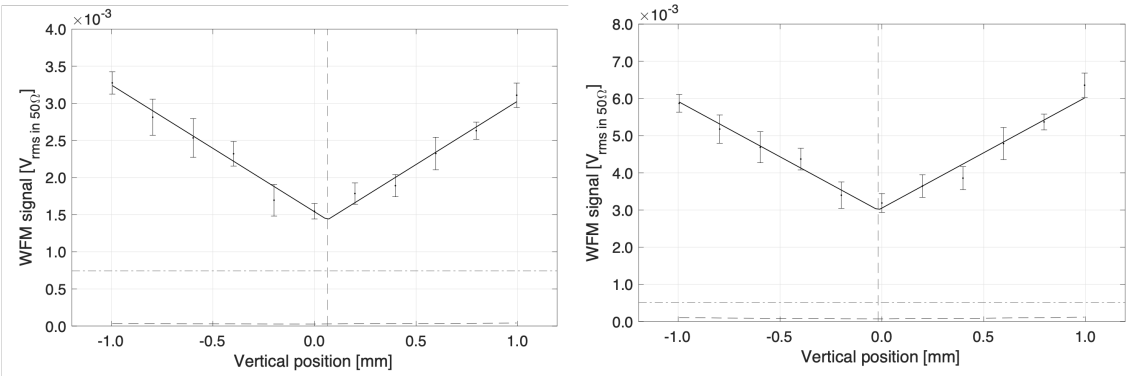

(A) (B)

FIGURE 3.36: The final results for the scan reported in Figs. 3.35 from the TE-like (at 24 GHz) sum signals and TM-like (at 18 GHz) delta signals in (A) and (B), respectively.

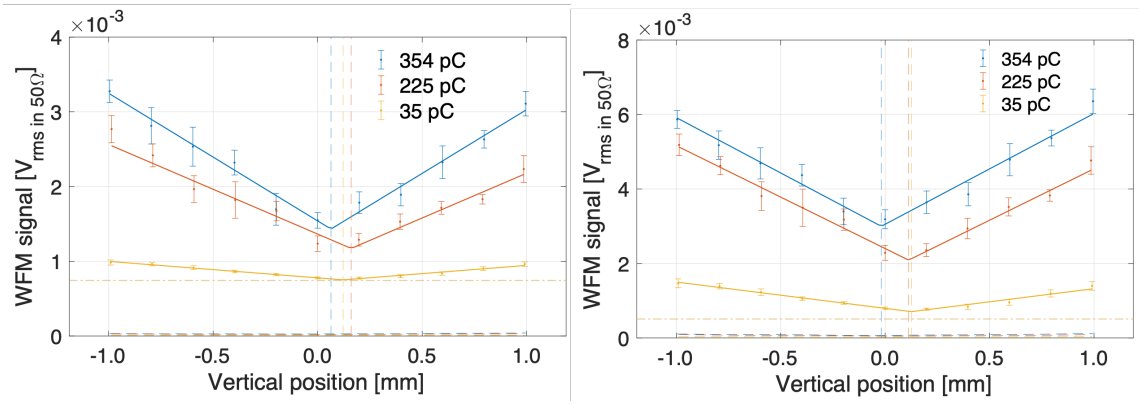

(A) (B)

FIGURE 3.37: The final results for three scans performed with a bunch charge of 354 pC, 225 pC, and 35 pC from the TE-like (at 24 GHz) sum signals and TM-like (at 18 GHz) delta signals in (A) and (B), respectively.

in the identification of the displacement that gives the lower WFMs signals, highlighted also with a vertical dashed line. The two horizontal dashed-dotted lines represent the cross-talk and the noise floor of the measurement.

Performing such measurement, for different scans at different beam conditions, the response of the WFMs in different configurations can be studied.

In Figs. 3.37, three different scans with the same number of bunches (i.e., twenty bunches), the same energy (i.e., 211 MeV), the same bunch length (i.e., 3 ps), but with a different charge per bunch (i.e., 354 pC, 225 pC, and 35 pC) is reported.

From Figs. 3.37 already a qualitative evaluation of the agreement between the two modes at different charges can be achieved. Each scan was repeated three times, in order to have some more detailed information on the reproducibility of the WFMs results. In Fig. 3.38, the center identified by each mode at at each scan are shown. From Fig. 3.38, two main conclusion can be taken: (i) at a low charge,

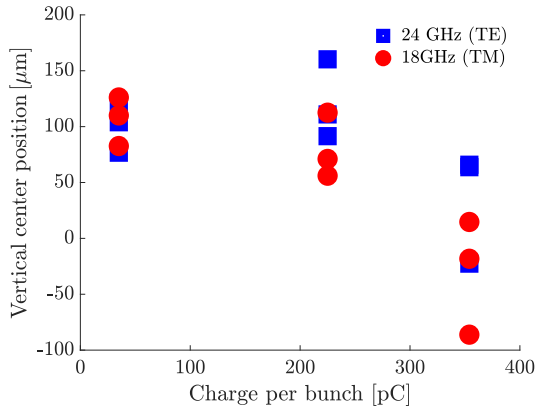

FIGURE 3.38: The vertical center position versus the charge per bunch for each scan performed (i.e., three times for each charge) from both frequencies, 24 GHz (blue squares) and 18 GHz (red circles).

the results are compatible, showing that the center can be identified systematically within $\pm 25\,\mu\mathrm{m}$, and (ii) accuracy in the identification of the center degrades while increasing the charge. At the highest charge the center is identified within $\pm 75\,\mu\mathrm{m}$. However, such an effects it is probably not driven by the nature of the excitation and of the WFMs response, but most likely, is driven by the beam quality that gets more tricky to hold while increasing the charge per bunch.

3.6 Discussion and outlook

This chapter presented the results from experimental and simulation campaigns on two different methodologies for identifying the region less affected by transverse wakefield in the CLIC accelerating structure's latest prototype.

The results obtained with the kick study are promising. Thanks to this study, different milestones were achieved to understand the wakefield effects in such type of device. It was proved the validity of the measurement method and that the assumption of being dominant by dipole mode wakefield is correct in single and multi bunch regime. Moreover, thanks to the study, the type of wakefield affecting the beam while passing through the accelerating structure was characterized. For each measurement campaign, a determination of the normalized kick in units of $\mathrm{V/(m\,mm\,pC)}$ is reported. These quantities are derived from a linear fit applied on the measured kick versus the charge. Comparing the results, it can be understood that all the measured kicks are overall compatible. However, there are discrepancies between the obtained slopes. This discrepancy can indicate that the long-range wakefields are adding a contribution to the measured kick. Further studies to better understand this topic are required. In the near future, this knowledge will allow the development of a methodology for better damp the parasitic effect of wakefield. Also, a full study on the often neglected dependence on the bunch length was carried out. The comparison between the

model and the experiment has shown that both have the same behavior. However, the bunch longitudinal profile is playing an important role, and so far, it was neglected in the CLIC framework. In the near future, a more detailed study, taking into account the longitudinal bunch distribution is foreseen.

On the WFMs side, a full calibration of the system was performed. A discrepancy between the frequency of the mode and the flat top region of the filters was found. However, the signals were still measurable. The obtained results, even if preliminary, are promising. The effective capacity of the WFMs to coherently assess the displacement of the beam.

Both experiments still require to optimize the beam quality once achieving a high value of charge per bunch. The presented results were obtained by modifying the beam trajectory while keeping the structure in a fixed position, all in the vertical plane. Such an operating method was chosen because of the difficulties found in controlling the structure movers. In the spring of 2021, a new system for acting on the structure position will be ready. Thanks to the new system, firstly, all the performed measurement will be bench marked. And later, the new system will allow to perform finer scans around the presumed center. In addition, during the spring of 2021, inductive BPMs to better monitor the beam charge and trajectory while performing the scan (i.e., not intercepting the beam) will be installed. Another fascinating idea of installing a deflector right after the CLIC accelerating structure is under study. A set of preliminary simulations have shown the potentiality of investigate the effect of the kick as a function of the coordinate along the bunch.

Chapter 4

Bunch length measurements

In this chapter, the bunch length measurement studies are presented. Initially, the theoretical treatment of the conventional layout, normally used for bunch length measurements using a Radio-Frequency transverse deflector (RFD), is reported. Improvements to the standard measurement production model are presented. Later, the theory to include in the model a generic linear beam transport element between the RFD and the screen is presented. The results obtained show the promising possibility of using the latter layout to perform the measurement and improve the system performances. The focus is on the comparison, in terms of resolution and uncertainty, between the conventional and non-conventional layout. In the chapter, the term "conventional layout" points to the configuration only with a drift space between the RFD and the screen (Fig. 4.1 top), while the term "non-conventional" points to the presence of a generic linear element between the RFD and the screen (Fig. 4.1 bottom). The quantities of the conventional layout are reported using lowercase subscripts "on"/"off"/"cal"; while the ones for the non-conventional layout are reported using uppercase subscript "ON"/"OFF"/"CAL".

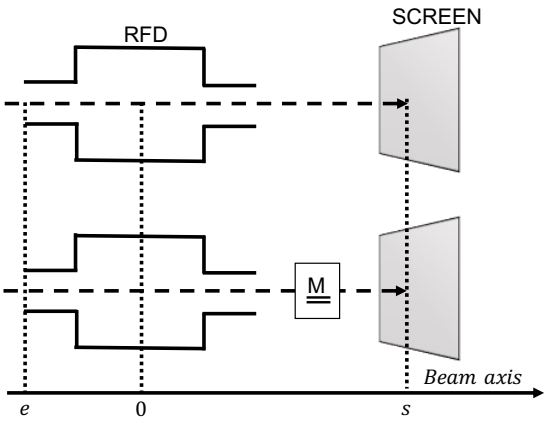

FIGURE 4.1: On the top, the conventional layout without elements between the RFD and the screen. On the bottom, the non-conventional layout, with a generic linear element between the RFD and the screen described by the matrix $\underline{\underline{M}}$.

The theoretical derivation is presented, and the theory's predictions are shown to be supported by experiments and simulations. The simulations are performed

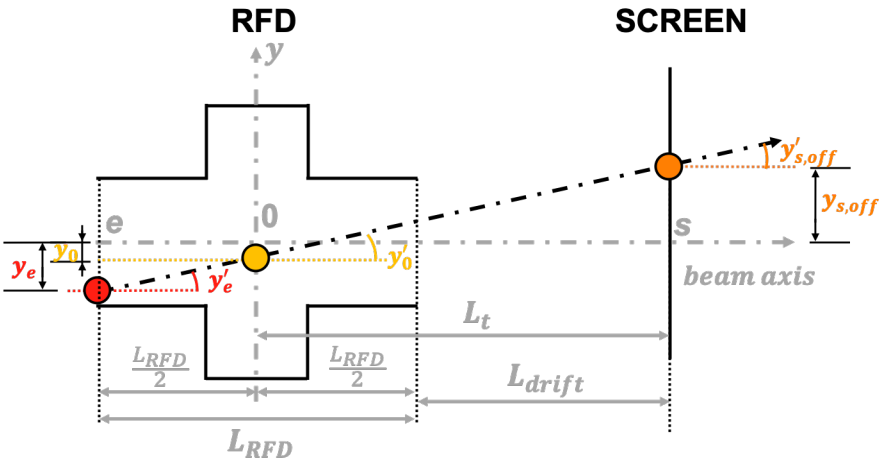

FIGURE 4.2: The particle vertical trajectory and parameters from the RFD entrance until the screen once the RFD is switched off.

using the ELEctron Generation ANd Tracking (ELEGANT) code. In the theoretical derivations, the confident assumption of relativistic particles was assumed.

The conventional layout study is based on simulations performed for many novel accelerators, with a particular focus on the Gamma Beam Source (GBS). The non-conventional layout experimental study is based on the CLEAR accelerator, where the RFD is installed at the end of the accelerating section (Fig. 1.8), and a triplet of quadrupoles is installed between the RFD and the screen. In each comparison, the relative beam and RFD characteristics are reported.

4.1 Measurement methods for conventional layout

In this section, the equations describing the measurement process in the conventional layout are derived initially. Later, the standard and the improved models for the measurement production are reported.

4.1.1 Theoretical treatment

For the sake of simplicity, the theoretical derivation is split into two physical scenarios. In the first one, the deflector is turned off and thus, it is not affecting the beam. In the second one, the deflector is turned on, allowing to extract information about the longitudinal plane.

RFD off

Assuming the RFD is turned off, the experimental layout is reported in Fig. 4.2. The equations of the vertical particle motion from the RFD center to the screen are

$$\begin{cases} y_{s,off} = & y_0 + L_t y'_0 \\ y'_{s,off} = & y'_0 \end{cases}, \tag{4.1}$$

where L_t is the length of the drift space between RFD center and screen (i.e., $L_t = {}^{L_{RFD}}/_2 + L_{drift}$), y_0 and y'_0 are the particle vertical position and divergence at RFD center, respectively; $y_{s,off}$ and $y'_{s,off}$ are the particle vertical position and angle at the screen with RFD turned off, respectively. For a bunch, the vertical position average and the vertical divergence average can be defined on the screen as

$$\begin{aligned} &C_{y_s,off} \equiv \langle y_{s,off} \rangle = \langle y_0 + L_t y'_0 \rangle = \langle y_0 \rangle + L_t \langle y'_0 \rangle = C_{y_0} + L_t C_{y'_0}, \\ &C_{y'_s,off} = C_{y'_0}. \end{aligned} \tag{4.2}$$

There are no devices that change the divergence of the bunch in this layout, and if the bunch is traveling with an angle with respect to the accelerator axis, it will be preserved. In the same way, if the incoming bunch travels parallel to the accelerator axis ($C_{y'_0} \approx 0\,\mathrm{rad}$) at the screen, the bunch will arrive with the same offset.

A bunch can be described using its first and second-order statistical moments (i.e., average and variance). The RMS vertical spot size at the screen, starting from the RFD center, can be calculated as

$$\begin{aligned} \sigma^2_{y_s,off} &= \left\langle \left(y_{s,off} - \langle y_{s,off} \rangle\right)^2 \right\rangle = \left\langle y^2_{s,off} \right\rangle - \langle y_{s,off} \rangle^2 = \\ &= \left\langle \left(y_0 + L_t y'_0\right)^2 \right\rangle - \left(\langle y_0 \rangle + L_t \langle y'_0 \rangle\right)^2 = \\ &= \left\langle y_0^2 \right\rangle + 2L_t \langle y_0 y'_0 \rangle + L_t^2 \left\langle y_0'^2 \right\rangle - \langle y_0 \rangle^2 - 2L_t \langle y_0 \rangle \langle y'_0 \rangle - L_t^2 \langle y'_0 \rangle^2 = \\ &= \sigma^2_{y_0} + 2L_t \sigma_{y_0 y'_0} + L_t^2 \sigma^2_{y'_0}, \end{aligned} \tag{4.3}$$

where $\sigma_{y_0 y'_0} = \langle (y_0 - \langle y_0 \rangle)(y'_0 - \langle y'_0 \rangle) \rangle = \langle y_0 y'_0 \rangle - \langle y_0 \rangle \langle y'_0 \rangle$ is the covariance between vertical particle positions and divergences at RFD center, $\sigma_{y_0} = \langle y_0^2 \rangle - \langle y_0 \rangle^2$ is the RMS bunch vertical dimension at RFD center, and $\sigma_{y'_0} = \langle y_0'^2 \rangle - \langle y'_0 \rangle^2$ is the variance of the particle vertical divergences at RFD center. Between the RFD center and the screen, there is only a drift space. As a consequence, the variance of the vertical particle divergences at the screen is equal to the one at the RFD center, from Eq. 4.1,

$$\sigma_{y'_{s,off}} = \sigma_{y'_0}. \tag{4.4}$$

Due to the absence of perturbation in beam angle, the correlation between the vertical particle divergences and the other longitudinal quantities (i.e., the position and the energy) are preserved. Moreover, the longitudinal plane is also unaffected; thus, the correlation between the particle longitudinal position and energy is preserved. In particular, this is true since, as mentioned before, the particles are assumed to be relativistic.

RFD on

If the RFD is switched on, when the bunch goes through the RFD it sees a deflecting voltage, modeled as a vertical kick at the RFD center (Eq. 2.29). The schematic representation is shown in Fig. 4.3. The equations of the vertical particle motion

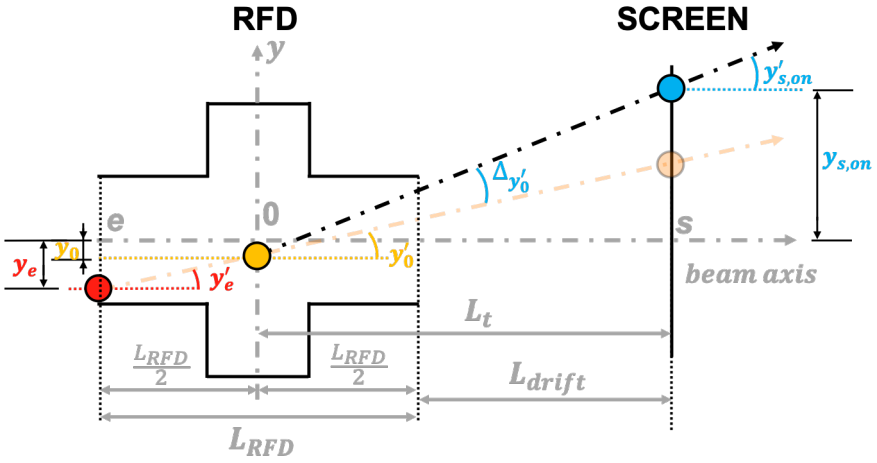

FIGURE 4.3: The particle vertical trajectory and parameters from the RFD entrance until the screen when the RFD is switched on.

from the RFD center to the screen are

$$\begin{cases} y_{s,on} = & y_0 + L_t\,(y'_0 + \Delta y'_0) \\ y'_{s,on} = & y'_0 + \Delta y'_0 \end{cases}, \tag{4.5}$$

where $y_{s,on}$ and $y'_{s,on}$ are the particle vertical position and divergence at screen with RFD on.

Centroid assessment The vertical bunch centroid at screen can be assessed from Eqs. 2.29, 4.2, and 4.5

$$\begin{aligned} C_{y_{s,on}} = \langle y_{s,on}\rangle &= \langle y_0 + L_t\,(y'_0 + \Delta y'_0)\rangle = \langle y_0 + L_t y'_0 + L_t C_{RFD0}\,[kz_0\cos(\varphi) + \sin(\varphi)]\rangle = \\ &= \langle y_0\rangle + L_t\langle y'_0\rangle + L_t k\cos(\varphi)\langle C_{RFD0} z_0\rangle + L_t\sin(\varphi)\langle C_{RFD0}\rangle = \\ &= C_{y_s,off} + L_t k\cos(\varphi)\langle C_{RFD0} z_0\rangle + L_t\sin(\varphi)\langle C_{RFD0}\rangle. \end{aligned} \tag{4.6}$$

Considering $\langle C_{RFD0} z_0\rangle = \langle C_{RFD0} ct_0\rangle = c\sigma_{t_0 C_{RFD0}}$, because $\langle ct_0\rangle = \langle z_0\rangle = 0$ (i.e., the reference system is imposed to have the zero at the center of the RFD), the vertical bunch centroid at the screen from Eq. 4.6 can be written as

$$C_{y_{s,on}} = C_{y_s,off} + L_t 2\pi f_{RF}\sigma_{t_0 C_{RFD0}}\cos(\varphi) + L_t\langle C_{RFD0}\rangle\sin(\varphi). \tag{4.7}$$

As in Eq. 2.30, C_{RFD0} can be approximated using the Taylor series stopped at first order around the particle energy average $\langle E_0\rangle$

$$\begin{aligned} C_{RFD0} = \frac{V_t}{E_0} &= V_t\left\{\left[\frac{1}{E_0}\right]_{\langle E_0\rangle} + \left[-\frac{1}{E_0^2}\right]_{\langle E_0\rangle}(E_0 - \langle E_0\rangle) + \ldots\right\} = \\ &\approx \frac{V_t}{\langle E_0\rangle}\,(1-\delta_0) = C_{RFD0a}\,(1-\delta_0)\,, \end{aligned} \tag{4.8}$$

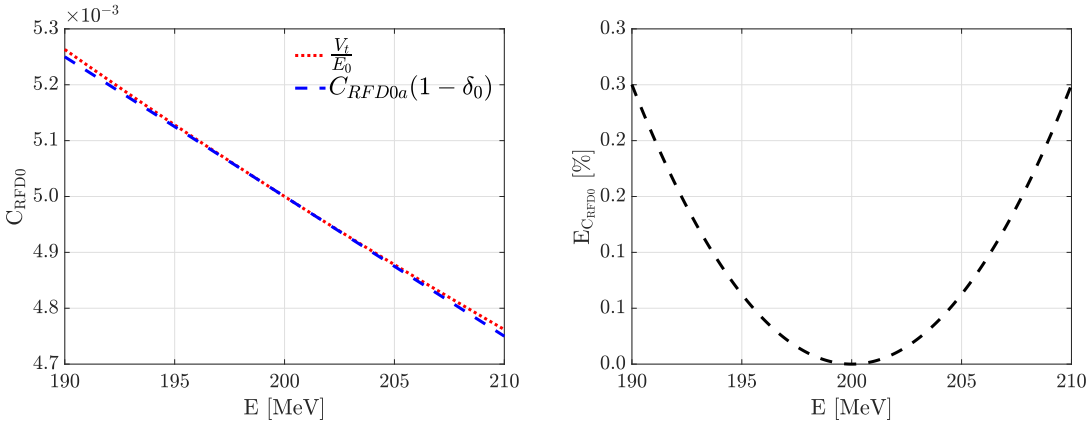

(A) (B)

FIGURE 4.4: In (A), the RFD coefficient in red dotted line (Eq. 2.30) and its Taylor approximation in blue dashed line (Eq. 4.8) versus the particle energy in the CLEAR accelerator. In (B), the percentage relative error using the Taylor approximation versus the particle energy, below 1%.

where δ_0 is the energy spread (element $[6,6]$ of Eq. 2.4).

In the case of the CLEAR accelerator ($V_t > 1\,\mathrm{MV}$, $\langle E_0 \rangle = 200\,\mathrm{MeV}$, and $\sigma_{\delta_0} < 5\%$) the RFD coefficient in Eq. 2.30 is well approximated by means of the Taylor series stopped at first order (Eq. 4.8), as shown in Fig. 4.4 (A). The RFD coefficient reletive **e**rror between the C_{RFD0} and its Taylor approximation stopped at the first order (i.e., $E_{CRF0} = 100 \cdot {}^{|C_{RFD0} - C_{RFD0a}(1-\delta_0)|}/_{C_{RFD0}}$) is less than 1% (from Fig. 4.4 (B)).

The average of C_{RFD0} and $\sigma_{t_0 C_{RFD0}}$ (in Eq. 4.7) can be calculated, using Eq. 4.8

$$\langle C_{RFD0} \rangle \approx \left\langle \frac{V_t}{\langle E_0 \rangle} (1 - \delta_0) \right\rangle = \frac{V_t}{\langle E_0 \rangle} = C_{RFD0a}, \tag{4.9}$$

$$\begin{aligned} \sigma_{t_0 C_{RFD0}} &= \langle t_0 C_{RFD0} \rangle - \langle t_0 \rangle \langle C_{RFD0} \rangle \approx \langle t_0 C_{RFD0a} (1 - \delta_0) \rangle - \langle t_0 \rangle C_{RFD0a} = \\ &= C_{RFD0a} \langle t_0 \rangle - C_{RFD0a} \langle t_0 \delta_0 \rangle - C_{RFD0a} \langle t_0 \rangle = -C_{RFD0a} \langle t_0 \delta_0 \rangle. \end{aligned} \tag{4.10}$$

Adding a null term in Eq. 4.10 ($\langle \delta_0 \rangle = 0$, for the definition of δ_0), it can be written

$$\sigma_{t_0 C_{RFD0}} = -C_{RFD0a} \langle t_0 \delta_0 \rangle + C_{RFD0a} \langle t_0 \rangle \langle \delta_0 \rangle = -C_{RFD0a} \sigma_{t_0 \delta_0}. \tag{4.11}$$

Finally, substituting Eqs. 4.9 and 4.11 in Eq. 4.7

$$C_{y_{s,on}} = C_{y_{s,off}} + L_t C_{RFD0a} \sin(\varphi) - L_t C_{RFD0a} 2\pi f_{RF} \sigma_{t_0 \delta_0} \cos(\varphi). \tag{4.12}$$

The first two terms of Eq. 4.12 are the vertical centroids at the screen after the RFD of the literature [176, 177]. The last term depends on the energy chirp (element $[5,6]$ of Eq. 2.4) and, therefore, the correlation between particle longitudinal positions and energies could affect the vertical centroid.

Spot size assessment At this stage, the vertical spot size at screen from Eqs. 2.29, 4.5, and 4.6 can be assessed

$$\begin{aligned}\sigma^2_{y_{s,on}} &= \langle (y_{s,on} - \langle y_{s,on}\rangle)^2\rangle = \langle y^2_{s,on}\rangle - \langle y_{s,on}\rangle^2 = \langle (y_0 + L_t y'_0 + L_t \Delta y'_0)^2\rangle - C^2_{y_{s,on}} = \\ &= \underline{\langle y_0^2\rangle + L_t^2\langle y_0'^2\rangle} + L_t^2\langle C^2_{RFD0}\left[kz_0\cos(\varphi) + \sin(\varphi)\right]^2\rangle \underline{+2L_t\langle y_0 y'_0\rangle} \\ &+ 2L_t\langle y_0 C_{RFD0}\left[kz_0\cos(\varphi) + \sin(\varphi)\right]\rangle + 2L_t^2\langle y'_0 C_{RFD0}\left[kz_0\cos(\varphi) + \sin(\varphi)\right]\rangle + \\ &\underline{-\langle y_0\rangle^2 - L_t^2\langle y'_0\rangle^2} - L_t^2k^2\cos^2(\varphi)\langle C_{RFD0}z_0\rangle^2 - L_t^2\sin^2(\varphi)\langle C_{RFD0}\rangle^2 \underline{-2L_t\langle y_0\rangle\langle y'_0\rangle} + \\ &- 2L_tk\cos(\varphi)\langle y_0\rangle\langle C_{RFD0}z_0\rangle - 2L_t\sin(\varphi)\langle y_0\rangle\langle C_{RFD0}\rangle + \\ &- 2L_t^2k\cos(\varphi)\langle y'_0\rangle\langle C_{RFD0}z_0\rangle - 2L_t^2\sin(\varphi)\langle y'_0\rangle\langle C_{RFD0}\rangle + \\ &- 2L_t^2k\cos(\varphi)\sin(\varphi)\langle C_{RFD0}\rangle\langle C_{RFD0}z_0\rangle.\end{aligned} \tag{4.13}$$

The underlined terms in Eq. 4.13 are the vertical spot size at the screen with RFD off, in Eq. 4.3, as a consequence, it can be rewritten as

$$\begin{aligned}\sigma^2_{y_{s,on}} &= \sigma^2_{y_s,off} + L_t^2k^2\cos^2(\varphi)\,\langle (C_{RFD0}z_0)^2\rangle + 2L_t^2k\cos(\varphi)\sin(\varphi)\,\langle C^2_{RFD0}z_0\rangle + \\ &+ L_t^2\sin^2(\varphi)\,\langle C^2_{RFD0}\rangle + 2L_tk\cos(\varphi)\,\langle y_0 z_0 C_{RFD0}\rangle + 2L_t\sin(\varphi)\,\langle y_0 C_{RFD0}\rangle + \\ &+ 2L_t^2k\cos(\varphi)\,\langle y'_0 z_0 C_{RFD0}\rangle + 2L_t^2\sin(\varphi)\,\langle y'_0 C_{RFD0}\rangle - L_t^2k^2\cos(\varphi)\,\langle C_{RFD0}z_0\rangle^2 + \\ &- L_t^2\sin^2(\varphi)\,\langle C_{RFD0}\rangle^2 - 2L_tk\cos(\varphi)\,\langle y_0\rangle\langle C_{RFD0}z_0\rangle - 2L_t\sin(\varphi)\,\langle y_0\rangle\langle C_{RFD0}\rangle + \\ &- 2L_t^2k\cos(\varphi)\,\langle y'_0\rangle\langle C_{RFD0}z_0\rangle - 2L_t^2\sin(\varphi)\,\langle y'_0\rangle\langle C_{RFD0}\rangle + \\ &- 2L_t^2k\cos(\varphi)\sin(\varphi)\langle C_{RFD0}\rangle\,\langle C_{RFD0}z_0\rangle\,.\end{aligned} \tag{4.14}$$

The highlighted terms are the variances

$$\sigma^2_{C_{RFD0}t_0} = \langle (C_{RFD0}ct_0 - \langle C_{RFD0}ct_0\rangle)^2\rangle = c^2\left(\langle (C_{RFD0}t_0)^2\rangle - \langle C_{RFD0}t_0\rangle^2\right), \tag{4.15}$$

and

$$\sigma^2_{C_{RFD0}} = \langle (C_{RFD0} - \langle C_{RFD0}\rangle)^2\rangle = \left(\langle (C_{RFD0})^2\rangle - \langle C_{RFD0}\rangle^2\right); \tag{4.16}$$

and the covariances

$$\begin{aligned}\sigma_{C_{RFD0}C_{RFD0}\cdot t_0} &= \langle (C_{RFD0} - \langle C_{RFD0}\rangle)\,(C_{RFD0}ct_0 - \langle C_{RFD0}ct_0\rangle)\rangle = \\ &= c\left(\langle C^2_{RFD0}t_0\rangle - \langle C_{RFD0}\rangle\langle C_{RFD0}t_0\rangle\right),\end{aligned} \tag{4.17}$$

$$\begin{aligned}\sigma_{y_0C_{RFD0}\cdot t_0} &= \langle (y_0 - \langle y_0\rangle)\,(C_{RFD0}ct_0 - \langle C_{RFD0}ct_0\rangle)\rangle = \\ &= c\left(\langle y_0C_{RFD0}t_0\rangle - \langle y_0\rangle\langle C_{RFD0}t_0\rangle\right),\end{aligned} \tag{4.18}$$

$$\sigma_{y_0C_{RFD0}} = \langle (y_0 - \langle y_0\rangle)\,(C_{RFD0} - \langle C_{RFD0}\rangle)\rangle = \langle y_0C_{RFD0}\rangle - \langle y_0\rangle\langle C_{RFD0}\rangle\,, \tag{4.19}$$

$$\begin{aligned}\sigma_{y_0' C_{RFD0}\cdot t_0} &= \langle (y_0' - \langle y_0' \rangle)\,(C_{RFD0} ct_0 - \langle C_{RFD0} ct_0 \rangle) \rangle = \\ &= c\,(\langle y_0' C_{RFD0} t_0 \rangle - \langle y_0' \rangle \langle C_{RFD0} t_0 \rangle)\,,\end{aligned} \tag{4.20}$$

and

$$\sigma_{y_0' C_{RFD0}} = \langle (y_0' - \langle y_0' \rangle)\,(C_{RFD0} - \langle C_{RFD0} \rangle) \rangle = \langle y_0' C_{RFD0} \rangle - \langle y_0' \rangle \langle C_{RFD0} \rangle\,. \tag{4.21}$$

Using Eqs 4.15, 4.16, 4.17, 4.18, 4.19, 4.20, and 4.21 Eq. 4.14 can be rewritten as

$$\begin{aligned}\sigma^2_{y_{s,on}} &= \sigma^2_{y_{s,off}} + L_t^2\,(2\pi f_{RF})^2 \cos^2(\varphi)\,\sigma^2_{C_{RFD0}\cdot t_0} + \\ &+ 2L_t^2 (2\pi f_{RF}) \cos(\varphi) \sin(\varphi)\,\sigma_{C_{RFD0} C_{RFD0}\cdot t_0} + L_t^2 \sin^2(\varphi)\,\sigma^2_{C_{RFD0}} + \\ &+ 2L_t 2\pi f_{RF} \cos(\varphi) \left[\sigma_{y_0 C_{RFD0}\cdot t_0} + L_t\,\sigma_{y_0' C_{RFD0}\cdot t_0}\right] + \\ &+ 2L_t \sin(\varphi) \left[\sigma_{y_0 C_{RFD0}} + L_t\,\sigma_{y_0' C_{RFD0}}\right].\end{aligned} \tag{4.22}$$

It is useful to define the calibration factor as

$$K_{cal}(\varphi) = 2\pi f_{RF} L_t C_{RFD0a} cos\,(\varphi)\,. \tag{4.23}$$

Substituting Eq. 4.23 in Eq. 4.22

$$\begin{aligned}\sigma^2_{y_{s,on}} = \sigma^2_{y_{s,off}} &+ \underbrace{\frac{K^2_{cal}(\varphi)}{C^2_{RFD0a}}\sigma^2_{C_{RFD0}\cdot t_0}}_{\text{Second term}} + \underbrace{2\frac{K^2_{cal}(\varphi)}{2\pi f_{RF} C^2_{RFD0a}} \tan(\varphi)\sigma_{C_{RFD0} C_{RFD0}\cdot t_0}}_{\text{Third term}} + \\ &+ \underbrace{\frac{K_{cal}(\varphi)^2 \tan(\varphi)}{(2\pi f_{RF})^2 C^2_{RFD0a}}\sigma^2_{C_{RFD0}}}_{\text{Fourth term}} + \underbrace{2\frac{K_{cal}(\varphi)}{C_{RFD0a}}\left[\sigma_{y_0 C_{RFD0}\cdot z_0} + L_t \sigma_{y_0' C_{RFD0}\cdot t_0}\right]}_{\text{Fifth term}} + \\ &+ \underbrace{2\frac{K_{cal}(\varphi) tan(\varphi)}{2\pi f_{RF} C_{RFD0a}}\left[\sigma_{y_0 C_{RFD0}} + L_t \sigma_{y_0' C_{RFD0}}\right]}_{\text{Sixth term}}.\end{aligned} \tag{4.24}$$

Taylor approximation Using the Taylor approximation, as in Eq. 4.8, the variance and the covariance in Eq. 4.24 can be simplified.

The variance present in the second term of Eq. 4.24 can be rewritten as

$$\begin{aligned}\sigma^2_{C_{RFD0}\cdot t_0} &= \langle (C_{RFD0} t_0)^2 \rangle - \langle C_{RFD0} t_0 \rangle^2 = \\ &\approx C^2_{RF0Da} \langle (t_0 - t_0\delta_0)^2 \rangle - C^2_{RFD0a}\,(\langle t_0 - t_0\delta_0 \rangle)^2 = \\ &= C^2_{RFD0a} \left[\underline{\langle t_0^2 \rangle} - 2\underline{\underline{\langle t_0 t_0 \delta_0 \rangle}} + \underline{\underline{\langle (t_0\delta_0)^2 \rangle}} - \underline{\langle t_0 \rangle^2} - 2\underline{\underline{\langle t_0 \rangle \langle t_0 \delta_0 \rangle}} - \underline{\underline{\langle t_0 \delta_0 \rangle^2}}\right].\end{aligned} \tag{4.25}$$

Considering the variances

$$\sigma^2_{t_0} = \underline{\langle t_0^2 \rangle - \langle t_0 \rangle^2}, \tag{4.26}$$

$$\sigma^2_{t_0\cdot\delta_0} = \underline{\underline{\langle (t_0\delta_0)^2\rangle - \langle t_0\delta_0\rangle^2}}, \tag{4.27}$$

and the covariance

$$\sigma_{t_0 t_0\cdot\delta_0} = \underline{\underline{\langle t_0 t_0\delta_0\rangle - \langle t_0\rangle\langle t_0\delta_0\rangle}}; \tag{4.28}$$

finally, substituting Eqs. 4.26, 4.27 and 4.28 in Eq. 4.25 it can be **w**ritten

$$\sigma^2_{C_{RFD0}\cdot t_0} \approx C^2_{RFD0a}\left(\sigma^2_{t_0} + \sigma^2_{t_0\cdot\delta_0} - 2\sigma_{t_0 t_0\cdot\delta_0}\right). \tag{4.29}$$

The covariance present in the third term of Eq. 4.24 can be rewritten as

$$\begin{aligned}\sigma_{C_{RFD0}C_{RFD0}\cdot t_0} &= \langle C^2_{RFD0} t_0\rangle - \langle C_{RFD0}\rangle\langle C_{RFD0} t_0\rangle = \\ &\approx C^2_{RFD0a}\langle (1-\delta_0)^2 t_0\rangle - C_{RFD0a}C_{RFD0a}\langle (1-\delta_0) t_0\rangle = \\ &= C^2_{RFD0a}\left(\cancel{\langle t_0\rangle} - 2\langle t_0\delta_0\rangle + \langle t_0\delta_0^2\rangle - \cancel{\langle t_0\rangle} + \langle t_0\delta_0\rangle\right) = \\ &= C^2_{RFD0a}\left(\langle t_0\delta_0^2\rangle - \langle t_0\delta_0\rangle\right).\end{aligned} \tag{4.30}$$

Adding null terms ($\langle\delta_0\rangle = 0$)

$$\sigma_{C_{RFD0}C_{RFD0}\cdot t_0} \approx C^2_{RFD0a}\left(\underline{\underline{\langle t_0\delta_0\delta_0\rangle}} - \underline{\underline{\langle t_0\delta_0\rangle\langle\delta_0\rangle}} - \underline{\langle t_0\delta_0\rangle} + \underline{\langle t_0\rangle\langle\delta_0\rangle}\right). \tag{4.31}$$

Considering the covariances

$$\sigma_{t_0\delta_0} = \underline{\langle t_0\delta_0\rangle - \langle t_0\rangle\langle\delta_0\rangle}, \tag{4.32}$$

and

$$\sigma_{t_0\cdot\delta_0\delta_0} = \underline{\underline{\langle t_0\delta_0\delta_0\rangle - \langle t_0\delta_0\rangle\langle\delta_0\rangle}}; \tag{4.33}$$

finally, substituting Eqs. 4.32 and 4.33 in Eq. 4.31 it can be written

$$\sigma_{C_{RFD0}C_{RFD0}\cdot t_0} \approx C^2_{RFD0a}\left(\sigma_{t_0\cdot\delta_0\delta_0} - \sigma_{t_0\delta_0}\right). \tag{4.34}$$

Considering the RMS value of C_{RFD0}

$$\langle C^2_{RFD0}\rangle \approx C^2_{RFD0a}\left\langle (1-\delta_0)^2\right\rangle = C^2_{RFD0a}\left(1 - 2\langle\delta_0\rangle + \langle\delta_0^2\rangle\right) = C^2_{RFD0a}\left(1 + \langle\delta_0^2\rangle\right), \tag{4.35}$$

the variance present in the fourth term of Eq. 4.24, using Eq. 4.35, and adding a null term ($\langle\delta_0\rangle^2$) can be rewritten as

$$\begin{aligned}\sigma_{C^2_{RFD0}} &= \langle C^2_{RFD0}\rangle - \langle C_{RFD0}\rangle^2 \approx C^2_{RFD0a}\left(1 + \langle\delta_0^2\rangle\right) - C^2_{RFD0a} = \\ &= C^2_{RFD0a}\left(\langle\delta_0^2\rangle - \langle\delta_0\rangle^2\right) = C^2_{RFD0a}\sigma^2_{\delta_0}.\end{aligned} \tag{4.36}$$

The covariance present in the fifth term of Eq. 4.24 can be rewritten as

$$\begin{aligned}\sigma_{y_0 C_{RFD0}\cdot t_0} &= \langle y_0 C_{RFD0} t_0\rangle - \langle y_0\rangle\langle C_{RFD0} t_0\rangle = \\ &\approx C_{RFD0a}\left(\langle y_0 t_0(1-\delta_0)\rangle - \langle y_0\rangle\langle t_0(1-\delta_0)\rangle\right) = \\ &= C_{RFD0a}\left(\underline{\langle y_0 t_0\rangle} - \underline{\underline{\langle y_0 t_0\delta_0\rangle}} - \underline{\langle y_0\rangle\langle t_0\rangle} + \underline{\underline{\langle y_0\rangle\langle t_0\delta_0\rangle\rangle}}\right).\end{aligned} \tag{4.37}$$

Considering the covariances

$$\sigma_{y_0 t_0} = \underline{\langle y_0 t_0 \rangle - \langle y_0 \rangle \langle t_0 \rangle}, \tag{4.38}$$

and

$$\sigma_{y_0 t_0 \cdot \delta_0} = \underline{\underline{\langle y_0 t_0 \delta_0 \rangle - \langle y_0 \rangle \langle t_0 \delta_0 \rangle}}; \tag{4.39}$$

finally, substituting Eqs. 4.38 and Eq. 4.39 in Eq. 4.37

$$\sigma_{y_0 C_{RFD0} \cdot t_0} \approx C_{RFD0a} \left(\sigma_{y_0 t_0} - \sigma_{y_0 t_0 \cdot \delta_0} \right). \tag{4.40}$$

With the same calculation it can be written

$$\sigma_{y_0' C_{RFD0} \cdot t_0} \approx C_{RFD0a} \left(\sigma_{y_0' t_0} - \sigma_{y_0' t_0 \cdot \delta_0} \right). \tag{4.41}$$

The covariance present in the sixth term of Eq. 4.24, can be rewritten as

$$\begin{aligned} \sigma_{y_0 C_{RFD0}} &= \langle y_0 C_{RFD0} \rangle - \langle y_0 \rangle \langle C_{RFD0} \rangle \approx C_{RFD0a} \left(\langle y_0 (1 - \delta_0) \rangle - \langle y_0 \rangle \langle 1 - \delta_0 \rangle \right) = \\ &= C_{RFD0a} \left(\cancel{\langle y_0 \rangle} - \underline{\langle y_0 \delta_0 \rangle} - \cancel{\langle y_0 \rangle} + \underline{\langle y_0 \rangle \langle \delta_0 \rangle} \right). \end{aligned} \tag{4.42}$$

Considering the covariance

$$\sigma_{y_0 \delta_0} = \underline{\langle y_0 \delta_0 \rangle - \langle y_0 \rangle \langle \delta_0 \rangle}, \tag{4.43}$$

finally, substituting Eq. 4.43 in Eq. 4.42 it can be written

$$\sigma_{y_0 C_{RFD0}} \approx -C_{RFD0a} \sigma_{y_0 \delta_0}. \tag{4.44}$$

With the same calculation it can be written

$$\sigma_{y_0' C_{RFD0}} \approx -C_{RFD0a} \sigma_{y_0' \delta}. \tag{4.45}$$

Finally, substituting Eqs. 4.29, 4.34, 4.36, 4.40, 4.41, 4.44, and 4.45 in Eq. 4.24

$$\begin{aligned} \sigma^2_{y_{s,on}} = {} & \sigma^2_{y_s,off} + K^2_{cal}(\varphi) \left(\sigma^2_{t_0} + \sigma^2_{t_0 \cdot \delta_0} - 2\sigma_{t_0 t_0 \cdot \delta_0} \right) + \\ & + 2 \frac{K^2_{cal}(\varphi)}{2\pi f_{RF}} \tan(\varphi) \left(\sigma_{t_0 \cdot \delta_0 \delta_0} - \sigma_{t_0 \delta_0} \right) + \frac{K^2_{cal}(\varphi)^2 \tan^2(\varphi)}{\left(2\pi f_{RF}\right)^2} \sigma^2_{\delta_0} + \\ & + 2K_{cal}(\varphi) \left(\sigma_{y_0 t_0} - \sigma_{y_0 t_0 \cdot \delta_0} + L_t \sigma_{y_0' t_0} - L_t \sigma_{y_0' t_0 \cdot \delta_0} \right) + \\ & - 2 \frac{K_{cal}(\varphi) tan(\varphi)}{2\pi f_{RF}} \left(\sigma_{y_0 \delta_0} + L_t \sigma_{y_0' \delta_0} \right). \end{aligned} \tag{4.46}$$

In the majority of high brightness LINACs it is reasonable to assume

- $\sigma^2_{t_0} >> \sigma^2_{t_0 \cdot \delta_0},\ \sigma_{t_0 t_0 \cdot \delta_0}$
- $\sigma_{t_0 \delta_0} >> \sigma_{t_0 \delta_0 \delta_0}$
- $\sigma_{y_0 t_0},\ L_t \sigma_{y_0' t_0} >> \sigma_{y_0 t_0 \cdot \delta_0}, L_t \sigma_{y_0' t_0 \cdot \delta_0}$,

Therefore, Eq. 4.46 can be simplified

$$\sigma^2_{y_{s,on}}(\varphi) = \sigma^2_{y_s,off} + K^2_{cal}(\varphi)\sigma^2_{t_0} - \frac{2K^2_{cal}(\varphi)}{2\pi f_{RF}}\tan(\varphi)\sigma_{t_0\delta_0} + \frac{K^2_{cal}(\varphi)}{(2\pi f_{RF})^2}\tan^2(\varphi)\,\sigma^2_{\delta_0} + \\ + 2K_{cal}(\varphi)\left(\sigma_{y_0t_0} + L_t\sigma_{y'_0t_0}\right) - 2\frac{K_{cal}(\varphi)}{2\pi f_{RF}}\tan(\varphi)\left(\sigma_{y_0\delta_0} + L_t\sigma_{y'_0\delta_0}\right). \tag{4.47}$$

Summarizing, in Eq. 4.47 the terms which affect the vertical spot size at the screen with RFD on are: the vertical spot size at the screen with RFD off (i.e., the first term), the measurand bunch length (i.e., the second term), the energy chirp and spread (i.e., the third and fourth terms, respectively),

and the correlations between vertical and longitudinal plane (i.e., the fifth and sixth terms, respectively).

Moreover, in most high brightness LINACs, it is common to neglect the energy spread contribution. As a consequence, Eq. 4.47 can be further simplified as

$$\sigma^2_{y_{s,on}}(\varphi) = \sigma^2_{y_s,off} + K^2_{cal}(\varphi)\sigma^2_{t_0} + 2K_{cal}(\varphi)\sigma_{y_0t_0} + 2K_{cal}(\varphi)L_t\sigma_{y'_0t_0}. \tag{4.48}$$

The same result can also be obtained performing the measurement with a phase φ equal to $0\,\mathrm{rad}$ or $\pi\,\mathrm{rad}$. Such a condition is the one commonly followed in the measurement procedure.

4.1.2 Measurement methods

In this section, firstly, the standard measurement method is recalled. Later, the novel measurement methods are introduced. The first new measurement method allows, thanks to a polynomial fit, to assess the bunch length, the energy chirp, and the energy spread. The second one can give information on the correlation terms between the particle positions/divergence and energy.

Standard measurement methods

In the standard measurement technique, from Eq. 4.47, the correlations between the vertical and the longitudinal plane (i.e., the correlation between the transverse position with the longitudinal position, the transverse divergence with the longitudinal position, the transverse position with the energy, and the transverse divergence with the energy) are removed averaging the square of two bunch length measurement performed at $\varphi\,\mathrm{rad}$ and $\varphi + \pi\,\mathrm{rad}$ [12, 163]. Moreover, the contributions of energy chirp and energy spread, from Eq. 4.47, if the measurement is performed without phase offset at $\varphi = 0\,\mathrm{rad}$ and $\varphi = \pi\,\mathrm{rad}$, gets removed.

$$\overline{\sigma_{y_{s,on}}}^2(\varphi) = \frac{\sigma^2_{y_{s,on}}(\varphi) + \sigma^2_{y_{s,on}}(\varphi+\pi)}{2} = \sigma^2_{y_{s,off}} + K^2_{cal}(\varphi)\sigma^2_{t_0}. \tag{4.49}$$

For reader convenience, the terms $\overline{\sigma_{y_{s,on}}}(\varphi)$ and $K_{cal}(\varphi)$ are often indicated as $\overline{\sigma_{y_{s,on}}}$ and K_{cal}, respectively; implicitly assuming their dependence from the RFD

phase. The information about the bunch length is contained only in the last term of Eq. 4.49. Therefore, it should be non-negligible with respect to the first term; otherwise, the measurement will not be feasible. For this reason, *(i)* K_{cal} needs to be increased, and *(ii)* $\sigma_{y_s,off}$ needs to be decreased. From Eq. 4.49, the bunch length can be assessed as

$$\sigma_{t_0} = \frac{\sqrt{\overline{\sigma^2_{y_{s,on}}} - \sigma^2_{y_s,off}}}{|K_{cal}(\varphi)|}. \tag{4.50}$$

Perform the measurement around $0\,\mathrm{rad}$ or $\pi\,\mathrm{rad}$ (or neglecting the contribution of the energy chirp) the vertical bunch centroid at screen (from Eq. 4.12), can be written as [176, 177]

$$C_{y_{s,on}} = L_t C_{RFD0a} \sin(\varphi). \tag{4.51}$$

Comparing Eq. 4.51 with the definition of the calibration factor, in Eq. 4.23, the relation between the two can be identified [163]

$$K_{cal} = 2\pi f_{RF} \frac{\mathrm{d}C_{y_{s,on}}}{\mathrm{d}\varphi}. \tag{4.52}$$

The calibration factor can be directly calculated by measuring the bunch centroid position variation at the screen with the deflecting phase. Consequently, one needs to know only the deflecting voltage frequency, which is usually a well defined parameter easy to access, determined by the RF source and the deflector being used. Thanks to this property, the measurement method is defined as self calibrated.

The measurement can then be performed even without knowing other parameters of the deflecting cavity or of the system, some of which can be difficult to assess precisely (e.g., the deflecting voltage amplitude and the average particle energy).

The standard model of measurement production is reported in Fig. 4.5. To perform the measurement correctly, it is necessary to measure: the vertical spot size at the screen (i.e., $\sigma_{y_{s,off}}$) with the RFD turned off, and the displacement of the beam centroid for different deflecting phases around $0\,\mathrm{rad}$ or $\pi\,\mathrm{rad}$ (i.e., $C_{y_{s,on}}$) with the RFD turned on. After that, and always with the RFD turned on, the vertical spot size at the screen (i.e., $\sigma_{y_{s,on}}$) at $\varphi\ \mathrm{rad}$ and $\varphi + \pi\ \mathrm{rad}$ needs to be measured.

The measurement of the vertical displacement of the bunch centroid while varying the deflecting phase in a small range centered around $0\,\mathrm{rad}$ or $\pi\,\mathrm{rad}$ ($\sin(\varphi) \approx \varphi$), gives the calibration. The derivative ${}^{dC_{y_{s,on}}}/_{d\varphi}$ can be calculated as the slope of the vertical bunch centroid as a function of the RFD phase, evaluated by means of a linear fit. By multiplying the slope by $2\pi f_{RF}$, the $K_{cal}(\varphi)$ can be obtained. From the measurements of the vertical spot size at the screen with the RFD turned on at different phases, using an average of the squared value, $\overline{\sigma_{y_{s,on}}}$ can be obtained. Finally, the bunch length can be assessed subtracting from $\overline{\sigma_{y_{s,on}}}$ the $\sigma_{y_{s,off}}$ under square root and dividing by the absolute value of $K_{cal}(\varphi)$.

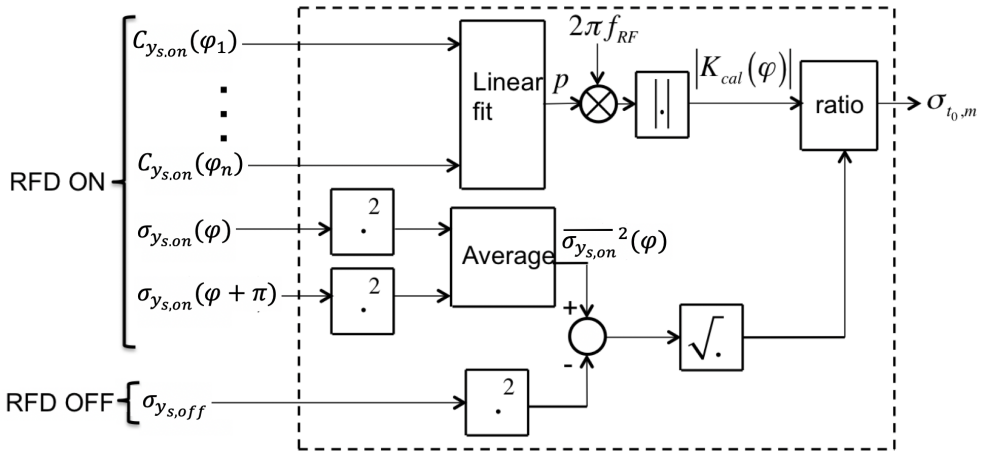

FIGURE 4.5: The model of the measurement production of the bunch length based on the cancellation of the correlations [174].

Novel measurement methods

In this section, two measurement methods for (i) energy chirp and spread and (ii) correlations between particle positions, divergences, and energies are presented [15].

Energy Chirp and Spread Starting from Eq. 4.47, without neglecting/cancelling the energy spread contribution, by following the same procedure used in Eq. 4.49, the fifth and the sixth term of the Eq. 4.47 can be cancelled by averaging between $\sigma^2_{y_s}(\varphi)$ and $\sigma^2_{y_s}(\varphi+\pi)$. Furthermore, considering a small range of the deflecting voltage phase around the voltage zero-crossing, it can be written

$$\begin{aligned} A^2(\varphi_i) &= \frac{\sigma^2_{y_{s,on}}(\varphi_i)+\sigma^2_{y_{s,on}}(\varphi_i+\pi)}{2} = \\ &= \sigma^2_{y_s,off} + K^2_{cal}\left[\sigma^2_{t_0} - \underline{\frac{\sigma_{t_0\delta_0}}{\pi f_{RF}}\varphi_i} + \underline{\underline{\frac{\sigma^2_{\delta_0}}{(2\pi f_{RF})^2}\varphi_i^2}}\right] = \\ &= p_3 + p_2\varphi_i + p_1\varphi_i^2, \end{aligned} \tag{4.53}$$

for each i-measurement at φ_i phase. The third (underline) and the fourth terms (double underline) of Eq. 4.53 are the contributions of the energy chirp and spread to the vertical spot size at the measurement screen with the RFD active. They are sources of deterministic errors in the bunch length measurements [197], and they are typically calibrated away with independent measurements of $\sigma_{t_0\delta_0}$ and σ_{δ_0}, or removed measuring without phase offset at $\varphi_i = 0\,\mathrm{rad}$ or $\varphi_i = \pi\,\mathrm{rad}$. On the other hand, these contributions can be used to measure the energy chirp and spread from the vertical spot size measurements versus the deflecting voltage phase. In particular, Eq. 4.53 is a quadratic polynomial of the variable φ_i. The energy

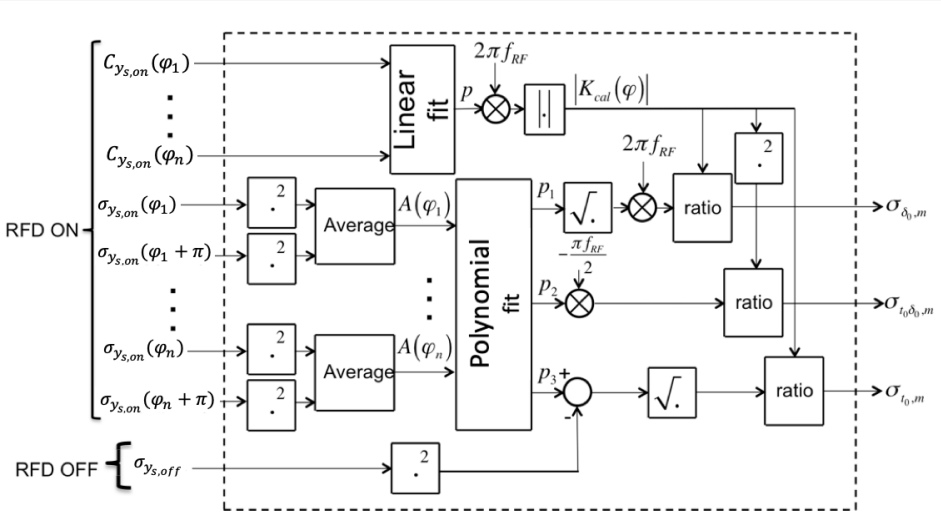

FIGURE 4.6: The model of measurement production for energy spread, energy chirp, and bunch length [198].

spread, the energy chirp, and the bunch length can be calculated as

$$\sigma_{\delta_0,m} = \sqrt{p_1}\frac{2\pi f_{RF}}{K_{cal}}, \quad \sigma_{t_0\delta_0,m} = -p_2\frac{2\pi f_{RF}}{2K_{cal}^2}, \text{ and } \sigma_{t_0,m} = \frac{\sqrt{p_3 - \sigma_{y_s,off}^2}}{K_{cal}}; \tag{4.54}$$

where p_1, p_2, and p_3 are the coefficients of the polynomial fits defined in the Eq. 4.53. Some further considerations from Eq. 4.53 can be made.

Firstly, in order to perform a good measurement, the first term of the second line in Eq. 4.53 should be non-dominant with respect to the other terms, since they are the ones that contain information about the measurands: the bunch length (i.e., σ_{t_0}), energy chirp (i.e., $\sigma_{t_0\delta_0}$), and energy spread (i.e., σ_{δ_0}). In order to ensure this, *(i)* K_{cal} can be increased (increasing the distance between the RFD and the screen and/or the deflecting voltage amplitude) and *(ii)* $\sigma_{y_s,off}$ can be decreased, e.g. using a vertically focusing quadrupole placed before the RFD. Moreover, to get information on all measurands, the second, the third, and the fourth term should have a non-negligible impact on vertical spot size individually. Thus proposed measurement method can be applied when the measurands give a non-negligible contribution to the vertical spot size, i.e., for a bunch with suitable pr**o**perties in length, energy chirp, and energy spread. When the energy spread contribution is negligible (fourth terms in Eq. 4.53), $A^2(\varphi)$ becomes a linear function of the deflecting voltage phase.

The bunch length measurement model, shown in Fig. 4.6, is based firstly on the measurements of the spot size at the screen when the RFD is turned off (i.e., obtaining $\sigma_{y_{s,off}}$). Secondly, by switching on the RFD, the vertical bunch centroid and spot size at the screen can be measured for different values of the RFD phase φ_i (i.e., obtaining $C_{y_{s,on}}(\varphi_i)$, $\sigma_{y_s}(\varphi_i)$, and $\sigma_{y_s}(\varphi_i + \pi)$). As a second step (data processing), the calibration factor K_{cal} is computed with Eq. 4.52; thus applying the

Eq. 4.53 also the coefficients p_1, p_2, and p_3 are computed by means of a polynomial fit. As a last step, using the Eqs. 4.54 the measured energy spread ($\sigma_{\delta_0,m}$), energy chirp ($\sigma_{t_0\delta_0,m}$), and bunch length ($\sigma_{t_0,m}$) are obtained.

The presented model requires new steps of data acquisition and elaboration with respect to the standard method of the bunch length measurement shown in Fig. 4.5; in particular, a polynomial fit of the vertical spot size squared values at the screen varying the RFD phase is required.

Correlations between particle positions, divergences, and energies As shown in Eq. 4.49 and 4.53 the contributions given by the correlations between particle positions, divergences and energies at RFD center can be corrected, through an average between $\sigma^2_{y_{s,on}}(\varphi)$ and $\sigma^2_{y_{s,on}}(\varphi+\pi)$. On the other hand, the variations of the vertical spot size due to these correlations can be used to obtain some information on them. For the deflecting voltage phases φ and $\varphi+\pi$, all the terms of $\sigma^2_{y_{s,on}}$, from Eq. 4.47 do not change their signs and values, but the correlation contributions change their sign. Therefore, the correlation terms can be isolated by taking the differences of the squared values of the vertical spot size at the screen around the two zero-crossing phases (using the approximation of a small phase φ around $0\,\mathrm{rad}$)

$$\begin{aligned} cor_{l_0v_0}(\varphi) &= \frac{\sigma^2_{y_{s,on}}(\varphi) - \sigma^2_{y_{s,on}}(\varphi+\pi)}{2} = \\ &= 2K_{cal}cor_{t_0v_0} - 2\frac{K_{cal}}{2\pi f_{RF}}cor_{\delta_0v_0}\varphi = \\ &= q_{cor} + p_{cor}\varphi, \end{aligned} \tag{4.55}$$

where

$$cor_{t_0v_0} = \sigma_{y_0t_0} + L_t\sigma_{y'_0t_0} \text{ and } cor_{\delta_0v_0} = \sigma_{y_0\delta_0} + L_t\sigma_{y'_0\delta_0}. \tag{4.56}$$

The information about the correlations can be found with a linear fit of $cor_{l_0v_0}(\varphi)$ thus, the measured values are

$$cor_{\delta_0v_0,m} = -\frac{\pi f_{RF}}{K_{cal}}p_{cor} \text{ and } cor_{t_0v_0,m} = \frac{q_{cor}}{2K_{cal}}. \tag{4.57}$$

The model of measurement production for the correlation terms is shown in Fig. 4.7. The first stage consists of the measurements of the vertical bunch centroid position and spot size at the screen for different values of the deflecting voltage phase φ_i (close to the zero-crossing), obtaining $C_{y_{s,on}}(\varphi_i)$, $\sigma_{y_{s,on}}(\varphi_i)$, and $\sigma_{y_{s,on}}(\varphi_i+\pi)$. Afterwords, one can compute the calibration factor K_{cal} from Eq. 4.52, the coefficients p_{cor} and q_{cor} from Eq. 4.55, as well as evaluate the correlation terms $cor_{\delta_0v_0,m}$ and $cor_{t_0v_0,m}$ from Eq. 4.57.

4.1.3 Simulation tools

The use of state-of-the-art tracking codes (e.g., ELEGANT [200], A Space Charge Tracking Algorithm (ASTRA) [201], Methodical Accelerator Design-X (MAD-X) [202],

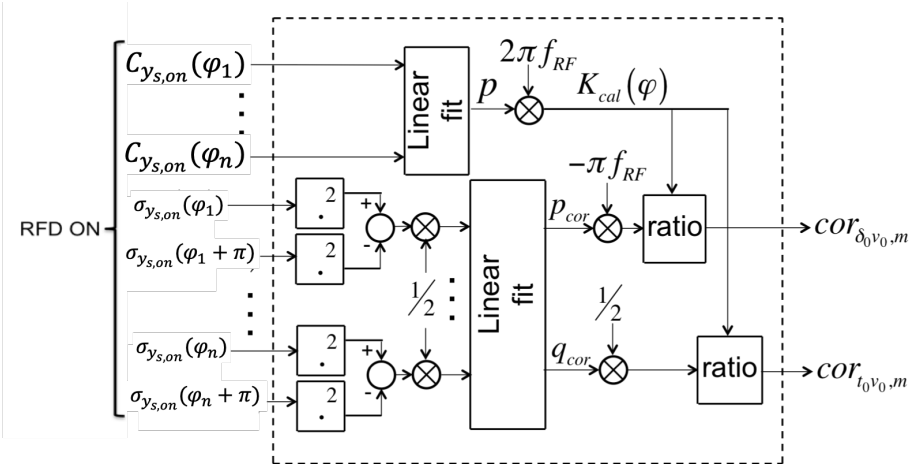

FIGURE 4.7: The model of measurement production for the correlation terms between longitudinal position, divergence, and energies [199].

and so on) as a metrological reference is a standard procedure in particle accelerator design and engineering, both in single systems (as done here) and in the whole particle accelerator layout as a whole. The ELEGANT code is well established; it has been, through the years, validated against a vast number of different practical cases. Nowadays, it is exploited in LINACs design as well as their commissioning. Moreover, ELEGANT simulations are considered so reliable that they can detect measurement artifacts, especially in the accelerator commissioning or development. Such an approach is mandatory in complex particle accelerator systems where particularly challenging beam conditions can be accessed only when the accelerator is fully built. Dedicated ELEGANT simulations are carried out to validate the derived equations.

4.1.4 Case studies for conventional layout

The case studies concern different kinds of high-brightness electron LINACs, very relevant in the world-wide R&D effort on novel particle accelerators. Some particular examples of Compton sources, FEL injectors, and plasma-based accelerators are discussed. These three machines use bunches with different σ_{t_0}, σ_{δ_0}, and $\sigma_{t_0\delta_0}$. The Compton source case study is the GBS LINAC at Extreme Light Infrastructure - Nuclear Physics (ELI-NP), and the parameters used in the numerical studies are obtained from the start-to-end simulations used in the design of the machine [203]. For the other two cases (i.e., FELs and plasma accelerators), two different sets of bunch properties meaningful for many machines with a similar aim are presented. In this case, CLEAR is less suitable for a case study due to the longer bunch length and smaller chirp and spread. Furthermore, for the GBS, a start to end simulation was already available.

The RFD deflector parameters used in the simulations ($V_t = 1\,\mathrm{MV}$, $f_{RF} = 2.856\,\mathrm{GHz}$) are extremely conventional, and they can be accessible in many of the

high brightness LINACs nowadays in operation. The distance of the measurement screen from the RFD is $L_t = 1.138\,\mathrm{m}$ and the beam energy is $\langle E_0 \rangle = 118\,\mathrm{MeV}$; those values are the ones used in GBS, and they are kept constant also in the other examples for simplicity, and because they are quite common and reasonable. A bunch composed of 50,000 macro-particles (with a total charge of $250\,\mathrm{pC}$ for the GBS case, $100\,\mathrm{pC}$ in the FEL cases, and $10\,\mathrm{pC}$ for the plasma cases) is tracked by the ELEGANT code [200] through the RFD up to the measurement screen. The bunch is travelling on axis without any angle ($C_{y_0} = 0\,\mathrm{m}$ and $C_{y'_0} = 0\,\mathrm{rad}$). As mentioned above, the measurement procedure for measuring the correlation between particle position, divergence, and energy can only be applied if the correlation terms give a significant contribution to the vertical spot size measurements (Eq. 4.47). Therefore, there is a threshold for carrying out the measurement method with acceptable accuracy. The contribution of the correlation terms to the vertical spot size at the measurement screen can become negligible in the case of longer bunches. For this reason, the study is restricted to the most challenging case study with the longest bunches, namely the GBS.

It is worth noticing that the variation of the RMS vertical spot size needed in all the case-studies is in the order of a few tens of $\mu\mathrm{m}$, and it may require advanced diagnostic tools. The vertical beam dimension on the measurement screen can be increased: (i) in percentage, using better magnetic optics when the RFD is switched off (to decrease $\sigma_{y_{s,off}}$); (ii) in absolute terms, increasing the deflecting voltage amplitude and/or the distance between the RFD and the measurement screen (to increase K_{cal}).

The bunch longitudinal parameters (i.e., σ_{t_0}, σ_{δ_0}, and $\sigma_{t_0\delta_0}$) as well as the foreseen measurement results (i.e., $\sigma_{t_0,m}$, $\sigma_{\delta_0,m}$, and $\sigma_{t_0\delta_0,m}$) are reported case by case. For reader convenience a column with the relative percentage deterministic error for each quantity X with measured value X_m is added (i.e., $E_{X_m} = 100 \cdot |X - X_m|/X$); in addition, the uncertainties reported represents a 1-sigma interval.

Compton sources - Gamma Beam Source

In the GBS injector, a $250\,\mathrm{pC}$ bunch beam with a nominal RMS bunch length of $1\,\mathrm{ps}$ and a few 0.1% energy spread is delivered to the interaction chamber to collide with a laser [204]. In this case study, the values used for the beam parameters are the results of start-to-end simulations of the whole LINAC before the RFD, according to [203], and therefore they are representative of a real beam. Figures 4.8 shows the longitudinal phase space. The beam transverse parameter at the RFD center are: $\sigma_{y_0} = 346.4\,\mu\mathrm{m}$, $\sigma_{y'_0} = 57.57\,\mu\mathrm{rad}$, and $\sigma_{y_0 y'_0} = -19.86\,\mathrm{nm}$.

Energy chirp and spread simulations The energy chirp contribution to the vertical spot size is significant, while the energy spread contribution is negligible. Thus only the energy chirp can be measured by means of the proposed measurement method (i.e., through a linear fit of the vertical spot size versus the deflecting voltage phase). The simulation results are shown in Tab. 4.1. The reported uncertainties are introduced from the polynomial fit. The other uncertainty sources

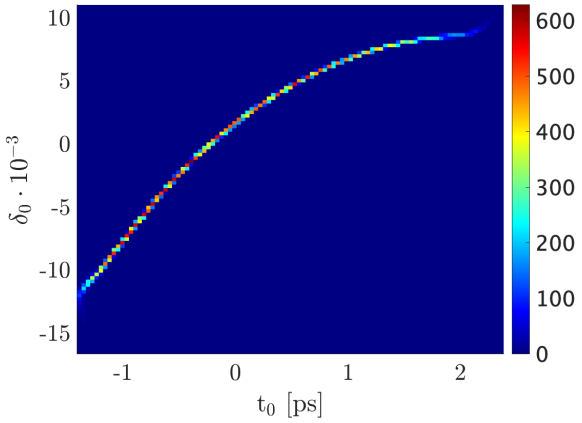

FIGURE 4.8: The longitudinal phase space at RFD center, obtained by start-to-end simulations for the GBS accelerator [15].

TABLE 4.1: Simulation parameters and results for the Compton source case study, for the energy spread, the measurement method is Not Applicable (NA).

σ_{t_0} [fs]	$\sigma_{t_{0,m}}$ [fs]	$E_{\sigma_{t_{0,m}}}$
912	907.9 ± 3.0	0.4%
σ_{δ_0} [%]	$\sigma_{\delta_{0,m}}$ [%]	$E_{\sigma_{\delta_{0,m}}}$
0.6054	NA	NA
$\sigma_{t_0\delta_0}$[fs]	$\sigma_{t_0\delta_{0,m}}$[fs]	$E_{\sigma_{t_0\delta_{0,m}}}$
5.329	5.06 ± 0.38	5.0%

(e.g., phase stability, beam jitter, spot size jitter) are neglected in these simulations in order to validate the measurement methods.

The vertical bunch centroid and spot size measurements, while varying the deflecting voltage phase, are shown in Figs. 4.9 (A) and (B), respectively. The centroid variation with respect to the RFD phase can be used to compute K_{cal} from Eq. 4.52. The uncertainty on K_{cal} as well as the measured energy chirp and bunch length is only due to the linear fit. The RMS spot size when the RFD is switched off is $\sigma_{y_{s,off}} = 281\,\mu\text{m}$ and from the linear fit $|K_{cal}| = (172.95 \pm 0.15)\,\mu\text{m/ps}$, where, the uncertainty comes from the uncertainty propagation on Eq. 4.52 considering the uncertainty on the centroid positions due to the linear fit. Since the energy spread contribution is negligible, the squared value of the vertical spot size is linear (from Eq. 4.53) over the deflecting voltage phase range (Fig. 4.9 (B) left). The averages of the squared values of vertical spot size at the screen are not affected by significant inaccuracy because the correlations between vertical and longitudinal planes are weak (Fig. 4.9 (B) right).

Correlations simulations The correlations between particle positions, angles, and energies are unwanted effects, possibly caused by misalignments, position

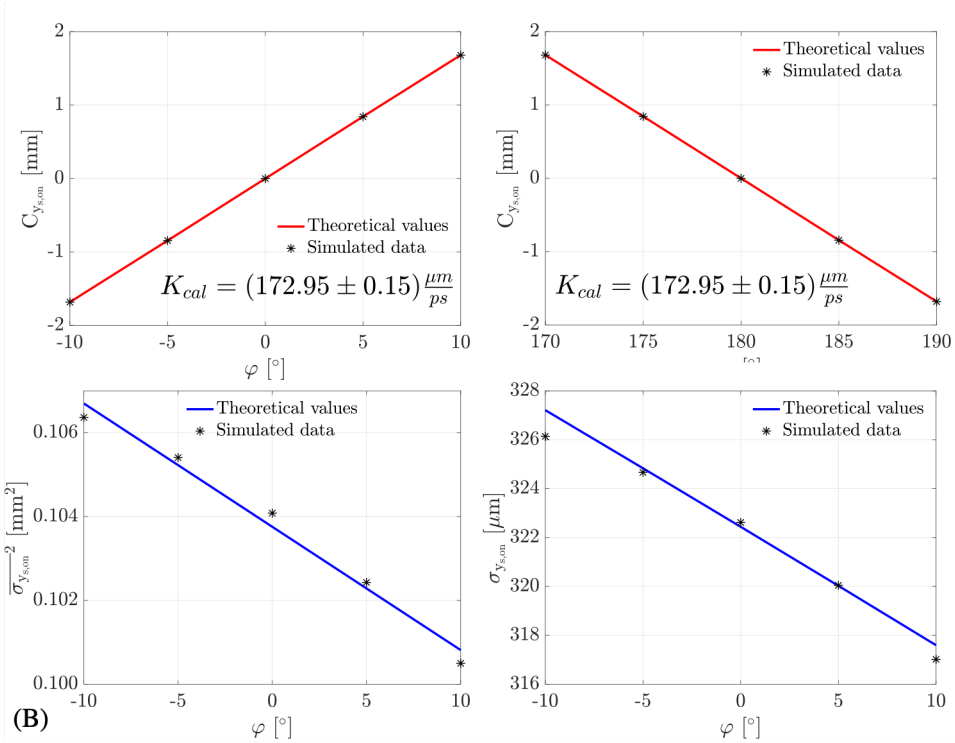

FIGURE 4.9: In (A), the vertical bunch centroids versus φ and $\varphi + \pi$ in left and right, respectively. In (B), the spot sizes measured at the screen versus φ without and with averaging over two zero-crossing phases, left and right, respectively. The simulated data reported as stars and the linear fit reported as solid lines [15].

jitters, field imperfections, and so on. In the GBS layout, the considered correlations could be caused by a $2\,\mathrm{mm}$-misalignment of the first accelerating section and the focusing magnet (quadrupole) upstream of the RFD; such a misalignment is within the design tolerance of the machine. Figures 4.10 reports the relevant phase spaces obtained by a start-to-end simulation of the whole machine (i.e., upstream the RFD) considering the misalignments. All the data **v**irtually measured at the RFD center are: $\sigma_{y_0} = 348.8\,\mu\mathrm{m}$, $\sigma_{y'_0} = 60.15\,\mu\mathrm{rad}$, $\sigma_{y_0 y'_0} = -19.15\,\mathrm{nm}$. The proposed measurement technique aims to estimate the correlations by measuring spot-sizes of the deflected beam at the measurement screen. Applying the measurement production model, in Fig. 4.7, the simulations and the data processing results are reported in Tab. 4.2. The uncertainty on the correlations terms is only due to the linear fits and, as done for the energy chirp and spread, the other uncertainties sources are neglected in these simulations in order to validate the measurement methods. The vertical bunch centroid measured while varying the deflecting voltage phase shows the same slope of the case without misalignment. Such an effect is obtained because the possible field inhomogeneities are neglected as anticipated in Sec. 2.3.3.

The differences between Fig. 4.11 (A) and (B) are caused by the significant correlation contributions to the vertical spot size at the screen. From the results in Figs. 4.11 and 4.9, the requirements on the resolution and on the Field Of View

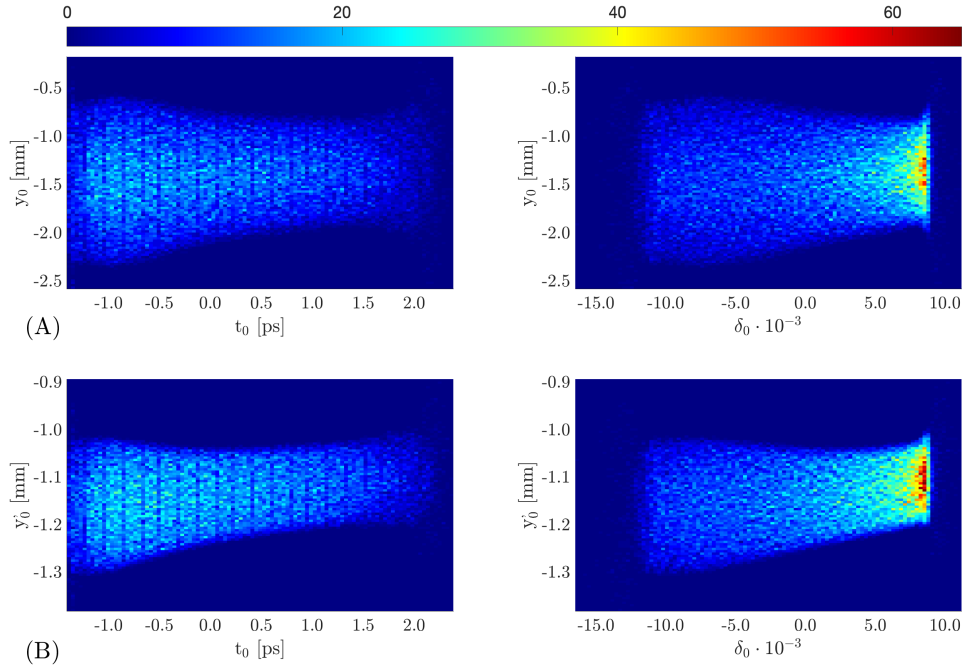

FIGURE 4.10: In (A), the particle vertical positions versus longitudinal positions with $r_{y_0 t_0} = 0.12$ (left) and particle energies with $r_{y_0 \delta_0} = 0.11$ (right). In (B), the particle vertical divergences versus longitudinal positions with $r_{y_0' t_0} = 0.29$ (left) and particle energies with $r_{y_0' \delta_0} = 0.28$ (right) [15].

TABLE 4.2: Simulations and data processing results from Eq. 4.52, and 4.57.

	Reference value	Measured value	Relative error
K_{cal} ($\varphi \approx 0$ rad)	$173.7\,\mu m/ps$	$172.81 \pm 0.15\,\mu m/ps$	$\approx 0.5\%$
K_{cal} ($\varphi \approx \pi$ rad)	$-173.7\,\mu m/ps$	$-173.10 \pm 0.15\,\mu m/ps$	$\approx 0.1\%$
$cor_{t_0 v_0}$	$54.96\,\mu m\,ps$	$54.35 \pm 0.21\,\mu m\,ps$	$\approx 1\%$
$cor_{\delta_0 v_0}$	$0.3499\,\mu m$	$0.348 \pm 0.029\,\mu m$	$\approx 0.5\%$

(FOV) of the optical system used to image the beam footprint can be assessed. Weaker correlations imply smaller correlation terms (i.e., small variations of the vertical spot size at the screen) and, therefore, they require better resolution.

The approximation of a constant calibration factor (calculated from vertical centroid measurements) is used. In the RFD phase range investigated, it leads to a negligible relative error, less than 1.5%, compared with the theoretical calibration factor (from Eq. 4.23) as shown in Figs. 4.12.

Free electron Laser (FEL) sources

The second case study concerns two extreme cases of LINAC used as an injector for FELs. The first case is a $250\,fs$-long bunch with a moderate energy spread and a strong energy chirp (correlation factor $r_{t_0 \delta_0} = -0.8$). Similar bunches are

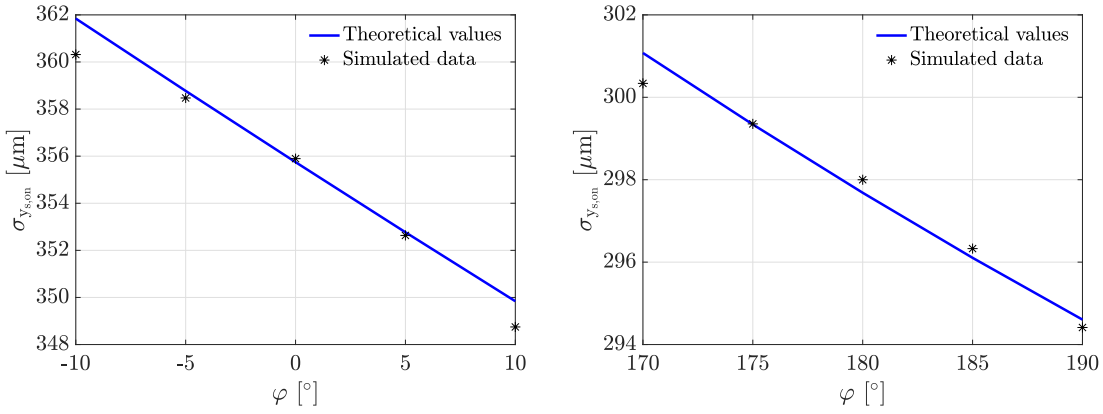

FIGURE 4.11: The vertical spot size at the screen in case of misalignment, over the deflecting voltage range of $-10°$ to $10°$ and (B) $170°$ to $190°$ in (A) and (B), respectively. The simulated data reported as black stars and the theoretical values (Eq. 4.47) reported as solid blue lines [15].

used for single-spike FEL radiation [205, 206]. The longitudinal phase space at the RFD center is given in Fig. 4.13 (A), where the negative value of the energy chirp is clear. The second case deals with novel ideas being discussed in the scientific community on future FEL injectors, aiming to a much higher beam current (in the few kA range) than conventional FELs. If those currents are reached while keeping a small energy spread (e.g., half of the one considered in the first case), ultra-high brightness can be reached. This result will imply a strong reduction in the length of the undulator magnets, which are nowadays limiting the compactness of FELs. A positive strong chirps, with a high correlation factor $r_{t_0\delta_0} = 0.9$, is considered (longitudinal phase space at the RFD center is given in Fig. 4.13 (B)). The spot size variation at the measurement screen when the RFD is switched on is quite relevant (50% for the first case). Thus a non-negligible contribution is given to the spot size from the additional terms to be measured. In Tab. 4.3 and 4.4, the simulation results for the longitudinal parameters and the relative errors for the two FEL cases are reported, respectively. As for the Compton sources, the uncertainty is only driven by the polynomial fit. In the first case, the error of the measured energy spread is larger than the second one. A small energy spread can be measured if the bunch length is small enough. However, it is needed that the energy spread contribution is significant (from Eq. 4.47).

Plasma-based particle accelerators

Plasma-based particle accelerators are encountering an intense development. The huge accelerating fields (three orders of magnitude larger than conventional RF fields used in accelerators) require a high degree of control of the beam parameters to reach the same stability and reliability of conventional accelerators. At the

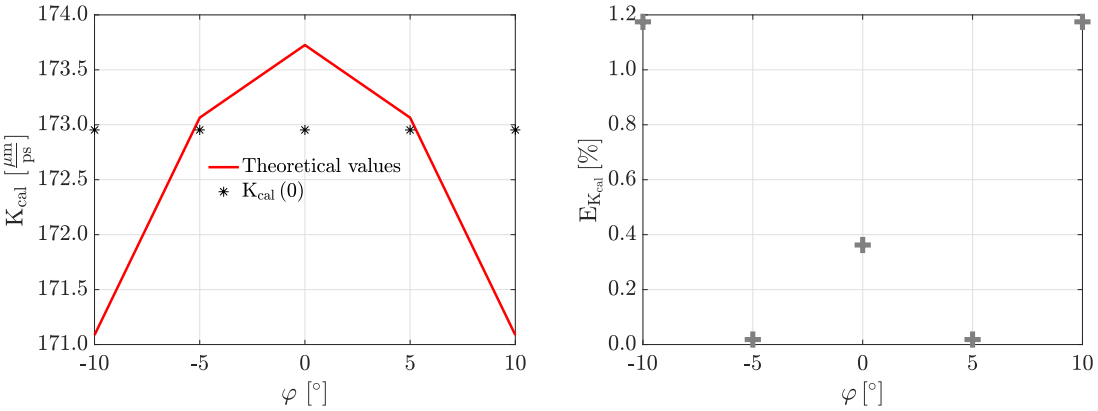

(A) (B)

FIGURE 4.12: In (A), the theoretical calibration factor (Eq.4.23) in red line and calibration factor calculated from vertical bunch centroid measurements (Eq.4.52) in black star. In (B), the relative error between the theoretical calibration factor and the calibration factor calculated from the bunch centroid $|K_{cal,t}(\varphi) - K_{cal}(0)|/|K_{cal,t}(\varphi)|$ [174].

TABLE 4.3: Simulation parameters and results for the first case of the FEL-injector.

σ_{t_0} [fs]	$\sigma_{t_0,m}$ [fs]	$E_{\sigma_{t_0,m}}$
250	250.86 ± 0.23	0.3%
σ_{δ_0} [%]	$\sigma_{\delta_0,m}$ [%]	$E_{\sigma_{\delta_0,m}}$
1	0.8932 ± 0.0099	10.7%
$\sigma_{t_0\delta_0}$[fs]	$\sigma_{t_0\delta_0,m}$[fs]	$E_{\sigma_{t_0\delta_0,m}}$
-2.06	-2.070 ± 0.034	0.5%

TABLE 4.4: Simulation parameters and results for the second case of the FEL-injector.

σ_{t_0} [fs]	$\sigma_{t_0,m}$ [fs]	$E_{\sigma_{t_0,m}}$
25	24.84 ± 0.10	0.6%
σ_{δ_0} [%]	$\sigma_{\delta_0,m}$ [%]	$E_{\sigma_{\delta_0,m}}$
0.5	0.4973 ± 0.0010	0.5%
$\sigma_{t_0\delta_0}$[fs]	$\sigma_{t_0\delta_0,m}$[fs]	$E_{\sigma_{t_0\delta_0,m}}$
0.1125	0.10870 ± 0.00036	3.4%

moment, several solutions are being investigated [207], ranging from laser to particle driven accelerators. The two case studies are representative of two typical cases. The first case, with about 100 fs beam and 1% energy spread, have parameters typical of particle-driven solutions, while the second case investigates ultra-short bunches (10 fs), with significant energy spreads (4%) similar to the one used in the laser-driven solutions. Both the cases exhibit quite strong energy chirps (correlation coefficient almost 1), a so typical situation in plasma accelerator that specific solutions are being addressed [208]. The longitudinal phase spaces of the beam at the RFD center are described in Fig. 4.13 (C) for the first case and Fig. 4.13 (D) for the second case. Applying the measurement procedure, the percentage variation of the RMS vertical spot size at the screen is again about 50% when the RFD is switched on. Thus a non-negligible contribution is given to the spot size from the additional terms to be measured. In Tab. 4.5 and 4.6 the expected and obtained in simulation values are reported, as well as the relative

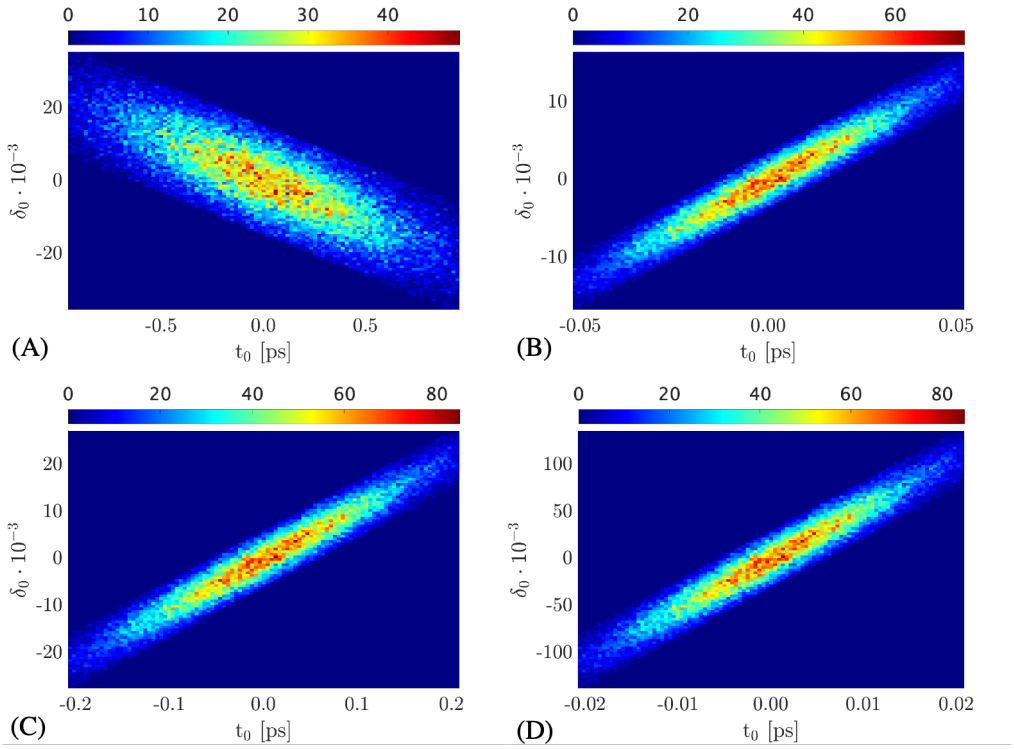

FIGURE 4.13: The longitudinal phase spaces at RFD center. The first row concerns the FEL injector, the first (i.e., single spike) and the second case (i.e., high current) in (A) and (B), respectively. The second row concerns plasma accelerator, the first (i.e., particle-drive) and the second case (i.e., laser-drive) in (C) and (D), respectively [15].

measurement error. As for the Compton sources and FEL sources, the uncertainty is only driven by the polynomial fit.

4.2 Measurement methods for non-conventional layout

Usually, in the conventional layout, a considerable drift space is kept between the RFD and the screen to achieve sufficient deflection of the bunch. Moreover, it is common to use some focusing elements before the RFD to minimize the beam spot on the screen [161, 209]. However, dimensional problems can arise in the installation (e.g., reduce the space between the klystron and the deflecting cavity by consequently shortening the **n**ecessary waveguides) and squeeze down the available space in the accelerator. In various accelerators focusing elements are installed between the RFD and the screen in order to save space (e.g., CLEAR [210], ATF [211], and DESY [212]) and kept off during the bunch length measurement [16]. In this section, their impact on the bunch length measurement, not investigated until now, is presented.

TABLE 4.5: Simulation parameters and results for the first case of plasma-based accelerators (i.e., particle-driven solution).

σ_{t_0} [fs]	$\sigma_{t_0,m}$ [fs]	$E_{\sigma_{t_0,m}}$
100	100.21 ± 0.22	0.2%
σ_{δ_0} [%]	$\sigma_{\delta_0,m}$ [%]	$E_{\sigma_{\delta_0,m}}$
1	0.9824 ± 0.0042	1.8%
$\sigma_{t_0\delta_0}$[fs]	$\sigma_{t_0\delta_0,m}$[fs]	$E_{\sigma_{t_0\delta_0,m}}$
0.965	0.9542 ± 0.0025	1.2%

TABLE 4.6: Simulation parameters and results for the second case of plasma-based accelerators (i.e., laser-driven solution).

σ_{t_0} [fs]	$\sigma_{t_0,m}$ [fs]	$E_{\sigma_{t_0,m}}$
10	9.70860 ± 0.00097	2.9%
σ_{δ_0} [%]	$\sigma_{\delta_0,m}$ [%]	$E_{\sigma_{\delta_0,m}}$
4	4.0094 ± 0.0032	0.2%
$\sigma_{t_0\delta_0}$[fs]	$\sigma_{t_0\delta_0,m}$[fs]	$E_{\sigma_{t_0\delta_0,m}}$
0.36	0.3400 ± 0.0048	5.5%

4.2.1 Theoretical treatment

Similar to the procedure followed for the conventional layout, the analytical equations are also derived for the non-conventional layout. The contributions given from the energy chirp and spared are neglected. These assumptions are needed because otherwise, each particle will follow different trajectories while passing through the additional focusing element. In particular, firstly, the **s**pot size and the centroid with the RFD turned off are presented; later, the same quantities, including the calibration factor, are derived in the case the RFD is turned on.

RFD OFF

Similarly to what was done in Eq. 4.1, the transfer matrix to evaluate the particles vertical motion for the RFD turned off, from the RFD center to the screen can be written as

$$\begin{pmatrix} y_{s,OFF} \\ y'_{s,OFF} \end{pmatrix} = \begin{pmatrix} M_{11} & M_{12} \\ M_{21} & M_{22} \end{pmatrix} \begin{pmatrix} y_0 \\ y'_0 \end{pmatrix}, \tag{4.58}$$

The vertical spot size at the screen, with RFD off, can be calculated using Eq. 4.58

$$\begin{aligned} \sigma^2_{s,OFF} = \langle y^2_{s,OFF}\rangle - \langle y_{s,OFF}\rangle^2 = \langle M^2_{11}y^2_0\rangle + \langle M^2_{12}y^{2'}_0\rangle + \langle 2M_{11}M_{12}y_0y'_0\rangle + \\ - \langle M_{11}y_0\rangle^2 - \langle M_{12}y'_0\rangle^2 - 2\langle M_{11}y_0\rangle\langle M_{12}y'_0\rangle \end{aligned} \tag{4.59}$$

Using the property of linearity of the average and the approximation that all the particles have the same energy (i.e., small energy spread), can be written as

$$\sigma^2_{y_{s,OFF}} = M^2_{11}(\underline{\langle y^2_0\rangle - \langle y_0\rangle^2}) + M^2_{12}(\underline{\underline{\langle y'^2_0\rangle - \langle y'_0\rangle^2}}) + 2M_{11}M_{12}(\underline{\underline{\langle y_0y'_0\rangle - \langle y_0\rangle\langle y'_0\rangle}}). \tag{4.60}$$

Equations 4.60, renaming the variances and covariance highlighted in the brackets, can be rewritten as

$$\sigma^2_{y_{s,OFF}} = M^2_{11}\underline{\sigma^2_{y_0}} + M^2_{12}\underline{\underline{\sigma^2_{y'_0}}} + 2M_{11}M_{12}\underline{\underline{\sigma_{y_0y'_0}}}. \tag{4.61}$$

Similarly to Eq. 4.2, from Eq. 4.58, using the property of linearity of the average and that all the particles have the same energy, the bunch centroid can be assessed as

$$C_{y_{s,OFF}} = \langle y_{s,OFF} \rangle = \langle M_{11} y_0 \rangle + \langle M_{12} y_0' \rangle = M_{11} \langle y_0 \rangle + M_{12} \langle y_0' \rangle. \tag{4.62}$$

RFD ON

As done in Eq. 4.58, for the RFD turned on, the transfer matrix for assessing the equation of the vertical particle motion is

$$\begin{pmatrix} y_{s,ON} \\ y'_{s,ON} \end{pmatrix} = \begin{pmatrix} M_{11} & M_{12} \\ M_{21} & M_{22} \end{pmatrix} \begin{pmatrix} y_0 \\ y_0' + \Delta y_0' \end{pmatrix}, \tag{4.63}$$

where $\Delta y_0'$ is the transverse kick given from the deflector in Eq. 2.29.

Spot size assessment Also, in this case, the vertical spot size at the screen can be assessed as

$$\begin{aligned}
\sigma_{s,ON}^2 &= \langle y_{s,ON}^2 \rangle - \langle y_{s,ON} \rangle^2 = \\
&= \langle (M_{11} y_0 + M_{12} y_0' + M_{12} \Delta y_0')^2 \rangle - (\langle M_{11} y_0 + M_{12} y_0' + M_{12} \Delta y_0' \rangle)^2 = \\
&= \langle M_{11}^2 y_0^2 + M_{12}^2 y_0^{2'} + M_{12}^2 \Delta y_0^{2'} + 2 M_{11} M_{12} y_0 y_0' + 2 M_{11} M_{12} y_0 \Delta y_0' + \\
&+ 2 M_{11}^2 y_0' \Delta y_0' \rangle - [\langle M_{11} y_0 \rangle^2 + \langle M_{12} y_0' \rangle^2 + \langle M_{12} \Delta y_0' \rangle^2 + \\
&+ 2 \langle M_{11} y_0 \rangle \langle M_{12} y_0' \rangle + 2 \langle M_{11} y_0 \rangle \langle M_{12} \Delta y_0' \rangle + 2 \langle M_{12} y_0' \rangle \langle M_{12} \Delta y_0' \rangle] = \\
&= \langle M_{11}^2 y_0^2 \rangle + \langle M_{12}^2 y_0^{2'} \rangle + \langle M_{12}^2 \Delta y_0^{2'} \rangle + \langle 2 M_{11} M_{12} y_0 y_0' \rangle + \\
&+ \langle 2 M_{11} M_{12} y_0 \Delta y_0' \rangle + \langle 2 M_{11}^2 y_0' \Delta y_0' \rangle - \langle M_{11} y_0 \rangle^2 - \langle M_{12} y_0' \rangle^2 + \\
&- \langle M_{12} \Delta y_0' \rangle^2 - 2 \langle M_{11} y_0 \rangle \langle M_{12} y_0' \rangle - 2 \langle M_{11} y_0 \rangle \langle M_{12} \Delta y_0' \rangle + \\
&- 2 \langle M_{12} y_0' \rangle \langle M_{12} \Delta y_0' \rangle.
\end{aligned} \tag{4.64}$$

Using the same assumption used in Eq. 4.60 (i.e., all the particles at the same energy), from Eq. 4.64, the beam spot size with the RFD on can be written as

$$\begin{aligned}
\sigma_{s,ON}^2 &= M_{11}^2 \langle y_0^2 \rangle + M_{12}^2 \langle y_0^{2'} \rangle + M_{12}^2 \langle \Delta y_0^{2'} \rangle + 2 M_{11} M_{12} \langle y_0 y_0' \rangle + \\
&+ 2 M_{11} M_{12} \langle y_0 \Delta y_0' \rangle + 2 M_{11}^2 \langle y_0' \Delta y_0' \rangle - M_{11}^2 \langle y_0 \rangle^2 - M_{12}^2 \langle y_0' \rangle^2 + \\
&- M_{12}^2 \langle \Delta y_0' \rangle^2 - 2 M_{11} M_{12} \langle y_0 \rangle \langle y_0' \rangle - 2 M_{11} M_{12} \langle y_0 \rangle \langle \Delta y_0' \rangle + \\
&- 2 M_{12} M_{12} \langle y_0' \rangle \langle \Delta y_0' \rangle
\end{aligned} \tag{4.65}$$

Sorting and grouping the terms with the same dependence

$$\begin{aligned}
\sigma_{s,ON}^2 &= M_{11}^2 \left(\langle y_0^2 \rangle - \langle y_0 \rangle^2 \right) + M_{12}^2 \left(\langle y_0'^2 \rangle - \langle y_0' \rangle^2 \right) + M_{12}^2 \left(\langle \Delta y_0'^2 \rangle - \langle \Delta y_0' \rangle^2 \right) + \\
&+ 2 M_{11} M_{12} \left(\langle y_0 y_0' \rangle - \langle y_0 \rangle \langle y_0' \rangle \right) + 2 M_{11} M_{12} \left(\langle y_0 \Delta y_0' \rangle - \langle y_0 \rangle \langle \Delta y_0' \rangle \right) + \\
&+ 2 M_{12}^2 \left(\langle y_0' \Delta y_0' \rangle - \langle y_0' \rangle \langle \Delta y_0' \rangle \right).
\end{aligned} \tag{4.66}$$

From Eq. 4.66, substituting the highlighted terms in the brackets with the respective variance and covariance, it can be written

$$\begin{aligned}\sigma^2_{s,ON} = M^2_{11}\,\sigma^2_{y_0} + M^2_{12}\,\sigma^2_{y'_0} + M^2_{12}\,\sigma^2_{\Delta y'_0} + \\ + 2M_{11}M_{12}\,\sigma_{y_0 y'_0} + 2M_{11}M_{12}\,\sigma_{y_0 \Delta y'_0} + 2M^2_{12}\,\sigma_{y'_0 \Delta y'_0}.\end{aligned} \tag{4.67}$$

Taylor approximation The results obtained in Eq. 4.67 can be further simplified. In particular, specifying the deflector's transverse kick and thus, the variance and the covariance that involve it. From from Eqs. 2.29 and 2.30, the therms $\Delta y'_0$ can be rewritten as

$$\Delta y'_0 = \frac{V_t}{E_0} k z_0 \cos(\varphi) + \frac{V_t}{E_0}\sin(\varphi). \tag{4.68}$$

The variance in the third term of Eq. 4.67 can be rewritten as

$$\begin{aligned}\sigma_{\Delta y'_0} &= \langle\left(\frac{V_t}{E_0}k\cos(\varphi)z_0 + \frac{V_t}{E_0}\sin(\varphi)\right)^2\rangle - \langle\frac{V_t}{E_0}k\cos(\varphi)z_0 + \frac{V_t}{E_0}\sin(\varphi)\rangle^2 = \\ &= \left(\frac{V_t}{E_0}k\cos(\varphi)\right)^2\langle z_0^2\rangle + \cancel{\left(\frac{V_t}{E_0}\sin(\varphi)\right)^2} + 2\left(\frac{V_t}{E_0}\right)^2 \cancel{k\cos(\varphi)\sin(\varphi)\langle z_0\rangle} + \\ &- \left(\frac{V_t}{E_0}k\cos(\varphi)\right)^2\langle z_0\rangle^2 - \cancel{\left(\frac{V_t}{E_0}\sin(\varphi)\right)^2} - 2\left(\frac{V_t}{E_0}\right)^2 \cancel{k\cos(\varphi)\sin(\varphi)\langle z_0\rangle} = \\ &= \left(\frac{V_t}{E_0}k\cos(\varphi)\right)^2(\langle z_0^2\rangle - \langle z_0\rangle^2) = \left(\frac{V_t}{E_0}k\cos(\varphi)\right)^2\sigma^2_{z_0}.\end{aligned} \tag{4.69}$$

The covariance in the fifth term of Eq. 4.67 can be rewritten as

$$\begin{aligned}\sigma_{y_0\Delta' y_0} &= \langle y_0\left(\frac{V_t}{E_0}k\cos(\varphi)z_0 + \frac{V_t}{E_0}\sin(\varphi)\right)\rangle - \langle y_0\rangle\langle\frac{V_t}{E_0}k\cos(\varphi)z_0 + \frac{V_t}{E_0}\sin(\varphi)\rangle = \\ &= \frac{V_t}{E_0}k\cos(\varphi)\langle y_0 z_0\rangle + \cancel{\frac{V_t}{E_0}\sin(\varphi)\langle y_0\rangle} - \frac{V_t}{E_0}k\cos(\varphi)\langle y_0\rangle\langle z_0\rangle - \cancel{\frac{V_t}{E_0}\sin(\varphi)\langle y_0\rangle} = \\ &= \frac{V_t}{E_0}k\cos(\varphi)(\langle y_0 z_0\rangle - \langle y_0\rangle\langle z_0\rangle) = \frac{V_t}{E_0}k\cos(\varphi)\sigma_{y_0 z_0}.\end{aligned} \tag{4.70}$$

With the same calculation, the covariance in the sixth term of Eq. 4.67 can be written as

$$\sigma_{y'_0\Delta' y_0} = \frac{V_t}{E_0}k\cos(\varphi)\sigma_{y'_0 z_0}. \tag{4.71}$$

Finally, substituting Eqs. 4.69, 4.70, and 4.71 in Eq. 4.67

$$\begin{aligned}\sigma^2_{s,ON} = \underline{M^2_{11}\sigma^2_{y_0}} + \underline{M^2_{12}\sigma^2_{y'_0}} + M^2_{12}\left(\frac{V_t}{E_0}k\cos(\varphi)\right)^2\sigma^2_{z_0} + \\ + \underline{2M_{11}M_{12}\sigma_{y_0 y'_0}} + 2M_{11}M_{12}\frac{V_t}{E_0}k\cos(\varphi)\sigma_{y_0 z_0} + 2M^2_{12}\frac{V_t}{E_0}k\cos(\varphi)\sigma_{y'_0 z_0}.\end{aligned} \tag{4.72}$$

The underlined terms in Eq. 4.72 are the vertical spot size at the screen with RFD off, in Eq. 4.61. As a consequence, Eq. 4.72 can be rewritten as

$$\begin{aligned}\sigma^2_{s,ON} = \sigma^2_{s,OFF} + M^2_{12}\left(\frac{V_t}{E_0}k\cos(\varphi)\right)^2\sigma^2_{z_0} + \\ + 2M_{11}M_{12}\frac{V_t}{E_0}k\cos(\varphi)\sigma_{y_0 z_0} + 2M^2_{12}\frac{V_t}{E_0}k\cos(\varphi)\sigma_{y'_0 z_0}.\end{aligned} \tag{4.73}$$

Centroid assessment The calibration factor can be introduced, as done in Eq. 4.23, with the same crucial physical meaning shown in Eq. 4.52, it is useful to start from the equation of the vertical bunch centroid. Repeating the same step of Eq. 4.6, the centroid when the RFD is turned on can be written as

$$C_{y_{s,ON}}(\varphi) = \langle y_s\rangle = \langle M_{11}y_0\rangle + \langle M_{12}y'_0\rangle + \langle M_{12}\Delta' y_0\rangle, \tag{4.74}$$

under the assumption that all the particles have the same energy it becomes

$$\begin{aligned}C_{y_{s,ON}}(\varphi) &= M_{11}\langle y_0\rangle + M_{12}\langle y'_0\rangle + \langle M_{12}\frac{V_t}{E_0}kz_0\cos(\varphi)z_0 + M_{12}\frac{V_t}{E_0}\sin(\varphi)\rangle = \\ &= M_{11}\langle y_0\rangle + M_{12}\langle y'_0\rangle + M_{12}\frac{V_t}{E_0}kz_0\cos(\varphi)\langle z_0\rangle + M_{12}\frac{V_t}{E_0}\sin(\varphi) = \\ &= \underline{M_{11}\langle y_0\rangle} + \underline{M_{12}\langle y'_0\rangle} + M_{12}\frac{V_t}{E_0}k\cos(\varphi)\langle z_0\rangle + M_{12}\frac{V_t}{E_0}\sin(\varphi).\end{aligned} \tag{4.75}$$

The underlined terms in Eq. 4.75 are the centroid contributions when the RFD is turned off in Eq. 4.62. As a consequence, Eq. 4.75 can be rewritten as

$$C_{y_{s,ON}}(\varphi) = C_{y_{s,OFF}} + M_{12}\frac{V_t}{E_0}k\cos(\varphi)\langle z_0\rangle + M_{12}\frac{V_t}{E_0}\sin(\varphi). \tag{4.76}$$

Defining the calibration factor, K_{CAL}, as

$$K_{CAL}(\varphi) = 2\pi f_{RF}M_{12}C_{RFD0a}\cos(\varphi), \tag{4.77}$$

also for the non-conventional layout, the calibration factor can be directly calculated by measuring the bunch centroid as reported in Eq. 4.52.

Substituting Eq. 4.77 in Eq. 4.73 the spot size with the RFD on can be written as

$$\sigma^2_{y_{s,ON}}(\varphi) = \sigma^2_{y_{s,OFF}} + K^2_{CAL}(\varphi)\sigma^2_{t_0} + 2M_{11}K_{CAL}(\varphi)\sigma_{y_0 t_0} + 2M_{12}K_{CAL}(\varphi)\sigma_{y'_0 t_0}. \tag{4.78}$$

The Eqs. 4.77, 4.61, and 4.78 are a general expression of the Eq. 4.23,4.3, and 4.48, respectively. In the case of conventional layout $M_{11} = 1$ and $M_{12} = L_t$. Moreover, also in the non-conventional layout, the terms due to the correlations between the vertical position divergence and the longitudinal divergence can be

canceled by averaging two measurements in phase opposition

$$\overline{\sigma_{y_{s,ON}}}^2(\varphi) = \frac{\sigma^2_{y_{s,ON}}(\varphi) + \sigma^2_{y_{s,ON}}(\varphi+\pi)}{2} = \sigma^2_{y_{s,OFF}} + K^2_{CAL}(\varphi)\sigma^2_{t_0}. \tag{4.79}$$

The term $\overline{\sigma_{y_{s,ON}}}^2$ is equal to $\sigma^2_{y_{s,ON}}$ in absence of correlations between the vertical and longitudinal planes. For reader convenience, as for the conventional layout, the terms $\overline{\sigma_{y_{s,on}}}(\varphi)$ and $K_{cal}(\varphi)$ are often indicated as $\overline{\sigma_{y_{s,on}}}$ and K_{cal}, respectively; implicitly assuming their dependence from the RFD phase.

4.2.2 Measurement methods

From Eq. 4.79, the formula for the bunch length can be written in the same form as in literature [209]

$$\sigma_{t_0} = \frac{\sqrt{\overline{\sigma_{y_{s,ON}}}^2 - \sigma^2_{y_{s,OFF}}}}{|K_{CAL}(\varphi)|}. \tag{4.80}$$

In Eq. 4.80, the measured values are $\overline{\sigma_{y_{s,ON}}}$ and $\sigma_{y_{s,OFF}}$, while the measurand is σ_{t_0}. If the values of $\sigma_{y_{s,OFF}}$ and $\overline{\sigma_{y_{s,ON}}}$ are too close, the information on the m**e**asurand could be lost in the uncertainty or in the resolution of the measurement.

From Eqs. 4.77, 4.78, and 4.79, some preliminary points can be underline

- the standard model of the measurement production, in Fig. 4.5, can be used;
- a calibration factor can be defined with the same meaning of the conventional layout (i.e., including the variation of the centroid on the screen);
- the non-conventional layout does not introduce any deterministic error source in the measurement;
- the possibility of removing the correlation effects (i.e., $\sigma_{y'_0 t_0}$ and $\sigma_{y_0 t_0}$) is preserved. It can be achieved carrying out two different measurements of $\sigma_{y_{s,ON}}$ in phase opposition (at φ and $\varphi+\pi$), and then evaluating the average between their squared values [213, 214];
- thanks to the dependence of $\sigma_{y_{s,ON}}$ and $\sigma_{y_{s,OFF}}$ on the focal length, these quantities can be optimized over a wider range of beam parameters. Allowing an improvement in the measurement performance (i.e., improve the resolution and reduce uncertainty).

However, driven by the dependence of the measurement from the focal length, some critical value preventing the feasibility of the measurements is identified. This issue needs to be taken into account to perform a correct measurement procedure.

Besides, the additional advantage of measuring the correlations is obtained. The correlation terms can be measured from Eq. 4.78 by assessing the difference between the two $\sigma_{y_{s,ON}}$ in phase opposition

$$\tau = \sigma^2_{y_{s,ON}}(\varphi) - \sigma^2_{y_{s,ON}}(\varphi+\pi) = 4M_{11}K_{CAL}(\varphi)\sigma_{y_0 t_0} + 4M_{12}K_{CAL}(\varphi)\sigma_{y'_0 t_0}, \tag{4.81}$$

TABLE 4.7: Range of the CLEAR main parameters.

Parameters	Value/Range
Energy ($\langle E_0 \rangle$) [MeV]	60 – 220
Bunch charge (q) [pC]	10 – 2000
σ_{t_0} [ps]	1 – 10
ϵ_{xy} [nm]	100
Energy Spread (δ_0)	<5%
$\beta_{x,y}$ [m]	0.5 – 40
$\alpha_{x,y}$	-10 – 10
L_q [m]	0.226
L_{RFD} [m]	0.116
f_{RF} [GHz]	2.9985
V_t [MV]	0.5; 1.6; 4
$\lvert f_{min} \rvert$ [m]	0.29
$\sigma_{y_{res}}$ [µm]	25
Field Of View (FOV) [cm]	8x8
f^* [m]	0.44
Macro particles	500,000

where τ is the sum of the correlation terms, each one multiplied by known factors. In the non-conventional layout, the two correlation terms have different dependence on the focal length of the quadrupole. Thus their individual effects can be isolated and quantified. In fact, the terms M_{11} is multiplied by the correlation terms $\sigma_{y_0 t_0}$, and the term M_{12} is multiplied by the correlation terms $\sigma_{y'_0 t_0}$. This advantage is not present in the case of the conventional layout [215].

The non-conventional layout opens new opportunities with a substantial impact on the accelerators physics community.

4.2.3 CLEAR case study

As anticipated in Sec. 2.3, the CLEAR machine is a particularly suitable case study for the bunch length, due to the different diagnostics devoted to monitoring this parameter [18]. Moreover, in CLEAR, a quadrupole triplet is installed between the RFD [17] and the screen. It can be turned off and on to compare the performances of the conventional and non-conventional layout.

In a conservative assumption, the main parameters of the CLEAR accelerator (i.e., Twiss parameters at the entrance of the RFD, beam geometrical emittance, energy, energy spread, charge, and bunch length), the acquisition system used for the measurements (i.e., the acquisition system resolution and the field of view), the RFD characteristics (i.e., deflecting voltage and frequency), and the beamline characteristics (e.g., the maximum quadrupole power, the quadrupole sensitivity, and the distances) are summarized in Tab. 4.7. The quantity f_{min} is the minimum focal length which depends on the beam stiffness and the type of quadrupole (the quadrupole parameters correspond to the Scanditronix QL3 magnets used

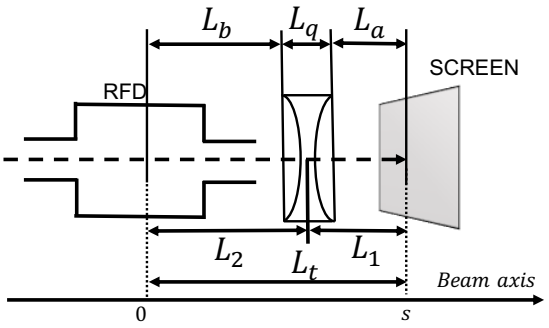

FIGURE 4.14: The layout with a vertical focusing element installed between the RFD and the screen [16].

in CLEAR [216]). For the values in Tab. 4.7, the beam energy of $220\,\mathrm{MeV}$ (i.e., the highest achievable) was assumed.

The focusing and defocusing quadrupole positions are different because they correspond to two different quadrupoles which are physically installed next to each other. As the presented studies were performed as a part of different experimental campaigns, the beam and RFD characteristics are not identical. Furthermore, the beamline was modified between the experimental campaigns in order to upgrade the EOS experiment (explained in Sec. 2.3.2); because of this, the magnet position changes between studies. In the simulations, the distances, beam, and RFD characteristics agree with the experimental case they are compared to.

Single quadrupole case

In the case of a single thick focusing quadrupole, the transport matrix $\underline{\underline{M}}$, between the RFD and the screen, is obtained from the multiplication of the matrices

$$\begin{aligned}\underline{\underline{M}} &= M_{\mathrm{drift_a}}\, M_{\mathrm{quad}}\, M_{\mathrm{drift_b}} = \\ &= \begin{bmatrix} 1 & L_a \\ 0 & 1 \end{bmatrix} \begin{bmatrix} \cos\left(\sqrt{K}L_q\right) & \frac{1}{\sqrt{K}}\sin\left(\sqrt{K}L_q\right) \\ -\sqrt{K}\sin\left(\sqrt{K}L_q\right) & \cos\left(\sqrt{K}L_q\right) \end{bmatrix} \begin{bmatrix} 1 & L_b \\ 0 & 1 \end{bmatrix},\end{aligned} \tag{4.82}$$

where K is the focusing strength of the quadrupoles. The quantities L_a, L_b, and L_q are the length of the drift space between the end of the quadrupole and the screen, the length of the drift space between the RFD center the beginning of the quadrupole, and the length of the quadrupole, respectively (as shown in Fig. 4.14). In case of $K > 0$, Eq. 4.82 describes a horizontally focusing quadrupole, while $K < 0$, Eq. 4.82 describes a horizontally defocusing quadrupole (in this case, the trigonometric functions become hyperbolic functions).

It is convenient, in order to make some considerations, to use the well-known thin lens approximation [59]. As a consequence, the matrix $\underline{\underline{M}}$ becomes

$$\underline{\underline{M}} = M_{\mathrm{drift_1}}\, M_{\mathrm{quad-thin}}\, M_{\mathrm{drift_2}} = \begin{bmatrix} 1 & L_1 \\ 0 & 1 \end{bmatrix} \begin{bmatrix} 1 & 0 \\ -\frac{1}{f} & 1 \end{bmatrix} \begin{bmatrix} 1 & L_2 \\ 0 & 1 \end{bmatrix}, \tag{4.83}$$

where f is the quadrupole focal length, L_1 is the distance between the quadrupole center and the screen (i.e., $L_1 = L_a + \frac{L_q}{2}$), and L_2 is the distance between the RFD center and the quadrupole center (i.e., $L_2 = L_b + \frac{L_q}{2}$). The relation between the focusing strength and the focal length is

$$f = \frac{1}{KL_q}. \tag{4.84}$$

For a focusing magnet in the plane of interest (i.e., vertical), f is positive, while in the same plane for a defocusing magnet, f is negative.

With this approximation, the terms M_{11} and M_{12} are

$$M_{11} = 1 - \frac{L_1}{f} \quad \text{and} \tag{4.85}$$

$$M_{12} = (L_1 + L_2) - \frac{L_1 L_2}{f}. \tag{4.86}$$

In the non-conventional layout, the term M_{12} is present in K_{CAL} (Eq. 4.77), which as a consequence depends on the focal length of the quadrupole (from Eq. 4.86). Also, $\sigma_{y_{s,OFF}}$ depends on the focal length (Eq. 4.61). Therefore, it cannot be decorrelated from the deflecting power as in the conventional layout.

Another result that comes from Eq. 4.86 is the possibility to make M_{12} zero, and consecutively also $K_{CAL}(\varphi)$ (from Eq. 4.77). It happens when the focal length is equal to

$$f^* \equiv \frac{L_1 L_2}{L_1 + L_2}. \tag{4.87}$$

From a physical point of view, operating with such a value of focal length means that the RFD increases the bunch spot size on the screen by the same amount as the quadrupole is squeezing it. In other words, there is a phase advance of π between the RFD center and the screen. Therefore, for this value of focal length, the measurement cannot be carried out.

All the derived equations and considerations can be extended for a general configuration such as a doublet, triplet, or FOcusing/DefOcusing (FODO) cell.

4.2.4 Validation using simulations

In this section, the validation of the theory derived so far is reported. Firstly the equations are validated using the simulation tracking code ELEGANT (introduced in Sec.4.1.3), and later the experiments are carried out for assessing the validity of the proposed measurement methods. As for the conventional layout, the uncertainties reported represents a 1-sigma interval.

Measurement method

The comparisons between theoretical values (solid line without quadrupole, and dashed line with quadrupole) and the simulation results (stars without quadrupole, and dots with quadrupole) for K_{CAL}, $\sigma_{y_{s,OFF}}$, and $\sigma_{y_{s,ON}}$ are shown in Fig. 4.15 (A),

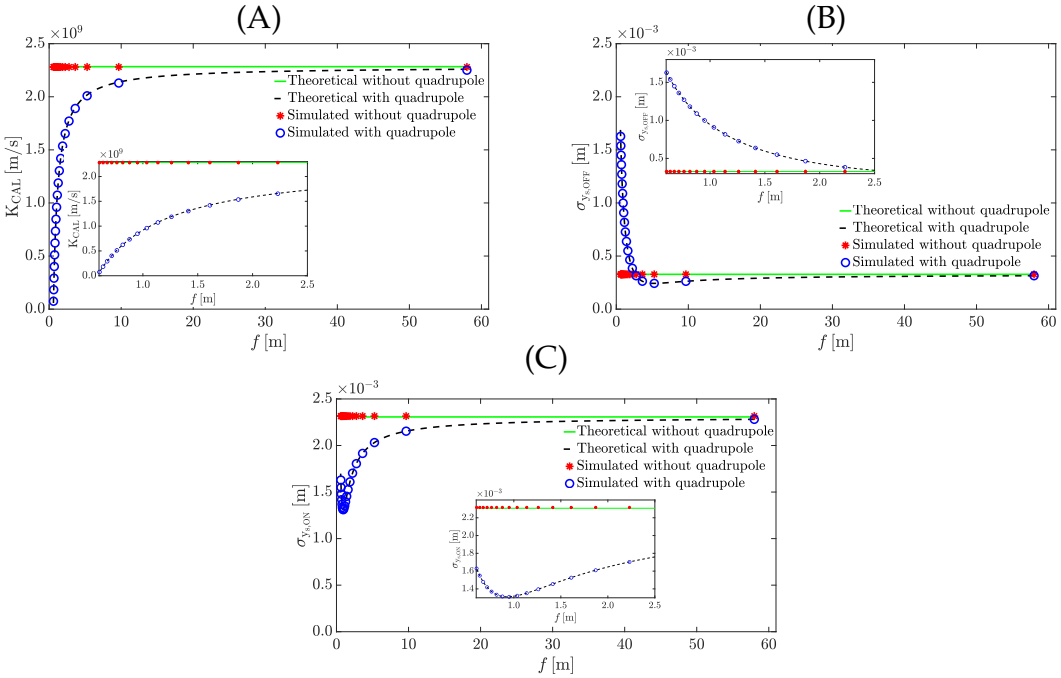

FIGURE 4.15: The comparison between theoretical values (solid line without quadrupole, and dashed line with quadrupole) and simulation results (stars without quadrupole, and dots with quadrupole) for: (A) K_{CAL} (Eq. 4.77), (B) $\sigma_{y_{s,OFF}}$ (Eq. 4.61), and (C) $\sigma_{y_{s,ON}}$ (Eq. 4.78), versus the focal length (zoom at low f on the side) [16].

TABLE 4.8: Parameters adopted in the simulations to validate the theoretical derivation.

$\langle E_0 \rangle = 220\,\text{MeV}$	$\delta_0 = 3\,\%$	$q = 500\,\text{pC}$	$\sigma_{t_0} = 1\,\text{ps}$
$\epsilon_{y_0} = 10\,\text{nm}$	$\beta_{y_0} = 10\,\text{m}$	$\alpha_{y_0} = 3.0$	$L_{RFD} = 0.1160\,\text{m}$
$f_{RF} = 2.9985\,\text{GHz}$	$V_t = 10\,\text{MV}$	$L_b = 0.8680\,\text{m}$	$L_q = 0.2260\,\text{m}$
$L_a = 1.575\,\text{m}$	$\sigma_{y_{res}} = 25\,\mu\text{m}$	FOV $= 8\,\text{cm}$	Macro particles $= 500,000$

(B), and (C) respectively. The dashed lines and the dots are used for the conventional layout, while the solid lines and the stars are used for the non-conventional layout.

For the conventional layout, the values of the K_{cal}, σ_{off}, and σ_{on} do not depend on the focal length, owing to the absence of the quadrupole. Conversely, for the non-conventional layout, the values change with the focal length of the quadrupole. For this reason, the optimum resolution, in the conventional layout obtained focusing the beam on the screen with the optics upstream the RFD, is not necessarily obtained by minimizing the beam size on the screen with the RFD off, like in the conventional layout.

The parameters used in the simulations are reported in Tab. 4.8.

For the sake of simplicity, only the case of the focusing quadrupole is reported. The minimum focal length used in the simulations is f^*, derived from Eq. 4.87. Its

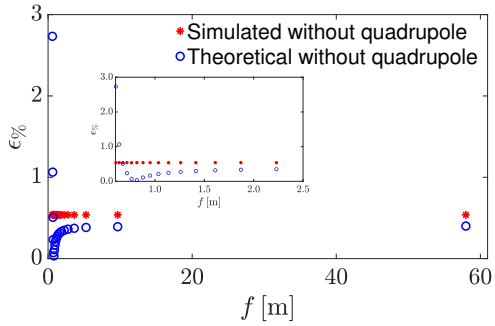

FIGURE 4.16: The relative error (Eq. 4.88) from the simulations (stars without quadrupole and circles with quadrupole) on the assessment of the bunch length versus the focal length [16].

numerical value is shown in the row before the last of Tab. 4.7. The Twiss parameter used (Tab. 4.8) position the waist after the screen. All the curves representing the non-conventional layout quantities tend to the curve of the conventional layout while increasing the focal length. This can be explained from Eqs. 4.77, 4.61, and 4.78; that contains the terms M_{12} and/or M_{11}. When f approaches infinity, these terms tend to their value in the conventional layout. Consequently, as known from the theory, switching off the quadrupole is equivalent to let f approach infinity. In this configuration, the maximum calibration factor is obtained in the absence of the focusing quadrupole.

In Fig. 4.15 (B), all the points of the solid line (i.e., $\sigma_{y_{s,OFF}}$ in the non-conventional layout) above the dashed line (i.e., $\sigma_{y_{s,off}}$ in the conventional layout) correspond to a condition of over-focusing. In such a condition, the quadrupole makes the beam larger on the screen than without the quadrupole. On the other hand, there are values of focal length that make $\sigma_{y_{s,OFF}}$ smaller than the conventional layout value. The minimum of $\sigma_{y_{s,OFF}}$ corresponds to the focal length that imposes the waist at the screen position. In the considered range, all the values of $\sigma_{y_{s,ON}}$ of the non-conventional layout are smaller than the values of the conventional layout for all the focal lengths, as seen in Fig. 4.15 (C).

A satisfying agreement between the theory and the simulation is achieved: for K_{CAL}, σ_{OFF}, and σ_{ON}, the maximum difference is less than 0.6%. From Eq. 4.80 in order to have a good measurements a relatively large difference between $\sigma_{y_{s,ON}}$ and $\sigma_{y_{s,OFF}}$ is needed. Thanks to the flexibility added by additional focusing elements, it is easier to achieve these conditions. A simulation is performed at $f = f^*$ (as defined in Eq. 4.87), by imposing $\sigma_{y_{s,ON}} = \sigma_{y_{s,OFF}}$. In this case, the bunch length cannot be measured because no information on the measurand can be obtained from the bunch's size. The relative error, between the theoretical σ_{t_0} and the simulated $\sigma_{t_{0,m}}$ values, using Eq. 4.80, is defined as

$$\epsilon_{\%} = 100 \cdot \frac{|\sigma_{t_0} - \sigma_{t_{0,m}}|}{\sigma_{t_0}}. \tag{4.88}$$

The error is overall smaller than 0.5%, and it is shown in Fig. 4.16.

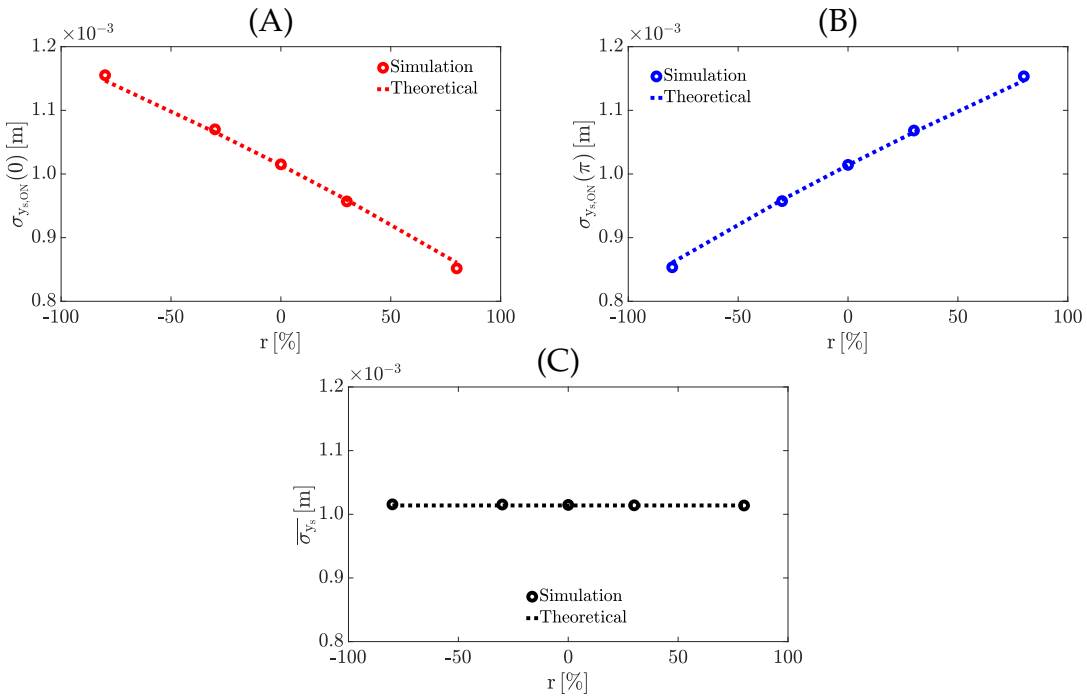

FIGURE 4.17: In (A), $\sigma_{y_{s,ON}}(0)$, in (B) $\sigma_{y_{s,ON}}(\pi)$, and in (C) $\overline{\sigma_{y_{s,ON}}}$ versus r. The theoretical results (dashed lines) are compared with the simulation results (dots). The theoretical results for (A) and (B) are from Eq. 4.78, and for (C) from Eq. 4.79 [16].

Cancellation of correlations

The correlations between the longitudinal particle positions and the position, divergence in the vertical plane are analyzed. In particular, the correlation terms of Eq. 4.78 (proportional to $\sigma_{y_0 t_0}$ and $\sigma_{y'_0 t_0}$) are compared with the simulation results. Furthermore, the cancellation of the correlation terms (Eq. 4.79) is validated with simulations in Figs. 4.17.

From Eq. 2.6, the correlations can be written as

$$\begin{aligned} \sigma_{y_0 t_0} &= r_{y_0 t_0} \sigma_{y_0} \sigma_{t_0} \quad \text{and} \\ \sigma_{y'_0 t_0} &= r_{y'_0 t_0} \sigma_{y'_0} \sigma_{t_0}, \end{aligned} \tag{4.89}$$

where $r_{y_0 t_0}$ and $r_{y'_0 t_0}$ are the correlation factors between the longitudinal positions and the vertical positions, and between the longitudinal positions and the vertical divergences, respectively.

Simulations of the beam spot size with the RFD turned on at two different RF phases ($0\,\mathrm{rad}$ and $\pi\,\mathrm{rad}$), and varying the correlation coefficients $r_{y_0 t_0}$ and $r_{y'_0 t_0}$, are shown in Fig. 4.17 (A) and (B), respectively. In the scan, the correlation coefficients are equal, and the axis notation is simplified correspondingly: $r_{yt} = r_{y't} = r$. Five correlation coefficients are chosen (-80%, -30%, 0%, 30%, and 80%). All the simulation parameters are kept the same reported in Tab. 4.8. The simulations were repeated with $\alpha_0 = -3$, which produced identical results.

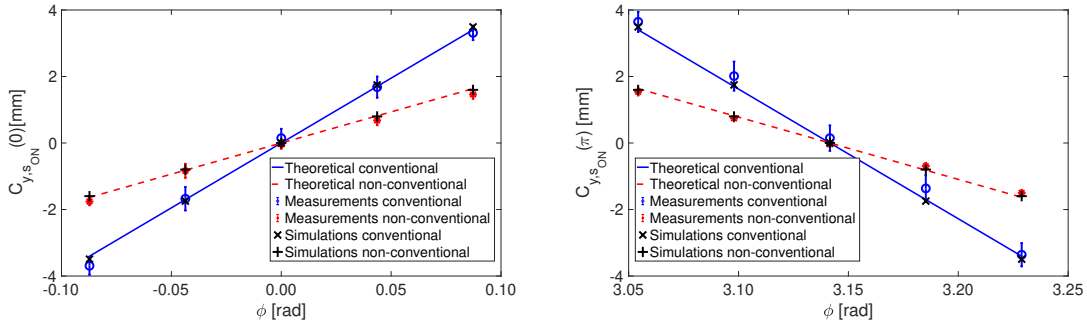

(A) (B)

FIGURE 4.18: The vertical centroid positions ($C_{y_{s,ON}}$) versus RFD phase in conventional and non-conventional layout around $0\,\mathrm{rad}$ and $\pi\,\mathrm{rad}$ in (A) and (B), respectively. The measurements (circles and stars for conventional and non-conventional layout, respectively), the theoretical values (solid and dashed lines for conventional and non-conventional layout), and the simulation points (crosses and plus signs for conventional and non-conventional, layout respectively) are compared [16].

In Fig. 4.17(A) and (B), $\sigma_{y_{s,ON}}(0)$ and $\sigma_{y_{s,ON}}(\pi)$ are plotted respectively (theoretical results from Eq. 4.78 with dashed lines and simulation results with dots). The value of $\sigma_{y_{s,ON}}(0)$ and $\sigma_{y_{s,ON}}(\pi)$ are only equal when the correlation coefficients are zero. In Fig. 4.17 (C), the average of the squared value between $\sigma_{y_{s,ON}}(\pi)$ and $\sigma_{y_{s,ON}}(0)$ (i.e., $\overline{\sigma_{y_{s,ON}}}$ from Eq. 4.79) is shown. A satisfying agreement between theoretical values and simulation results (error less than a percent) is experienced.

4.2.5 Experimental validation

In this section, the results of the experimental validation, supported with simulation results, are shown for the conventional and non-conventional layout. The experimental campaign consists of two test sessions, with the quadrupole off and on, corresponding to both the conventional and non-conventional layouts. In the same beam conditions, it is needed to verify that if compatible values of bunch length are measured. Moreover, it is needed to compare the theoretical, simulation, and measurement results for the vertical centroid position versus the RF phase.

The explored RF phase range is $0.174\,\mathrm{rad}$. The current in the quadrupole is $58\,\mathrm{A}$, corresponding to a focal length of $1\,\mathrm{m}$, chosen intentionally far from the value of f^* (from Eq. 4.87). When the quadrupole is off (conventional layout), $\sigma_{y_{s,off}} = 183\,\mu\mathrm{m}$, while when on (non-conventional layout), $\sigma_{y_{s,OFF}} = 147\,\mu\mathrm{m}$. In Fig. 4.18 (A) and (B), the vertical centroid positions ($C_{y_{s,ON}}$) versus the RFD phase is shown around $0\,\mathrm{rad}$ and $\pi\,\mathrm{rad}$, respectively, for both the conventional and non-conventional layout. The measurements are pointed out with markers (circles and stars for conventional and non-conventional layout, respectively), the theoretical values with lines (solid and dashed lines for conventional and non-conventional layout, respectively), and the simulations with points (crosses and

TABLE 4.9: Parameters adopted in the simulations to validate the measurement results.

$\langle E_0 \rangle = 200\,\mathrm{MeV}$	$\delta_0 = 2\,\%$	$q = 80.0\,\mathrm{pC}$	$\sigma_{t_0} = \mathrm{NA}$
$\epsilon_{y_0} = 10\,\mathrm{nm}$	$\beta_{y_0} = 7.3\,\mathrm{m}$	$\alpha_{y_0} = 1.4$	$L_{RFD} = 0.1160\,\mathrm{m}$
$f_{RF} = 2.9985\,\mathrm{GHz}$	$V_t = 3.9\,\mathrm{MV}$	$L_b = 0.6870\,\mathrm{m}$	$L_q = 0.2260\,\mathrm{m}$
$L_a = 1.087\,\mathrm{m}$	$\sigma_{y_{res}} = 25\,\mu\mathrm{m}$	$\mathrm{FOV} = 8\,\mathrm{cm}$	$\mathrm{Macro\ particles} = 500,000$

plus signs for conventional and non-conventional layout, respectively). The one sigma repeatability bar for each RF phase is the standard deviation of 10 measurements. In parameters while performing the measurement campaign are reported in Tab. 4.9. The K_{CAL} can be evaluated in both cases from the data shown in Figs. 4.18, using Eq. 4.52, and for the conventional layout $K_{cal} = (7.37 \pm 0.15) \cdot 10^{11}\mathrm{m/s}$, while for the non-conventional layout, $K_{CAL} = (3.30 \pm 0.10) \cdot 10^{11}\mathrm{m/s}$.

Figures 4.18 highlights a satisfying agreement between measurements, simulations, and theory (the maximum absolute error, between measurements and theory, is in the range between $0.019\,\mathrm{mm}$ and $0.34\,\mathrm{mm}$). Furthermore, the bunch length evaluated using Eq. 4.80 is the same, within experimental errors, for both configurations $(1.9 \pm 0.3)\mathrm{ps}$. All the results are consistent with the theory prediction.

4.3 Resolution enhancement

In this section, a detailed study on the resolution is performed, by comparing the achievable performance in both the layouts. First, the theoretical derivation, valid for both the layouts, is presented. Then, the validation, performed on the CLEAR case study and with the ELEGANT tracking code (introduced in Sec.4.1.3), is analyzed.

4.3.1 Theoretical treatment

The measurement system resolution can be evaluated by assessing the smallest measurable difference, between $\overline{\sigma_{y_{s,ON}}}$ and $\sigma_{y_{s,OFF}}$. The smallest difference between $\sigma_{y_{s,OFF}}$ and $\sigma_{y_{s,ON}}$ is the so-called acquisition system resolution, $\pm\sigma_{y_{res}}$, which is determined by the imaging methodology (i.e., the screen technology, the camera used, and the measurement setup). The minimum value reachable from $\overline{\sigma_{y_{s,ON}}}$ can be written as

$$\overline{\sigma^2_{y_{s,ON}}}^{\,min} = \frac{\sigma^2_{y_{res}} \pm 2\sigma_{y_{res}}\sigma^2_{y_{s,OFF}} + \sigma^2_{y_{s,OFF}} + \sigma^2_{y_{res}} \pm 2\sigma_{y_{res}}\sigma^2_{y_{s,OFF}} + \sigma^2_{y_{s,OFF}}}{2}. \quad (4.90)$$

Using Eq. 4.90, under a conservative assumption, with Eq. 4.80, the measurement system resolution can be written as

$$\sigma_{t_{res}} = \frac{\sqrt{\sigma^2_{y_{res}} + 2\sigma_{y_{res}}\sigma_{y_{s,OFF}}}}{|K_{CAL}|}. \quad (4.91)$$

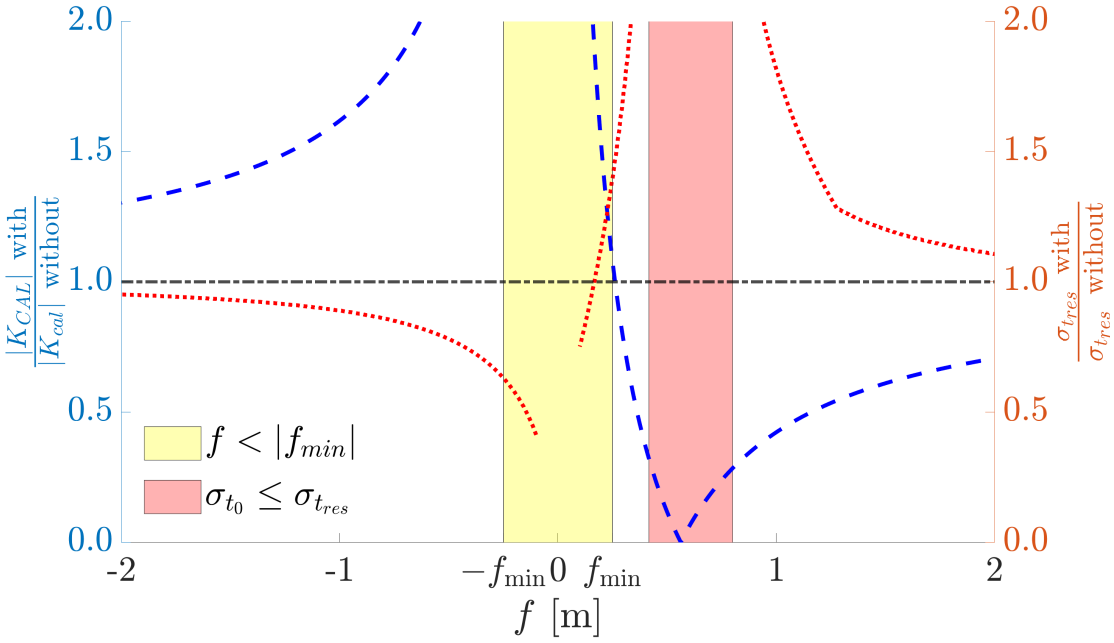

FIGURE 4.19: On the left axis, the calibration factors ratio (dashed blue line), while on the right axis, the measurement system resolutions ratio (dotted red line), both versus the additional focusing element's focal length.

Equation 4.91 is valid both in the conventional (i.e., $\sigma_{y_{s,off}}$ and K_{cal}) and in the non-conventional (i.e., $\sigma_{y_{s,OFF}}$ and K_{CAL}) layout.

In the conventional layout, $\sigma_{t_{res}}$, can be improved by: (i) increase the K_{cal}, acting on the characteristics of the deflecting structure (i.e., f_{RF} and/or V_t) or (ii) modify the characteristics of the beamline (i.e., L_t and/or E_0). Often the latter quantities are not modifiable and are not chosen to enhance the measurement performance. For this reason, the improvements of the deflecting structure have been pursued during the last years. Firstly, structures with higher V_t [217] have been designed and lately structure working at higher frequencies (i.e., X-band deflecting structures [218]) have been developed. In the non-conventional, thanks to the additional focusing elements, there are additional degrees of freedom (e.g., the focal length or the additional focusing element position).

In Fig. 4.19 the ratio of the achievable values of K_{CAL} (dashed blue line) and $\sigma_{t_{res}}$ (dotted red line) with and without the additional focusing element are reported in order to compare the two layouts. For the layout without the additional focusing element, the most suitable Twiss parameters for enhancing the resolution of bunch length measurement are used. The same procedure is used, at each focal length, for the layout with the additional focusing element. For the comparisons in Fig. 4.19 the parameters in Tab. 4.10 are used. As can be seen from the second row of Tab. 4.10, the whole ranges of Twiss parameters achievable in CLEAR were investigated to identify the parameters that improve the measurement system resolution. These parameter ranges are shared between many S-band high brightness photoinjector based accelerators.

TABLE 4.10: Parameters adopted in the simulations to validate the resolution enhancement study.

$\langle E_0 \rangle = 203\,\mathrm{MeV}$	$\delta_0 = 2\,\%$	$q = 200\,\mathrm{pC}$	$\sigma_{t_0} = 1ps$
$\epsilon_{y_0} = 10\,\mathrm{nm}$	$\beta_{y_0} = 0.5 - 40\,\mathrm{m}$	$\alpha_{y_0} = -10 - 10$	$L_{RFD} = 0.1160\,\mathrm{m}$
$f_{RF} = 2.9985\,\mathrm{GHz}$	$V_t = 0.97\,\mathrm{MV}$	$L_b = 0.7870\,\mathrm{m}$	$L_q = 0.2260\,\mathrm{m}$
$L_a = 1.687\,\mathrm{m}$	$\sigma_{y_{res}} = 25\,\mu\mathrm{m}$	$\mathrm{FOV} = 8\,\mathrm{cm}$	Macro particles $= 500,000$

In Fig. 4.19, two vertical axes are defined both versus the focal length f of the additional focusing element. The left axis is reporting the ratio between the calibration factors of the non-conventional layout (with the additional focusing element) over the one of the conventional layout(without the additional focusing element). The right axis is reporting the ratio between the $\sigma_{t_{res}}$ in the same order (i.e., with the additional focusing element over without the additional focusing element). The yellow region highlights the zone not accessible in terms of focal length using the CLEAR-like quadrupole. This limitation is driven by the assumed beam energy and from the CLEAR-like quadrupole specification. As a general constrain, it is needed to ensure that the measurement system resolution, is smaller than the value of measurand (i.e., $\sigma_{t_{res}} \leq \sigma_{t_0}$). In the zone highlighted in red in Fig. 4.19, such condition is not respected for focal length in the vicinity of f^*. This region, as explained in Sec. 4.2.3, should be avoided in order to perform the measurement.

In the conventional layout, as expected from the theory, the best result in terms of resolution is obtained with beam parameters capable of strongly focusing the beam on the screen (i.e., $\beta = 27\,\mathrm{m}$ and $\alpha = 10$). From Eq. 4.91, the minimum value of measurable bunch length correspond to $385\,\mathrm{fs}$. Thanks to the effects of the additional focusing elements, in a CLEAR-like configuration (i.e., $\alpha = 10$ and $\beta = 11\,\mathrm{m}$), operating with a defocusing quadrupole at $f = -f_{min} = 0.29\,\mathrm{m}$ (Tab. 4.7) from Eq. 4.91 bunch length down to $243\,\mathrm{fs}$ can be measured, decreasing the $\sigma_{t_{res}}$ of the 37%. The resolution improvement is limited from the minimum focal length reachable. Penetrating the yellow region (i.e., using slightly more powerful quadrupoles), reaching $f = -0.1\,\mathrm{m}$, bunch length down to $158\,\mathrm{fs}$ can be measured, obtaining a reduction of the $\sigma_{t_{res}}$ by 59%. Such reduction is explained by the strong growth of the K_{CAL} that, as can be seen directly from Eq. 4.91, drive the reduction of $\sigma_{t_{res}}$. In the case of conventional layout, from Eq.4.23, the $K_{cal} = 0.244\,\mathrm{mm/ps}$ and, thanks to the additional focusing element, in the CLEAR-like configuration, from Eq.4.77, it can grow up to $K_{CAL} = 0.905\,\mathrm{mm/ps}$.

4.3.2 Experimental and simulation validation

Different measurements, supported with simulations are carried out in order to validate the equations and the considerations derived so far. In particular, seven different types of measurement campaigns using the same beam parameters are performed. The first three additional measurement campaigns are performed, imposing different quadrupole focal lengths but having constant the transverse

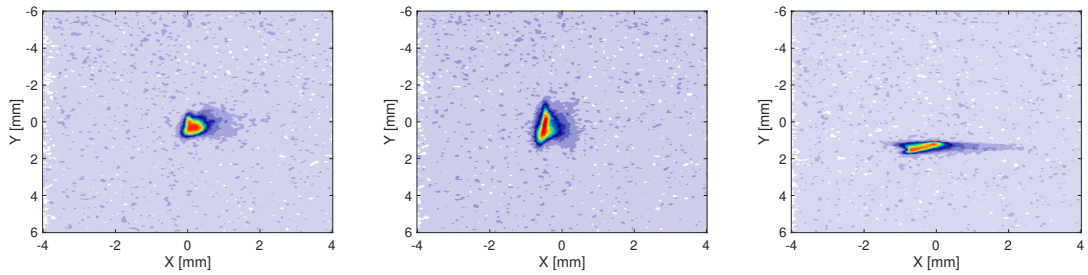

(A) $\sigma_{y_{s,off}}$ with quadrupole off

(B) $\sigma_{y_{s,OFF}}$ with defocusing quadrupole

(C) $\sigma_{y_{s,OFF}}$ with focusing quadrupole

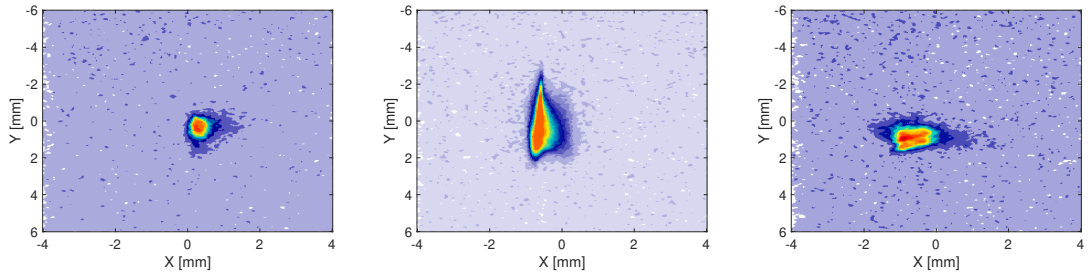

(D) $\sigma_{y_{s,on}}$ with quadrupole off

(E) $\sigma_{y_{s,ON}}$ with defocusing quadrupole

(F) $\sigma_{y_{s,ON}}$ with focusing quadrupole

FIGURE 4.20: The three different beam spots with the quadrupole switched off, in case of strong defocusing ($f = -2.50\,\mathrm{m}$), and in case of strong focusing ($f = 1.47\,\mathrm{m}$) from left to right. Obtained with the RFD off and on, in the first and second row, respectively.

deflecting voltage. Later, other four additional measurement campaigns are performed at different transverse deflecting voltage with the additional focusing element switched off. In the simulations, the common parameters are the same as the ones used in the theoretical treatment reported in Tab. 4.10.

The deflecting voltage used are: $1.53\,\mathrm{MV}$, $1.34\,\mathrm{MV}$, $0.97\,\mathrm{MV}$, and $0.55\,\mathrm{MV}$. The focal length tested to assess the measurement system resolution enhancement are: $f = -2.50\,\mathrm{m}$ (i.e., strong defocusing), $f = -4.99\,\mathrm{m}$ (i.e., weak defocusing), and $f = 1.47\,\mathrm{m}$ (i.e., strong focusing). The three different beam spots **o**btained with the RFD off with the: (i) quadrupole switched off, (ii) strong defocusing quadrupole ($f = -2.50\,\mathrm{m}$), and (iii) strong focusing quadrupole ($f = 1.47\,\mathrm{m}$) are shown in Fig. 4.20 (A),(B), and (C), respectively. Analogously the three different beam spots obtained with the RFD are shown in Fig. 4.20 (D), (E), and (F), respectively.

While varying the RFD phase, the beam spot needs to remains inside the field of view of the acquisition system (Tab. 4.7). However, using a defocusing quadrupole, the beam spots size, both with RFD on and off, becomes bigger (Figs. 4.20). At the same time, the beam centroid displacement with the RFD phase (i.e., $\frac{\mathrm{d}C_{y_{s,on}}}{\mathrm{d}\varphi}$) increases. Thus, the use of a defocusing quadrupole can drive issues with the field of view of the acquisition system, while the opposite effects are obtained while using a focusing quadrupole (i.e., the beam spot size can reach the acquisition system resolution). Consequently, to compare the different

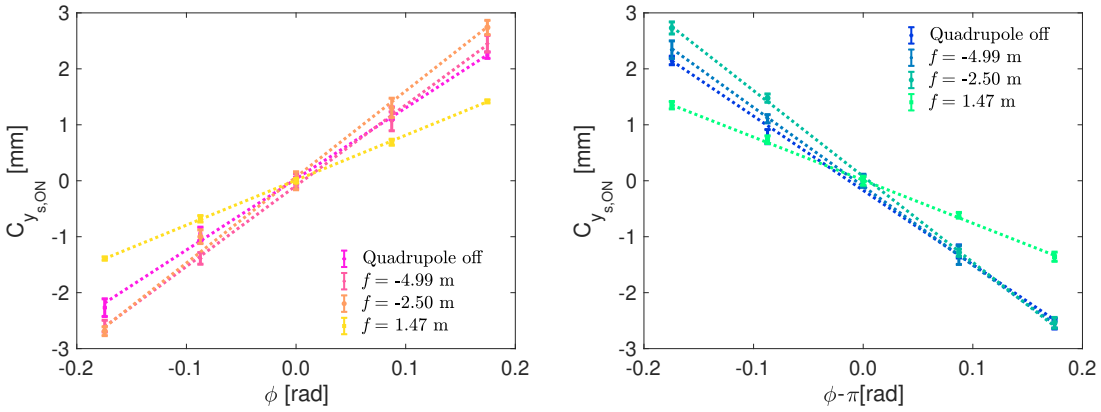

(A) (B)

FIGURE 4.21: The beam centroid measured versus the RFD phases for different focal length around $0\,\mathrm{rad}$ and $\pi\,\mathrm{rad}$ in (A) and (B), respectively.

TABLE 4.11: Value of $^{dC_{y_{s,ON}}}/_{d\varphi}$ from the measurement of the beam centroid variation around $0\,\mathrm{rad}$ and $\pi\,\mathrm{rad}$ reported in Figs. 4.21.

f	$0\,\mathrm{rad}$	$\pi\,\mathrm{rad}$
∞	$(12.7 \pm 0.3)\ \frac{\mathrm{mm}}{\mathrm{rad}}$	$(13.2 \pm 0.3)\frac{\mathrm{mm}}{\mathrm{rad}}$
$-4.99\,\mathrm{m}$	$(14.4 \pm 0.4)\ \frac{\mathrm{mm}}{\mathrm{rad}}$	$(14.0 \pm 0.3)\frac{\mathrm{mm}}{\mathrm{rad}}$
$-2.50\,\mathrm{m}$	$(15.3 \pm 0.3)\ \frac{\mathrm{mm}}{\mathrm{rad}}$	$(15.3 \pm 0.3)\frac{\mathrm{mm}}{\mathrm{rad}}$
$1.47\,\mathrm{m}$	$(\ 8.0 \pm 0.1)\ \frac{\mathrm{mm}}{\mathrm{rad}}$	$(\ 7.7 \pm 0.2)\frac{\mathrm{mm}}{\mathrm{rad}}$

quadrupole settings, the transverse deflecting voltage is chosen to comfortably allow the measurement taking into account the field of view and the resolution of the acquisition system in all the experimental conditions (i.e., equal to $0.97\,\mathrm{MV}$).

The different variations of the centroid position for the quadrupole turned off, and the other three quadrupole configurations are reported in Fig. 4.21 around $0\,\mathrm{rad}$ and $\pi\,\mathrm{rad}$ in (A) and (B), respectively. For each focal length, the centroid position is measured for different RFD phases, and each centroid position is the result of the average on ten measurements. In Tab. 4.11, the slopes (i.e., $^{\mathrm{d}C_{y_{s,ON}}}/_{d\varphi}$) and the uncertainty, obtained from the experimental data shown in Figs. 4.21 are reported. From the slopes reported in Tab. 4.11, the K_{CAL} can be assessed. Figure 4.22 shows that, the use of a defocusing element in the vertical plane enhances the K_{CAL}; while the use of a focusing element in the vertical plane degrades it. In Fig. 4.22, the results from the four additional measurement campaigns performed with the additional focusing elements turned off at different deflecting tension (V_t) are shown. Thanks to the additional defocusing element, the same effects of a higher value of V_t is emulated. Enhancing the calibration factor and, as a consequence, improve the measurement system resolution.

As a final result, in Fig. 4.23, a comparison between the theoretical model, the measurement, and the ELEGANT simulations, in terms of the K_{CAL} versus the focal length, is presented. The experimental results (black crosses) are compatible

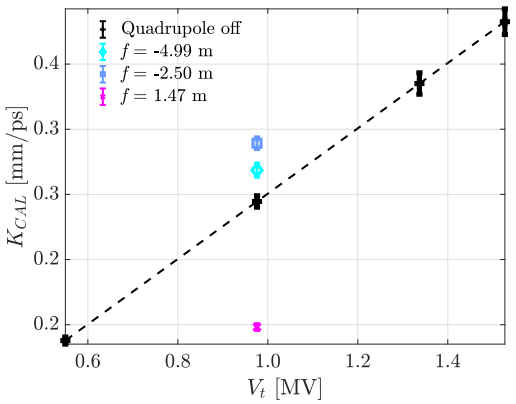

FIGURE 4.22: The K_{CAL} measurements using different deflecting voltage with the additional quadrupole switched off (black markers). The K_{CAL} measurements with a constant deflecting voltage ($V_t = 0.976\,\mathrm{MV}$) using different focal length (colored markers).

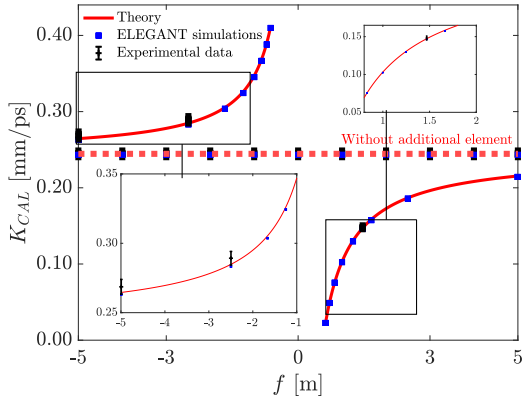

FIGURE 4.23: The K_{CAL} versus the focal length, obtained with the theoretical prediction (red lines), the experimental results (black crosses), and the ELEGANT simulations (blue dots).

with both simulations (blue dots) and theoretical predictions (red lines). A good agreement is obtained between the theoretical model and the simulation, with a percentage relative error below 0.5%.

4.4 Uncertainty reduction

As already mentioned, if $\sigma_{y_{s,OFF}}$ and $\overline{\sigma_{y_{s,ON}}}$ are too close, the information about the measurand could be lost. This information lost is driven from the grow of uncertainty that tends to infinity when $\sigma_{y_{s,OFF}}$ approach $\overline{\sigma_{y_{s,ON}}}$. In this section, a detailed study of the uncertainty by comparing the two layouts is performed. Moreover, for the non-conventional layout, the possible limitation that can increase the uncertainty are analyzed. Finally, the validations, using the ELEGANT tracking code (introduced in Sec.4.1.3), for all the derived equation is presented.

4.4.1 Theoretical treatment

In the following derivation, in order to obtain an analytical formula, the use of Guide Uncertainty Measurement (GUM) propagation is applied [219]. It is reasonable to assume, that: (i) the first order Taylor series is an appropriate approximation, (ii) all the input quantities can be expressed in terms of their first two momenta (i.e., the mean value and the standard deviation), and (iii) the quantities are uncorrelated. The used symbols refer to the non-conventional layout. However, the same treatment can be performed for the conventional one. It is needed to assess the uncertainty $\overline{\sigma_{y_{s,ON}}}$ (Eq. 4.79) in order to assess the relative uncertainty on the bunch length (Eq. 4.80). Under the assumption that the uncertainty of the beam spot size is the same at φ and $\varphi + \pi$ (i.e., $u(\sigma_{y_{s,ON}}(\varphi)) = u(\sigma_{y_{s,ON}}(\varphi + \pi)) = u(\sigma_{y_{s,ON}})$), using the uncertainty propagation on Eq. 4.79

$$u(\overline{\sigma_{y_{s,ON}}}) = \sqrt{\left(\frac{\partial\overline{\sigma_{y_{s,ON}}}}{\partial\sigma_{y_{s,ON}}(\varphi)}\right)^2 u^2(\sigma_{y_{s,ON}}) + \left(\frac{\partial\overline{\sigma_{y_{s,ON}}}}{\partial\sigma_{y_{s,ON}}(\varphi+\pi)}\right)^2 u^2(\sigma_{y_{s,ON}})}, \quad (4.92)$$

where the derivative from Eq. 4.79 can be written respectively as

$$\frac{\partial\overline{\sigma_{y_{s,ON}}}}{\partial\sigma_{y_{s,ON}}(\varphi)} = \frac{\sigma_{y_{s,ON}}(\varphi)}{\sqrt{2(\sigma^2_{y_{s,ON}}(\varphi) + \sigma^2_{y_{s,ON}}(\varphi+\pi))}} \quad \text{and} \quad (4.93)$$

$$\frac{\partial\overline{\sigma_{y_{s,ON}}}}{\partial\sigma_{y_{s,ON}}(\varphi+\pi)} = \frac{\sigma_{y_{s,ON}}(\varphi+\pi)}{\sqrt{2(\sigma^2_{y_{s,ON}}(\varphi) + \sigma^2_{y_{s,ON}}(\varphi+\pi))}}. \quad (4.94)$$

Substituting Eqs. 4.93 and 4.94 into Eq. 4.92, $u(\overline{\sigma_{y_{s,ON}}})$ can be assessed

$$\begin{aligned} u(\overline{\sigma_{y_{s,ON}}}) &= \left[\frac{\sigma^2_{y_{s,ON}}(\varphi)}{2(\sigma^2_{y_{s,ON}}(\varphi) + \sigma^2_{y_{s,ON}}(\varphi+\pi))}u^2(\sigma_{y_{s,ON}}) + \right. \\ &\left. + \frac{\sigma^2_{y_{s,ON}}(\varphi+\pi)}{2(\sigma^2_{y_{s,ON}}(\varphi) + \sigma^2_{y_{s,ON}}(\varphi+\pi))}u^2(\sigma_{y_{s,ON}})\right]^{\frac{1}{2}} = \\ &= \sqrt{\frac{\sigma^2_{y_{s,ON}}(\varphi) + \sigma^2_{y_{s,ON}}(\varphi+\pi)}{2(\sigma^2_{y_{s,ON}}(\varphi) + \sigma^2_{y_{s,ON}}(\varphi+\pi))}u^2(\sigma_{y_{s,ON}})} = \frac{1}{\sqrt{2}}u(\sigma_{y_{s,ON}}). \end{aligned} \quad (4.95)$$

As expected, the uncertainty $\overline{\sigma_{y_{s,ON}}}$ is smaller than the one of $\sigma_{y_{s,ON}}$. Once assessed Eq. 4.95, by following the same approach used in Eq. 4.92, neglecting the uncertainty on the K_{CAL}, the uncertainty on the bunch length can be written as

$$u(\sigma_{t_0}) = \sqrt{\left(\frac{\partial\sigma_{t_0}}{\partial\overline{\sigma_{y_{s,ON}}}}\right)^2 u^2(\overline{\sigma_{y_{s,ON}}}) + \left(\frac{\partial\sigma_{t_0}}{\partial\sigma_{y_{s,OFF}}}\right)^2 u^2(\sigma_{y_{s,OFF}})}, \quad (4.96)$$

where the derivative from Eq. 4.79 can be written as

$$\frac{\partial \sigma_{t_0}}{\partial \overline{\sigma_{y_{s,ON}}}} = \frac{\overline{\sigma_{y_{s,ON}}}}{|K_{CAL}(\varphi)|\sqrt{\overline{\sigma_{y_{s,ON}}}^2 - \sigma^2_{y_{s,OFF}}}} \quad \text{and} \tag{4.97}$$

$$\frac{\partial \sigma_{t_0}}{\partial \sigma_{y_{s,OFF}}} = \frac{-\sigma_{y_{s,OFF}}}{|K_{CAL}(\varphi)|\sqrt{\overline{\sigma_{y_{s,ON}}}^2 - \sigma^2_{y_{s,OFF}}}} \tag{4.98}$$

respectively.

Substituting Eqs. 4.97 and 4.98 into Eq. 4.96, under the assumption that $u(\sigma_{y_{s,ON}}) = u(\sigma_{y_{s,OFF}})$ and knowing that $u(\sigma_{y_{s,ON}}) = \sqrt{2}u(\overline{\sigma_{y_{s,ON}}})$ (from Eq. 4.95), $u(\sigma_{t_0})$ can be assessed

$$\begin{aligned} u(\sigma_{t_0}) &= \left[\frac{\overline{\sigma_{y_{s,ON}}}^2}{|K^2_{CAL}(\varphi)|(\overline{\sigma_{y_{s,ON}}}^2 - \sigma^2_{y_{s,OFF}})} u^2(\overline{\sigma_{y_{s,ON}}}) + \right. \\ &\left. + \frac{\sigma^2_{y_{s,OFF}}}{|K^2_{CAL}(\varphi)|(\overline{\sigma_{y_{s,ON}}}^2 - \sigma^2_{y_{s,OFF}})} u^2(\sigma_{y_{s,OFF}}) \right]^{\frac{1}{2}} = \\ &= \left[\frac{\overline{\sigma_{y_{s,ON}}}^2}{|K^2_{CAL}(\varphi)|(\overline{\sigma_{y_{s,ON}}}^2 - \sigma^2_{y_{s,OFF}})} u^2(\overline{\sigma_{y_{s,ON}}}) + \right. \\ &\left. + \frac{\sigma^2_{y_{s,OFF}}}{|K^2_{CAL}(\varphi)|(\overline{\sigma_{y_{s,ON}}}^2 - \sigma^2_{y_{s,OFF}})} 2u^2(\overline{\sigma_{y_{s,ON}}}) \right]^{\frac{1}{2}}. \end{aligned} \tag{4.99}$$

Defining the $G = \frac{\overline{\sigma_{y_{s,ON}}}}{\sigma_{y_{s,OFF}}}$, Eq. 4.99 can be rewrite as

$$u(\sigma_{t_0}) = \sqrt{\frac{1}{|K^2_{CAL}(\varphi)|(1 - G^{-2})} u^2(\overline{\sigma_{y_{s,ON}}}) + \frac{G^{-2}}{|K^2_{CAL}(\varphi)|(1 - G^{-2})} 2u^2(\overline{\sigma_{y_{s,ON}}})}. \tag{4.100}$$

It is convenient to rewrite Eq. 4.80 using the G-factor

$$\sigma_{t_0}|K_{CAL}| = \sqrt{\overline{\sigma_{y_{s,ON}}}^2(1 - G^{-2})}. \tag{4.101}$$

Finally, dividing Eq. 4.100 with Eq. 4.80, the relative uncertainty can be written as

$$\begin{aligned} \frac{u(\sigma_{t_0})}{\sigma_{t_0}} &= \sqrt{\frac{1}{(1 - G^{-2})^2} \frac{u^2(\overline{\sigma_{y_{s,ON}}})}{\overline{\sigma_{y_{s,ON}}}^2} + \frac{2G^{-2}}{(1 - G^{-2})^2} \frac{u^2(\overline{\sigma_{y_{s,ON}}})}{\overline{\sigma_{y_{s,ON}}}^2}} = \\ &= \frac{\sqrt{1 + 2G^{-2}}}{1 - G^{-2}} \frac{u(\overline{\sigma_{y_{s,ON}}})}{\overline{\sigma_{y_{s,ON}}}} = U_f \cdot \frac{u(\overline{\sigma_{y_{s,ON}}})}{\overline{\sigma_{y_{s,ON}}}}. \end{aligned} \tag{4.102}$$

In Eq. 4.102, the relative uncertainty on the bunch length is equal to fact**o**r (i.e., U_f) times the relative uncertainty on transverse beam size measurements at the screen with the RFD turned on after the cancellation of the correlation (i.e., $u(\overline{\sigma_{y_{s,ON}}})/\overline{\sigma_{y_{s,ON}}}$). The defined G-factor (contained in U_f) is defined between 1 and $+\infty$. When the

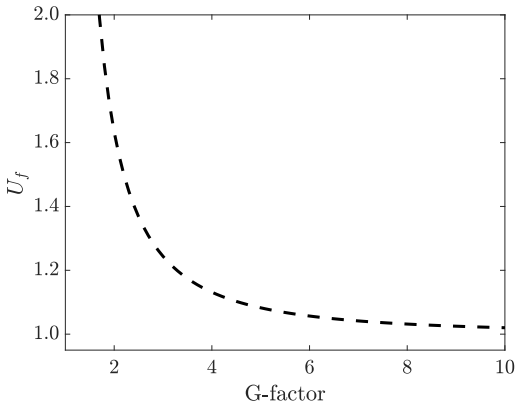

FIGURE 4.24: The multiplicative uncertainty factor between the relative uncertainty U_f (Eq. 4.102), versus the G-factor.

G-factor tends to 1, $\overline{\sigma_{y_{s,ON}}}$ tends to $\sigma_{y_{s,OFF}}$ and the uncertainty of the measurand tends to infinity. When the G-factor tends to $+\infty$, $\overline{\sigma_{y_{s,ON}}} \gg \sigma_{y_{s,OFF}}$ and the uncertainty of the measurand tends to the minimum value, which is the relative uncertainty of $\overline{\sigma_{y_{s,ON}}}$. Therefore, the G-factor has to be maximized to minimize the uncertainty on the measurand.

From Eq. 4.102, the ideal scenario for the minimization of uncertainty, would be to realize an infinity large $\overline{\sigma_{y_{s,ON}}}$ and an infinity small $\sigma_{y_{s,OFF}}$. In an actual scenario, considering a single measurement, both these quantities are limited by the acquisition system. The maximum measurable spot size is limited by the maximum FOV of the acquisition system, while the resolution of the acquisition system limits the minimum measurable spot size. For the maximum measurable spot size, additional constrains needs to be considered: (i) the dimension of the spot size measured on the screen is N times the RMS values, and (ii) in order to calibrate the meas**u**rement, the vertical centroid has to be measured at varying the RFD phase, therefore, there is a vertical displacement of the spot size. Both these considerations need to be taken into account. In Fig. 4.24, U_f as a function of the G-factor is shown. For $G > 5$ (i.e., $\overline{\sigma_{y_{s,ON}}}$ five times $\sigma_{y_{s,OFF}}$) the relative uncertainty is growing less than 10%.

Substituting the general terms of $\sigma_{y,OFF}$ (from Eq. 4.61) and $\overline{\sigma_{y,ON}}$ (from Eq. 4.79) into Eq. 4.102, the G-factor can be rewritten in a generic form, function of the matrix elements (M_{11} and M_{12}), of the RFD characteristics (V_t, f_{RF}, and φ), and the beam parameters at the RFD center (σ_{t_0}, E_0, ϵ_{y_0}, α_{y_0}, β_{y_0}, and γ_{y_0})

$$G^2 = 1 + \frac{K_{CAL}^2(\varphi)\sigma_{t_0}^2}{\sigma_{y,OFF}^2} = 1 + \frac{1}{F^2 R}, \tag{4.103}$$

where the terms F and R can be respectively written as

$$F = \frac{\sqrt{\epsilon_{y_0}}}{(2\pi\sigma_{t_0} f_{RF}\frac{V_t}{E_0})\cos(\varphi)} \quad \text{and} \quad R = \left(\frac{M_{11}}{M_{12}}\right)^2 \beta_{y_0} - 2\frac{M_{11}}{M_{12}}\alpha_{y_0} + \gamma_{y_0}. \tag{4.104}$$

The coefficient R is obtained combining Eq. 4.61 with the equations to pass between the two different representation of the bunch reported in Eqs. 2.12, 2.13, and 2.14. The beam emittance is into the coefficient F since it is constant over the whole accelerators. Morover, it is useful to define the ratio between the matrix elements as $M_r(f) = {}^{M_{11}}/_{M_{12}(f)}$.

$$R = M_r^2 \beta_{y_0} - 2M_r \alpha_{y_0} + \gamma_{y_0}. \tag{4.105}$$

Owning the different dependencies of the G-factor, the conventional and non-conventional layout, are studied separately.

4.4.2 Conventional layout

In the conventional layout, by substituting the matrix relative matrix from Eq. 4.3 (i.e., considering $M_r = {}^1/_{L_t}$) the G-factor can be written as

$$G_c^2(\alpha_{y_0}, \beta_{y_0}) = 1 + \frac{L_t^2}{F^2(\beta_{y_0} - 2L_t\alpha_{y_0} + L_t^2\gamma_{y_0})}, \tag{4.106}$$

where L_t is the distance between the RFD center and the screen (i.e., $L_t = L_1 + L_2$), as shown in Fig. 4.14. As known in literature [176, 177], in the conventional layout, to minimize the uncertainty (i.e., obtain the maximum value of the G-factor), it is needed to squeeze down the spot size at the screen, realizing a so-called waist. Tuning the optics upstream the RFD, the Twiss parameters at the RFD center can be modified in order to impose the waist on the screen. The waist determined from the optics upstream and downstream of the RFD, they are called natural and quadrupole waist, respectively.

Solving the equation $\frac{\partial \sigma_{y_{off}}^2(\alpha_{y_0}, \beta_{y_0})}{\partial L_t} = 0$ (i.e., founding the minimum spot size as a function of β_{y_0} and α_{y_0}), the relation between the Twiss parameters at the RFD center that impose the natural waist on the screen is

$$\beta_{y_0} = L_t \frac{1 + \alpha_{y_0}^2}{\alpha_{y_0}}. \tag{4.107}$$

Substituting Eq. 4.107 in Eq. 4.106 the maximum G-factor in the conventional layout can be written as

$$G_c^2(\alpha_{y_0}) = 1 + \frac{L_t \alpha_{y_0}}{F^2}. \tag{4.108}$$

From Eqs. 4.108 some preliminary consideration can be done. The G_c is inversely proportional to the geometrical emittance (hidden in F, from Eq 4.104), while it is proportional to the bunch length. It means that machines with longer bunches and lower emittance will have a higher G_c (i.e., lower uncertainty). Moreover, due to the proportionality of G_c with L_t, having a long distance between the RFD center and the screen improve the measurement uncertainty.

From Eq. 4.108, using the largest achievable value of α_{y_0} (i.e., $\alpha_{y_{0_{max}}}$) allows to reach the largest value of the G-factor (i.e., $G_{c_{max}}$).

4.4.3 Non-conventional layout

In the non-conventional layout, additional degrees of freedom are available to minimize the uncertainty. For each Twiss parameter at the RFD center, the strategy is to find the focal length to maximize the G-factor (i.e., minimize the R in Eq. 4.105).

The focal length which minimizes $R(f, \alpha_{y_0}, \beta_{y_0})$, named f_G, can be found imposing $\frac{\partial R(f,\alpha_0,\beta_0)}{\partial M_r(f)} = 0$. From such condition it is obtained

$$M_r(f_G) = \frac{\alpha_{y_0}}{\beta_{y_0}}. \tag{4.109}$$

If f_G can be found the maximum value of the G-factor is obtained substituting Eq. 4.109 in Eqs. 4.103 and Eq. 4.105

$$G_{NC}^2(\beta_{y_0}) = 1 + \frac{\beta_{y_0}}{F^2}. \tag{4.110}$$

In this case, the G_{NC} does not depends directly from α_0 and L_t, these dependences are hidden hidden in selection of f_G. However, it increases when: (i) F is small, and/or (ii) β_{y_0} is large.

Comparing Eq. 4.108 with Eq. 4.110, both the layout benefit from a reduction of F; two different strategies can be followed to reduce F. The first is to act on the beam characteristics reducing the geometrical emittance; the second is to enhance the deflector's characteristics (i.e., increase the deflecting voltage amplitude and/or frequency), which corresponds to increase the calibration factor.

Moreover, by comparing Eq. 4.108 and Eq. 4.110 for some values of the focal length, if the additional focusing element is correctly tuned, the G-factor of the non-conventional layout can become larger than the conventional layout (i.e., the uncertainty of the measurement can be improved). Such improvement decrease for the Twiss parameters, which approximate the best condition for the conventional layout (i.e., the natural waist close to the screen) until it vanishes for the natural waist on the screen (i.e., the best condition for the conventional layout cannot be improved). However, a large variety of beam configurations in the non-conventional layout reach a better uncertainty than the best configuration achievable with the conventional layout.

From Eq. 4.110, using the largest achievable value of β_{y_0} (i.e., $\beta_{y_{0_{max}}}$) allows to reach the largest value of the G_{NC} (i.e., $G_{NC_{max}}$).

Focusing element strength

There are sets of Twiss parameters at the RFD center for which it is not possible to identify a focal length to satisfy Eq. 4.109. For all the sets of Twiss parameter for witch, for any f, $Mr(f)$ is between $M_r(-f_{min})$ and $M_r(f_{min})$, is not possible to identify f_G. These correspond to cases where a high current is required to move the natural waist. Examples are parameters that impose the natural waist close (or, in the worse cases, inside) the quadrupole.

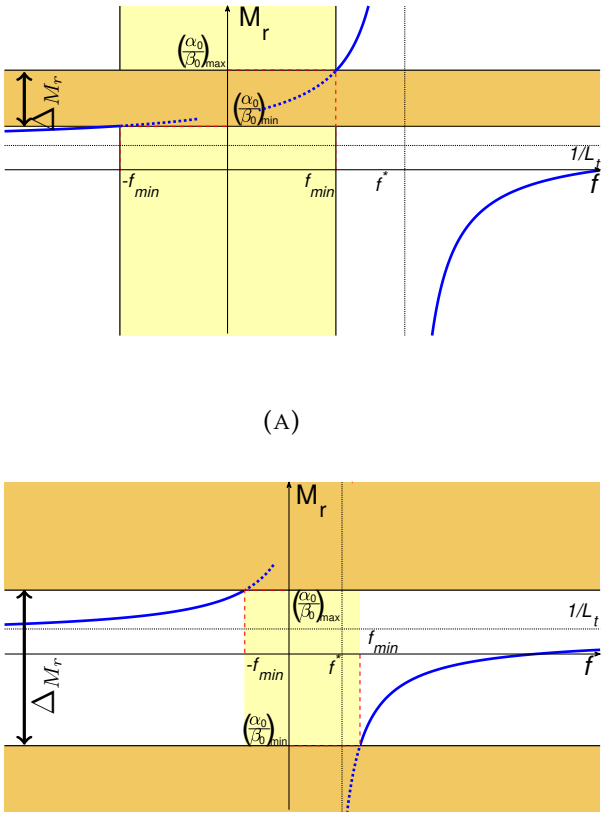

(A)

(B)

FIGURE 4.25: The M_r versus the focal length f, for $f^* \geq f_{min}$ and $f^* < f_{min}$ in (A) and (B), respectively. The regions highlighted in orange are where the quadrupole is not able to satisfy the condition in Eq. 4.109. The regions highlighted in yellow are where the focal lengths are too small to be achieved with the quadrupole.

In Figs. 4.25, the two possible conditions for the location of f_{min} before and after f^* (i.e., $f^* \geq f_{min}$ or $f^* < f_{min}$) are shown, where f^* is the focal length defined Eq. 4.87. In Figs. 4.25, the regions highlighted in orange represent where the quadrupole cannot satisfy the condition in Eq. 4.109 (i.e., the M_r for which it is not possible to find f_G). The regions highlighted in yellow represent where the focal length is too small to be reached (i.e., the $f \leq f_{min}$). Morover, the quantity Δ_{M_r} is defined as $|M_r(f_{min}) - M_r(-f_{min})|$.

In Fig. 4.25 (A), the case for $f^* > f_{min}$ is reported. In this case, it is not possible to find f_G for the $\frac{\alpha_{y0}}{\beta_{y0}}$ between $M_r(-f_{min})$ and $M_r(f_{min})$. Thus, the gap Δ_{M_r} is to be minimize. In Fig. 4.25 (B), the case for $f^* \leq f_{min}$ is reported. In this case, only for the $\frac{\alpha_{y0}}{\beta_{y0}}$ between $M_r(-f_{min})$ and $M_r(f_{min})$ the $f_{G_{max}}$ can be found. Thus, the gap Δ_{M_r} it is to be maximize. The case in which the measurement is made depends on the experimental layout (i.e., the position of the elements) and the limitation of the focusing element.

In the regions highlighted in orange (i.e., where the Eq. 4.109 is not satisfied),

the maximum value of the G-factor is achieved using a focal length that better approximates the condition

$$\left(M_r(\widetilde{f_G}) - \frac{\alpha_{y_0}}{\beta_{y_0}} \right) \approx 0, \tag{4.111}$$

where, $\widetilde{f_G}$ is the focal length that allows to better approximate such condition. In this case, the maximum reachable G-factor is smaller than the one reported in Eq. 4.110, and it is also dependent on α_{y_0}.

From Figs. 4.25 it can be noted that increasing the focal length, M_r tends to the horizontal asymptote $1/L_t$, i.e., the same value of the conventional layout. For focal length that tends to infinity, the quadrupole tends to be equivalent to a drift space (i.e., the quadrupole is switching off the quadrupole). Thus, the non-conventional layout tends to be equivalent to the conventional layout. As a consequence, the M_r tends to the value of the conventional layout.

Focusing element position

Due to the dependence of the G-factor from M_r (as shown in Eq. 4.105), the quadrupole position is also impacting the uncertainty. Such dependence is of significant interest in the design phase of the accelerators.

It is needed to analyze the impact of the quadrupole position on the M_r in order to assess the impact on the uncertainty. During the study, a CLEAR-like quadrupole is assumed (i.e., $f_{min} = 0.29\,\mathrm{m}$), and the distance between RFD and the screen is compatible with the currently available in CLEAR (i.e., $L_t = 2.058\,\mathrm{m}$). As in Sec. 4.4.3, two different cases are analyzed, when f^* is smaller or larger equal of f_{min}. In both cases, it is required to maximize the Twiss parameters for which f_G can be found (i.e., minimize the regions highlighted in orange in Figs. 4.25).

In Fig. 4.26 (A), the trend of f^* (derived similarly to Eq. 4.87 but without the thin lens approximation) is reported. In Fig. 4.26 (B) the trend of Δ_{M_r} (i.e., the difference of the ratio between Eqs. 4.85 and 4.86 evaluate**d** in $\pm f_{min}$ without the thin lens approximation) is reported. Both the quantities are plotted versus the distance between the RFD center and the quadrupole center. Using Fig. 4.26 (A), in Fig. 4.26 (B), two vertical lines where added, to identify where f^* becomes large then f_{min}.

From Fig. 4.26 (B), in the region of $f^* < f_{min}$ (the M_r shown in Fig. 4.25 (B)), the largest gap is obtained once the quadrupole is close to the RFD. In the other region, $f^* \geq f_{min}$ (the M_r shown in Fig. 4.25 (A)), the smallest gap is obtained positioning the quadrupole at the center between the RFD and the screen.

The quadrupole's best location is strongly dependent on the needed range of the reachable Twiss parameters (i.e., it is not worth increasing the acceptable Twiss parameters at the RFD center if the accelerator will anyway not reach such parameters). However, from Figs. 4.26 a general conclusion can be made: it is mandatory to avoid installing the quadrupole close to the screen because the Δ_{M_r} tends to zero and, therefore, no Twiss parameter value can be reached by means of any focal length.

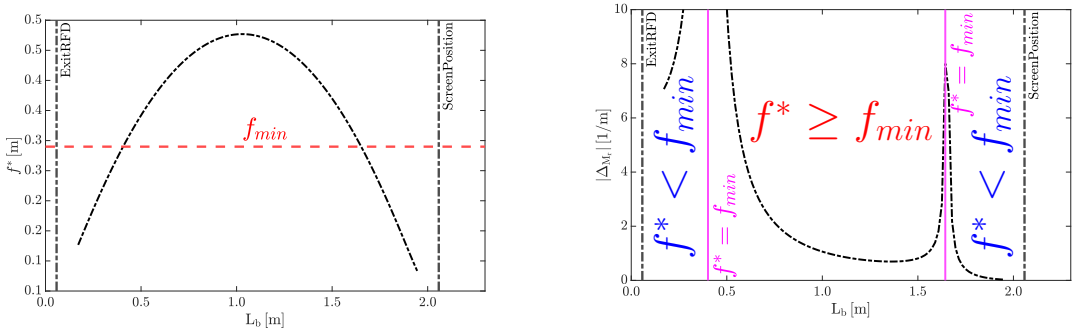

(A) (B)

FIGURE 4.26: The f^* and the Δ_{M_r} versus the distance between the RFD center and the quadrupole center in (A) and (B), respectively. In (B) two vertical lines were added at $f^* = f_{min}$ in order to distinguish the two conditions (i.e., $f^* < f_{min}$ and $f^* > f_{min}$).

4.4.4 Validation using simulations

A sensitivity analysis on the Twiss parameter at the RFD center is performed in order to compare the performances of the two layouts, conventional and non-conventional. Moreover, the non-conventional layout relies also on a sensitivity analysis of the quadrupole focal length in order to identify the G_{NC}.

The comparison is performed between:

- analytical model, where the G-factor is calculated directly from Eqs. 4.108 and 4.110 for the conventional and non-conventional layout, respectively;
- Semi-analytical model, the G-factor is assessed from the ratio of the beam spot sizes with the RFD turned off and on (assuming to have canceled the contribution from the correlations). The beam spot sizes are calculated using Eqs. 4.3 and 4.49; and Eqs. 4.61 and 4.73 for the conventional and non-conventional layout, respectively;
- Simulations, where the beam spot sizes are assessed using the ELEGANT tracking code and the G-factor is calculated as the ratio of these quantities for both the layouts.

As for the previous comparative study on the resolution, performed in Sec. 4.3 the validation is performed using the parameter range achievable in the CLEAR accelerator used as a case study.

All the potentially achievable values of α_{y_0} and β_{y_0} at the center of the RFD at CLEAR were tested for both conventional and non-conventional layout in order to identify the best Twiss parameter. The parameters used are reported in Tab. 4.12

In Fig. 4.27 (A) and (B), two 3D plots of the G-factor for the conventional and non-conventional layout, obtained with the analytical model (i.e., Eqs. 4.108 and 4.110, respectively) versus α_{y_0} and β_{y_0} are shown. While, in Fig. 4.27 (C), five cuts at different α_{y_0} from G-factor of the non-conventional layout and the $G_{c_{max}}$

TABLE 4.12: Parameters adopted in the simulations to validate the uncertainty reduction.

$\langle E_0 \rangle = 203\,\mathrm{MeV}$	$\delta_0 = 2\,\%$	$q = 200\,\mathrm{pC}$	$\sigma_{t_0} = 5ps$
$\epsilon_{y_0} = 10\,\mathrm{nm}$	$\beta_{y_0} = 0.50 - 40\,\mathrm{m}$	$\alpha_{y_0} = -10 - 10$	$L_{RFD} = 0.1160\,\mathrm{m}$
$f_{RF} = 2.9985\,\mathrm{GHz}$	$V_t = 1.0\,\mathrm{MV}$	$L_b = 0.7870\,\mathrm{m}$	$L_q = 0.2260\,\mathrm{m}$
$L_a = 1.687\,\mathrm{m}$	$\sigma_{y_{res}} = 25\,\mu\mathrm{m}$	$\mathrm{FOV} = 8\,\mathrm{cm}$	$\text{Macro particles} = 500,000$

(i.e., the maximum G-factor reachable in the conventional case) are shown versus β_{y_0}. The $G_{c_{max}}$ is reported as an horizontal line since it is independent from β_{y_0} (Eq. 4.108). In Fig. 4.27 (C), the analytical models (dashed lines), the semi-analytical models (dotted lines), and the simulation results (crosses) are reported for both conventional and non-conventional layout. For the conventional layout, Fig. 4.27 (A), as predicted from the theory (Sec. 4.4.2), the maximum value of the G-factor is obtained with Twiss parameters that impose the natural waist on the screen (obtaining the G_c reported in Eq. 4.108). Using the largest achievable value of α_{y_0}, $G_{c_{max}}$ can be obtained. For the non-conventional layout, Fig. 4.27 (B) as predicted from the theory (Sec. 4.4.3) the maximum value of the G-factor is obtained using the largest achievable value of β_{y_0} for which f_G can be found (obtaining the $G_{NC_{max}}$). Moreover, by comparing Fig. 4.27 (A) and (B), it is clear that for a vast quantity of Twiss parameter at the RFD center, the additional focusing element allows achieving a G-factor higher than $G_{c_{max}}$. From the comparison in Fig. 4.27 (C), the analytical and semi-analytical results are in perfect agreement (relative error less than 0.1%), and also with the simulation results (error less than 0.5%).

From Fig. 4.27 (B) and (C) in the non-conventional layout, the G-factor does not dependent on α_{y_0} if f_G is found (i.e., G_{NC}) as demonstrated in the analytical derivation. However, there are regions (i.e., the valleys) where it is not possible to find f_G (Eq. 4.109) due to the limitation of the quadrupole configuration. In these regions, due to the presence of $\widetilde{f_G}$, the G-factor depends from both α_{y_0} and β_{y_0}. This phenomenon is more evident for $\alpha_{y_0} < 0$; because a converging beam drives a smaller natural waist, and as a consequence, stronger focusing element (i.e., lower value of focal length) are needed to shift it.

It is useful to indicate the percentage uncertainty reduction as

$$U_{f_R} = 100 \cdot \frac{U_{f_{con}} - U_{f_{non-con}}}{U_{f_{con}}}, \tag{4.112}$$

where $U_{f_{con}}$ and $U_{f_{non-con}}$ are the uncertainty factor for the conventional and non-conventional layout, respectively. Using Eq. 4.112, it is possible to compare the best result obtained with the two layouts. The best configuration of the conventional reaches $U_{f_{con}} = 1.03$ while the beast case of the non-conventional layout can achieve $U_{f_{non-con}} = 1.01$. Thus, between the two best cases, a negligible relative uncertainty reduction (about $U_{f_R} = 2\%$) can be obtained. However, if the comparison is not carried out in between the two best configurations, the relative uncertainty reduction becomes quite larger (i.e., it can reach up to $U_{f_R} = 86\%$).

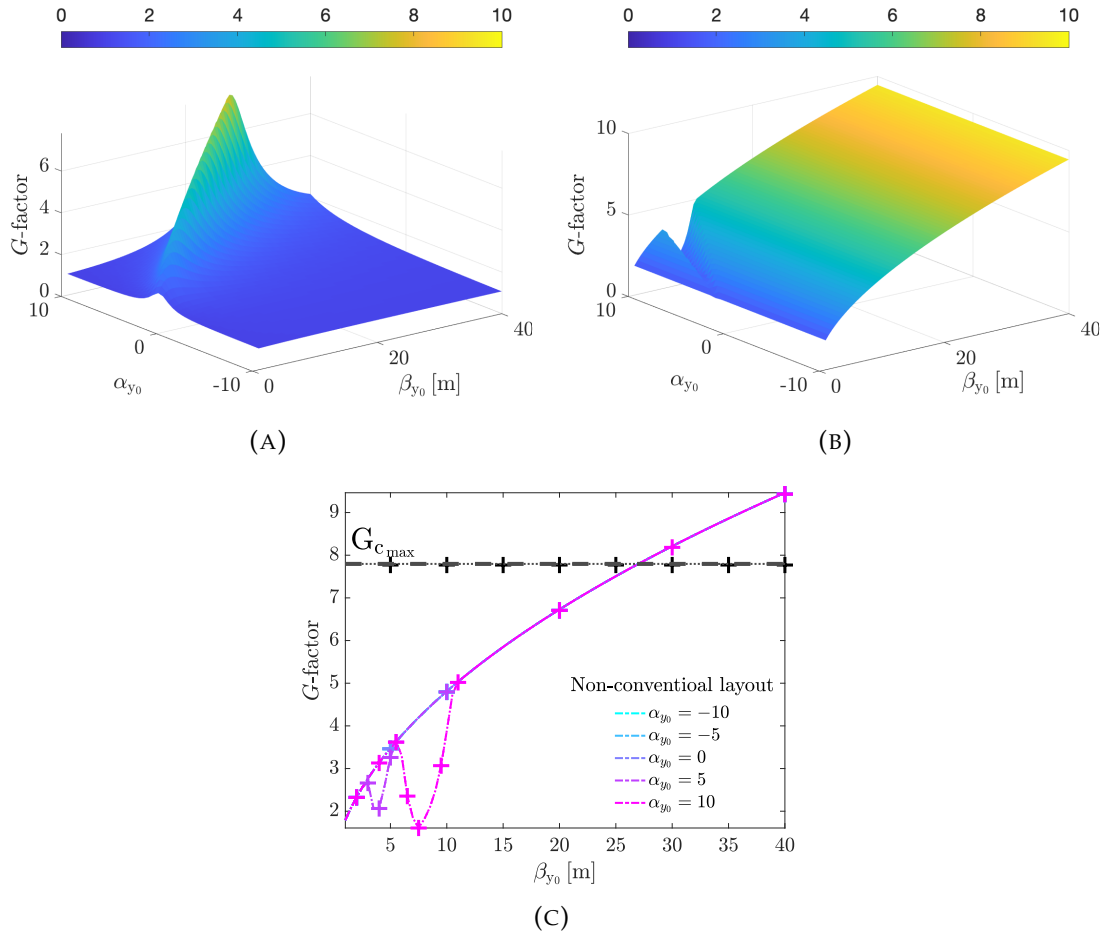

FIGURE 4.27: In (A) and (B), two 3D plots of the G-factor for the conventional and non-conventional layout, obtained with the analytical model (Eqs. 4.108 and 4.110, respectively) versus α_{y_0} and β_{y_0}. In (C), five cuts at different α_{y_0} from G-factor of the non-conventional layout and the $G_{c_{max}}$ (i.e., the maximum G-factor reachable in the conventional case) versus β_{y_0}. The analytical models (dashed lines), semi-analytical models (dotted lines), and the simulation results (crosses) are compared.

Following, simulations are carried out to compare the result obtainable varying the minimum focal length achievable and the quadrupole position between the RFD and the screen.

Focusing element strength validation

A comparison between the two layouts is performed for three different minimum achievable focal lengths. For the non-conventional layout, imposing $\alpha_{y_0} = 10$, for each $|f_{min}|$, a sensitivity analysis over β_{y_0}, is performed. For the conventional layout, only the value of $G_{c_{max}}$ is reported. In the comparison, all the parameters involved are kept equal to the one shown in Tab. 4.12.

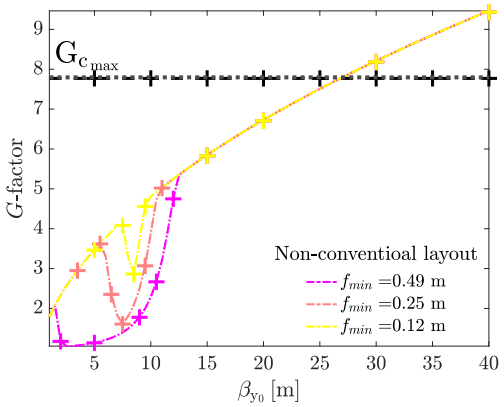

FIGURE 4.28: The three different curves of the G-factor for the non-conventional layout obtained with three different $|f_{min}|$ and the $G_{c_{max}}$ (horizontal line) versus β_{y_0}. The analytical models (dashed lines), semi-analytical models (dotted lines), and the simulation results (crosses) are compared.

To change the $|f_{min}|$ achievable from the additional focusing element, an accelerator layout redesign is needed. Such effect can be achieved or changing the quadrupole installed or, if the installed quadrupole is suitable, increasing maximum powering current.

In Fig. 4.28, assuming $\alpha_{y_0} = 10$, three curves of G-factor for the non-conventional layout, obtained with three different $|f_{min}|$ are shown. In addition the $G_{c_{max}}$ (i.e., the maximum G-factor reachable in the conventional case) is reported as horizontal line. From the results shown in Fig. 4.28, similarly to what was obtained in Fig. 4.27 (C), a perfect agreement can be observed between the analytical and semi-analytical results (error less than 0.1%), and with the simulation results (error less than 0.5%)

As expected from the theory derived in Sec. 4.4.3, while decreasing the minimum achievable focal length (i.e., increasing the quadrupole strength), the valleys reduce. For more Twiss parameters, f_G, such to satisfy Eq. 4.109 can be found (i.e., for more Twiss parameters, G_{NC} can be found). Furthermore, from Fig. 4.28 another interesting result can be understood. Using lower focal length is not increasing the maximum achievable value of the G-factor. It means that without requiring a high-performance focusing element, the maximum reduction in terms of uncertainty can be obtained.

Focusing element position validation

As shown in the theoretical treatment in Sec. 4.4.3, the quadrupole position also affects the G-factor. A comparison between the two layouts is performed for four different quadrupole positions. For the non-conventional layout, imposing $\alpha_{y_0} = 10$, for each quadrupole position, a sensitivity analysis over β_{y_0}, is performed. For the conventional layout, only the value of $G_{c_{max}}$ is reported. In the comparison, all the parameters involved are kept equal to the ones shown in Tab. 4.12. From the results shown in Fig. 4.29, similarly to what was obtained

in Fig. 4.27 (C) and Fig. 4.28, a perfect agreement can be observed between the analytical and semi-analytical results (error less than 0.1%), and with the simulation results (error less than 0.5%). Moreover, in Fig. 4.29 can be observed that the theoretical predictions obtained analyzing Figs. 4.26 are respected. When the quadrupole is close to the RFD for more value of β_{y_0}, the focal length f_G such to maximize the G-factor can be found. While moving quadrupole close to the screen (the magenta curve) just for few values of β_{y_0} a value of focal length that maximizes the G-factor can be found. In particular, the only values for which satisfying conditions can be achieved are the one that imposes the natural waist close the screen (i.e., the same condition that maximizes the conventional layout). In other words, if the quadrupole is too close to the screen, the best condition is achieved for the Twiss parameters that are optimal for the conventional layout. In this case, no reduction in terms of uncertainty can be achieved. Thus it is better to turn off the additional focusing element.

A full sensitivity analysis is performed on the additional focusing element position in order to assess the best one. For each location, an additional sensitivity analysis on the Twiss parameters and focal length is performed. The parameters are kept the same shown in Tab. 4.12. In Fig. 4.30, is shown the maximum of the G-factor for the conventional and non-conventional layout for each position versus the distance between the RFD center and quadrupole center (i.e., L_b as shown in Fig. 4.14). Both the analytical models (dashed lines) and semi-analytical models (dotted lines) are shown. A perfect agreement (error less than 0.1%) between them is achieved. From Fig. 4.30, two main regions can be identified: (i) $L_b \leq L^*$, and (ii) $L_b > L^*$. In the first region, independently from the quadrupole position, it is always possible to find a combination of Twiss parameter at RFD center to respect the conditions reported in Eq. 4.109 (i.e., find G_{NC}). In the second region, the quadrupole is gradually unable to optimize the G-factor until it is so close to the screen that the best value is obtained with Twiss parameters that do not

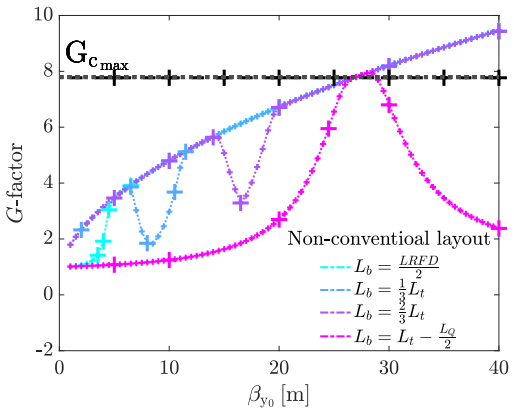

FIGURE 4.29: The G-factor for the non-conventional at $\alpha_{y_0} = 10$ for four different quadrupole positions and the maximum value of G-factor achievable with the conventional layout (i.e., $G_{c_{max}}$) versus β_{y_0}. Both the analytical models (dashed lines), semi-analytical models (dotted lines), and the simulation results (crosses) are compared.

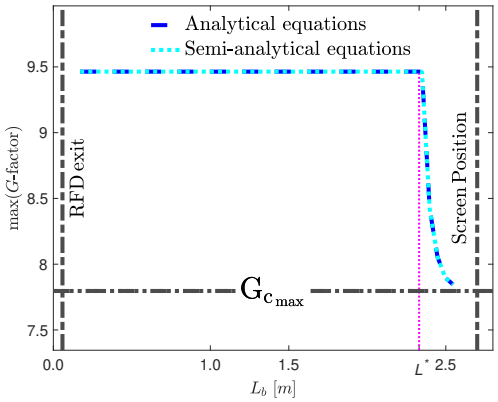

FIGURE 4.30: The maximum of the G-factor for the non-conventional layout for each position of the additional focusing element versus the distance between the RFD center and quadrupole center (i.e., L_b shown in Fig. 4.14). The maximum G-factor for the conventional layout (i.e., $G_{c_{max}}$) is reported as horizontal line. Both the analytical models (dashed lines) and semi-analytical models (dotted lines) are compared.

require at all the use of the quadrupole. In this case, the G-factor of the conventional layout approach the maximum achievable of the conventional layout (i.e., $G_{c_{max}}$). This limitation is driven by the minimal achievable focal length of the quadrupole.

4.4.5 Overview of other LINACs cases study

Other topical case studies are compared, in order to assess the possible advantages of the additional focusing element. In particular, cases comparable with parameters representative to a particle-driven plasma-based accelerator [220]and a high-brightness collider accelerator [221] are analyzed. The following comparisons use the same RFD characteristics, distances, beam energy, α_{y_0}, and FOV reported in Tab. 4.12. These parameters are commons in the novel high-brightness electron LINACs. Conversely, the range of achievable Twiss parameters achievable at the RFD center, the acquisition system resolution, the typical bunch length, and the typical emittance are chosen in agreement with the case under study. In particular the β_{y_0} is assumed to be vary between $0.5\,\mathrm{m}$ and $100\,\mathrm{m}$ (in general, other optics can be installed before the RFD) and $\sigma_{t_{res}} = 10\,\mu\mathrm{m}$ (in line with state of art resolution [222]). The other two parameters (i.e., the beam emittance and the bunch length) change case by case. For each case study, a sensitivity analysis on the Twiss parameters at the RFD entrance is performed. Moreover, as usual, for the non-conventional layout, an additional sensitivity analysis is performed on the focal length.

In Tab. 4.13, for each case considered the $G_{c_{max}}$ and the maximum $G_{NC_{max}}$ for conventional and non-conventional, respectively are shown. Moreover, in the last column, the percentage uncertainty reduction (Eq. 4.112) is reported. From the results of Tab 4.13, a sensible reduction in terms of uncertainty can be achieved

TABLE 4.13: Simulation parameters and results by comparing the uncertainty for the considered cases in the accelerator community.

Case study	σ_{t_0}	ϵ_y	$G_{c_{max}}$	$G_{NC_{max}}$	U_{f_R}
Plasma-based acc.	60 fs	1 nm	1.35	2.02	49%
Collider acc.	2 ps	1 µm	1.39	2.11	48%

TABLE 4.14: The beam spot size ratio, G-factor, and the relative uncertainty factor measured during the resolution experimental validation campaign.

f [m]	K_{CAL} [$\frac{\text{mm}}{\text{ps}}$]	U_f	G-factor
∞	0.24	1.08	5.20
-4.99	0.27	1.09	4.68
-2.50	0.29	1.45	2.29
1.49	0.15	1.01	11.10

for some accelerators. Moreover, as previously anticipated, once the G-factor approach the unity, the measurement is not feasible at all because the contribution from the measurand (i.e., σ_{t_0} from Eq. 4.50) is completely lost because $\sigma_{y_{s,ON}}$ and $\sigma_{y_{s,OFF}}$ are too close. Thus, as highlighted from the results of Tab. 4.13 the measurement is not feasible using the conventional layout, but thanks to the non-conventional layout, the measurement becomes comfortably feasible in all the presented cases.

In addition, as shown in Figs. 4.27, in many beam conditions, not optimize for the bunch length measurement; thanks to the use of the additional focusing element, an essential reduction of uncertainty can be achieved.

4.5 Trade-off between resolution and uncertainty

In the previous sections, the resolution and uncertainty were shown separately. However, in this section, their behaviors are monitored together.

In Tab. 4.14, the measured beam spot size ratio (i.e., the G-factor) are reported for the experimental points assessed during the resolution experimental validation campaign shown in Sec. 4.3.2. From the results of Tab. 4.14, it is evident that while improving the measurement system resolution (i.e., increasing the calibration factor), the uncertainty is growing (i.e., the G-factor is decreasing and U_f is increasing). However, studying the beam envelop for the different initial beam conditions, there are beam conditions that can improve bot**h** the measurement system resolution and the uncertainty. An example of such type of beam condition is shown in Fig. 4.31. The beam conditions in Fig. 4.31 corresponds to initial Twiss parameters that impose the natural waist between the RFD and the screen. Switching on the defocusing quadrupole, the natural waist position slide towards the screen, and as a consequence, the beam spot size on the screen reduces. Such effects are pointed out using the blue color in Fig. 4.31.

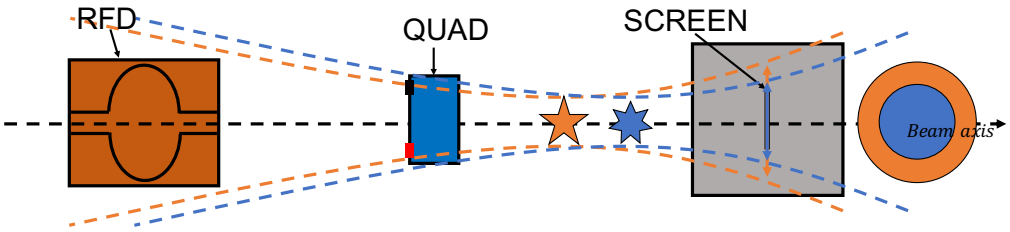

FIGURE 4.31: The favorable beam characteristics allow enhancing both measurement system resolution and uncertainty. The waist positions are highlighted with stars, the beam envelope with dashed lines, and the and spot sizes are the circles on the right side. The blue and orange colors represent when the additional focusing element is turned on and off, respectively.

TABLE 4.15: The Twiss parameters at the RFD center, $\sigma_{t_{res}}$, and the uncertainty factor U_f; for both layout without and with the additional focusing element.

Parameters			Conventional		Non-conventional			U_f reduction
α_{y_0}	β_{y_0} [m]	ϵ_y [m]	$\sigma_{t_{res}}$ [fs]	U_f	$\sigma_{t_{res}}$ [fs]	U_f	f [m]	U_{f_R}
3	5	10^{-8}	69	1.11	46	1.04	-1.38	6%
6	6	10^{-8}	104	1.56	30	1.05	-0.27	33%

From one side, this condition can enhance the measurement system resolution performances and from the others, improve the uncertainty.

For both the layouts, ELEGANT simulations are performed in order to verify this consideration. The parameters for the simulations are kept CLEAR-like (Tab. 4.12) with the only difference that the maximum deflecting voltage reachable in CLEAR (i.e., $V_t = 10\,\mathrm{MV}$) is used to compare the resolution limit in both the layout.

In Tab. 4.15, the results in terms of G-factor, relative uncertainty, and calibration factor are reported.

From the results of Tab. 4.15, using the non-conventional layout, not only the much shorter bunch length can be measured, but also a much lower uncertainty (a reduction up to 33%) can be achieved.

4.6 Discussion and outlook

In this chapter, a method for measuring the longitudinal bunch parameters and the correlations between particle positions, divergences, and energies was presented. This was done using the conventional layout. The RFD-based measurement theory was extended to quantify the effect of energy chirp and correlation terms, opening the way to define two models of measurement production of those quantities. The possibility of measuring energy spread and chirps by means of only the RFD is particularly interesting for novel high-brightness LINACs. The

case studies covered all the kinds of LINACs being designed or operated as radiation sources (i.e., Compton sources and FELs), as well as LINACs intended to exploit the plasma acceleration. Simulations were carried out using the ELEGANT tracking code in order to assess the method's validity and accuracy. In all those cases, the relative error of the measured energy chirp, obtained by means of the proposed technique, is around 5%. In GBS, when strong correlations due to machine misalignment may be present, relative errors of the correlation term measurements are below 1%.

Later, the effect on the bunch length measurement technique of additional focusing elements between the RF deflector and the screen was modeled and analyzed, the so-called non-conventional layout. As for the conventional layout, all the derived equations are numerically validated using the ELEGANT code. Moreover, an experimental validation was carried out at the CLEAR facility. A good agreement was found for all the physical quantities between theoretical predictions, simulation results, and measurements. It was proven that: (i) a calibration factor with the same meaning as in the conventional layout can be defined soundly; (ii) the absence of additional terms that could introduce systematic errors is shown; (iii) the possibility of removing correlation effects is preserved, by first two independent measure**m**ents of the spot size with the RFD on in phase opposition, and then by assessing the average between their squared values; (iv) the additional advantage of individually measuring the correlations; and (v) thanks to the dependence of the beam sizes on the focal length a wider range of beam parameters can be exploited at the entrance of the RFD. Furthermore, a critical value of the focal length, which prevents the measurements from being performed, was identified. This focal length should therefore be avoided. In the non-conventional layout both the calibration factor and the $\sigma_{y_{s,OFF}}$ with RFD off depend on the focal length of the focusing element. For this reason, the optimum resolution is not necessarily obtained by minimizing the beam size on the screen with the RFD turned off, which it is in the conventional layout. While this implies a more complex experimental configuration, it opens up the possibility of a further enhancement in the input range, making further improvement of resolution possible.

For this reason, a theoretical derivation is presented to study the possible enhancement of the metrological performance. It was found that the resolution can be reduced up to 37% assuming CLEAR-like parameters. At the same time, the possible drawback is the uncertainty of the measurement method. However, it was shown the possibility to improve both the measurement system resolution and the uncertainty at the same time.

Furthermore, to improve the uncertainty in the measurement, important points, especially during the design phase of the accelerator, were investigated. In particular, regarding the most suitable Twiss parameters at the input of the measurement system (i.e., a high value of β_{y_0}) and on the best location to install the additional focusing element. Moreover, a much wider range of suitable input Twiss parameters to correctly perform the measurement was found.

All the results were obtained considering a realistic additional focusing element and acquisition system, with their limitation. The two main results that come from the physical limitation are linked together. There are initial Twiss

parameters that impose the natural waist, too close to the quadrupole. Consequently, the screen size cannot be optimized due to the finite current that can be used. This limitation can drive (i) degradation of the uncertainty and (ii) the saturation of the field of view of the acquisition system. In this case, as for the previous studies, the results were validated by simulations with the ELEGANT tracking code.

These interesting results open a broad research field that deserves a deep investigation already taken into account in the design phase of future accelerators.

Conclusions

In this thesis, transverse wakefield measurements and bunch length measurements performed using the Radio Frequency Deflector (RFD) method, were presented. Both these studies are linked to an electromagnetic transverse field that affects the electron beam while it is traveling in the accelerator. Moreover, there is a direct connection between the two studies: the wakefield effect on an electron bunch grows proportionally with the bunch length, while the measurement of the bunch length can be spoiled by possible additional terms introduced by the wakefield during the acceleration phase. These two studies are then strictly related, the main difference being that the wakefields are an unwanted and generally detrimental effect while the transverse field of the RFD, used to perform bunch length measurement, is intentionally caused.

For the wakefield study, two methods for assessing the wakefield effect in the CLIC accelerating structure's novel prototype were presented. One method directly measures the field inside the structure thanks to pickup antennas, named WakeField Monitors (WFMs), installed inside an accelerating cell. The other one uses a beam screen, a device commonly installed in any beamlines, to measure the wakefield effect on the beam. Each method has peculiarities which can be of particular interest for future accelerators. The WFMs have the advantages of performing a direct measurement sensing the field directly inside the structure.

However, the system is also complicated since it needs a careful calibration process in order to get quantitative information on the field and its effect on the beam, and to design, build and operate a detection chain adapted to the wakefield high frequency signal is not straightforward. **A**n uncalibrated WFM signal is indeed anyway useful for beam correction, since minimizing the signal should bring the beam to the structure center. However the WFMs signal is mainly local, relative to the cell where the pickup antennas are installed. Thus, in case of an angle between the structure and the beam trajectory or a misalignment between the structure cells, a residual kick may be present even for a minimized WFM signal.

The direct measurement of the wakefield kick on the beam, using a screen or a beam position monitor is particularly interesting since it gives a global information on the wakefield excited in the whole structure and their effects on the beam. On the other side, it is not easy to separate the contribution from different wakefield sources, possibly including the beam pipe neighbouring the structure.

For both studied methods, experimental campaigns were carried out at CLEAR, where the CLIC accelerating structure's baseline prototype is installed. The experiments were based on the principle of exciting a wakefield by inducing an offset between the electric center of the accelerating structure and the beam.

During the initial test it was observed that the active alignment system used

to move the structure was not working correctly. For this reason, an alternative method was developed where the beam itself was displaced by a carefully controlled bump produced by two corrector magnets. Such method was found to be precise, faster, and more practical than the active alignment system and was therefore used even when the issue with the latter was fixed. As a first result, the study confirmed the kick effect expected by a dipole mode wakefield and its linear dependence from the beam displacement. Moreover, the results showed that no strong build up effect is present, meaning that the short-range wakefields dominate the dynamics, as was indeed expected from the simulation model. Also, the often neglected dependence of the wakefield from the bunch length was investigated. Recently, a completely new, simpler movement system was designed and eventually installed. Furthermore, the accelerator layout is under revision aiming to improve the beam quality. These improvements, based on the experience gained during the thesis experimental work, will allow a higher precision and faster data taking for future measurement campaigns.

For the bunch length measurement, two different studies were performed. The first aim was to extend the range of bunch lengths (especially towards smaller lengths) accessible with the standard measurement layout. Beyond that, the potentiality of a novel measurement layout was studied and documented. The novel layout has the advantage of using devices that are often already installed in the accelerator between the RFD and the screen, but are usually kept switched off during the measurement. For the standard measurement layout, two advanced measurement procedures were proposed. The first procedure allows measuring the energy chirp and the energy spread directly.

The second one allows to obtain information on the correlation terms between the longitudinal and transverse plane. The theoretical treatment predictions were compared to results from tracking code simulations. A particular case study is the **G**BS, for which start to end simulations (i.e., simulation of the whole accelerator line) were performed. The novel layout uses an additional focusing element installed between the RFD and the screen. Following the results of a theoretical approach, supported by both simulation and experiment, it was proven that no spurious effects which may compromise the measurements were introduced by the new layout, with respect to the standard measurement method and characteristics are preserved. Moreover, thanks to the additional degrees of freedom, the new layout has shown interesting potentialities. For example, it is possible to directly measure the correlation terms for which only indirect information could be obtained in the conventional layout. Additionally, if correctly tuned, the focusing elements can enhance the resolution of the measurement. Finally, a detailed study on the uncertainty was carried out, extensively by comparing the two layouts to show the possibility of an uncertainty reduction in some cases. The results are opening exciting possibilities, the novel layout can improve the measurement metrological characteristics without requiring in most cases a redesigning of the layout or the installation of expensive, and still not commonly available, high frequency deflecting cavities.

References

[1] A. Degiovanni, W. Wuensch, and Giner Navarro J. "Comparison of the conditioning of high gradient accelerating structures". In: *Physical Review Accelerators and Beams* 19 (3 Mar. 2016), p. 6. DOI: 10.1103/PhysRevAccelBeams.19.032001.

[2] E. Esarey, P. Sprangle, J. Krall, and A. Ting. "Overview of plasma-based accelerator concepts". In: *IEEE Transactions on Plasma Science* 24.2 (1996), pp. 252–288. DOI: 10.1109/27.509991.

[3] B. Aune et al. "Superconducting TESLA cavities". In: *Physical Review Special Topics-Accelerators and Beams* 3 (9 Sept. 2000), p. 25. DOI: 10.1103/PhysRevSTAB.3.092001.

[4] A. Degiovanni et al. "High-Gradient test results from a CLIC prototype accelerating structure: TD26CC". In: (June 2014), p. 4. URL: https://cds.cern.ch/record/1742280.

[5] J.Y. Raguin. "The Swiss FEL S-band accelerating structure: RF design". In: *Proceedings of LINAC2012, Tel-Aviv, Israel* (2012), pp. 498–500. URL: https://accelconf.web.cern.ch/linac2012/papers/tupb011.pdf.

[6] A. Grudiev and W. Wuensch. "Design of the CLIC Main LINAC Accelerating Structure for CLIC Conceptual Design Report". In: *Proceedings, 25th International Linear Accelerator Conference, LINAC2010: Tsukuba, Japan*. Sept. 2011. URL: http://accelconf.web.cern.ch/AccelConf/LINAC2010/papers/mop068.pdf.

[7] T. Weiland and R. Wanzenberg. "Wake fields and impedances". In: *Frontiers of Particle Beams: Intensity Limitations*. Berlin, Heidelberg: Springer Berlin Heidelberg, 1992, pp. 39–79. ISBN: 978-3-540-46797-7.

[8] G. Rumolo, A. Latina, and D. Schulte. "Effects of Wake Fields in the CLIC BDS". In: (July 2006). URL: https://cds.cern.ch/record/971898.

[9] F. Peauger et al. "Wakefield monitor development for CLIC accelerating structure". In: (Sept. 2010), p. 3. URL: https://cds.cern.ch/record/1347203.

[10] H. Mainaud Durand et al. "PACMAN Project: a new solution for the high-accuracy alignment of accelerator aomponents". In: (2016). DOI: 10.18429/JACoW-IPAC2016-MOOCB01.

[11] H. Mainaud Durand et al. "Main achievements of the PACMAN project for the alignment at micrometric scale of accelerator components". In: *IPAC17, Copenhagen, Denmark* (2017). DOI: 10.18429/JACoW-IPAC2017-TUPIK077.

[12] R. Akre, L. Bentson, P. Emma, and P. Krejcik. "Bunch length measurements using a transverse RF deflecting structure in the SLAC LINAC". In: *Proceedings of the EPAC2002 conference*. 2002. URL: https://accelconf.web.cern.ch/e02/PAPERS/THPRI097.pdf.

[13] A. Cianchi et al. "Observations and diagnostics in high brightness beams". In: *Nuclear Instruments and Methods in Physics Research Section A: Accelerators, Spectrometers, Detectors and Associated Equipment* 829 (2016), pp. 343–347. ISSN: 0168-9002. DOI: 10.1016/j.nima.2016.03.076.

[14] R. Akre, L. Bentson, P. Emma, and P. Krejcik. "A transverse RF deflecting structure for bunch length and phase space diagnostics". In: *PACS2001. Proceedings of the 2001 Particle Accelerator Conference*. Vol. 3. 2001, pp. 2353–2355. DOI: 10.1109/PAC.2001.987379.

[15] L. Sabato et al. "A Measurement Method Based on RF Deflector for Particle Bunch Longitudinal Parameters in Linear Accelerators". In: *IEEE Transactions on Instrumentation and Measurement* 70 (2021), pp. 1–9. DOI: 10.1109/TIM.2020.3009342.

[16] P. Arpaia et al. "Enhancing particle bunch-length measurements based on Radio Frequency Deflector by the use of focusing elements". In: *Scientific RepoRtS* 10.1 (2020), pp. 1–12. DOI: 10.1038/s41598-020-67997-1.

[17] K. N. Sjobak et al. "Status of the CLEAR Electron Beam User Facility at CERN". In: *Proceedings, 10th Int. Particle Accelerator Conf. (IPAC'19), Melbourne, Australia*. May 2019. DOI: 10.18429/JACoW-IPAC2019-MOPTS054.

[18] P. Arpaia, R. Corsini, A. Gilardi, and K.N. Sjobak. "Beam–based alignment of the CLIC high-gradient X-Band accelerating structure using beam-screen". In: *2019 IEEE International Instrumentation and Measurement Technology Conference (I2MTC)*. IEEE. 2019, pp. 1–6. DOI: 10.1109/I2MTC.2019.8827121.

[19] D. Gamba et al. "The CLEAR user facility at CERN". In: *Nuclear Instruments and Methods in Physics Research Section A: Accelerators, Spectrometers, Detectors and Associated Equipment* 909 (2018), pp. 480–483. ISSN: 0168-9002. DOI: 10.1016/j.nima.2017.11.080.

[20] J.J. Thomson. "Cathode rays". In: *The London, Edinburgh, and Dublin Philosophical Magazine and Journal of Science* 44.269 (1897), pp. 293–316. DOI: 10.1080/14786449708621070.

[21] E. Rutherford. "The scattering of α and β particles by matter and the structure of the atom". In: *The London, Edinburgh, and Dublin Philosophical Magazine and Journal of Science* 21.125 (1911), pp. 669–688. DOI: 10.1080/14786435.2011.617037.

[22] R. Oerter. *The theory of almost everything: The standard model, the unsung triumph of modern physics*. Penguin, 2006. DOI: 10.1063/1.2337829.

[23] U.S. Department of Energy. *Standard Models - Overview*. 2020-19-05. URL: https://www.symmetrymagazine.org/standard-model.

[24] G. Aad et al. "Observation of a new particle in the search for the Standard Model Higgs boson with the ATLAS detector at the LHC". In: *Physics Letters B* 716.1 (2012), pp. 1–29. DOI: 10.1016/j.physletb.2012.08.020.

[25] P. West. *Introduction to Supersymmetry and Supergravity*. Revised and Extended Second. World Scientific, 1990. DOI: 10.1142/1002.

[26] D.J. Griffiths. *Introduction to Quantum Mechanics*. Prentice Hall, 1994. ISBN: 978-0-13-124405-4.

[27] L. De Broglie. "The reinterpretation of wave mechanics". In: *Foundations of Physics* 1.1 (1970), pp. 5–15. DOI: 10.1007/BF00708650.

[28] M. Planck. "On the law of distribution of energy in the normal spectrum". In: *Annalen der physik* 4.553 (1901), p. 1. URL: http://fizika.unios.hr/~ilukacevic/dokumenti/materijali_za_studente/qm1/Planck_1901.pdf.

[29] O. Barbalat. "Applications of particle accelerators; rev. version". In: (Feb. 1994), p. 23. DOI: 10.5170/CERN-1994-001.841.

[30] M. Bai. "Accelerators for America's Future". In: *APS April Meeting Abstracts*. Vol. 2016. APS Meeting Abstracts. Mar. 2016. URL: https://ui.adsabs.harvard.edu/abs/2016APS..APR.A1003B.

[31] R.W. Hamm and M.E. Hamm. *Industrial accelerators and their applications*. World Scientific, 2012. DOI: 10.1142/7745.

[32] G. Cuttone. *Applications of Particle Accelerators in Medical Physics*. Tech. rep. Geneva: CERN, Sept. 2008. URL: https://cds.cern.ch/record/1514553.

[33] C.D. Bowman et al. "Nuclear energy generation and waste transmutation using an accelerator-driven intense thermal neutron source". In: *Nuclear Instruments and Methods in Physics Research Section A: Accelerators, Spectrometers, Detectors and Associated Equipment* 320.1-2 (1992), pp. 336–367. ISSN: 0168-9002. DOI: 10.1016/0168-9002(92)90795-6.

[34] A. Sessler and E. Wilson. *Engines of discovery: a century of particle accelerators*. World Scientific, 2014. DOI: 10.1142/8552.

[35] O.S. Brüning et al. *LHC Design Report*. CERN Yellow Reports: Monographs. Geneva: CERN, 2004. DOI: 10.5170/CERN-2004-003-V-1.

[36] The FCC Collaboration. "FCC-ee: The Lepton Collider: Future Circular Collider Conceptual Design Report Volume 2". In: *European Physical Journal: Special Topics* 228.2 (June 2019), pp. 261–623. ISSN: 1951-6355. DOI: 10.1140/epjst/e2019-900045-4.

[37] T.K. Charles et al. "The Compact Linear Collider (CLIC)-2018 Summary Report". In: CERN Yellow Reports: Monographs (Dec. 2018). DOI: 10.23731/CYRM-2018-002.

[38] H. Baer et al. "The International Linear Collider Technical Design Report - Volume 2: Physics". In: (June 2013). DOI: 10.2172/1347944.

[39] M. Krammer. "The update of the European strategy for particle physics". In: *Physica Scripta* T158 (Dec. 2013). DOI: 10.1088/0031-8949/2013/t158/014019.

[40] H.H. Braun et al. "Emittance growth and energy loss due to coherent synchrotron radiation in a bunch compressor". In: *Physical Review Special Topics-Accelerators and Beams* 3 (12 Dec. 2000), p. 5. DOI: 10.1103/PhysRevSTAB.3.124402.

[41] P. Roloff, R. Franceschini, U. Schnoor, and A. Wulzer. "The Compact Linear e^+e^- Collider (CLIC): Physics Potential". In: (Dec. 2018). URL: https://cds.cern.ch/record/2652257.

[42] A. Robson et al. *The Compact Linear e^+e^- Collider (CLIC): Accelerator and Detector*. Tech. rep. Dec. 2018. URL: https://cds.cern.ch/record/2652846.

[43] A. Mosnier et al. "The probe beam linac in CTF3". In: *Tenth European Particle Accelerator Conference "EPAC'06"*. June 2006, pp. 679–681. URL: http://hal.in2p3.fr/in2p3-00118817.

[44] M. Aicheler et al. *A Multi-TeV Linear Collider Based on CLIC Technology: CLIC Conceptual Design Report*. CERN Yellow Reports: Monographs. Geneva: CERN, 2012. DOI: 10.5170/CERN-2012-007.

[45] I. Syratchev and A. Cappelletti. "A new high-power RF device to vary the output power of CLIC power extraction and transfer structures (PETS)". In: (May 2010), p. 4. URL: https://cds.cern.ch/record/1287859.

[46] E. Adli. "A Study of the Beam Physics in the CLIC Drive Beam Decelerator". PhD thesis. 2009. URL: https://cds.cern.ch/record/1239173.

[47] M. Aicheler et al. "The Compact Linear Collider (CLIC) - Project Implementation Plan". In: (Mar. 2019). URL: https://ui.adsabs.harvard.edu/abs/2019arXiv190308655A.

[48] D. Schulte et al. "Status of the exploration of an alternative CLIC first energy stage based on klystrons". In: (May 2013), p. 3. URL: https://cds.cern.ch/record/1588126.

[49] D. Schulte et al. *Exploration of a klystron-powered first energy stage of CLIC*. Tech. rep. Geneva: CERN, July 2012. URL: https://cds.cern.ch/record/1611741.

[50] J. De Blas et al. "The CLIC potential for new physics". In: (2018). DOI: 10.23731/CYRM-2018-003.

[51] FermiLab Today. *Cross-Section*. URL: https://cms.cern/news/what-do-we-mean-cross-section-particle-physics.

[52] R. Corsini. "Final Results From the Test Facility (CTF3)". In: *Proc. 8 th Int. Particle Accelerator Conf., IPAC2017, Copenhagen, Denmark*. 2017, p. 6. ISBN: 978-3-95450-182-3. DOI: 10.18429/JACoW-IPAC2017-TUZB1.

[53] N. Catalan-Lasheras et al. "Experience Operating an X-band High-Power Test Stand at CERN". In: (June 2014), p. 4. URL: https://cds.cern.ch/record/1742951.

[54] R. Corsini et al. "First full beam loading operation with the CTF3 LINAC". In: (Aug. 2004). URL: https://cds.cern.ch/record/791372.

[55] R. Corsini, A. Ferrari, L Rinolfi, P Royer, and F. Tecker. "Experimental results on electron beam combination and bunch frequency multiplication". In: *Physical Review Special Topics-Accelerators and Beams* 7.4 (Apr. 2004). DOI: 10.1103/PhysRevSTAB.7.040101.

[56] R. Ruber et al. "The CTF3 two-beam test stand". In: *Nuclear Instruments and Methods in Physics Research Section A: Accelerators, Spectrometers, Detectors and Associated Equipment* 729 (2013), pp. 546–553. ISSN: 0168-9002. DOI: 10.1016/j.nima.2013.07.055.

[57] H. Braun et al. "A new method for RF power generation for two-beam linear colliders". In: *AIP Conference Proceedings CONF-981099*. Vol. 474. 1. American Institute of Physics. 1999, pp. 1–12. DOI: 10.1063/1.59012.

[58] P. Urschütz et al. "Beam Dynamics and First Operation of the Sub-Harmonic Bunching System in the CTF3 Injector". In: (July 2006). URL: https://cds.cern.ch/record/972321.

[59] H. Wiedemann. *Particle accelerator physics*. Springer Nature, 2015. DOI: 10.1007/978-3-319-18317-6.

[60] R. Corsini et al. "First experiments at the CLEAR User Facility". In: (2018), p. 4. DOI: 10.18429/JACoW-IPAC2018-THPMF014.

[61] *2020 Update of the European Strategy for Particle Physics*. Tech. rep. Geneva, 2020. DOI: 10.17181/ESU2020.

[62] *Joint Universities Accelerator School (JUAS)*. URL: https://www.esi-archamps.eu/Thematic-Schools/Discover-JUAS.

[63] *CLEAR WebPages*. URL: https://clear.cern.

[64] X. Wu et al. "High-gradient breakdown studies of an X-band Compact Linear Collider prototype structure". In: *Physical Review Accelerators and Beams* 20.5 (May 2017). DOI: 10.1103/PhysRevAccelBeams.20.052001.

[65] O. Grasset et al. "JUpiter ICy moons Explorer (JUICE): An ESA mission to orbit Ganymede and to characterise the Jupiter system". In: *Planetary and Space Science* 78 (2013), pp. 1–21. ISSN: 0032-0633. DOI: 10.1016/j.pss.2012.12.002.

[66] M. Tali et al. "High-energy electron-induced SEUs and Jovian environment impact". In: *IEEE Transactions on Nuclear Science* 64.8 (2017), pp. 2016–2022. DOI: 10.1109/TNS.2017.2713445.

[67] M. Tali et al. "Mechanisms of Electron-Induced Single-Event Latchup". In: *IEEE Transactions on Nuclear Science* 66.1 (2019), pp. 437–443. DOI: 10.1109/TNS.2018.2884537.

[68] D. Soderstrom et al. "Electron-Induced Upsets and Stuck Bits in SDRAMs in the Jovian Environment". In: *IEEE Nuclear and Space Radiation Effects Conference (NSREC)*. Nov. 2020. URL: https://hal-lirmm.ccsd.cnrs.fr/lirmm-03028881.

[69] P. Montay-Gruel et al. “Irradiation in a FLASH: Unique sparing of memory in mice after whole brain irradiation with dose rates above 100 Gy/s”. In: *Radiotherapy and Oncology* 124.3 (Sept. 2017), pp. 365–369. DOI: 10.1016/j.radonc.2017.05.003.

[70] E. Schüler et al. “Very high-energy electron (VHEE) beams in radiation therapy; Treatment plan comparison between VHEE, VMAT, and PPBS”. In: *Medical physics* 44.6 (June 2017), pp. 2544–2555. DOI: doi:10.1002/mp.12233.

[71] S. Reinhardt, M. Hillbrand, J.J. Wilkens, and W. Assmann. “Comparison of Gafchromic EBT2 and EBT3 films for clinical photon and proton beams”. In: *Medical physics* 39.8 (2012), pp. 5257–5262. DOI: 10.1118/1.4737890.

[72] M. McManus et al. “The challenge of ionisation chamber dosimetry in ultra-short pulsed high dose-rate Very High Energy Electron beams”. In: *Sci. Rep.* 10.1 (2020). DOI: 10.1038/s41598-020-65819-y.

[73] F. Romano et al. “Challenges in dosimetry of particle beams with ultra-high pulse dose rates”. In: *Journal of Physics: Conference Series* 1662.1 (2020). DOI: 10.1088/1742-6596/1662/1/012028.

[74] A. Lagzda et al. “Very-High Energy Electron (VHEE) Studies at CERN’s CLEAR user facility”. In: *9th Int. Particle Accelerator Conf.(IPAC’18), Vancouver, BC, Canada*. JACOW Publishing, Geneva, Switzerland. May 2018, pp. 445–448. DOI: 10.18429/JACoW-IPAC2018-MOPML023.

[75] K. Kokurewicz et al. “Dosimetry for new radiation therapy approaches using high energy electron accelerators”. In: *Frontiers in Physics* 8 (2020), p. 493. ISSN: 2296-424X. DOI: 10.3389/fphy.2020.568302.

[76] D. Poppinga et al. “VHEE beam dosimetry at CERN Linear Electron Accelerator for Research under ultra-high dose rate conditions”. In: *Biomedical Physics & Engineering Express* 7.1 (Dec. 2020). DOI: 10.1088/2057-1976/abcae5.

[77] J.J. Su, T. Katsouleas, J.M. Dawson, and R. Fedele. “Plasma lenses for focusing particle beams”. In: *Physical Review A* 41.6 (Mar. 1990), pp. 3321–3331. DOI: 10.1103/PhysRevA.41.3321.

[78] C.A. Lindstrøm et al. “Overview of the CLEAR plasma lens experiment”. In: *Nuclear Instruments and Methods in Physics Research Section A: Accelerators, Spectrometers, Detectors and Associated Equipment* 909 (2018), pp. 379–382. ISSN: 0168-9002. DOI: 10.1016/j.nima.2018.01.063.

[79] C. A. Lindstrøm et al. “Emittance preservation in an aberration-free active plasma lens”. In: *Physical review letters* 121.19 (2018). DOI: 10.1103/PhysRevLett.121.194801.

[80] B. Green et al. “High-field high-repetition-rate sources for the coherent THz control of matter”. In: *Scientific reports* 6 (2016). DOI: 10.1038/srep22256.

[81] A. Curcio et al. "Beam-based sub-THz source at the CERN linac electron accelerator for research facility". In: *Physical Review Accelerators and Beams* 22.2 (Feb. 2019). DOI: 10.1103/PhysRevAccelBeams.22.020402.

[82] A. Curcio et al. "Noninvasive bunch length measurements exploiting Cherenkov diffraction radiation". In: *Physical Review Accelerators and Beams* 23 (2 Feb. 2020), p. 13. DOI: 10.1103/PhysRevAccelBeams.23.022802.

[83] S. Casalbuoni, B. Schmidt, P. Schmüser, V. Arsov, and S. Wesch. "Ultrabroadband terahertz source and beamline based on coherent transition radiation". In: *Physical Review Special Topics-Accelerators and Beams* 12.3 (Mar. 2009). DOI: 10.1103/PhysRevSTAB.12.030705.

[84] H.L. Andrews et al. "Reconstruction of the time profile of 20.35 GeV, subpicosecond long electron bunches by means of coherent Smith-Purcell radiation". In: *Physical Review Special Topics-Accelerators and Beams* 17.5 (May 2014). DOI: 10.1103/PhysRevSTAB.17.052802.

[85] A.M. Cook et al. "Observation of narrow-band terahertz coherent Cherenkov radiation from a cylindrical dielectric-lined waveguide". In: *Physical Review Letters* 103.9 (Aug. 2009). DOI: 10.1103/PhysRevLett.103.095003.

[86] E. Gschwendtner et al. "AWAKE, the advanced proton driven plasma wakefield acceleration experiment at CERN". In: *Nuclear Instruments and Methods in Physics Research Section A: Accelerators, Spectrometers, Detectors and Associated Equipment* 829 (2016), pp. 76–82. ISSN: 0168-9002. DOI: 10.1016/j.nima.2016.02.026.

[87] A.W. Chao, K.H. Mess, M. Tigner, and F. Zimmermann. *Handbook of accelerator physics and engineering*. Hackensack, USA: World Scientific, 2013. ISBN: 978-981-4415-84-2. DOI: 10.1142/8543.

[88] M. Hÿtch and P W Hawkes. *Advances in Imaging and Electron Physics*. Vol. 193. Elsevier Science, 2016. ISBN: 978-0-1280-5231-0.

[89] F. L. Coolidge. *Statistics: A Gentle Introduction*. Sage Publications, 2012. ISBN: 978-1-4129-9171-1.

[90] K.L.F. Bane, P.B Wilson, and T Weiland. "Wake fields and wake field acceleration". In: *AIP Conference Proceedings*. Vol. 127. 1. American Institute of Physics. 1985, pp. 875–928. DOI: 10.1063/1.35182.

[91] P.B. Wilson. "Introduction to wakefields and wake potentials". In: *AIP Conference Proceedings*. Vol. 184. 1. American Institute of Physics. 1989, pp. 525–564. DOI: 10.1063/1.38045.

[92] M. Dohlus and R. Wanzenberg. "An introduction to wake fields and impedances". In: *CERN Yellow Reports: School Proceedings* 3 (2017). DOI: 10.23730/CYRSP-2017-003.15.

[93] A.W. Chao. *Physics of collective beam instabilities in high energy accelerators*. Wiley, 1993. ISBN: 978-0-471-55184-3.

[94] W. Bruns. "GdfidL: A finite difference program with reduced memory and CPU usage". In: *Proceedings of the 1997 Particle Accelerator Conference (Cat. No. 97CH36167)*. Vol. 2. IEEE. 1997, pp. 2651–2653. DOI: 10.1109/PAC.1997.751304.

[95] H. Spachmann and U. Becker. "Electron gun simulation with CST particle studio". In: *Nuclear Instruments and Methods in Physics Research Section A: Accelerators, Spectrometers, Detectors and Associated Equipment* 558.1 (2006), pp. 50–53. ISSN: 0168-9002. DOI: 10.1016/j.nima.2005.11.075.

[96] L. Ge et al. "Advances in parallel finite element code suite ACE3P". In: *6th Int. Particle Accelerator Conf.(IPAC'15), Richmond, VA, USA*. JACOW, Geneva, Switzerland. May 2015, pp. 702–704. DOI: 10.18429/JACoW-IPAC2015-MOPMN002.

[97] G. De Michele. "Wakefield simulations and measurements for the CLIC RF accelerating structure". PhD thesis. 2014. DOI: 10.5075/epfl-thesis-6185.

[98] J. Ögren. "Beam Diagnostics and Dynamics in Nonlinear Fields". PhD thesis. Acta Universitatis Upsaliensis, 2017. ISBN: 978-9-1513-0121-1.

[99] S. Vaganian and H. Henke. "The Panofsky-Wenzel theorem and general relations for the wake potential". In: *Part. Accel.* 48 (1995), pp. 239–242. URL: https://cds.cern.ch/record/1108316.

[100] A. Wolski. *Beam Dynamics in High Energy Particle Accelerators*. London: Imperial College Press, 2014. ISBN: 978-1-78326-277-9. DOI: 10.1142/p899.

[101] K. N. Sjøbæk. "Avoiding vacuum arcs in high gradient normal conducting RF structures". PhD thesis. Oslo U., June 2016. URL: https://cds.cern.ch/record/2226840.

[102] D. Schulte. *Multi-bunch calculations in the CLIC main LINAC*. Tech. rep. July 2009, p. 4. URL: https://cds.cern.ch/record/1227215.

[103] A. Latina et al. "Compact-Light design study". In: *60th ICFA Advanced Beam Dynamics Workshop on Future Light Sources (FLS'18), Shanghai, China*. JACOW Publishing, Geneva, Switzerland. Mar. 2018, pp. 85–88. ISBN: 978-3-95450-206-6. DOI: 10.18429/JACoW-FLS2018-WEP1WC02.

[104] J. Stohr. *LINAC coherent light source II (LCLS-II) Conceptual Design Report*. Tech. rep. SLAC National Accelerator Lab., Menlo Park, CA (United States), 2011. DOI: 10.2172/1029479.

[105] C.J. Milne et al. "SwissFEL: the Swiss X-ray Free Electron Laser". In: *Applied Sciences* 7.7 (2017), p. 720. ISSN: 2076-3417. DOI: 10.3390/app7070720.

[106] A. Latina, D. Schulte, Y. Levinsen, and J. Snuverink. *Evolution of the tracking code PLACET*. Tech. rep. CERN-ACC-2013-0083. May 2013, p. 3. URL: https://cds.cern.ch/record/1574813.

[107] *PLACET Web-Page*. URL: https://twiki.cern.ch/twiki/bin/view/ABPComputing/Placet.

[108] T. Weiland. "Transverse beam cavity interaction. Part I: Short range forces". In: *Nuclear Instruments and Methods in Physics Research* 212.1-3 (1983), pp. 13–21. ISSN: 0167-5087. DOI: 10.1016/0167-5087(83)90672-5.

[109] W.K.H. Panofsky and R.B. Neal. "Electrons Accelerated to the 10-to 20-GeV Range". In: *Science* 152.3727 (1966), pp. 1353–1355. ISSN: 0036-8075. DOI: 10.1126/science.152.3727.1353.

[110] H. Zha et al. "Beam-based measurements of long-range transverse wakefields in the Compact Linear Collider main-LINAC accelerating structure". In: *Physical Review Accelerators and Beams* 19 (1 Jan. 2016), p. 9. DOI: 10.1103/PhysRevAccelBeams.19.011001.

[111] R.E. Shafer. "Beam Position Monitoring". In: *AIP conference proceedings*. Vol. 249. 1. AIP. 1992. DOI: 10.1063/1.41980.

[112] F. J. Decker et al. *Long range wakefields and split-tune lattice at the SLC*. Tech. rep. Stanford Linear Accelerator Center, 1996. URL: https://inspirehep.net/files/10f8cdb1e70862f8dccfd53ff512104f.

[113] Y.M. Shin et al. *Beam-Dynamics Analysis of Long-Range Wakefield Effects on the SCRF Cavities at the Fast Facility*. Tech. rep. 2018. DOI: 10.18429/JACoW-FEL2017-TUP016.

[114] K.L.F. Bane, A. Mosnier, A. Novokhatsky, and K. Yokoya. *Calculation of the short-range longitudinal wakefields in the NLC LINAC*. Tech. rep. Stanford Linear Accelerator Center (SLAC), Menlo Park, CA (United States), 1998, pp. 137–139. URL: https://accelconf.web.cern.ch/e98/PAPERS/THP29C.PDF.

[115] A. Latina et al. "Tests of Wakefield-Free Steering at ATF2". In: (2015), p. 4. URL: https://cds.cern.ch/record/2141787.

[116] A. Latina et al. "Experimental demonstration of a global dispersion-free steering correction at the new linac test facility at SLAC". In: *Physical Review Special Topics-Accelerators and Beams* 17.4 (Apr. 2014). DOI: 10.1103/PhysRevSTAB.17.042803.

[117] A. Latina, J. Pfingstner, D. Schulte, and E. Adli. "Tests of Beam-based Alignment at FACET". In: *5th International Particle Accelerator Conference*. July 2014. DOI: 10.18429/JACoW-IPAC2014-TUPRO065.

[118] P. Bambade et al. "Present status and first results of the final focus beam line at the KEK Accelerator Test Facility". In: *Physical Review Special Topics-Accelerators and Beams* 13 (4 Apr. 2010), p. 10. DOI: 10.1103/PhysRevSTAB.13.042801.

[119] J. Snuverink et al. "Measurements and simulations of wakefields at the Accelerator Test Facility 2". In: *Physical Review Accelerators and Beams* 19.9 (Sept. 2016). DOI: 10.1103/PhysRevAccelBeams.19.091002.

[120] T. Okugi. "Achievement of small beam size at ATF2 beamline". In: *28th International Linear Accelerator Conference*. 2017. DOI: 10.18429/JACoW-LINAC2016-MO3A02.

[121] P. Korysko. "Intensity-dependent effects in the Accelerator Test Facility 2 and extrapolation to future electron-positron linear colliders". PhD thesis. University of Oxford, 2020. URL: https://cds.cern.ch/record/2728417.

[122] J. Resta-Lopez. "Single-bunch transverse emittance growth due to collimator wakefield effects". In: (Sept. 2013). URL: https://arxiv.org/pdf/1309.0480.pdf.

[123] P. Tenenbaum et al. "Direct measurement of the transverse wakefields of tapered collimators". In: *Physical Review Special Topics-Accelerators and Beams* 10.3 (2007). DOI: 10.1103/PhysRevSTAB.10.034401.

[124] S. Molloy et al. "Measurements of the transverse wakefields due to varying collimator characteristics". In: *2007 IEEE Particle Accelerator Conference (PAC)*. IEEE. 2007, pp. 4207–4209. DOI: 10.1109/PAC.2007.4440079.

[125] J.L. Fernandez-Hernando, S. Molloy, J.D.A. Smith, and N. K. Watson. "Measurements of collimator wakefields at End Station A". In: (). URL: https://inspirehep.net/files/849946cf4960db44018ea44e07c0c0e2.

[126] P. Tenenbaum and D. Onoprienko. *Direct Measurement of the Resistive Wakefield in Tapered Collimators*. Tech. rep. July 2004. URL: https://accelconf.web.cern.ch/e04/papers/weplt158.pdf.

[127] J. Resta-Lopez et al. "Proposal for Single-Bunch Collimator Wakefield Measurements at SLAC ESTB". In: (Dec. 2012). URL: https://arxiv.org/pdf/1212.6023.pdf.

[128] F. Fu et al. "Demonstration of nonlinear-energy-spread compensation in relativistic electron bunches with corrugated structures". In: *Physical Review Letters* 114.11 (Mar. 2015). DOI: 10.1103/PhysRevLett.114.114801.

[129] S. Bettoni, P. Craievich, A.A. Lutman, and M. Pedrozzi. "Temporal profile measurements of relativistic electron bunch based on wakefield generation". In: *Physical Review Accelerators and Beams* 19.2 (Feb. 2016). DOI: 10.1103/PhysRevAccelBeams.19.021304.

[130] M.W. Guetg et al. "Commissioning of the RadiaBeam/SLAC dechirper". In: *7th International Particle Accelerator Conference*. 2016. DOI: 10.18429/JACoW-IPAC2016-MOPOW044.

[131] Z. Zhang et al. "Electron beam energy chirp control with a rectangular corrugated structure at the Linac Coherent Light Source". In: *Physical Review Special Topics-Accelerators and Beams* 18.1 (Jan. 2015). DOI: 10.1103/PhysRevSTAB.18.010702.

[132] M. Benedikt et al. *Preliminary accelerator plans for maximizing the integrated LHC luminosity*. Tech. rep. Jan. 2006, p. 7. URL: https://cds.cern.ch/record/946248.

[133] N. Oshima et al. "Brightness enhancement method for a high-intensity positron beam produced by an electron accelerator". In: *Journal of Applied Physics* 103.9 (May 2008). DOI: 10.1063/1.2919783.

[134] F. Negoita et al. "Laser driven nuclear physics at ELI–NP". In: *Romanian Reports in Physics* 68.Supple (May 2016), S37–S144. URL: https://strathprints.strath.ac.uk/61644/.

[135] A. Degiovanni. "Accelerating Structures". In: (Apr. 2018). DOI: 10.23730/CYRSP-2017-001.91.

[136] W. Leemans and E. Esarey. "Laser-driven plasma-wave electron accelerators". In: *Phys. Today* 62.3 (2009), pp. 44–49. DOI: 10.1063/1.3099645.

[137] D. Filippetto et al. "Velocity bunching experiment at SPARC". In: *Proc. of the FEL 2009 conference, Liverpool, UK*. 2009. URL: https://accelconf.web.cern.ch/PAC2009/papers/mo6rfp071.pdf.

[138] Y. Otake et al. "Bunch length measurements at SCSS test accelerator toward XFEL/SPring-8". In: *Proc. of BIW* 10 (2010). URL: https://accelconf.web.cern.ch/BIW2010/papers/tupsm062.pdf.

[139] U. Iriso, G. Benedetti, and F. Pérez. "Experience with YAG and OTR screens at ALBA". In: *SAT* 5.2008.10 (2009), p. 15. URL: https://accelconf.web.cern.ch/d09/papers/tupb15.pdf.

[140] C. Martinez. "Determination of longitudinal electron bunch lengths on picosecond time scales". MA thesis. Barcelona, Polytechnic U., Sept. 1999. URL: http://cds.cern.ch/record/1164160.

[141] K. Scheidt. "Review of streak cameras for accelerators: features, applications and results". In: *7th European Particle Accelerator Conference (EPAC 2000)*. Vol. 2000. 2000, pp. 182–186. URL: https://accelconf.web.cern.ch/e00/papers/weyf202.pdf.

[142] C.P. Welsch et al. "Longitudinal beam profile measurements at CTF3 using a streak camera". In: *Journal of Instrumentation* 1.09 (2006). DOI: 10.1088/1748-0221/1/09/p09002.

[143] S. Bernd. *First Electro-Optical bunch length measurements at the E-XFEL*. Tech. rep. Sept. 2018. URL: https://accelconf.web.cern.ch/ibic2018/talks/weoa03_talk.pdf.

[144] I. Wilke et al. "Single-shot electron-beam bunch length measurements". In: *Phys. Rev. Lett.* 88 (12 Mar. 2002), p. 4. DOI: 10.1103/PhysRevLett.88.124801.

[145] J. T. Moody et al. "Ultrashort laser pulse driven inverse free electron laser accelerator experiment". In: *Phys. Rev. Accel. Beams* 19 (2 Feb. 2016). DOI: 10.1103/PhysRevAccelBeams.19.021305.

[146] R. Pompili et al. "First single-shot and non-intercepting longitudinal bunch diagnostics for comb-like beam by means of electro-optic sampling". In: *Nuclear Instruments and Methods in Physics Research Section A: Accelerators, Spectrometers, Detectors and Associated Equipment* 740 (Mar. 2014), pp. 216–221. ISSN: 0168-9002. DOI: 10.1016/j.nima.2013.10.031.

[147] M.M. Denisov and M.V. Fedorov. "Bremsstrahlung effect on relativistic electrons in a strong radiation field". In: *Sov. Phys. JETP* 26.4 (Apr. 1968), pp. 779–783. URL: http://jetp.ac.ru/cgi-bin/dn/e_026_04_0779.pdf.

[148] M.L. Cherry, G. Hartmann, D. Müller, and T.A. Prince. "Transition radiation from relativistic electrons in periodic radiators". In: *Physical Review D* 10.11 (Dec. 1974), pp. 3594–3607. DOI: 10.1103/PhysRevD.10.3594.

[149] V.P. Shestopalov. "Diffraction electronics". In: *KhIzV* (Jan. 1976). URL: https://ui.adsabs.harvard.edu/abs/1976KhIzV.....S.

[150] T. Nakazato et al. "Observation of coherent synchrotron radiation". In: *Physical review letters* 63.12 (Sept. 1989), pp. 1245–1248. DOI: 10.1103/PhysRevLett.63.1245.

[151] N. Akhmediev and M. Karlsson. "Cherenkov radiation emitted by solitons in optical fibers". In: *Physical Review A* 51.3 (Mar. 1995), pp. 2602–2607. DOI: 10.1103/PhysRevA.51.2602.

[152] D.B. Ion and W. Stocker. "Nuclear mesonic Cherenkov-like radiation from high energy nucleons". In: *Physical Review C* 52.6 (Dec. 1995), pp. 3332–3343. DOI: 10.1103/PhysRevC.52.3332.

[153] M. Veronese, R. Appio, P. Craievich, and G. Penco. "Absolute bunch length measurement using coherent diffraction radiation". In: *Phys. Rev. Lett.* 110 (7 Feb. 2013), p. 5. DOI: 10.1103/PhysRevLett.110.074802.

[154] L. Zhao et al. "Terahertz Oscilloscope for Recording Time Information of Ultrashort Electron Beams". In: *Phys. Rev. Lett.* 122 (14 Apr. 2019), p. 6. DOI: 10.1103/PhysRevLett.122.144801.

[155] J. H. Ko, S. H. Jung, H.S. Kang, I.S. Ko, and J. Park. "Electron bunch length measurement using coherent radiation source of fs-THz accelerator at Pohang accelerator laboratory". In: *Proceedings, 7th International Particle Accelerator Conference (IPAC 2016): Busan, Korea*. May 2016. DOI: 10.18429/JACoW-IPAC2016-MOPMR003.

[156] R. Corsini et al. "LIL bunch length and lattice parameters measurements in March 2000". In: *PS/LP Note* 1 (2000), pp. 2000–09. URL: http://citeseerx.ist.psu.edu/viewdoc/download?doi=10.1.1.538.6988&rep=rep1&type=pdf.

[157] Y. Honda et al. "Beam tuning and bunch length measurement in the bunch compression operation at the cERL". In: *Nuclear Instruments and Methods in Physics Research Section A: Accelerators, Spectrometers, Detectors and Associated Equipment* 875 (2017), pp. 156–164. DOI: 10.1016/j.nima.2017.09.027.

[158] R. Corsini et al. "New measurements of the LIL bunch length and lattice parameters". In: *PS/LP Note* 2 (2000), pp. 2000–13. URL: https://citeseerx.ist.psu.edu/viewdoc/download?doi=10.1.1.507.257&rep=rep1&type=pdf.

[159] Y. Ding et al. "Femtosecond X-ray pulse temporal characterization in Free-Electron Lasers using a transverse deflector". In: *Phys. Rev. ST Accel. Beams* 14 (12 Dec. 2011), p. 6. DOI: 10.1103/PhysRevSTAB.14.120701.

[160] J. Maxson et al. "Direct Measurement of Sub-10 fs relativistic electron ceams with ultralow emittance". In: *Phys. Rev. Lett.* 118 (15 Apr. 2017), p. 5. DOI: 10.1103/PhysRevLett.118.154802.

[161] G. Loew and O.H. Altenmueller. "Design and applications of RF separator structures at SLAC". In: *fifth Int. Conf. on High-Energy Accelerators, Frascati, Italy*. Aug. 1965. URL: https://inspirehep.net/files/a7460b2c44c8b040010 2bf312153debb.

[162] X.J. Wang. "Producing and measuring small electron bunches". In: *Proceedings of the 1999 Particle Accelerator Conference (Cat. No. 99CH36366)*. Vol. 1. IEEE. 1999, pp. 229–233. DOI: 10.1109/PAC.1999.795671.

[163] D. Alesini et al. "Sliced beam parameter measurements". In: *Proceedings of EPAC*. 2009. URL: http://accelconf.web.cern.ch/d09/papers/tuoa01.pdf.

[164] J. T. Moody, P. Musumeci, M. S. Gutierrez, J. B. Rosenzweig, and C. M. Scoby. "Longitudinal phase space characterization of the blow-out regime of RF photoinjector operation". In: *Phys. Rev. ST Accel. Beams* 12 (7 July 2009), p. 9. DOI: 10.1103/PhysRevSTAB.12.070704.

[165] Y. Ding et al. "Measurements and Simulations of Ultralow Emittance and Ultrashort Electron Beams in the LINAC Coherent Light Source". In: *Phys. Rev. Lett.* 102 (25 June 2009), p. 4. DOI: 10.1103/PhysRevLett.102.254801.

[166] M. Huning et al. *Observation of femtosecond bunch length using a transverse deflecting structure*. Tech. rep. 2005. URL: https://inspirehep.net/files/9ea ad9823d5deb79ed07e27612bae3af.

[167] J. Haimson. "Longitudinal Phase Space Measurements of Short Electron Bunches Using a 17 GHz Circularly Polarized Beam Deflector". In: *AIP Conference Proceedings*. Vol. 737. 1. 2004, pp. 95–108. DOI: 10.1063/1.184253 7.

[168] D. Alesini et al. "RF deflector design and measurements for the longitudinal and transverse phase space characterization at SPARC". In: *Nuclear Instruments and Methods in Physics Research Section A: Accelerators, Spectrometers, Detectors and Associated Equipment* 568.2 (2006), pp. 488–502. DOI: 10.1016/j.nima.2006.07.050.

[169] D. Filippetto et al. "Phase space analysis of velocity bunched beams". In: *Physical Review Special Topics-Accelerators and Beams* 14.9 (Sept. 2011). DOI: 10.1103/PhysRevSTAB.14.092804.

[170] M. Röhrs, C. Gerth, H. Schlarb, B. Schmidt, and P. Schmüser. "Time-resolved electron beam phase space tomography at a soft X-ray Free-Electron Laser". In: *Physical Review Special Topics-Accelerators and Beams* 12.5 (May 2009). DOI: 10.1103/PhysRevSTAB.12.050704.

[171] C. Swinson, M. Fedurin, M. Palmer, and I. Pogorelsky. "ATF Facilities upgrades and deflector cavity commissioning". In: *Proceedings, 6th International Beam Instrumentation Conference, IBIC2017*. 2017. DOI: 10.18429/JACo W-IBIC2017-MOPWC05.

[172] T. Plath et al. "Mapping few-femtosecond slices of ultra-relativistic electron bunches". In: *Scientific reports* 7.1 (2017), pp. 1–8. DOI: 10.1038/s41598 -017-02184-3.

[173] J. Haimson, B. Mecklenburg, G. Stowell, and B. Ishii. "A circularly polarized beam deflector for direct measurement of ultra short electron bunches". In: *AIP Conference Proceedings*. Vol. 647. 1. AIP. 2002, pp. 810–820. DOI: 10.1063/1.1524936.

[174] L. Sabato. "Bunch length measurements in the Gamma Beam System LINAC by Means of an RF Deflector at ELI–NP". PhD thesis. University of Sannio, 2017.

[175] K. Floettmann and V. V. Paramonov. "Beam dynamics in transverse deflecting RF structures". In: *Phys. Rev. ST Accel. Beams* 17 (2 Feb. 2014), p. 11. DOI: 10.1103/PhysRevSTAB.17.024001.

[176] R. Akre, L. Bentson, P. Emma, and P. Krejcik. "A transverse RF Deflecting structure for bunch length and phase space diagnostics". In: *Proc. of Particle Accelerator Conference (PAC)*. 2001, pp. 2353–2355. URL: http://accelconf.web.cern.ch/p01/PAPERS/WPAH116.PDF.

[177] P. Emma, J. Frisch, and P. Krejcik. "A transverse RF Deflecting structure for bunch length and phase space diagnostics". In: *LCLS Technical Note* 12 (2000). URL: https://www-ssrl.slac.stanford.edu/lcls/technotes/lcls-tn-00-12.pdf.

[178] K. Bongardt. *Calculation of the transfer matrix T in six dimensions for an RF–Deflector element*. Tech. rep. Los Alamos Scientific Lab., NM (USA), 1981. URL: https://cds.cern.ch/record/128202/files/la-8668-ms.pdf.

[179] K.L.F. Bane. *Short range dipole wakefields in accelerating structures for the NLC*. Tech. rep. Stanford Linear Accelerator Center, Menlo Park, CA (US), Mar. 2003. URL: https://inspirehep.net/files/950d76a578c95132eb3d8bf2f8721fe7.

[180] J.R. Towler et al. "Development and test of high resolution cavity BPMS for the CLIC main beam LINAC". In: (Sept. 2016), p. 5. DOI: 10.18429/JACoW-IBIC2015-TUPB060.

[181] T. Naito and T. Mitsuhashi. "Beam halo measurement utilizing YAG: Ce screen". In: *4th International Beam Instrumentation Conference (IBIC2015), Melbourne, Australia, 13-17 September 2015*. JACOW, Geneva, Switzerland. Sept. 2015, pp. 373–376. URL: https://accelconf.web.cern.ch/ibic2015/papers/proceed.pdf.

[182] G. Ising. "Prinzip einer methode zur herstellung von kanalstrahlen hoher voltzahl". In: *Ark. Mat. Astron. Fys.* 18 (1924), pp. 1–4. URL: https://cds.cern.ch/record/433984.

[183] R. Wideröe. "Über ein neues Prinzip zur Herstellung hoher Spannungen". In: *Arbeiten aus dem Elektrotechnischen Institut der Technischen Hochschule Aachen*. Springer, 1929, pp. 157–176. ISBN: 978-3-662-40440-9. DOI: 10.1007/978-3-662-40440-9_14.

[184] A. Grudiev, S. Calatroni, and W. Wuensch. "New local field quantity describing the high gradient limit of accelerating structures". In: *Physical Review Special Topics-Accelerators and Beams* 12.10 (Oct. 2009). DOI: 10.1103/PhysRevSTAB.12.102001.

[185] P. Arpaia, O.E. Berrig, L. De Vito, and A. Gilardi. "Reducing parasitic resonances in particle accelerators components by broadband Higher–Order–Mode couplers". In: *Measurement* 146 (2019), pp. 938–947. ISSN: 0263-2241. DOI: 10.1016/j.measurement.2019.07.034.

[186] D. Blechschmidt and D.J. Warner. *Parameters of the LEP injector LINACs*. Tech. rep. Geneva: CERN, Feb. 1988. URL: https://cds.cern.ch/record/2641876.

[187] F. Peauger et al. "Wakefield monitor development for CLIC accelerating structure". In: *Proceedings, 25th International Linear Accelerator Conference, LINAC2010: Tsukuba, Japan*. Sept. 2010, p. 3. URL: https://cds.cern.ch/record/1347203.

[188] R. Lillestøl et al. "Wakefield Monitor Experiments with X-Band Accelerating Structures". In: *Proceedings, 6th International Particle Accelerator Conference (IPAC 2015): Richmond, Virginia, USA*. May 2015, p. 4. DOI: 10.18429/JACoW-IPAC2015-MOPTY004.

[189] R. Lillestøl et al. "Status of Wakefield Monitor Experiments at the CLIC Test Facility". In: *Proceedings, 7th International Particle Accelerator Conference (IPAC 2016): Busan, Korea*. May 2016, p. 3. DOI: 10.18429/JACoW-IPAC2016-WEOBB02.

[190] R.H. Miller. *Comparison of standing-wave and traveling-wave structures*. Tech. rep. Stanford Linear Accelerator Center, Apr. 1986. URL: https://inis.iaea.org/search/search.aspx?orig_q=RN:18014094.

[191] R.L. Lillestol. *The CLIC Wake Field Monitor Study*. Tech. rep. Geneva: CERN, Nov. 2017. URL: http://cds.cern.ch/record/2751094.

[192] R. Chritin. *Mesures magnétiques d'un correcteur de type DJ*. Tech. rep. 2008. URL: http://ctf3-tbts.web.cern.ch/ctf3-tbts/beams/Rapport_correcteur_DJ.pdf.

[193] R. Talman. *Representation of thick quadrupoles by thin lenses*. Tech. rep. CERN, CH, Aug. 1985. URL: https://cds.cern.ch/record/533900/files/ssc-n-033.pdf.

[194] Keysight technologies. *83640A Synthesized Sweeper, 10 MHz to 40 GHz*. Tech. rep. URL: https://www.keysight.com/en/pd-1000001872%5C%3Aepsg%5C%3Apro-pn-83640A/synthesized-sweeper-10-mhz-to-40-ghz?pm=PL&nid=-32469.536880122&cc=FR&lc=fre.

[195] Keysight technologies. *E4413A Wide Dynamic Range Power Sensor, E-Series*. Tech. rep. URL: https://www.keysight.com/en/pd-1000002796%5C%3Aepsg%5C%3Apro-pn-E4413A/wide-dynamic-range-power-sensor-e-series?cc=FR&lc=fre.

[196] Keysight technologies. *E4418B EPM Series Single-Channel Power Meter*. Tech. rep. URL: https://www.keysight.com/en/pd-1000002798:epsg:pro-pn-E4418B/epm-series-single-channel-power-meter?cc=FR&lc=fre.

[197] L. Sabato et al. "Effects of energy chirp on bunch length measurement in linear accelerator beams". In: *Measurement Science and Technology* 28.8 (2017). DOI: 10.1088/1361-6501/aa6c8a.

[198] L. Sabato et al. "Energy Chirp Measurements by Means of an RF Deflector: a Case Study the Gamma Beam Source LINAC at ELI-NP". In: *Proc. of International Particle Accelerator Conference (IPAC), Copenhagen, Denmark*. JACoW, May 2017, pp. 242–245. ISBN: 978-3-95450-182-3. DOI: 10.18429/JACoW-IPAC2017-MOPAB059.

[199] L. Sabato et al. "RF deflector based measurements of the correlations between vertical and longitudinal planes at ELI–NP–GBS electron LINAC". In: *Proc. of International Beam Instrumentation Conference (IBIC), Grand Rapids, Michigan, USA*. Aug. 2017. URL: https://accelconf.web.cern.ch/ibic2017/papers/wepcc20.pdf.

[200] M. Borland. *Elegant: A flexible SDDS-compliant code for accelerator simulation*. Tech. rep. Argonne National Lab., IL (US), Aug. 2000. DOI: 10.2172/761286.

[201] K. Floettmann and V.V. Paramonov. "Beam dynamics in transverse deflecting RF structures". In: *Physical Review Special Topics-Accelerators and Beams* 17 (2 Feb. 2014), p. 11. DOI: 10.1103/PhysRevSTAB.17.024001.

[202] S.B. Geer Van Der and M.J. Loos de. "The general particle tracer code: design, implementation and application". PhD thesis. Department of Applied Physics, 2001. ISBN: 90-386-1739-9. DOI: 10.6100/IR542912.

[203] O. Adriani et al. "Technical design report eurogammas proposal for the ELI-NP gamma beam system". In: (July 2014). URL: https://arxiv.org/pdf/1407.3669.pdf.

[204] C.F. Ndiaye et al. "Low power commissioning of an innovative laser beam circulator for inverse Compton scattering γ-ray source". In: *Physical Review Accelerators and Beams* 22 (9 Sept. 2019), p. 25. DOI: 10.1103/PhysRevAccelBeams.22.093501.

[205] L. Giannessi et al. "Self-Amplified Spontaneous Emission Free-Electron Laser with an Energy-Chirped Electron Beam and Undulator Tapering". In: *Physical Review Letters* 106 (14 Apr. 2011), p. 4. DOI: 10.1103/PhysRevLett.106.144801.

[206] G. Marcus et al. "Time-domain measurement of a self-amplified spontaneous emission Free-Electron Laser with an energy-chirped electron beam and undulator tapering". In: *Applied Physics Letters* 101.13 (2012). DOI: 10.1063/1.4754612.

[207] M.K. Weikum et al. "EuPRAXIA - A compact, cost-efficient particle and radiation source". In: *Proc. of 25th International Conference on the Application of Accelerators in Research and Industry*. Vol. 2160. 1. 2019. DOI: 10.1063/1.5127692.

[208] V. Shpakov et al. "Longitudinal phase-space manipulation with beam-driven plasma wakefields". In: *Physical Review Letters* 122 (11 Mar. 2019), p. 5. DOI: 10.1103/PhysRevLett.122.114801.

[209] R. Akre, L. Bentson, P. Emma, and P. Krejcik. "A transverse RF deflecting structure for bunch length and phase space diagnostics". In: *PACS2001. Proceedings of the 2001 Particle Accelerator Conference (Cat. No. 01CH37268)*. Vol. 3. IEEE. June 2001, pp. 2353–2355. DOI: 10.1109/PAC.2001.987379.

[210] D. Gamba et al. "The CLEAR user facility at CERN". In: *Nuclear Instruments and Methods in Physics Research Section A: Accelerators, Spectrometers, Detectors and Associated Equipment* 909 (2018), pp. 480–483. ISSN: 0168-9002. DOI: 10.1016/j.nima.2017.11.080.

[211] I. Ben-Zvi. "The BNL accelerator test facility and experimental program". In: *AIP Conference Proceedings*. Vol. 279. 1. AIP. 1992, pp. 590–607. DOI: 10.1063/1.44076.

[212] D. Marx et al. "Simulation studies for characterizing ultrashort bunches using novel polarizable X-band transverse deflection structures". In: *Scientific Reports* 9.1 (Dec. 2019), pp. 1–17. DOI: 10.1038/s41598-019-56433-8.

[213] L. Sabato et al. "Effects of correlations between particle longitudinal positions and transverse plane on bunch length measurement: a case study on GBS electron LINAC at ELI-NP". In: *Measurement Science and Technology* 29.2 (Jan. 2018). DOI: 10.1088/1361-6501/aaa281.

[214] A. Cianchi et al. "Observations and diagnostics in high brightness beams". In: *Nuclear Instruments and Methods in Physics Research Section A: Accelerators, Spectrometers, Detectors and Associated Equipment* 829 (2016), pp. 343–347. ISSN: 0168-9002. DOI: 10.1016/j.nima.2016.03.076.

[215] L. Sabato et al. "RF deflector based measurements of the correlations between vertical and longitudinal planes at ELI–NP–GBS electron LINAC". In: *IBIC 2017*. 2017. DOI: 10.18429/JACoW-IBIC2017-WEPCC20.

[216] AT Division Project. *Resistive Small Aperture Quadrupole Magnets for the CLIC Test Facility 3 (CTF3)*. Tech. rep. 2003. URL: https://edms.cern.ch/ui/file/370107/1/QL3_TechnicalSpecification.pdf.

[217] M. Hüning. "Bunch Length Measurements using Transverse Deflecting Systems". In: *29th Linear Accelerator Conf.(LINAC'18), Beijing, China*. JACOW Publishing, Geneva, Switzerland. Sept. 2019, pp. 972–976. DOI: 10.18429/JACoW-LINAC2018-FR1A02.

[218] J. Tan et al. “Design, RF measurement, tuning, and high-power test of an X-band deflector for Soft X-ray Free Electron Lasers (SXFEL) at SINAP”. In: *Nuclear Instruments and Methods in Physics Research Section A: Accelerators, Spectrometers, Detectors and Associated Equipment* 930 (2019), pp. 210–219. DOI: 10.1016/j.nima.2019.03.093.

[219] Joint Committee for Guides in Metrology. “Evaluation of measurement data—guide to the expression of uncertainty in measurement”. In: *JCGM* 100.2008 (2008), pp. 1–116.

[220] D. Schulte. “Application of Advanced Accelerator Concepts for Colliders”. In: *Rev. Accel. Sci. Tech.* 09 (2016), pp. 209–233. DOI: 10.1142/S1793626816300103.

[221] M. Boland et al. *Updated baseline for a staged Compact Linear Collider*. CERN Yellow Reports: Monographs. Geneva: CERN, Aug. 2016. DOI: 10.5170/CERN-2016-004.

[222] G. Kube et al. “Transverse beam profile imaging of few-Micrometer beam sizes based on a scintillator screen”. In: *4th International Beam Instrumentation Conference*. 2016. DOI: 10.18429/JACoW-IBIC2015-TUPB012.

List of Figures

List of Tables